The Influence of Synthetic Gelatine on the Transient Loading and Response of Aluminium Panels Subjected to Blast Loading

Emma Osborne



This thesis is submitted for partial consideration towards the degree of Doctor of Philosophy in

The School of Mechanical, Aerospace and Civil Engineering at the University of Sheffield

March 2025

Abstract

This thesis has investigated the influence synthetic gelatine has on the structural response of aluminium panels from blast loading. To support this investigation, the compressive properties of synthetic gelatine in quasi-static and high-strain rate loading were characterised. Quasi-static compressive properties were determined experimentally using uniaxial compression experiments. The surface finish was found to affect the repeatability of these results, and friction was found to affect the stiffness response. Split-Hopkinson-pressure-bar experiments were conducted to explore high-strain rate loading. The experiments proved challenging at low velocities, with stress equilibrium not always being reached. The experiments found that the peak stress increased as the strain rate of the experiment increased. A numerical model was created for both these loading conditions, and good agreement was found with the experiments.

A novel experimental setup was developed using stereo-imaging to measure the effect synthetic gelatine has on the response of a clamped aluminium plate to an explosion. The addition of gelatine reduced the peak displacement and velocity of the target plate. It was also found to increase the time to peak displacement and velocity. These effects increased as the thickness of synthetic gelatine was increased. The gelatine was found to cause a lot of oscillations of the plate long after the loading had finished, lasting over 50 ms. The experimental setup was adapted to investigate the behaviour of deformable plates and synthetic gelatine in buried explosions. The plate responded later in the buried tests, but the peak transient displacement and velocity were found to be the same for a free-air and a buried charge. Showing that a shallow buried charge produces a similar effect on the target plate as the equivalent free-air charge in far-field explosions.

A simplified numerical simulation of blast-loaded hybrid gelatine/aluminium panels was developed to investigate the influence of gelatine on loading further. The model was found to correlate well with the free-air experimental data. Stresses were found to propagate across the width of the gelatine in the model, possibly causing the complex oscillations seen in the plate velocity data. This numerical model is a step toward understanding how a blast wave from an explosion propagates through synthetic gelatine.

Acknowledgements

Firstly, thank you to my supervisors, Prof. Genevieve Langdon and Prof. Sam Clarke, whose support has developed my skills as a researcher and dramatically improved my confidence. It is a pleasure to have two supervisors who are so interested in their research and dedicated to the development of their students.

To Dr Matteo Di Benedetti, Dr Harry Day and the rest of the Structures Lab teaching team. Teaching in the Structures Lab has neutered my teaching skills and increased my confidence in public speaking. I have found enjoyment in teaching and hope to continue to develop my skills in the future.

Thank you to all the technicians at Blastech for your support in carrying out the blast experiments for this PhD. I thoroughly enjoyed my time with you despite the sometimes challenging weather. Completing my experimental testing to such a high standard would not have been possible without you.

I would like to thank Andrew Fairburn for all your support in manufacturing my gelatine specimens, my gelatine baking as you liked to call it. Also, thank you to Holly Harris, who was always happy to answer my questions and support my well-being as a PhD student.

To all my friends in the blast research group and office F111, thank you for the great conversations at lunchtime and over coffee breaks. Your continued motivation has helped me keep going when progress is low. A special thank you to my friends in the Chapel Mountain Bikers and Chapel Runners groups for keeping me active and releasing stress.

Finally, thanks to all my family, especially my husband George and dog Lucy, your support has been really appreciated.

Contents

List of figures . . . ix
List of tables . . . x

1 Introduction **1**
1.1 Background . . . 1
1.2 Aims and Objectives . . . 2
1.3 Thesis Outline . . . 2

2 Literature Review **3**
2.1 Blast Injury . . . 3
2.2 Organic Ballistic Gelatine . . . 5
2.2.1 Quasi-Static Loading . . . 6
2.2.2 Dynamic Loading . . . 8
2.3 Modelling of Soft Materials . . . 11
2.4 Gelatine Behaviour during an Explosion . . . 15
2.5 Explosions in Air . . . 16
2.6 Behaviour of a Deformable Plate in an Explosion . . . 19
2.7 Buried Explosions . . . 20
2.8 Summary . . . 24

3 Behaviour of Synthetic Gelatine under Quasi-Static Loading **25**
3.1 Development of Experimental Method . . . 25
3.1.1 Initial Specimen Design and Manufacture . . . 25
3.1.2 Influence of Speckle Pattern Methods . . . 26
3.1.3 Effect of Surface Finish . . . 30
3.1.4 Preliminary Comparison to Organic 10% Gelatine . . . 31
3.1.5 Implications for Final Specimen Design and Manufacture . . . 31
3.2 Final Experimental Arrangement . . . 32
3.3 Experimental Results . . . 32
3.4 Insights from Simulations . . . 36
3.4.1 Model Description . . . 36
3.4.2 Influence of Constitutive Modelling Approach . . . 38
3.4.3 Extracting Material Properties . . . 43
3.4.4 Results from no Friction Model . . . 45
3.4.5 Determining the Friction Coefficient . . . 48
3.5 Summary of Findings . . . 50

4 Behaviour of Synthetic Gelatine under High Strain-Rate Loading **51**
4.1 Experimental Testing . . . 51
4.1.1 Specimen Design and Manufacture . . . 51
4.1.2 Test Arrangement . . . 52
4.1.3 Results and Discussion . . . 54

4.2 Numerical Analysis . . . 63
4.2.1 Numerical Model Set-up . . . 63
4.2.2 Results and Discussion . . . 64
4.3 Summary of Findings . . . 67

5 Behaviour of Synthetic Gelatine in an Explosion 68
5.1 Design of the Experiment . . . 68
5.1.1 Experimental Layout . . . 68
5.1.2 Threat . . . 68
5.1.3 Measurement Technique . . . 70
5.1.4 Design of Clamping Frame . . . 70
5.2 Specimen Design and Manufacture . . . 71
5.3 Experimental Results . . . 73
5.3.1 Test Series . . . 73
5.3.2 Bare Plates . . . 74
5.3.3 10 mm Gelatine Plates . . . 77
5.3.4 30 mm Gelatine Plates . . . 80
5.3.5 50 mm Gelatine Plates . . . 83
5.4 Discussion . . . 86
5.4.1 Post Test Photos . . . 86
5.4.2 Effect of Gelatine Thickness . . . 87
5.5 Numerical Analysis . . . 97
5.5.1 Initial Geometry . . . 97
5.5.2 Material Model and Equation of State . . . 98
5.5.3 Initial Results and Discussion . . . 100
5.5.4 Final Model Set-up . . . 102
5.5.5 Hybrid Gelatine/Aluminium Model . . . 105
5.6 Summary of Findings . . . 110

6 Behaviour of Synthetic Gelatine in a Buried Explosion 111
6.1 Soil Preparation . . . 112
6.2 Experimental Process . . . 113
6.3 Experimental Results . . . 115
6.3.1 Bare Plate Tests . . . 115
6.3.2 50 mm Gelatine Tests . . . 117
6.3.3 Shock Wave and Soil Ejecta Tracking . . . 121
6.4 Discussion . . . 129
6.4.1 Post Test Photos . . . 129
6.4.2 Comparison Between Free-air and Buried Data . . . 131
6.5 Summary of Findings . . . 139

7 Conclusions and Future Work 140
7.1 Conclusions . . . 140
7.2 Future Work . . . 141

List of Figures

2.1 Results from the dynamic compressibility experiment. Pressure–volumetric strain data for (a) stomach, (b) liver, (c) heart, and (d) lung tissues. (Saraf et al., 2007). 5
2.2 Sample held between the loading plates, left 1N loading and right 25% compression (Ravikumar et al., 2015). 6
2.3 Experimental results from Ravikumar et al. (2015) and Cronin and Falzon (2011). 7
2.4 Comparison between experimental and numerical data from Ravikumar et al. (2015). 7
2.5 Schematic of the split-Hopkinson-pressure-bar apparatus (Salisbury and Cronin, 2009). 8
2.6 Schematic of the Split-Hopkinson-pressure-bar apparatus (Kwon and Subhash, 2010). 10
2.7 Stress-strain curves for dynamic tests of 10% ballistic gelatine at different strain rates and comparison of stress-strain curves between dynamic and quasi-static conditions (Kwon and Subhash, 2010). 10
2.8 Stress-Strain curves of 10% ballistic gelatine at difference strain-rates (Richler and Rittel, 2014). 10
2.9 Stress-Strain curves of 10% ballistic gelatine at difference strain-rates (Salisbury and Cronin, 2009). 11
2.10 An example of Karahan experimental results compared to their model (Karahan et al., 2018). 12
2.11 Comparison between numerical and experimental images (Cuvillo et al., 2017). . 13
2.12 Results from bird impact at 150m/s (Cuvillo et al., 2017). 14
2.13 Comparison of modelling time from Aslam et al. (2020). 14
2.14 Fitzgerald experimental set up (Fitzgerald, 2019). 15
2.15 An example of results from Fitzgerald (2019). 15
2.16 Friedlander curve from (Wolf et al., 2009). 17
2.17 Numerical and experimental fireball expansion (Rigby et al., 2018). 18
2.18 Comparison of impulse data collected by Hopkinson pressure bars and DIC (Rigby et al., 2018). 19
2.19 Compiled peak pressure at each bar location (140 mm stand-off) (Rigby et al., 2016). 21
2.20 Confinement levels and geometry of test arrangement: (a) free air in Series A, (b) surface placement in Series B, (c) partial confinement in Series C and (d) full confinement in Series D (Clarke et al., 2020). 22
2.21 Pressure - time histories: Series A-D: influence of confinement (Clarke et al., 2020). 22
2.22 Pressure - time histories: Series D-F: influence of moisture content (Clarke et al., 2020). 23

3.1 Diagram of synthetic gelatine mould. 26
3.2 Synthetic gelatine mould and cutting process. 26
3.3 Painted gelatine specimen (left) and a gelatine specimen with tattoo paper (right). 27
3.4 Stress-strain results comparing speckle method. 27

3.5 The tattoo paper cracking as the gelatine specimen is compressed. 28
3.6 The process of dying gelatine. 28
3.7 Dyed gelatine (left) and dyed gelatine with final speckle pattern applied (right). . 29
3.8 Stress-strain results from tests on clear gelatine and dyed gelatine specimens. . . 29
3.9 Rough gelatine (left) and flat gelatine (right). 30
3.10 Engineering stress-strain graph comparing the variability caused by specimen manufacture. 30
3.11 Stress-strain results from initial experiments compared to Cronin and Falzon (2011) and Ravikumar et al. (2015). 31
3.12 Diagram of DIC set-up. 32
3.13 3D displacement plots from the DIC data of the gelatine at the start of the compression test (top) and at 45% strain (bottom). 33
3.14 Diagram showing the line slice used to extracted data points from the DIC data. 34
3.15 Horizontal displacement of gelatine specimen with no lubrication (red line: 40% strain). 34
3.16 Horizontal displacement of the gelatine specimen with lubrication (red line: 40% strain). 35
3.17 Engineering stress-strain graph for strain rates of 0.1 and 0.01 s^{-1}. 35
3.18 Engineering stress-strain graph comparing lubricated and friction specimens. . . 36
3.19 Geometry of the numerical model. 37
3.20 Engineering stress-strain results for different mesh sizes. 38
3.21 Simulation termination time vs mesh dimensions. 38
3.22 Stress-strain results from Linear Elastic material model compared to Cronin and Falzon (2011) and Ravikumar et al. (2015). 39
3.23 Stress-strain results from Elastic-Plastic material model compared to Cronin and Falzon (2011) and Ravikumar et al. (2015). 40
3.24 Stress-strain results from Mooney-Rivlin material model compared to Cronin and Falzon (2011) and Ravikumar et al. (2015). 41
3.25 Stress-strain results from Simplified Rubber/Foam material model compared to Cronin and Falzon (2011) and Ravikumar et al. (2015). 42
3.26 Diagram illustrating how the volume of gelatine was calculated. 43
3.27 Volumetric strain results. 44
3.28 Bulk modulus results. 44
3.29 Poisson's ratio results. 45
3.30 Results from numerical model with friction load curve. 46
3.31 Results from numerical model with lubricated load curve. 46
3.32 Results from numerical model with no friction factors. 47
3.33 Geometry of the numerical model with the loading plates added. 48
3.34 Results from numerical model with lubricated load curve with different friction factors. 49
3.35 Results from numerical model with friction load curve with different friction factors. 49

4.1 Drawing of gelatine mould and gelatine weighted out and ready to go in the oven. 52
4.2 Diagram of the gas gun and SHPB apparatus. 53
4.3 Right is strain gauge poition on the bars and left is the half Wheatstone bridge. . 54
4.4 Strain gauge signal from nylon tap test; time from striker impact. 54
4.5 Strain gauge signal without pulse shaping; time from striker impact. 56
4.6 Strain gauge signal with pulse shaping; time from striker impact. 56
4.7 Strain rate against specimen strain for a striker velocity of 5 m/s. 57
4.8 Strain rate against specimen strain for a striker velocity of 7 m/s. 58
4.9 Strain rate against specimen strain for a striker velocity of 9 m/s. 58

4.10 Front and back stress for a striker velocity of 5 m/s; time from specimen impact. 59
4.11 Front and back stress for a striker velocity of 7 m/s; time from specimen impact. 59
4.12 Front and back stress for a striker velocity of 9 m/s; time from specimen impact. 60
4.13 Stress - strain behaviour for a striker velocity of 5 m/s. 61
4.14 Stress - strain behaviour for a striker velocity of 7 m/s. 61
4.15 Stress - strain behaviour for a striker velocity of 9 m/s. 62
4.16 Stress - strain behaviour for all strain rates tested. 62
4.17 Stress in the incident pressure bar and the first gauge location for striker velocity of 7 m/s; time from striker impact. 63
4.18 Stress-strain load curve for numerical model. 64
4.19 Front and back stress for the numerical model; time from specimen impact. . . . 65
4.20 Front stress in the experiment and numerical model; time from specimen impact. 65
4.21 Back stress in the experiment and numerical model; time from specimen impact. 66
4.22 Mid-stress in the experiment and numerical model; time from specimen impact. . 66
4.23 Stress vs strain in the experiment and numerical model. 67

5.1 Engineering drawing of the Appliqué testing arrangement. 69
5.2 Charge dimensions and stand-off distance to the clamping frame. 69
5.3 Dimensions in mm of the camera's view and photograph of the cameras mounted to the testing frame. 70
5.4 Dimensions in mm of the clamping frame (right) and the target plates (left). . . 71
5.5 Manufacturing process for gelatine specimens; top is moulding process, bottom is final specimens and glueing to the plates. 72
5.6 Preparation of target plates; a) white spray paint, b) applying the speckle pattern and c) clamped plate with gelatine. 72
5.7 Full plate displacement over time of a bare plate. 75
5.8 Displacement over time across the width of the plate for a bare plate test. 76
5.9 Midpoint displacement for the bare plates. 76
5.10 a) Velocity over time across the width of the plate and b) midpoint velocity for the bare plates. 77
5.11 Full plate displacement over time of a plate with 10 mm of gelatine in front. . . . 78
5.12 Displacement over time across the width of a plate with 10 mm of gelatine in front. 78
5.13 Displacement profile of a plate with 10 mm of gelatine in front. 79
5.14 Midpoint displacement for the plates with 10 mm of gelatine in front. 79
5.15 Velocity over time across the width of a plate with 10 mm of gelatine in front. . . 80
5.16 Midpoint velocity for the plates with 10 mm of gelatine in front. 80
5.17 Full plate displacement over time of a plate with 30 mm of gelatine in front. . . . 81
5.18 Displacement over time across the width of a plate with 30 mm of gelatine in front. 81
5.19 Displacement profile of a plate with 30 mm of gelatine in front. 82
5.20 Midpoint displacement for the plates with 30 mm of gelatine in front. 82
5.21 Velocity over time across the width of a plate with 30 mm of gelatine in front. . . 83
5.22 Midpoint velocity for the plates with 30 mm of gelatine in front. 83
5.23 Full plate displacement over time of a plate with 50 mm of gelatine in front. . . . 84
5.24 Displacement over time across the width of a plate with 50 mm of gelatine in front. 84
5.25 Displacement profile of a plate with 50 mm of gelatine in front. 85
5.26 Midpoint displacement for the plates with 50 mm of gelatine in front. 85
5.27 Velocity over time across the width of a plate with 50 mm of gelatine in front. . . 86
5.28 Midpoint velocity for the plates with 50 mm of gelatine in front. 86
5.29 Post-test photos of a bare plate and 10 mm gelatine, 30 mm gelatine and 50 mm gelatine experiments 87
5.30 Displacement over time of a bare plate. 88

5.31 Displacement over time of a plate with 10 mm of gelatine. 88
5.32 Displacement over time of a plate with 30 mm of gelatine. 89
5.33 Displacement over time of a plate with 50 mm of gelatine. 89
5.34 Midpoint displacement for a bare plate and 10 mm, 30 mm and 50 mm of gelatine. 90
5.35 Velocity over time of a bare plate, velocity scale normalised. 91
5.36 Velocity over time of a plate with 10 mm of gelatine, velocity scale normalised. . 91
5.37 Velocity over time of a plate with 30 mm of gelatine, velocity scale normalised. . 91
5.38 Velocity over time of a plate with 50 mm of gelatine, velocity scale normalised. . 92
5.39 Midpoint velocity for a bare plate and 10 mm, 30 mm and 50 mm of gelatine. . . 92
5.40 Velocity for a bare plate and 10 mm gelatine plate. 93
5.41 Full plate velocity for a bare plate. 93
5.42 Full plate velocity for a 10 mm gelatine plate. 94
5.43 Velocity for a 30 mm and 50 mm gelatine plate. 95
5.44 Full plate velocity for a 30 mm gelatine plate. 96
5.45 Full plate velocity for a 50 mm gelatine plate. 96
5.46 Numerical model layout; left is the full domain, right is the clamp and plate with an outline version to view spring locations. 98
5.47 a) Displacement and b) velocity for the shell plate model compared to Test 208 at the midpoint (blue), 50 mm (green), 100 mm (red) and 125 mm (black) across the plate. 100
5.48 Velocity for a quarter of the plate for the shell plate model compared to Test 208. 101
5.49 a) Displacement and b) velocity for the solid plate model compared to Test 208 at the midpoint (blue), 50 mm (green), 100 mm (red) and 125 mm (black) across the plate. 102
5.50 Velocity for a quarter of the plate for the solid plate model compared to Test 208. 103
5.51 Displacement and velocity for different number of elements in plate thickness compared to Test 208 at the midpoint (blue), 50 mm (green), 100 mm (red) and 125 mm (black) across the plate. 104
5.52 Numerical model layout with 50 mm of gelatine. 105
5.53 Displacement for the gelatine model compared to Test 110 at the midpoint (blue), 50 mm (green), 100 mm (red) and 125 mm (black) across the plate; a) 15 ms, b) 4 ms. 106
5.54 Velocity for the gelatine model compared to Test 110 at the midpoint (blue), 50 mm (green), 100 mm (red) and 125 mm (black) across the plate. 107
5.55 Vertical stress data from the numerical model; t = 0.35 ms - t = 0.70 ms. 108
5.56 Vertical stress data from the numerical model; t = 0.75 ms - t = 2.55 ms.. 109

6.1 Sand bin dimensions, mm. 111
6.2 Photos of the sand bin preparation process; a) finished sand bin, b) sealed sand bin, c) mixing the sand, d) positioning of the charge. 112
6.3 Image showing calibration points used to measure pixel size. 114
6.4 Full plate displacement for a bare plate for a buried charge. 115
6.5 Displacement over time of a bare plate for a buried charge. 116
6.6 Midpoint displacement for a bare plate for a buried charge. 116
6.7 a) Velocity over time and b) midpoint Velocity of a bare plate for a buried charge. 117
6.8 Full plate displacement for a plate with 50 mm of gelatine in front for a buried charge. 118
6.9 Plate displacement profile of a plate with 50 mm of gelatine in front for a buried charge. 118
6.10 Displacement over time of a plate with 50 mm of gelatine in front for a buried charge, 15 ms. 119

6.11 Displacement over time of a plate with 50 mm of gelatine in front for a buried charge. . . . 119
6.12 Midpoint displacement for a plate with 50 mm of gelatine in front for a buried charge. . . . 120
6.13 Velocity over time of a plate with 50 mm of gelatine in front for a buried charge. 120
6.14 Midpoint velocity of a plate with 50 mm of gelatine in front for a buried charge. 121
6.15 Image difference plot where the lighter pixel correspond to movement in the video. 121
6.16 Image difference plot with polynomial of the shock wave at t = 1.113 ms for Test 215. . . . 122
6.17 Image difference plot with polynomial of the shock wave at t = 1.126 ms for Test 215. . . . 122
6.18 Midpoint velocity for Tests 215 and 214 with the arrival time of the shock wave and soil ejecta indicated. . . . 123
6.19 Raw image plot with polynomial of the shock wave at t = 1.126 ms for Test 215. 124
6.20 Raw image plot with polynomial of the soil ejecta at t = 1.3506 ms for Test 215. 124
6.21 Raw image plot with polynomial of the soil ejecta at t = 1.3631 ms for Test 215. 125
6.22 Plate displacement profiles for Test 215 plotted with the soil front curve fit at t = 1.36 ms. . . . 126
6.23 Plate displacement profiles for Test 214 plotted with the soil front curve fit at t = 1.29 ms. . . . 126
6.24 Image difference plot with polynomial of the shock wave at t = 0.944 ms for Test 213. . . . 127
6.25 Raw image plot with polynomial of the shock wave at t = 0.944 ms for Test 213. 127
6.26 a) Midpoint velocity for the 50 mm gelatine tests with the arrival time of the shock wave indicated, b) midpoint velocity for the 50 mm gelatine tests with Test 210 shifted. . . . 128
6.27 Raw image plot with polynomial of the shock wave at t = 0.848 ms for Test 210. 128
6.28 Post-test photos of a bare plate for a buried charge experiment. . . . 129
6.29 Post-test photos of a plate with 50 mm of gelatine for a buried charge experiment. 130
6.30 Displacement over time of a bare plate for a) a free air and b) a buried charge. . 131
6.31 Midpoint displacement for a bare plate for a free air and a buried charge; a) is raw data and b) is shifted so the peak displacement time line-up. . . . 132
6.32 Influence of confinement from Clarke et al. (2020). . . . 132
6.33 Velocity over time of a bare plate for a) a free air and b) a buried charge. . . . 133
6.34 Midpoint velocity for a bare plate for a free air and a buried charge; a) is raw data and b) is shifted so the peak velocity time line-up. . . . 133
6.35 Plate velocity across five time steps for a buried (left) and free-air (right) experiment. . . . 134
6.36 Velocity across the width of a bare plate for a) a free air and b) a buried charge. 135
6.37 Displacement over time of a plate with 50 mm of gelatine for a) a free air and b) a buried charge. . . . 136
6.38 Midpoint displacement for plates with 50 mm of gelatine for a free air and a buried charge; a) & c) is raw data and b) & d) are shifted so the peak displacements line-up. . . . 137
6.39 Velocity over time of a plate with 50 mm of gelatine for a) a free air and b) a buried charge. . . . 138
6.40 Midpoint velocity for plates with 50 mm of gelatine for a free air and a buried charge; a) is raw data and b) is shifted so the arrival times line-up. . . . 139

List of Tables

2.1 Wave speeds of different SHPB bar materials, data from Salisbury and Cronin (2009) and Curry (2011). 9

3.1 DIC hardware and analysis parameters. 32
3.2 Initial material properties for synthetic gelatine. 43
3.3 Material properties for synthetic gelatine from DIC analysis. 45

4.1 List of SHPB calibration experiments. 55
4.2 List of SHPB experiments with gelatine specimens. 55
4.3 Material properties for synthetic gelatine. 63

5.1 Test series for free air blast experiments. 73
5.2 Material model properties for air and PE4. 99
5.3 Equation of state model properties for air and PE4. 99
5.4 Material model properties for aluminium and mild steel. 99

6.1 Test series for the buried blast experiments. 113

Chapter 1

Introduction

1.1 Background

After conflicts have finished, small anti-personnel landmines and explosive remnants of war (ERW) are often left behind, which can cause injuries to civilians and military personnel. Injuries to the lower extremities of the body make up a large portion of the total blast injuries, with 81% of injured UK personnel receiving lower body injuries (Elgy et al., 2020). Previous research has looked closely at the resulting primary injuries to the lower leg from explosions (Cronin et al., 2011). However, limited research has looked at the effect the blast wave has on the upper leg as it transmits through the tissue. The blast wave is thought to produce forces that cause changes in soft tissues at the cellular and molecular levels, prompting physiological responses that have long-term implications for functional recovery (Spear et al., 2015). These include issues such as progressive soft tissue necrosis ('cell death') and heterotopic ossification (abnormal bone growth).

When studying the behaviour of the human body in dangerous scenarios, ballistic gelatine is often used as a stimulant for human tissue. This material is used because it exhibits similar properties to human tissue and is more ethical than using post-mortem human tissue samples or animals. Currently, experimental studies lack robust sensing methodologies to characterise shock wave transmission and pressures inside soft tissues reliably. Pressure sensor data have been shown to vary depending on the sensor orientation and air gaps (Clemedson and Jönsson, 1961). Sensors have also been found to change the stiffness of the soft tissue that is being studied (Clemedson et al., 1969). Using numerical models alongside experimental testing is key to better understanding the spatial behaviour of soft tissue; however, these models need to be validated.

Characterising the blast wave transmission through soft tissues is essential for understanding longer-term blast injuries caused by exposure to shock waves. More research is needed to determine the best numerical method to characterise the behaviour of soft tissue during an explosion and to develop an improved experimental plan to validate this model.

1.2 Aims and Objectives

This thesis aims to ascertain the influence synthetic gelatine has on the structural response of aluminium panels from blast loading and investigate the influence of the charge burial condition on the response. The compressive properties of synthetic gelatine at quasi-static and elevated strain rates will be analysed to develop a simplified numerical simulation of blast-loaded hybrid gelatine/aluminium panels. The experimental dataset will be used to validate the numerical simulation and develop an understanding of the mechanisms of shock wave propagation through gelatine. To meet these aims, the project therefore has the following objectives:

- Develop an experimental set-up to measure the effect gelatine has on the deformation of aluminium panels from an explosion, aiming to increase reliability.
- Investigate how detonating an explosive charge in soil affects the response of the hybrid gelatine/aluminium panels.
- Determine compressive properties of synthetic gelatine at quasi-static and elevated strain rates.
- Utilise a simplified numerical simulation of blast-loaded hybrid gelatine/aluminium panels to increase understanding of shock wave propagation through gelatine during blast loading.

1.3 Thesis Outline

An overview of relevant literature on the characterisation and response of soft materials to quasi-static, dynamic and blast loading is contained in Chapter 2. Chapter 3 details the characterisation of synthetic gelatine subjected to quasi-static compression. The behaviour of synthetic gelatine at elevated strain rates was determined through split-Hopkinson-pressure-bar experiments; this investigation's results are reported in Chapter 4. Chapter 5 investigates the effect synthetic gelatine has on the response of aluminium panels subjected to blast loading. A numerical model was created to simulate these experiments. More experiments were conducted in Chapter 6 to investigate how the loading from an explosion is affected when a charge is buried. Finally, Chapter 7 summarises the main conclusions from this current work and identifies opportunities for further research.

Chapter 2

Literature Review

2.1 Blast Injury

Blast injury is a term that has been used to encompass changes to the human body caused by exposure to an explosion, which can be internal or external injuries (Clemedson, 1956). Clemedson and Pettersson (1955) proposed that the primary damage to the body was not caused by the static pressures from the blast but by the dynamic unequal acceleration of body parts with different masses. Previous research has found that the shock wave from an explosive is changed by reflections and scattering when propagating through body parts. It's suggested that overpressure injuries are underreported due to the complicated multiple-injury scenario (Phillips et al., 1988). Cause of death may be determined as fragments because they are more visible when actual death could have been overpressure injuries.

Anti-personnel (AP) landmines are the most common form of landmines and are often left behind in communities after conflicts have finished (Cronin et al., 2011). Both AP and improvised mines were banned in 1999 under the terms of the Mine Ban Treaty (ICBL-CMC, 2024); however, they are still in use worldwide. In 2023, AP mines caused 833 casualties, which is the highest annual number on record since 2011. Civilians make up over 80% of all landmine casualties. This data highlights that landmines are still a threat. These landmines can be on the surface or buried below ground level, typically containing 28 to 500g of explosive. Injuries to the lower extremities of the body make up a large portion of the total blast injuries, with 81% of injured UK personnel receiving lower body injuries (Elgy et al., 2020). The degree of injuries to the lower extremities depends on proximity, variability of the explosive output, conditions of the soil around it and whether protection is worn (Cronin et al., 2011). The most common injuries in this region of the body include heel, ankle and lower tibia injuries. The propagation of a shock wave through the body is a complex event as the inhomogeneity of different regions influences it. For a proper understanding of the biological effects of shock waves, studies on the effects different body tissue has on the incident shock are needed (Clemedson, 1956).

Research into the behaviour of different body parts to blast loading has previously been investigated with small animals such as rabbits. Clemedson and Criborn (1955) initially attached strain gauges to various parts of rabbits and exposed them to open field and chamber blasts. Different levels of deflection were seen across the body, with the Thorax seeing very rapid deflection and the abdomen seeing long-lasting indentations. This early study highlights that various body parts respond differently to a shock wave, possibly linked to density, elasticity and other material properties. Clemedson and Pettersson (1955) performed further investigations by inserting pressure transducers into rabbit's skull, right thorax cavity, upper abdomen and femoral musculature (upper leg). Advances in pressure transducers were utilised later to measure the behaviour inside the lung (Clemedson and Jönsson, 1961). The transmission of

pressure was found to be a behaviour that was different throughout the body. For example, homogeneous brain tissue modified the signal much less than the thorax, which is mainly filled with air (Clemedson and Pettersson, 1955). The blast was found to cause damped vibrations arising from the interior movement of the thoracic tissue. Movement like this can cause significant lung damage. It is thought that similar phenomena will occur in other gas-containing parts of the body, such as the intestinal tract and the gut.

In subsequent research by Clemedson et al. (1969), the displacement of the thoracic and abdominal walls was investigated with pressure transducers and impulse gauges fixed to the animal's body. Lung injury was recorded by passing a pressure transducer through the mouth and down to the bronchus. The thorax and abdomen were exposed to the blast in isolation by placing them behind a cylinder with cut-outs exposing certain body parts. Chest-exposed animals recorded movement of both the thorax and abdominal walls, whereas abdominal-exposure animals saw no thoracic injuries. Attempts have been made to correlate inward movement of the chest wall with lung injuries. Clemedson's results suggested that no single parameter causes lung injury but rather a combination of amplitude, velocity and acceleration. The experiments when only the abdomen was exposed to the blast showed a significant variation in the severity of the injury, possibly caused by different levels of gas in the intestines.

Past research studies investigating the effect of dynamic loading on human tissue have tested actual human tissue samples. For example, Saraf et al. (2007) used post-mortem tissue samples from the heart, liver, lung and stomach of people aged between 18 and 30 whose death was not caused by damage to these organs. The axial and shear response of tissue samples at strain rates from 300 to 5000s^{-1} was determined using a confined split-Hopkinson-pressure-bar (SHPB) apparatus with aluminium bars. However, significant variations in responses were found from sample to sample, which may result from the variations in fibre orientation within the set of samples. There is also considerable variation in the material properties from person to person, causing samples to behave differently. The variation can be seen in Figure 2.1.

Spear et al. (2015) investigated whether blast injury to a limb resulted in damage to the endothelium (blood vessels), shown by the presence of endothelial cells in the circulation. The blood vessels were investigated by instrumenting the left carotid artery of rabbits to measure blood pressure and take samples. The animals were exposed to a blast wave via a compressed air device. No increase in the numbers of endothelial cells was observed in the no blast, low and medium exposure groups; however, significantly higher numbers were seen in the high exposure group. Visual observations found increasing pathological changes in the tissue from low to high exposure. The study was not of sufficient duration to determine the long-term effects of these responses. These findings show that the effects of haemorrhage and resulting shock could exacerbate blast injuries, so even low levels of blast exposure could have difficult outcomes.

Clemedson and Jönsson (1961) raised several uncertainties and difficulties with earlier measurement techniques. It was difficult to verify the pressure readings inside the animals with ones measured outside because pressure varies with distance to the charge and will also vary across the curved animal's surface. Also, the orientation of the pressure transducer with respect to the shock wave will affect the values recorded. Clemedson and Jönsson (1961) found that improper orientation of the pressure transducer and there being a gap between the sensor and the object resulted in a reduction of the maximum pressure by 25%. Also, the fur was found to cause disturbances in the pressure readings. Once the first pressure disturbance is recorded, it is difficult to determine whether any following disturbances are due to the explosion or due to the relative movement of the body. Instrumentation of the thoracic and abdomen walls was found to considerably increase the inward deflection, possibly due to the change in stiffness of

the system affecting the internal pressures of the system (Clemedson et al., 1969).

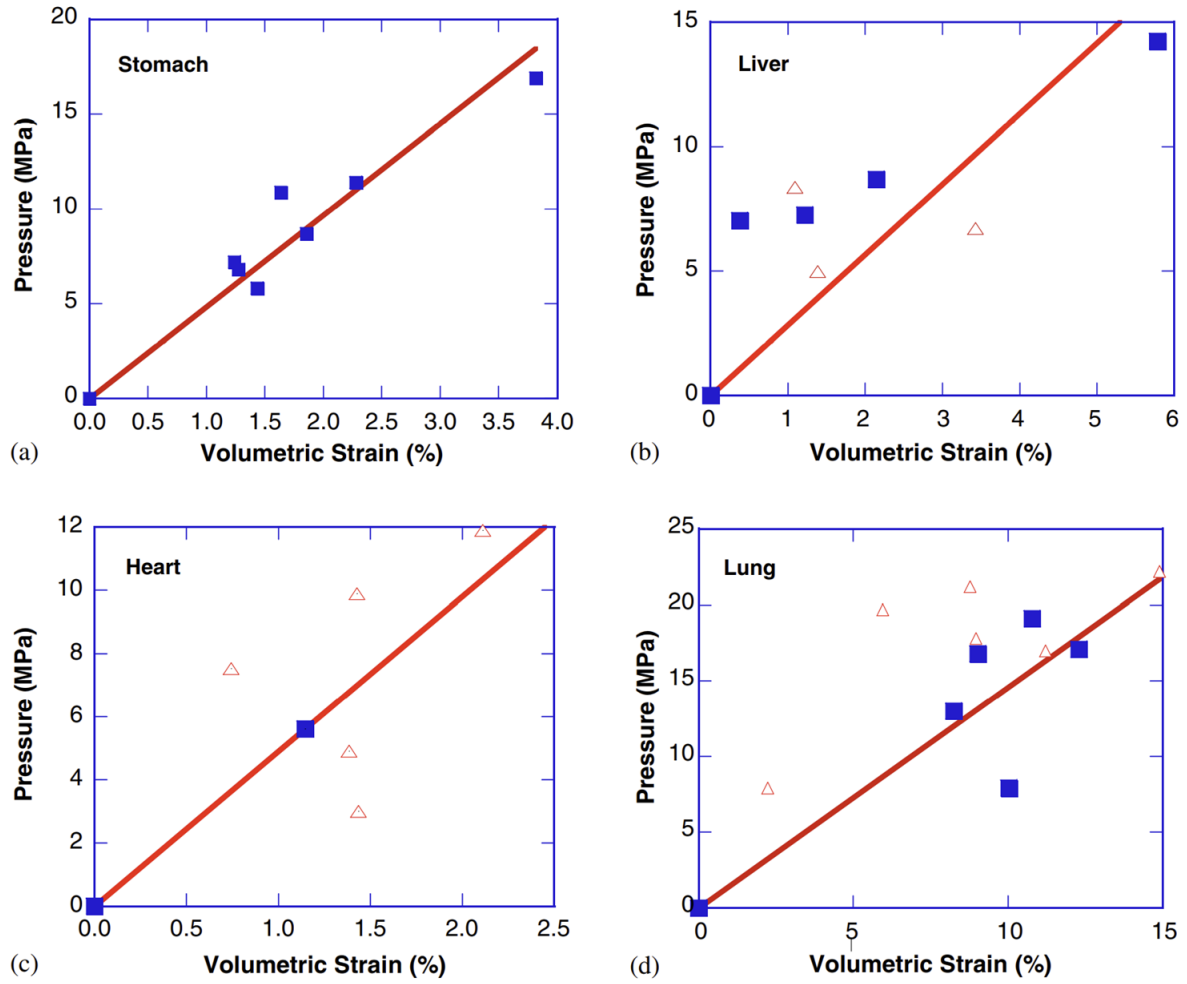

Figure 2.1: Results from the dynamic compressibility experiment. Pressure–volumetric strain data for (a) stomach, (b) liver, (c) heart, and (d) lung tissues. (Saraf et al., 2007).

2.2 Organic Ballistic Gelatine

Ballistic gelatine is widely used in ballistic research as a human tissue substitute, as it exhibits similar properties (Cronin and Falzon, 2011). The ballistic gelatine used in past research was an organic material made from pigs. A ballistic gelatine block is made by mixing gelatine powder with water at high temperatures. The percentage of gelatine powder added classifies the gelatine blocks; 10% and 20% are the most common. For example, 10% gelatine is produced by adding 1 part gelatine powder to 9 parts water. To validate that the gelatine block has been prepared correctly, they are calibrated using the procedure set out by Jussila (2004), where the gelatine is impacted several times using an air rifle (Cronin and Falzon, 2011). The speed and depth of penetration are recorded.

Organic ballistic gelatine is susceptible to small changes in temperature, and the preparation and storage conditioning vastly affect its mechanical behaviour. In its powder form, gelatine can be stored for years in a dry and dark place at room temperature, provided it is not exposed to formaldehyde, as this will make it insoluble in water (Jussila, 2004). Once the gelatine block

is moulded, it needs to be refrigerated at 4°C and can be stored for up to 2 days, after which it starts to biodegrade. When moulding, storage time can be increased by adding a microbial growth inhibitor to the mixture. The temperature of the gelatine block needs to be closely monitored when testing, as gelatine will start to break down and melt at temperatures above 35°C.

Cronin and Falzon (2011) evaluated the effect of ageing time and temperature on the mechanical properties of organic gelatine by executing mechanical compression tests. The testing temperature was increased above 4°C, and the failure stress was found to decrease as the temperature increased (Cronin and Falzon, 2011). A longer ageing time was found to reduce the strength of the material, with the optimum time being 72 hours. Jussila (2004) developed a standard method for preparing ballistic gelatine and a method for validating that the material's behaviour is correct. This method helps achieve homogenous gelatine blocks of consistent quality and helps increase the consistency of gelatine used across research projects.

2.2.1 Quasi-Static Loading

The behaviour of ballistic gelatine varies considerably depending on the loading rate it is subjected to. Cronin and Falzon (2011) and Ravikumar et al. (2015) tested gelatine under uniaxial compression at various strain rates. Figure 2.3 includes stress-strain data from their experiments at three strain rates. Cronin used a lubricant between the specimen and the loading plates, and Ravikumar did not and terminated the tests at 25% strain. It appears that increasing the strain rate resulted in higher stresses. By comparing Ravikumar's 0.001/s data and Cronin's data, it is evident that lubrication between the specimen and loading plates reduces the stiffness of gelatine. This data highlights that the boundary conditions influence the response of gelatine in compression. When approaching failure, vertical cracks appeared along the length of the specimen, with loading quickly dropping to zero as the specimen fractured (Cronin and Falzon, 2011). An exponential relationship between the loading and resulting deformation can also be seen in these results. Experimental images of this study's compression testing of ballistic gelatine are pictured in Figure 2.2. Some non-uniformity in the deformation of the gelatine can be seen in these pictures. These tests provide a base for high-strain rate testing.

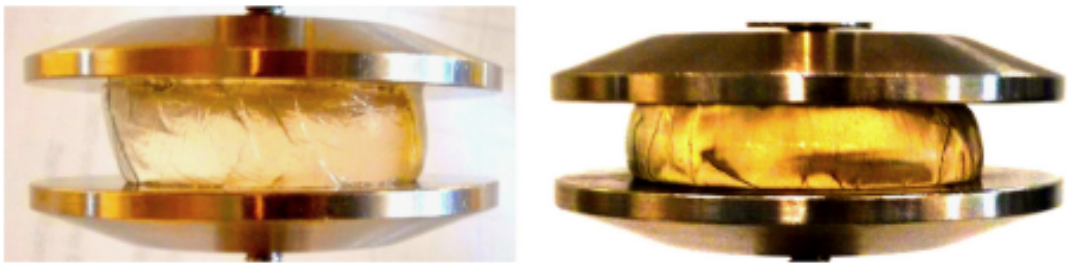

Figure 2.2: Sample held between the loading plates, left 1N loading and right 25% compression (Ravikumar et al., 2015).

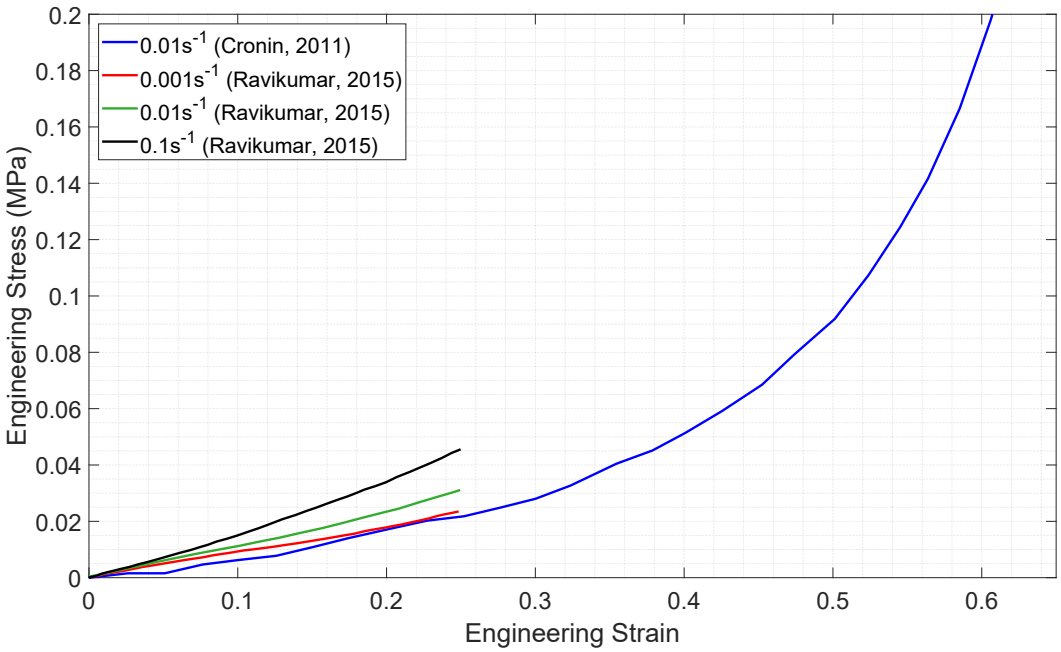

Figure 2.3: Experimental results from Ravikumar et al. (2015) and Cronin and Falzon (2011).

Ravikumar et al. (2015) also used Abaqus FE software to model their experiments, using the single-term Ogden visco-hyperelastic constitutive approach. The experiment was modelled as an axisymmetric 2D mesh, with Tie constraints used at the specimen–plate interface to account for friction. Other models, such as neo-Hookean and Mooney–Rivlin (both special cases of the Ogden model), were considered but could not fully describe the behaviour observed during the compression experiments. The parameters for this model were optimised using Abaqus. Figure 2.4 below compares the load-displacement curves for three different loading rates recorded in the experiments to the relationship predicted by the numerical model. The chosen numerical model closely follows the shape of the experimental results.

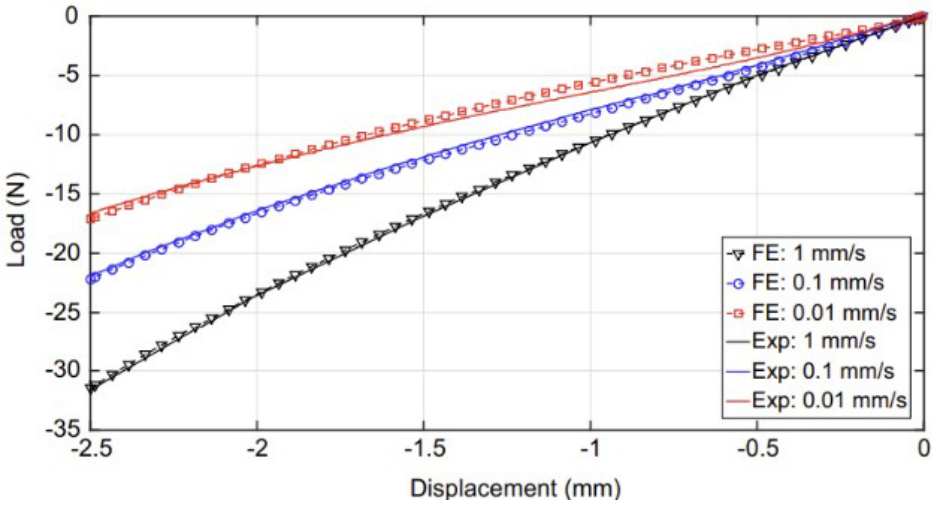

Figure 2.4: Comparison between experimental and numerical data from Ravikumar et al. (2015).

2.2.2 Dynamic Loading

Testing Methodology

Hopkinson pressure bars (HPBs) can be utilised to measure the dynamic properties of a material (Kolsky, 1949). This is achieved by placing a material sample between two HPBs and impacting one end with a striker bar. This impact sends a compressive wave down the incident bar, uninterrupted until it reaches the sample. A proportion of the wave is transmitted through the sample into the transmitter bar, applying a high-speed compression load to the sample. Strain gauges are placed on the bars to record the wave propagation. This setup is called a Split-Hopkinson-pressure-bar (SHPB) apparatus. SHPBs are highly effective for testing materials at high strain rates as they can implement a relatively uniform strain rate throughout the experiment (Richler and Rittel, 2014). However, this is highly dependent on the bar properties and the material response of the specimen. The velocity of the striker bar controls the amplitude of the compressive wave, and the length of the striker determines the duration of the test (Salisbury and Cronin, 2009).

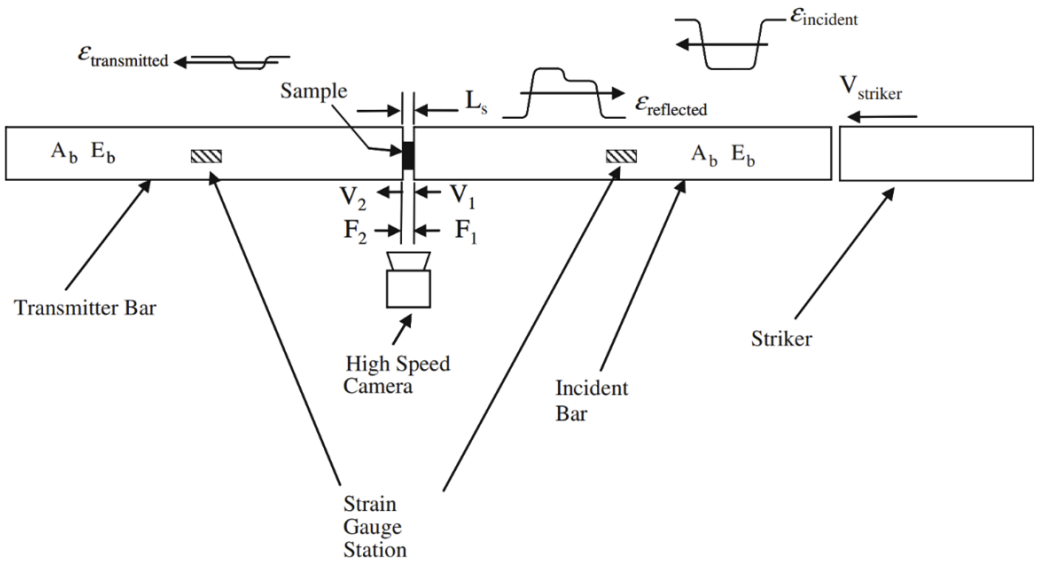

Figure 2.5: Schematic of the split-Hopkinson-pressure-bar apparatus (Salisbury and Cronin, 2009).

Dynamic stress equilibrium helps ensure uniform deformation of the specimen (Salisbury and Cronin, 2009). When testing gelatine, it is recommended to use a specimen with a small diameter-to-length ratio to minimise inertial and friction/barrelling effects during the test. Petroleum jelly can also be placed on the end of the incident bar to act as a pulse shaper to help the specimen reach dynamic stress equilibrium (Richler and Rittel, 2014).

HPBs are conventionally made from steel, which presents a problem when testing low-impedance materials such as gelatine. Gelatine has a low wave speed and a low density. Therefore, conventional metallic bars typically produce considerable noise in the signal. This noise can hide the true transmitted signal because the high impedance mismatch produces a small transmitted signal. This noise can be addressed by changing the bar material to a low-impedance material closer to the gelatine. Salisbury and Cronin (2009) trialled bars of aluminium, Acrylic and low-density polyethene (LDPE). Acrylic bars improved the signal-to-noise ratio the most due to a better impedance. Additionally, Acrylic results in a slower rise time compared to metallic bars, allowing for dynamic stress equilibrium and uniformity of deformation in the specimen (Salisbury and Cronin, 2009).

Polymeric SHPBs also result in wave attenuation and dispersion of the wave as it travels along the bar to the bar-specimen interface (Salisbury and Cronin, 2009). This is a problem because the material response is determined by the difference between the strain gauge signals, which are altered by attenuation and dispersion. This disruption can be corrected by comparing signals at multiple gauge locations. Using Bacon's method (1998), these are transformed into the frequency domain through a Fourier transformation. Bacon's method uses the assumption that the relationship between attenuation and dispersion is linear in the frequency domain. The signals are then compared to find the propagation coefficient needed to correct the gauge signal.

Curry (2011) (2012) tried three polymer materials (Nylon, Polymethyl Methacrylate (PMMA or Acrylic) and Polycarbonate) in SHPB experiments to characterise soft, viscoelastic materials. Calibration methods for polymer bars were extensively investigated, with the technique by Bacon being preferred as it required no parameter-driven models or iterative processes (Curry, 2011). The polycarbonate bar was recommended as the best of the three materials, as the SHPB data readings were tightly grouped, and wave peak shifts correlated well with data reads from a Magnesium bar that was used for validation.

To overcome polymer bars' dispersion and attenuation effects, Richler and Rittel (2014) proposed a novel, simple experimental setup using aluminium bars to investigate the dynamic material response of gelatine. Aluminium is on the lower end of the impedance scale for metals but still has a relatively high acoustic impedance compared to gelatine. To overcome this, Richer and Rittel (2014) attached two Flexiforce commercial pressure-sensitive force sensors on both specimen-bar interfaces to directly measure the difference in the forces. In addition, one strain gauge was placed on the incident bar to measure the strain that remained unchanged by the gelatine (Richler and Rittel, 2014). The force sensors were calibrated by placing the force sensor between the incident and transmission bars without a specimen, verifying that the measurement was the same when the striker propagated a wave down the system.

The literature discussed in this section has highlighted a wide range of previously used bar materials in SHPB gelatine testing. The wave speed of the material is an important factor when determining the impedance mismatch. The wave speed of each material reported by each paper is included in Table 2.1, and the one with a wave speed closest to gelatine will reduce the impedance mismatch.

Bar material	Wave speed (m/s)
Aluminium	5052
PMMA (Acrylic)	1716, 2180
Low-density polyethene (LDPE)	917
Nylon	1710
Polycarbonate	1436

Table 2.1: Wave speeds of different SHPB bar materials, data from Salisbury and Cronin (2009) and Curry (2011).

Dynamic Behaviour

Kwon and Subhash (2010) used polymer bars to characterise gelatine at strain - rates of 2000 to 3200 s^{-1}. Three strain gauges were placed on the incident bar to capture the dispersion and attenuation. Kwon's study shows that gelatine is highly sensitive to strain rate, with the dynamic results being 1000 times the static results (Figure 2.7). However, these stress-strain curves are very different in shape from other SHPB studies looking at the dynamic behaviour of

gelatine, see Figures 2.7 - 2.9. Richler and Rittel (2014) found good agreement with Salisbury's stress-strain curves for similar strain rates. Their results show that gelatine's stiffness increases with increasing strain rate. Kwon's results produced an almost metallic response for the gelatine.

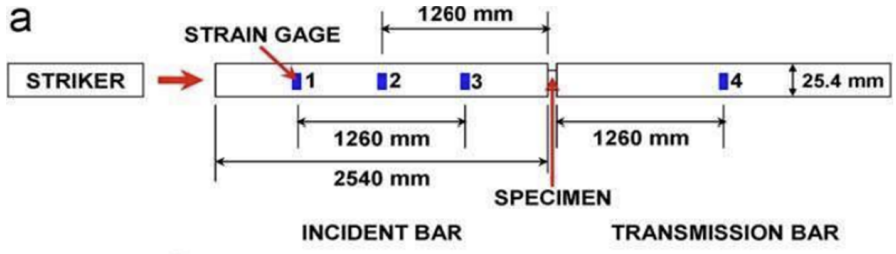

Figure 2.6: Schematic of the Split-Hopkinson-pressure-bar apparatus (Kwon and Subhash, 2010).

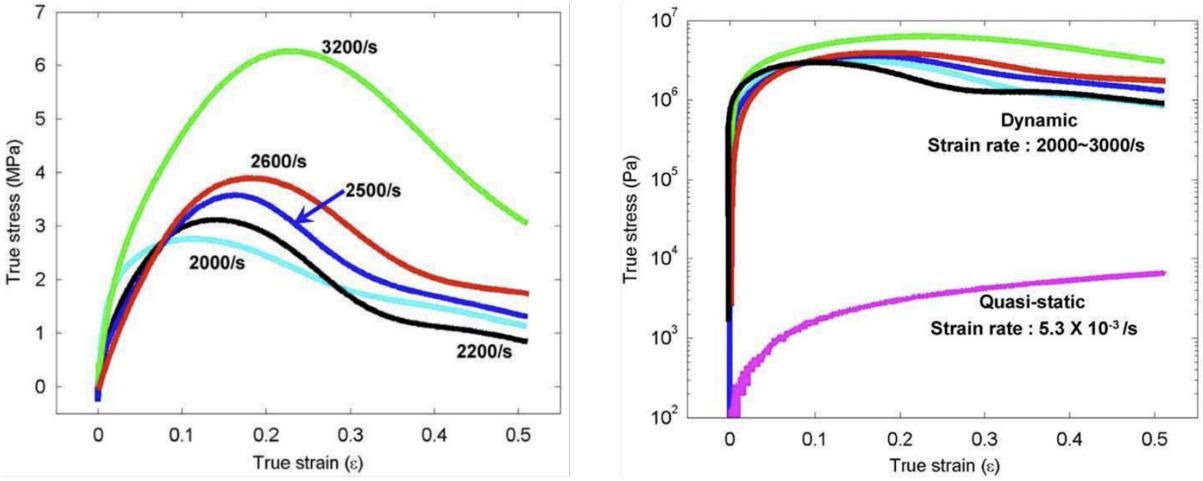

Figure 2.7: Stress-strain curves for dynamic tests of 10% ballistic gelatine at different strain rates and comparison of stress-strain curves between dynamic and quasi-static conditions (Kwon and Subhash, 2010).

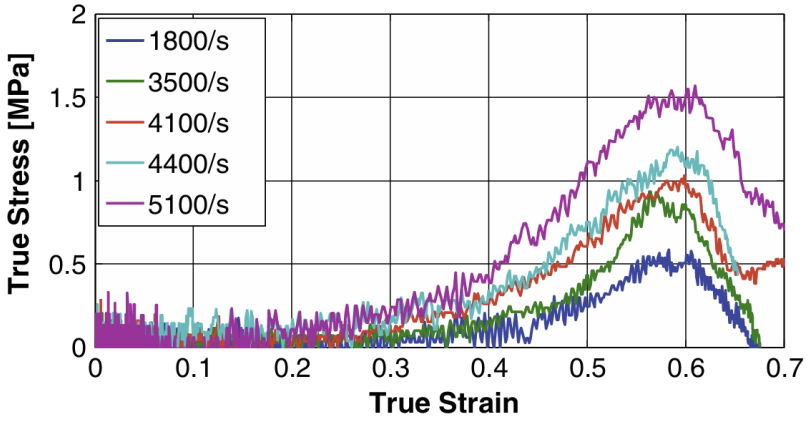

Figure 2.8: Stress-Strain curves of 10% ballistic gelatine at difference strain-rates (Richler and Rittel, 2014).

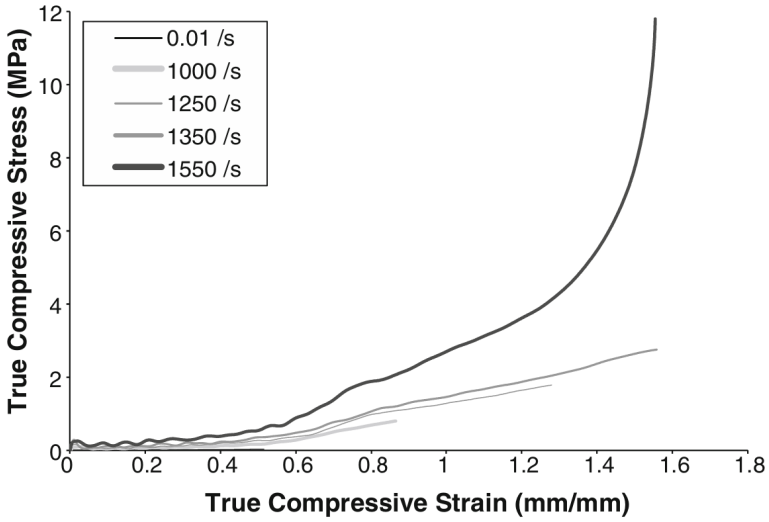

Figure 2.9: Stress-Strain curves of 10% ballistic gelatine at difference strain-rates (Salisbury and Cronin, 2009).

2.3 Modelling of Soft Materials

Past studies have investigated a range of alternative approaches to effectively simulate the properties of ballistic gelatine in high-pressure, short-duration loading events. Gilson et al. (2016) and Wen et al. (2013) adopted an elastic-plastic material model with associated linear polynomial EOS in LS Dyna for simulating the penetration of a ballistic projectile into a block of gelatine. This material model can erode mesh elements once they reach a set failure strain, reducing mesh distortion. However, this material model does not account for the strain rate effect of gelatine. The velocity and depth travelled by the projectile were well predicted by the simulation. However, the pressure in the simulation marginally correlated with the inserted pressure transducer from the experiment, indicating the need for further development.

A different approach was taken in Karahan's et al. (2018) investigation into the effectiveness of personal protective boots against mine blasts. Two types of military boots were tested against 40 g and 70 g C4 explosive charges. Inside these boots was a leg with bone made from PMMA, soft tissue from ballistic gelatine and a nylon skin coating (Karahan et al., 2018). This experimental set-up was modelled in LS Dyna, and the gelatine was modelled using a Johnson-Cook model as it demonstrates the exponential stress-strain relation. Bone fractures showed a good correlation with the experiment; however, little comparison was made between the soft tissue behaviour in the experiment and the numerical model, as the chemical processes for softening and burning could not be simulated (Karahan et al., 2018). The charge size made soft tissue analysis challenging and caused the investigation to focus mainly on the fracture of the leg bones. Smaller charge sizes should be used in future investigations into the characterisation of soft tissue in an explosion to avoid catastrophic failure of the material and reduce modelling challenges.

A recent study by Hampton et al. (2019) also investigated, via numerical modelling, lower leg injuries from a large axial impact. The numerical model was compared to post-mortem human subjects (PMHS) experimental tests conducted at the Medical College of Wisconsin (Hampton et al., 2019). The soft tissue was modelled using a hyper-visco-elastic soft tissue material model. Simulated peak force and impulse were higher in the numerical model than in the experiment (Hampton et al., 2019). This difference was caused by the simulation producing



Figure 2.10: An example of Karahan experimental results compared to their model (Karahan et al., 2018).

a different failure model for the end of the foot. Despite this, the stress was effectively simulated with stress concentration locations correlating with locations where experimental fractures were observed.

Singh and Basri (2022) undertook an in-depth study of the effect a landmine has on the lower limbs of the human body. The study was validated against Lower Extremity Assessment Program (LEAP) cadaveric test studies conducted by the United States Department of Defence (Singh and Basri, 2022). A numerical model was produced using Toyota's Total Human Model of Safety (THUMS) LS Dyna model. The THUMS model consists of a 3 - 5 mm mesh of all the human body's bones, tendons, soft tissues, and ligaments. The tendons and soft tissues are defined using the hyper-elastic Simplified Rubber/Foam model, a tabulated version of the hyper-elastic Ogden material law. In the experimental setup, load cells were implanted on the tibia mid-shaft and strain gauges were installed on the tibia distal media and the calcaneus inner surface. The lower limb was also placed inside various mine protective footwear to access protective levels. The THUMS model was adapted to include the load cells and the boots. The axial forces were modelled with high levels of accuracy with an error of 3.5%, and the injury comparisons were good. The results from this approach look promising for future studies.

Foams display similar behaviours to ballistic gelatine under high strain rate loading. The stress-strain curve of foams can be divided into three sections: initially linear behaviour, post-buckling densification and cell wall compression (Thom, 2009). The strength and the loading type affect whether the loading is amplified or attenuated when travelling through the foam. In shock tube experiments, foam can amplify the pressure behind the foam. However, in blast loading experiments, the foam was found to reduce the pressure behind the foam. The University of Waterloo has developed a Torso Model in LS Dyna to estimate lung injuries from blast loading (Greer, 2006). The model is a 2D slice of the human torso at the mid-eternal section and is based on a 50th-percentile male cadaver. The soft tissue in the model was simulated with a simplified hyperelastic material model. Rate sensitivity was included by defining a set of uniaxial stress-strain curves. Thom (2009) investigated the behaviour of foams in blast loading to explore their protection capabilities for lung injury. The blast loading was simulated by applying pressure time histories from the literature to the elements. A good correlation was found between the pressure recorded behind the foams, and increasing the thickness of foam reduced the peak pressure.

Authors have tried to model gelatine in accordance with the scenario of a bird striking a plane, another high-pressure, short-duration loading event (Cuvillo et al., 2017) (Aslam et al., 2020). Lagrangian and Smooth Particle Hydrodynamics (SPH) methods have been used; however, they have drawbacks. The Lagrangian method can have significant mesh distortion problems, often leading to energy errors (Aslam et al., 2020). However, this can be improved by implementing mesh erosion. SPH eliminates this problem with its meshless structure and helps illustrate the fluid nature of high-speed impacts. On the other hand, SPH is significantly more computationally expensive than Lagrangian and lacks the real material's sharp boundaries (Aslam et al., 2020).

Del Cuvillo et al. (2017) modelled gelatine as a fluid when simulating the high-speed impact of a bird strike. The mesh-free approximation approach in LS Dyna was used because large mesh deformation was excepted (Cuvillo et al., 2017). This approach is known as SPH, which is implemented using SECTION SPH. The simulation qualitatively reproduces the spreading of the sample along the plate when compared to the high-speed video footage from the experiments, Figure 2.11. There is relatively good agreement between the stress curves from the experiment and the model. Figure 2.12 shows how the numerical model does not capture the maximum stress.

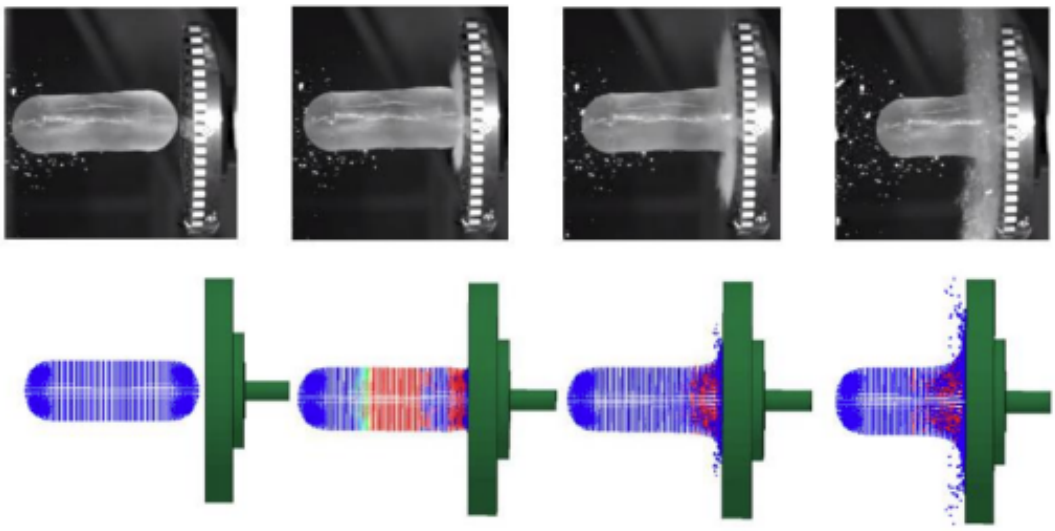

Figure 2.11: Comparison between numerical and experimental images (Cuvillo et al., 2017).

Aslam et al. (2020) compared the Lagrangian Mooney-Rivlin method with the SPH method in Autodyn to simulate a bird striking a target plate. The Lagrangian Mooney-Rivlin model predicted slightly higher stress, approximately 5% more than the experimental results (Aslam et al., 2020). However, the Lagrangian Mooney-Rivlin model predicted the deformation of the plate better than the SPH model. In addition, computational time was vastly different from the other method, with Lagrangian being 159% faster than the SPH model.

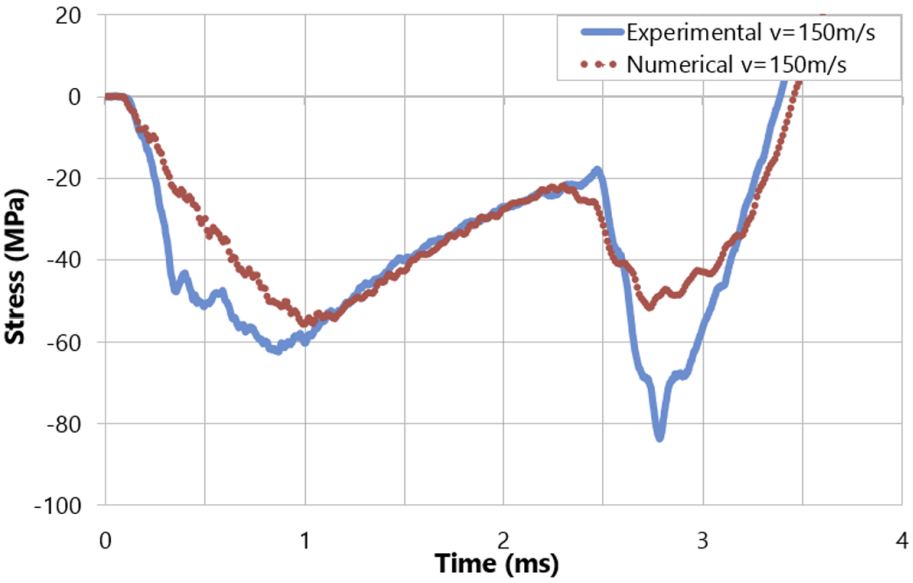

Figure 2.12: Results from bird impact at 150m/s (Cuvillo et al., 2017).

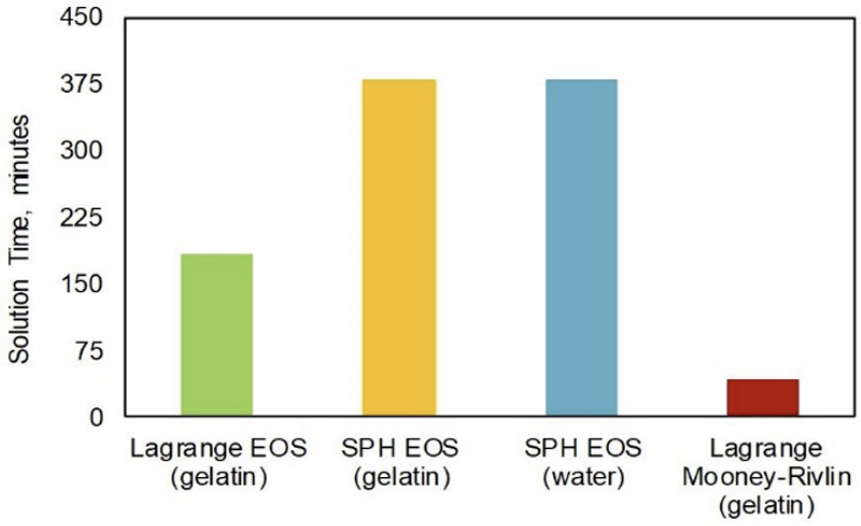

Figure 2.13: Comparison of modelling time from Aslam et al. (2020).

These studies highlight the differences in these methods. Even though SPH has been shown to simulate the fluid-like behaviour of gelatine well (Cuvillo et al., 2017), Aslam et al. (2020) has demonstrated that Lagrangian can produce similar accuracy in a fraction of the time. This makes it challenging for researchers to choose an appropriate method.

2.4 Gelatine Behaviour during an Explosion

Ballistic gelatine has been used to simulate human tissue in experiments to investigate the effect an explosion has on human tissue. Previous physical experiments were carried out at the University of Cape Town to investigate how the pressure experienced by 10% ballistic gelatine changes with depth when impacted by an explosion (Fitzgerald, 2019). This pressure was measured by inserting a pressure transducer at different depths in the back face of the gelatine block. A stand-off distance of 0.62 m was chosen to match the test conducted by Denny (2018), so the distance was larger than the fireball expansion, so the gelatine was not damaged (Fitzgerald, 2019).

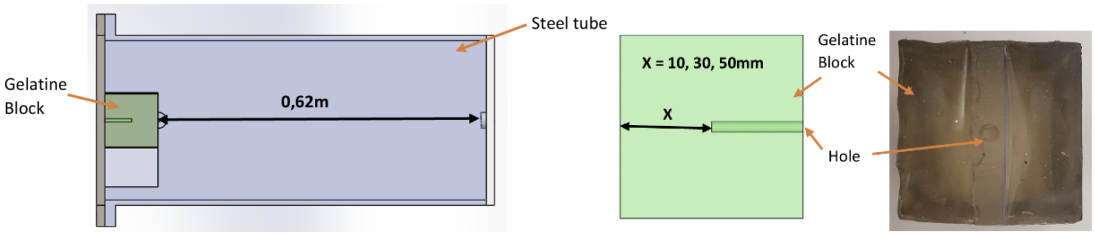

Figure 2.14: Fitzgerald experimental set up (Fitzgerald, 2019).

Many problems arose from this investigation, which should be considered for future physical experiments with gelatine. The main issue was that substantial variation in pressure readings was seen in tests. In tests 1 – 3, the maximum pressure was seen to increase. These tests were carried out in very close succession, less than 15 minutes apart, possibly causing the pressure transducer to overheat. This overheating could have caused the larger voltage readings in the results (Fitzgerald, 2019). This theory is also supported by Test 17, which had the same set-up but was carried out on a separate day and produced readings close to Test 1. As a result, it is recommended that significant time is given between tests for the system to return to its original state. The gelatine was also found to cause oscillation in the pressure signal in the results from Fitzgerald (2019), reducing in magnitude in a damping fashion. When comparing data recorded at different depths into gelatine, pressure and impulse decreased with increasing depth, but there were limited reliable repeats in the data to support this finding (Fitzgerald, 2019).

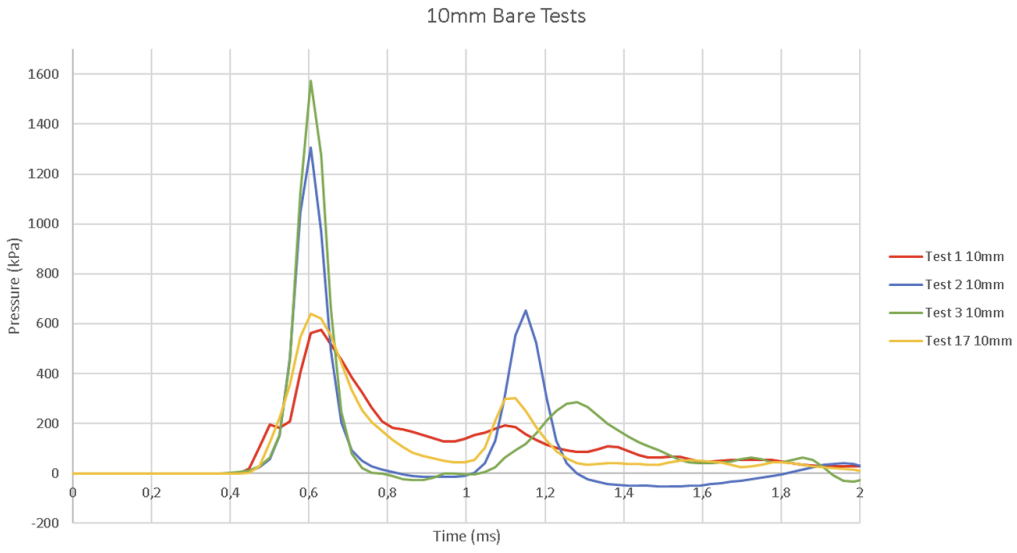

Figure 2.15: An example of results from Fitzgerald (2019).

When an explosion impinges on a vehicle, there are three main responses: localised hull response, internal dynamics from transmission of the hull reaction loads and global vehicle motions (Schutte, 2017). The effectiveness of the different mitigation measures in reducing the force exerted on the lower leg when an explosive impacts an armoured vehicle was investigated by Elgy et al. (2020) using a velocity impactor. A Hybrid III and a Mil-Lx leg were used in this investigation, which are instrumented dummy lower legs. The legs were positioned above a hollow box on an aluminium plate to represent the false floor of an armoured vehicle. When no mitigation was used, it was found that below a foot height of 77 mm, the compressive force rapidly increased as the foot height decreased. Above 77 mm, there was little decrease in force for an increase in foot height. The Mil-Lx leg recorded 30% lower force measurements in the lower tibia than the Hybrid III leg. This may be due to the compliant element of the Mil-Lx leg being softer than the Hybrid III leg, allowing the leg to be accelerated more gently. The mitigation systems were found to be less effective at reducing the forces than simply elevating the false floor to the same height.

Cronin et al. (2011) investigated blast injuries of human tissue resulting from a buried explosion using a physical surrogate leg. In this surrogate leg specimen, all the soft tissue was represented by 10% ballistic gelatine. 10% ballistic gelatine was used because data from SHPB tests showed that it had a similar non-linear stress-strain response, strain rate effects, and similar elastic wave velocity (approximately 1,550 m/s) compared to human tissue. Karahan et al. (2018) used a similar surrogate leg set-up when investigating the effectiveness of personal protective boots. C4 explosive charges of 25, 50, 75, and 100 g were buried 20 mm below the soil surface, and the leg was positioned centrally above the charge on the soil surface. The injuries sustained by the surrogate leg were evaluated by a qualified trauma surgeon with experience assessing and treating landmine injuries. This study did not investigate the magnitude of pressure and impulse from the buried explosive. The unprotected leg was found to experience a higher level of injury than the leg protected by a standard combat boot. The injury evaluation agreed with the other results in the literature. Limited material characterisation can be achieved from experimental tests because data readings will vary vastly depending on the location of the equipment.

2.5 Explosions in Air

When an explosive charge is detonated, the solid explosive is nearly instantaneously converted into a high-pressure, high-temperature gas (Wolf et al., 2009). This gas expansion causes a sudden rise in pressure, creating a blast wave that propagates outwards. As the blast wave propagates, it exponentially decays back to ambient conditions over time. The Friedlander curve, presented in Figure 2.16, graphically represents this rapid release of energy. The sudden rise in pressure and the exponential decay can be seen clearly in this figure. The maximum pressure of the blast wave is referred to as the overpressure. The positive phase is where all the pressure is released from the explosion. The positive phase is followed by a period of relatively low pressure due to the void created by the displaced air, called the negative phase. The Friedlander curve shows the simplest form of an explosion. However, in real life, a pressure-time curve is more complex, with pressure graphs having multiple spikes. The aspect ratio of a cylinder charge affects the shape of the blast wave. Davids et al. (2017) found that higher aspect ratios cause higher axial impulses than charges with equivalent masses.

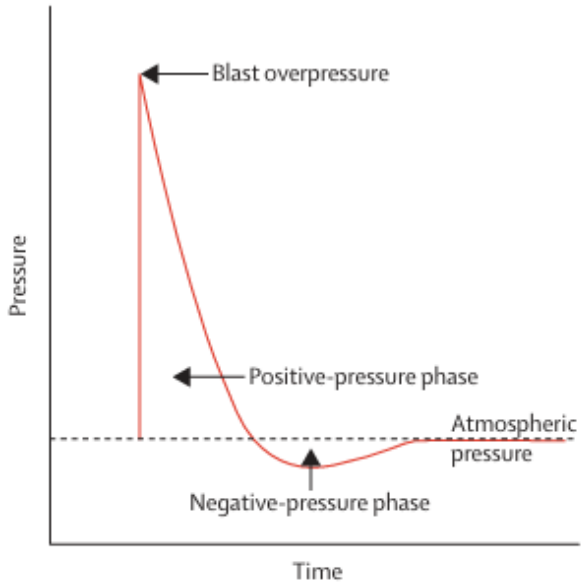

Figure 2.16: Friedlander curve from (Wolf et al., 2009).

One advantage of computational modelling over physical experiments is that data readings can be extracted from any point in the model domain. This method enables investigations with challenging experimental arrangements to be explored. When numerically modelling an explosion, LS Dyna is a popular choice as it specialises in high strain rate non-linear structural dynamics and can model the rapid compression and transport of gasses and their interaction with structures (Reay, 2014).

A Multi-Material Arbitrary Lagrangian/Eulerian solver (MMALE) was utilised to simulate an explosion in LS Dyna. This solver is widely utilised because the MMALE method can handle multi-material formulation. Rigby et al. (2018) and Davids et al. (2017) used a 2D mesh to define the air domain when they modelled the detonation of an explosive charge in air. The properties of the air are defined using MAT-Null and Linear-Polynomial equation of state, allowing an ideal gas to be simulated. For the explosive charge, the properties are assigned using the keyword files MAT-High-Explosive-Burn and JWL equation of state. The mesh size and density primarily affect the accuracy of a numerical model. A smaller mesh size will increase the model's accuracy but vastly increase the computational time. Therefore, a mesh study determines the optimal mesh size and shape.

To simulate the expansion of the charge from the detonation point, the keyword file Initial-Volume-Fraction-Geometery is used. This "fills" the air mesh with the explosive volume as it propagates away from the point of detonation (Rigby et al., 2018). The keyword file Constrained-Ladrange-in-Solid can define the Fluid-Structure Interaction (FSI) between a Lagrangian object (solid structure) and an Eulerian mesh domain (explosion). The keyword file works by constraining the velocity and/or acceleration of the Eulerian material at the FSI interface (Reay, 2014). In Rigby's model, the fixed surface was simulated by constraining the nodes on the surface against normal translations.

One issue with numerical modelling is that they are only as accurate as their inputs. To minimise this issue, constitutive equations, test geometry, and material properties are carefully chosen to closely match the simulated physical case. Validation data from physical experiments or known analytical solutions are used to ascertain the accuracy and appropriateness of model predictions. However, physical explosive detonations must also be evaluated for measurement

accuracy and repeatability. For example, Rigby et al. (2018) found that cylindrical charges did not agree well between the experimental data and the numerical simulation. Differences were seen in the form and magnitude of the pressure signal. Still, the fireball expansion rate and shape, seen in Figure 2.17, were similar to the experimental high-speed video footage.

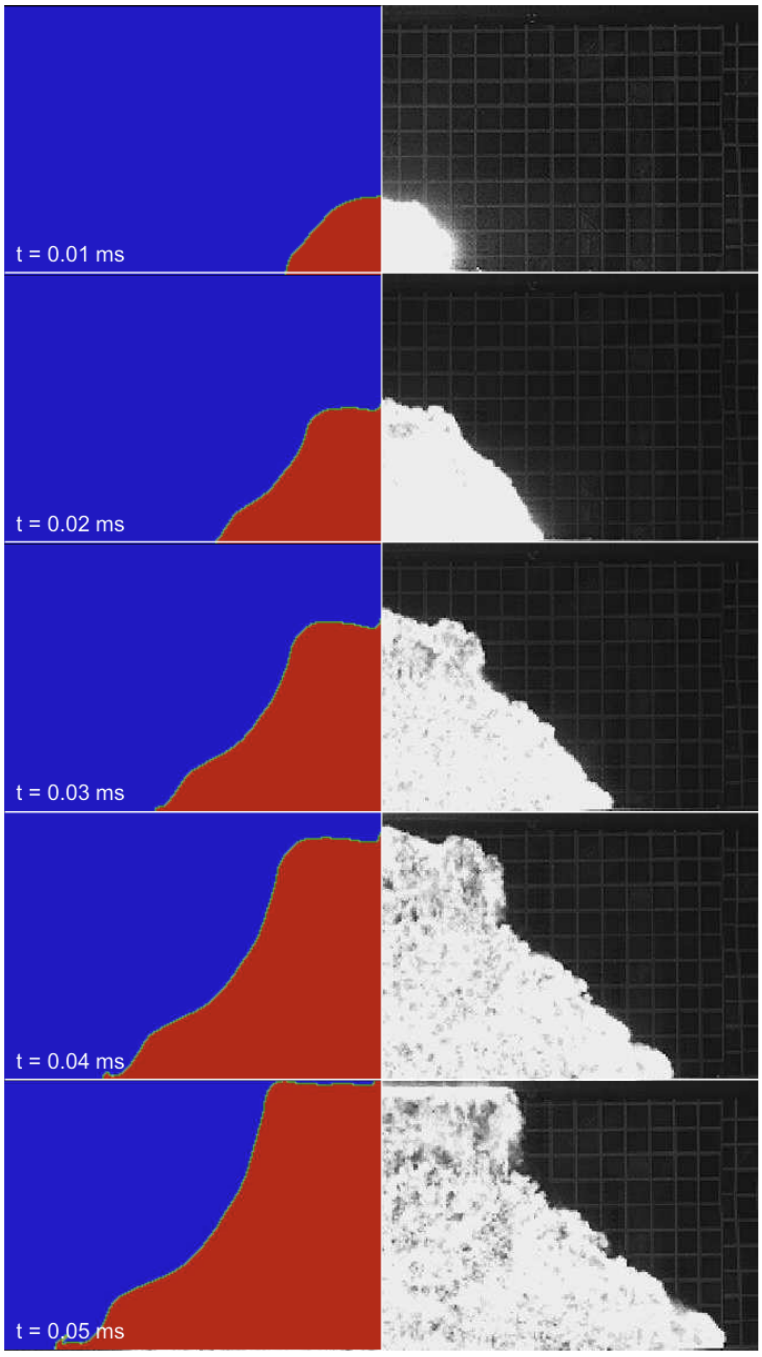

Figure 2.17: Numerical and experimental fireball expansion (Rigby et al., 2018).

2.6 Behaviour of a Deformable Plate in an Explosion

When investigating the human injury caused by an explosion, the response of deformable structures is also essential to understand because these often interact with the human body, like armoured vehicles. Menkes and Opat (1973) first defined the failure modes of blast loading on a clamped structure into three modes. Mode I involves large inelastic deformations. Mode II involves tensile tearing at the support and finally, transverse shear failure at the supports in Mode III. Earlier studies investigated the behaviour of deformable plates either by analysing the final deformed shape or using crush blocks to measure the maximum transient displacement (Langdon et al., 2014) (Davids et al., 2017) (Neuberger et al., 2007). These methods do not capture the full-field transient behaviour of the material. Digital image correction (DIC) has the benefit of recording full-field data, but placing instrumentation close to the test plate poses difficulties (Curry, 2017). These difficulties include the blast wave moving or damaging the camera during the experiment, causing the measurement technique to stop working. Also, the method's effectiveness is linked to the adhesion of the paint speckle on the target plate.

Using one camera positioned perfectly perpendicular to the surface of interest, 2D DIC can be utilised to view the planar movement of the surface. A surface's out-of-plane motion can be viewed using two cameras with 3D DIC. This method provides a field of data rather than discrete points produced by more traditional measurement methods like pressure transducers. Many studies, like Park et al. (2017), have reported that the speckle pattern size, density, and subset size affect the accuracy of the data recorded. Curry and Langdon (2017) utilised DIC to capture the full-field transient behaviour of a fully clamped Domex steel plate. The clamping frame left an exposed circular area with a diameter of 300 mm. The high-speed cameras were mounted on a rail system to isolate them from vibrations from the explosion and, so they could not move independently during the test. Independent movement would invalidate the calibration of the DIC system. Care was taken when applying the speckle pattern. The plates were thoroughly cleaned before applying the paint and degreased with acetone. The impulse from the explosion was measured using both a ballistic pendulum and 3D DIC.

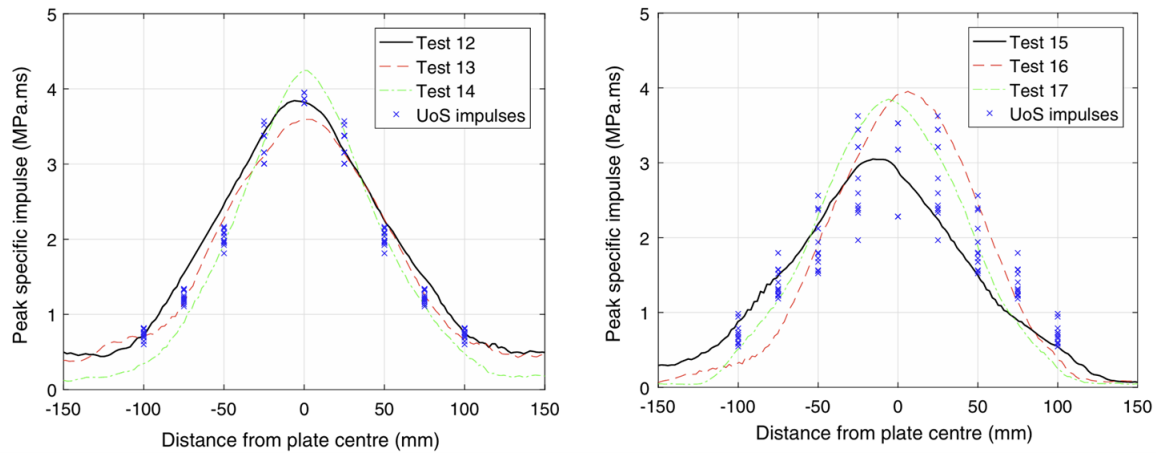

Figure 2.18: Comparison of impulse data collected by Hopkinson pressure bars and DIC (Rigby et al., 2018).

The high-speed cameras were calibrated by taking multiple images of the calibration target in different positions and processed in the Dantec Dynamics DIC software. The high-speed camera takes images of the plate as it deforms in response to the explosion. Afterwards, the software package is utilised to correlate the two cameras by tracking each pixel subset in the

images. A good correlation was seen between the specific impulse values recorded by the ballistic pendulum and from the DIC. In Rigby et al. (2018), the DIC data from Curry and Langdon (2017) was compared to data collected by a rigid target plate adopting Hopkinson pressure bars to record the pressure and impulse from an explosion. For these experiments, the specific impulses were found to closely match each other, supporting the use of DIC to analyse the response of an explosion.

Spranghers et al. (2013*b*) investigated the response of a clamped 3 mm thick Aluminium 1050A H24 plate to an explosion. Two Photron cameras were mounted behind the plate to capture the transient response with DIC. The aluminium was found to have a highly localised material response. The response of the clamped aluminium plate was simulated in LS Dyna using a Lagrangian mesh formulation and applying the blast as point loads. The point loads were estimated from ConWep. To simulate the behaviour of sheet metal, the constitutive equation needs to consider the influence of strains, strain rates and temperature effects (Nasri et al., 2023). The Johnson-Cook model is a temperature-dependent constitutive model with parameters determined by curve fitting to experimental data. The constitutive parameters are determined using data from tensile tests, Erichsen tests, and hot-forming tests. During the tensile testing of A1050 aluminium, Nasri et al. (2023) discovered negligible directional behaviour from the roll direction. Nasri et al. (2023) also found that decreasing the temperature sensitivity coefficient m, increases the forming temperature and that increasing the sheet temperature significantly increases metal formability.

Spranghers et al. (2013*a*) determined the required material properties for aluminium through an inverse method. The inverse method employed by Spranghers et al. (2013*a*) was based on minimising the discrepancy between the experimental and numerical displacement field data. The contact between the clamp and the plate was described by tying the plate nodes to the clamp surface. This method would overestimate the friction forces between the plate and clamp, implying that they are fully fixed together. The model was found to estimate the plate profile well qualitatively but underestimated the hardening behaviour of the plate.

Neuberger et al. (2007) also modelled the behaviour of a circular clamped plate in LS Dyna, using Kingery and Bulmash equations to apply the blast loading. A quarter symmetry mesh visualised the set-up, with the plate modelled using a Johnson-Cook material formulation. Numerical results at the midpoint were compared with experimental crush block data, and a good deflection correlation was found. Curry (2017) and Pickering (2012) also modelled the behaviour of clamped plates with fully integrated shell elements, and the contact between the clamp and the plate was modelled using automatic surface-to-surface contact. This method simulates the friction forces between the clamp and the plate. The air around the clamped plate was modelled as a solid ALE mesh, and the explosive was simulated using initial volume fraction geometry. The transient midpoint deflections from the simulation showed a good correlation with the experiments. Curry (2017) saw a slightly worse correlation for permanent deflection possibly because of the Johnson-Cook material model.

2.7 Buried Explosions

When a buried charge is detonated, there are three distinct phases (Bergeron et al., 1998). First, the detonation initiates a chemical reaction, causing a sudden release of energy as the explosive product converts into a dense gas. This extremely high pressure is transmitted to the soil, resulting in localised crushing of the soil immediately adjacent to the explosive. In the localised zone, the deformation is permanent plastic deformation and recoverable elastic defor-

mation further out from the explosive. The soil properties and the charge size will affect the location of these zones in the soil. Secondarily, the gas continues to expand, reaching the soil surface. This shock wave causes a soil cap to be ejected from the surface of the soil at supersonic velocity. As a result of the extremely high pressures, the soil ejecta continues to expand into the air in stage three. As a result, a large volume of soil is ejected into the surrounding medium. Wet and dry soils behave differently in this stage. Grujicic et al. (2006) suggested numerically that in dry soils, the soil ejecta bubble ruptures and vents the detonation products. Whereas in wet soils, the ejecta remains a bubble. These theories were later validated by experimental tests by Clarke et al. (2020).

Buried explosives can present a more significant threat than air-blast because the additional confinement of soil focuses the explosion vertically (Rigby et al., 2016). This channelling of the explosion amplifies the energy released and can cause significant damage. The focusing of the explosive energy vertically can be seen in the pressure data in Figure 2.19 (Rigby et al. (2016)), with peak pressure varying between 124 – 227 MPa at the centre and decreasing to between 16 - 135 MPa at a radial distance of 100 mm out. The combination of the impact from the soil and the focusing of the detonation product has generally been seen to result in higher magnitude and more spatially localised loading than an explosion in air (Clarke et al., 2020).

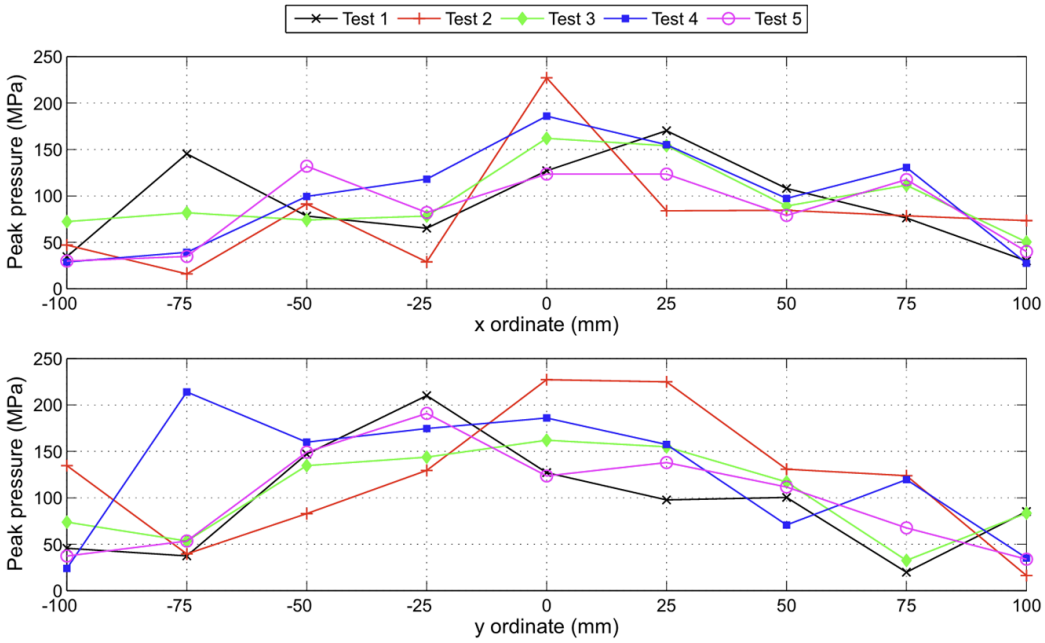

Figure 2.19: Compiled peak pressure at each bar location (140 mm stand-off) (Rigby et al., 2016).

Past experimental research into buried explosions has produced highly inconsistent results due to typically relatively poor control of geotechnical conditions before the blast event. It is important to control the soil properties accurately as the energy released in an explosion depends on the soil properties (Clarke et al., 2020). To increase the control of geotechnical conditions before the blast event, the University of Sheffield has developed a standard procedure for preparing the sand (Rigby et al., 2016), enabling them to achieve a repeatable density (within $\pm$ 0.2 Mg/m^3) and moisture content (within $\pm$ 0.05%).

Clarke et al. (2020) has previously investigated the effect of stand-off distance, confinement, and soil properties on the magnitude of a buried explosion. Four levels of confinement were

explored in this study. Figure 2.20 details the different levels of confinement A – D, which are air, surface, partial and full. The degree of confinement affected both the magnitude and distribution of the pressure on the target plate. Regarding Figure 2.21, Series C was found to be higher in magnitude and longer in duration than Series A and B because of confinement. Series D is similar in magnitude to Series A and B, but delayed arrival time is seen. When looking at the effect of stand-off distance, it was seen that as stand-off distance increases, the loading becomes lower in magnitude, with an increased time to a peak pressure (Clarke et al., 2020).

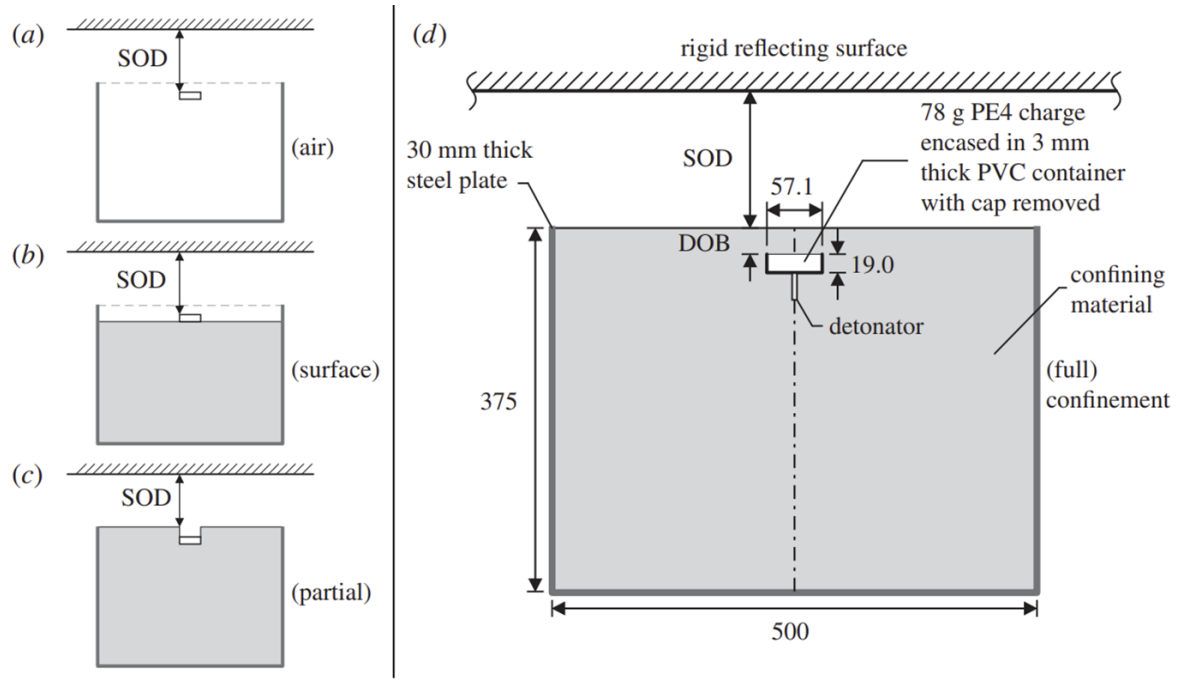

Figure 2.20: Confinement levels and geometry of test arrangement: (a) free air in Series A, (b) surface placement in Series B, (c) partial confinement in Series C and (d) full confinement in Series D (Clarke et al., 2020).

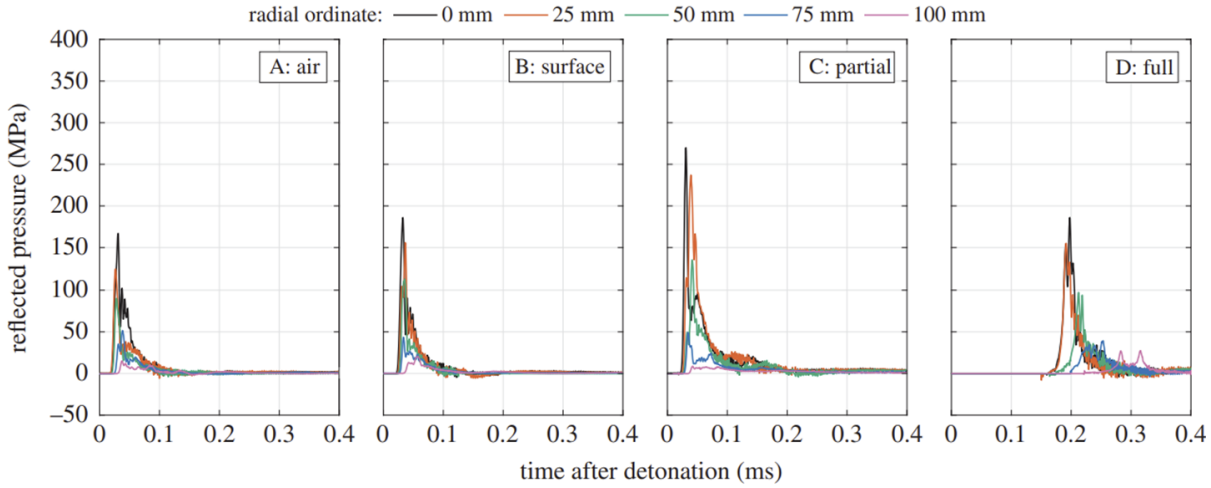

Figure 2.21: Pressure - time histories: Series A-D: influence of confinement (Clarke et al., 2020).

The soil's moisture content changes the shape of the pressure-time history curve (Clarke

et al., 2020). The pressure in the low-moisture content soils resembled the well-known 'Friedlander' curve and sharply rose to peak value, followed by gradual decay. However, the saturated soil exhibited an increase in peak pressure, followed by a near-symmetrical decay back to ambient pressure. This can be explained by looking at the high-speed video footage, which shows that in low-moisture soils, the soil bubble ruptures before the soil reaches the target, allowing gases to vent. In the saturated case, the soil bubble containing the detonation products remains intact when it reaches the target plate. The pressure distributions from the test in Figure 2.22 series F with saturated soil were similar to the signal with the confinement material as water (Clarke et al., 2020). This similarity suggests that the loading mechanism for the saturated soil is due to a highly pressurised fluid impact. This work agrees with earlier theories by Grujicic (Grujicic et al., 2006).

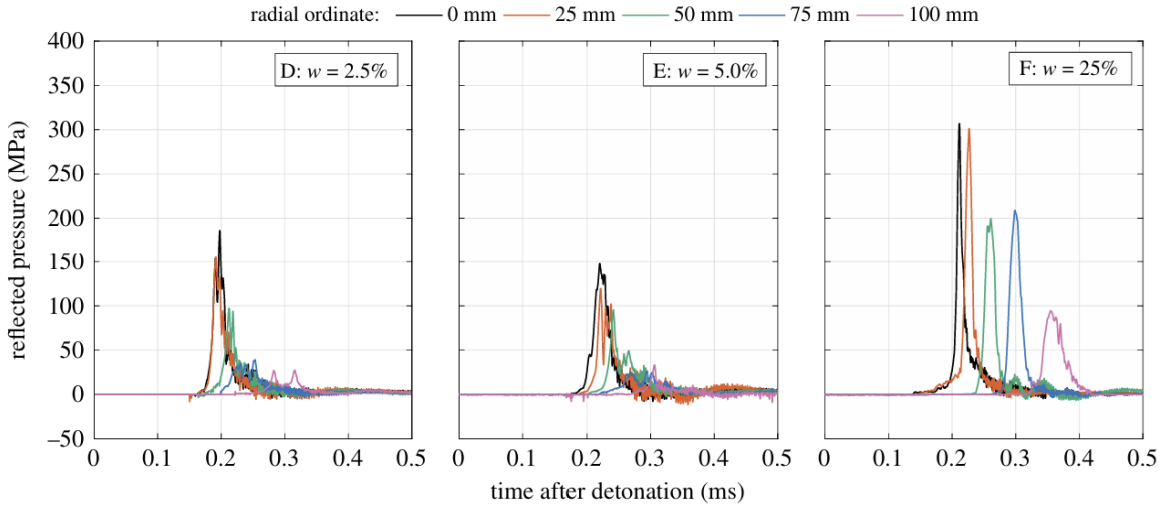

Figure 2.22: Pressure - time histories: Series D-F: influence of moisture content (Clarke et al., 2020).

2.8 Summary

The blast wave causes changes in soft tissues at the cellular and molecular levels, prompting physiological responses that have long-term implications for functional recovery. These findings show that blast exposure could exacerbate blast injuries, so even low blast exposure levels could have complex outcomes. Research investigating the causes of blast injuries on the human body has previously used small animals for experimental studies. Later, using organic ballistic gelatine improved the repeatability but proved susceptible to small temperature changes and only lasted for a short time before it biodegrades. This produces difficulties for improving experimental setups. Synthetic gelatine could be used instead of organic gelatine to facilitate improving experiment setups.

Many studies have explored the dynamic properties of organic gelatine through SHPB experiments, witnessing its high strain-rate dependency. However, limited studies have investigated the dynamic behaviour of organic gelatine when exposed to an explosion. Where these studies have been conducted, the main focus was the effectiveness of personal protective equipment (PPE) or the final blast injuries. Where these studies were conducted experimentally, results were not repeatable, and data readings varied depending on the location of the measuring equipment. Improper orientation of the pressure transducer with respect to the shock wave and gaps between the sensor and the object resulted in reductions in the maximum pressure recorded. Also, after the first pressure disturbance is recorded, it is difficult to determine whether any of the following disturbances are due to the explosion or the relative movement of the body. The addition of instrumentation has been found to change the stiffness of the system, affecting the behaviour of the material. Investigations into non-contact measurement techniques are needed to improve experimental measurement of this material's mechanical properties. These experiments also need to be conducted at lower far-field blast pressure to focus on material characterisation of ballistic gelatine.

Numerical modelling of the shock wave propagation through ballistic gelatine is key to better understanding the spatial movement of the material during loading. Previous studies have simulated the behaviour of gelatine in quasi-static and high strain rates loading situations. These models have shown a good correlation with experiments. Models investigating the response from blast loading have focused on the injury behaviour and not on how the blast wave interacts with the gelatine as it transmits through. More research is needed into methods to simulate the influence gelatine has on a blast wave to increase our understanding of how blast wave exposure will affect the human body. Improvements in experimental techniques will help validate these models and will be a step toward further understanding of the mechanisms of shock wave propagation through ballistic gelatine.

Chapter 3

Behaviour of Synthetic Gelatine under Quasi-Static Loading

This chapter aims to explore the quasi-static behaviour of synthetic gelatine. Quasi-static compression tests were carried out with the addition of high-resolution stereo cameras to obtain the out-of-plane motion of the synthetic gelatine. Specimen preparation was refined to increase the repeatability of results and developed further to allow the use of digital image correlation (DIC). The collection of this data allowed key material properties to be determined, which were then used to develop a numerical model for synthetic gelatine.

3.1 Development of Experimental Method

3.1.1 Initial Specimen Design and Manufacture

This study uses synthetic gelatine from Clear Ballistics (2023) for the experimental tests. Synthetic gelatine was chosen over the more widely used organic gelatine because it overcomes many of the disadvantages associated with organic gelatine. Even though Jussila (2004) developed a standard method for preparing organic gelatine, a wide range of mechanical properties for 10% gelatine have been reported from study to study. Synthetic gelatine overcomes this and other limitations, such as storage requirements and shelf-life (Read et al., 2022) as seen in Chapter 2.

Small gelatine specimens were required to perform these mechanical compression tests. The specimen size chosen was used by Cronin and Falzon (2011) in their mechanical compression tests, they used a 25 mm diameter by 25 mm long cylinder. The synthetic gelatine arrived as a premade block (16" x 6" x 6"). An aluminium mould was manufactured to shape the gelatine into the desired specimen dimensions. This mould consisted of a 25 mm deep aluminium block with 25 mm diameter circular holes drilled through. This was then attached to a base plate with screws. This allowed for easier removal of the gelatine specimens.

The specimens were produced following Clear Ballistics remoulding guidelines. Pieces of gelatine were removed from the block and carefully weighed to the correct mass. Then, the gelatine was heated in the mould to 125°C for 4 hours and left to cool overnight. Trials with this method found that as the gelatine cooled down, a meniscus formed on the open surface of the gelatine. This would invalidate the experimental test results because the specimen would not be fully in contact with the plate. Extra depth was added to the mould to overcome this problem, and extra gelatine was weighed out. The additional height of the specimen was then cut off using a hot wire cutter to leave a flat surface. The gelatine mould can be observed in Figure 3.1 and 3.2.

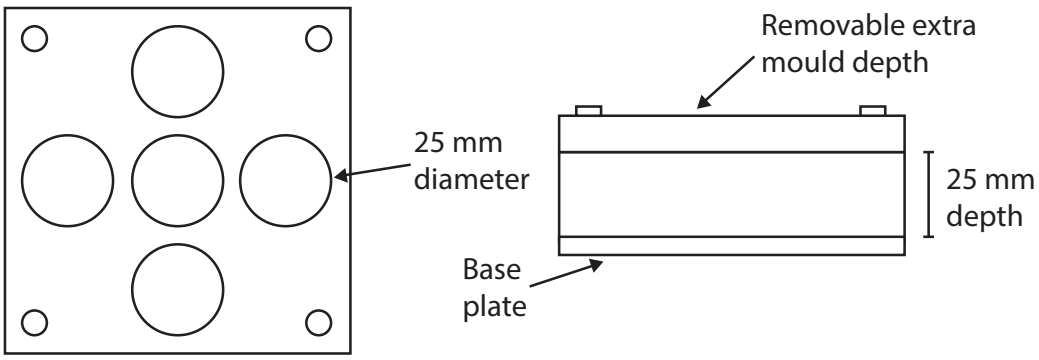

Figure 3.1: Diagram of synthetic gelatine mould.

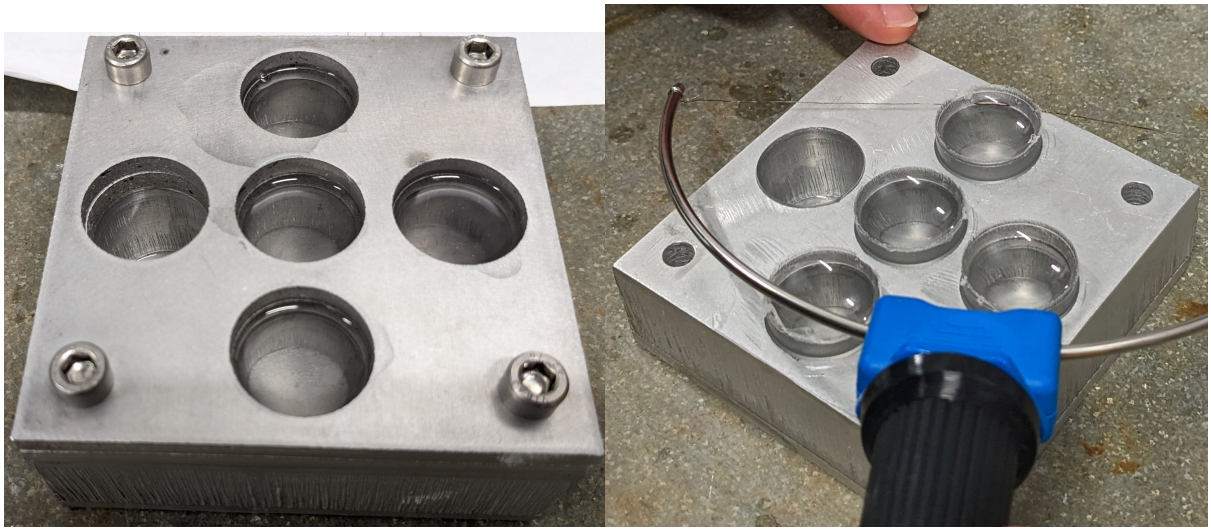

Figure 3.2: Synthetic gelatine mould and cutting process.

3.1.2 Influence of Speckle Pattern Methods

To visualise the non-uniform deformation seen in previous experiments (Ravikumar et al., 2015), stereo-imaging and digital image correlation (DIC) were used. The use of DIC also allowed the lateral deformation of the gelatine to be quantified, which is needed to calculate key input parameters for the numerical model. In this experiment, two high-resolution 5Mpx cameras were used to capture the full view of motion. A speckle pattern was applied to the gelatine so the movement of the gelatine could be measured. As the gelatine deforms, the speckle pattern deforms with it, resulting in a new position for each subset of pixels. This movement of the pixels is used to produce a field of displacement data for the gelatine. The size of the speckle pattern affects the accuracy of the measurement taken by the camera (Curry, 2017).

An opaque finish was first required to achieve a speckle pattern on synthetic gelatine, a transparent material. Painting the cooled gelatine specimen was considered. However, the paint needed to be very flexible so that the natural deformation of the gelatine was not affected. The solution to this was to use a highly flexible body paint. Then, to apply the speckle pattern, tattoo paper was trialled as this is a flexible material designed to cope with the movement of human skin. This method allowed for an accurate speckle arrangement to be printed onto the gelatine. The flexible body paint and tattoo paper applied to the gelatine are pictured in Figure 3.3.

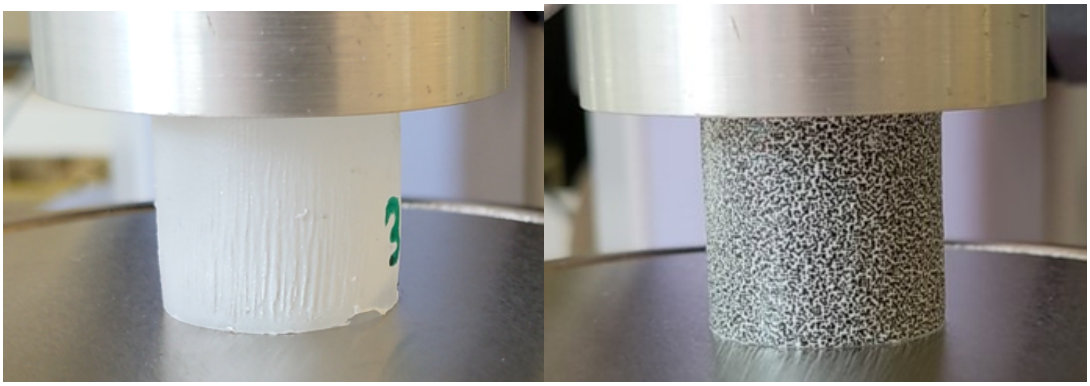

Figure 3.3: Painted gelatine specimen (left) and a gelatine specimen with tattoo paper (right).

The effect this paint and the tattoo paper had on the deformation of the gelatine was investigated by comparing compression test results with unpainted gelatine results. Unfortunately, as can be observed in Figure 3.4, the paint and the tattoo paper produced different results from the bare gelatine tests. Figure 3.4 shows the engineering stress-strain relationship for clear, painted and tattooed gelatine. For the same strain, a larger stress was required for the painted and tattooed specimens, restricting the gelatine and resulting in a stiffer response. Also, large cracks formed on the gelatine's surface, making DIC impossible. Figure 3.5 shows the existence of cracks in the tattoo paper when the gelatine was compressed.

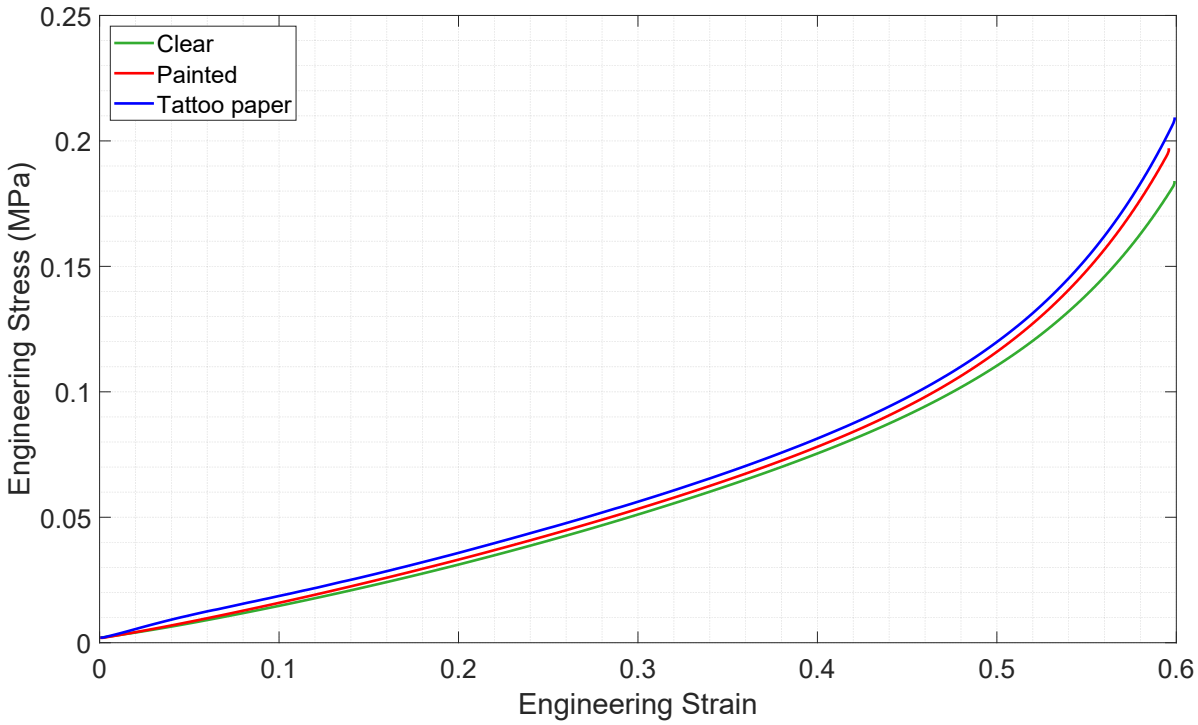

Figure 3.4: Stress-strain results comparing speckle method.

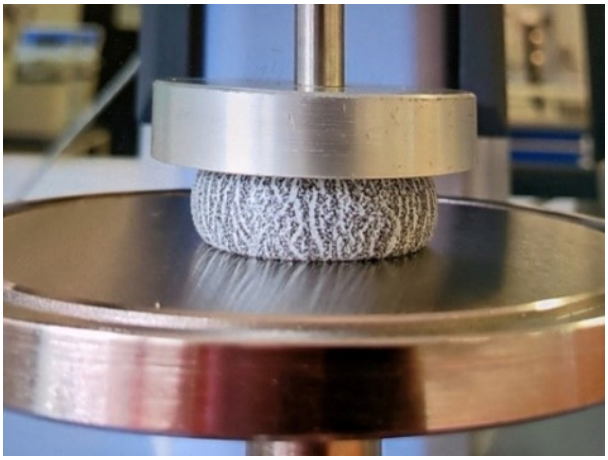

Figure 3.5: The tattoo paper cracking as the gelatine specimen is compressed.

Next, dyeing the gelatine white with epoxy resin dye was also trialled. Epoxy resin dye was the first dye trialled as it was cheap and easily accessible. Adding the dye to the melted gelatine while in the mould proved challenging due to the viscous and sticky nature of the gelatine. To overcome this, the gelatine was first melted in a larger batch, and the dye was added, as seen in Figure 3.6. After the larger batch had cooled, the dyed gelatine was carefully weighed to the correct mass for the mould and then placed in the oven. An example of a dyed gelatine specimen can be seen in Figure 3.7. More compression tests were subsequently conducted to investigate the effect of dye on specimen behaviour. As can be seen from the engineering stress-strain results in Figure 3.8, the dye made no discernible difference to the stress-strain curves.



Figure 3.6: The process of dying gelatine.

Once the white, opaque gelatine specimens were produced, a black speckle pattern was applied by rolling the gelatine on a premade DIC speckle stamp. The stamp used was from the speckle application kit from Correlated Solutions. The very smooth and pliable surface of the gelatine resulted in the speckle pattern being very prone to over-inking and smudging. However, through careful application, a consistent pattern was achieved. An example of the final speckle pattern is pictured in Figure 3.7, with a speckle size of 0.18 mm. These specimens were then used for the DIC testing.

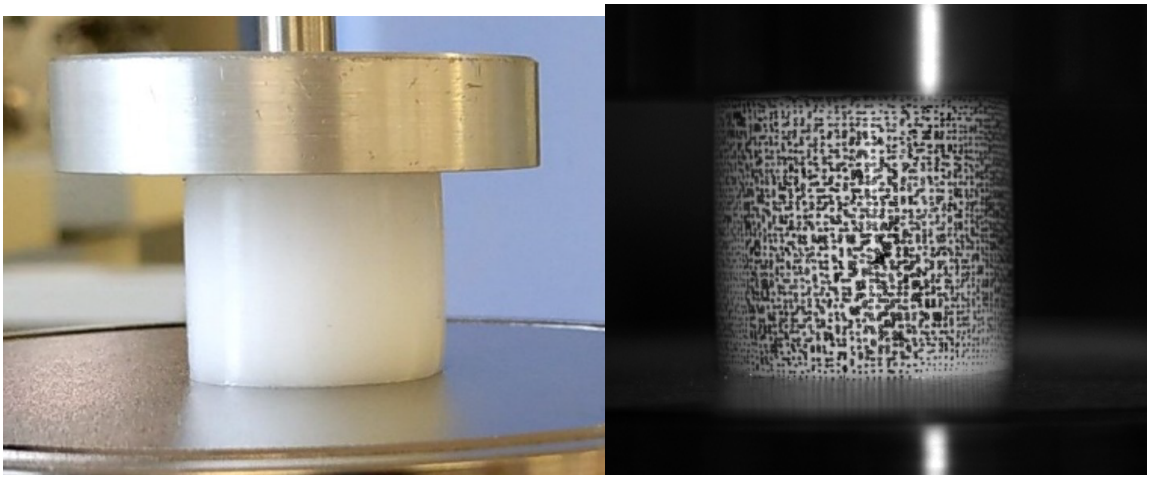

Figure 3.7: Dyed gelatine (left) and dyed gelatine with final speckle pattern applied (right).

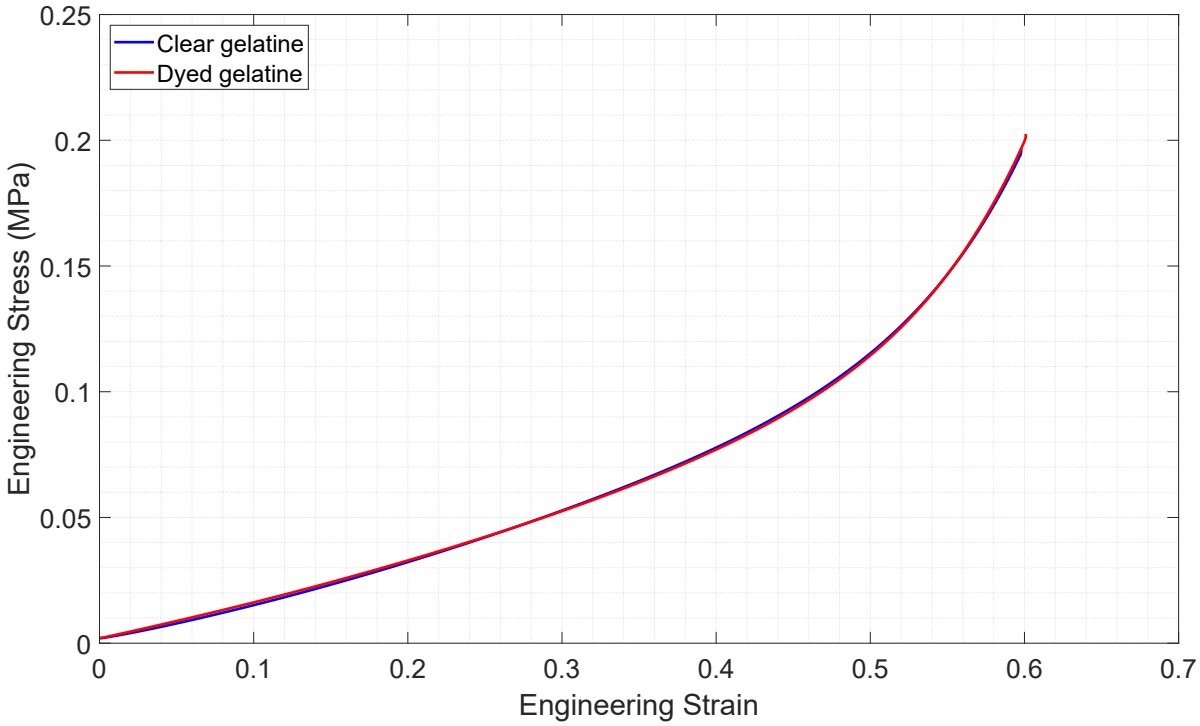

Figure 3.8: Stress-strain results from tests on clear gelatine and dyed gelatine specimens.

3.1.3 Effect of Surface Finish

The repeatability of the compression tests was investigated to refine the specimen preparation and testing process. The quality of the finish achieved by the hot-wire cutter affected the repeatability of results. The images in Figure 3.9 below show examples of different surface finishes. On the left is an example of an uneven, rough finish, and on the right is an example of a smooth, flat finish. The main reason for the inconsistencies in the gelatine's surface finish was caused by the way the hot-wire cutter was used. Cutting the gelatine in one smooth cut resulted in a flat, smooth finish. Judgement about the flatness of the gelatine surface was made through careful observation, as the gelatine was so soft that it was impractical to attempt to measure the surface roughness or how parallel the top and bottom faces were.

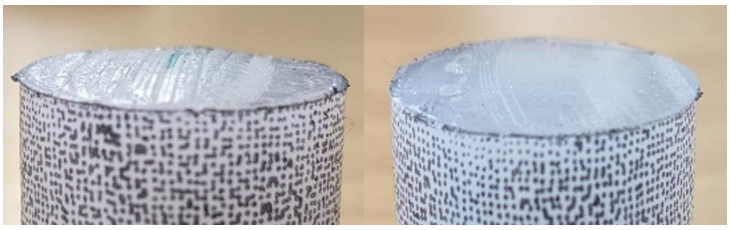

Figure 3.9: Rough gelatine (left) and flat gelatine (right).

The effect on repeatability was investigated by comparing engineering stress-strain results from three rough and three flat specimens, Figure 3.10. Figure 3.10 below clearly displays the effect the surface finish has on repeatability. The smooth, flat specimens are closely correlated to each other, whereas the specimens with a rough finish show large variability from test to test. These experiments highlight the importance of high-quality specimen manufacturing.

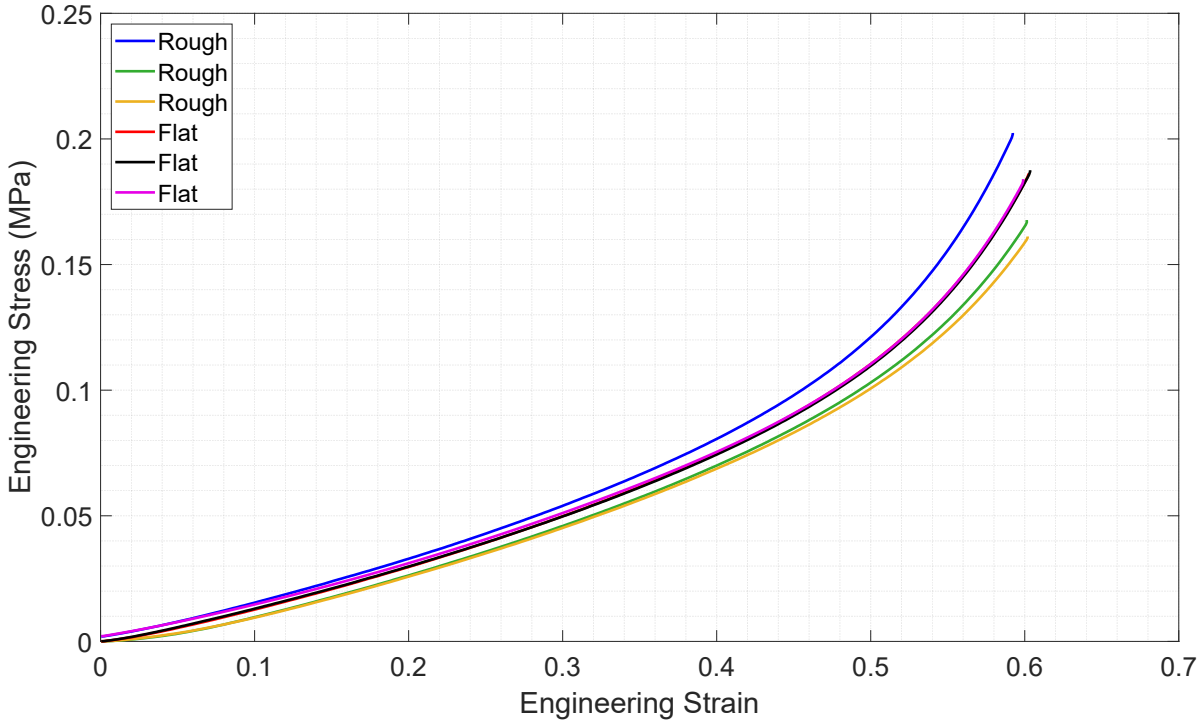

Figure 3.10: Engineering stress-strain graph comparing the variability caused by specimen manufacture.

3.1.4 Preliminary Comparison to Organic 10% Gelatine

Compression tests at a strain rate of 0.01 s^{-1} were conducted on the Shimadzu mechanical compression apparatus. These results were compared to stress-strain data from Cronin and Falzon (2011) and Ravikumar et al. (2015) at the same strain rate, Figure 3.11. Figure 3.11 shows how the engineering stress of the gelatine changes as the engineering strain is increased at a strain rate of 0.01 s^{-1}. The results are not expected to align exactly because Cronin and Falzon (2011) and Ravikumar et al. (2015) used organic gelatine. However, Figure 3.11 shows a similar exponential relationship for synthetic gelatine. The gradient of the curves indicates a similar relationship. In the initial section of the graph (from 0.05 to 0.25 strain), the gradient of the lubricated data is 24% larger than Cronin's data and 7% larger than Ravikumar's data, showing a close comparison to Ravikumar's results. Between the strains of 0.3 and 0.5, the gradients converge, with the friction data gradient being 6% smaller than Cronin's data and the lubricated data gradient being 15% smaller.

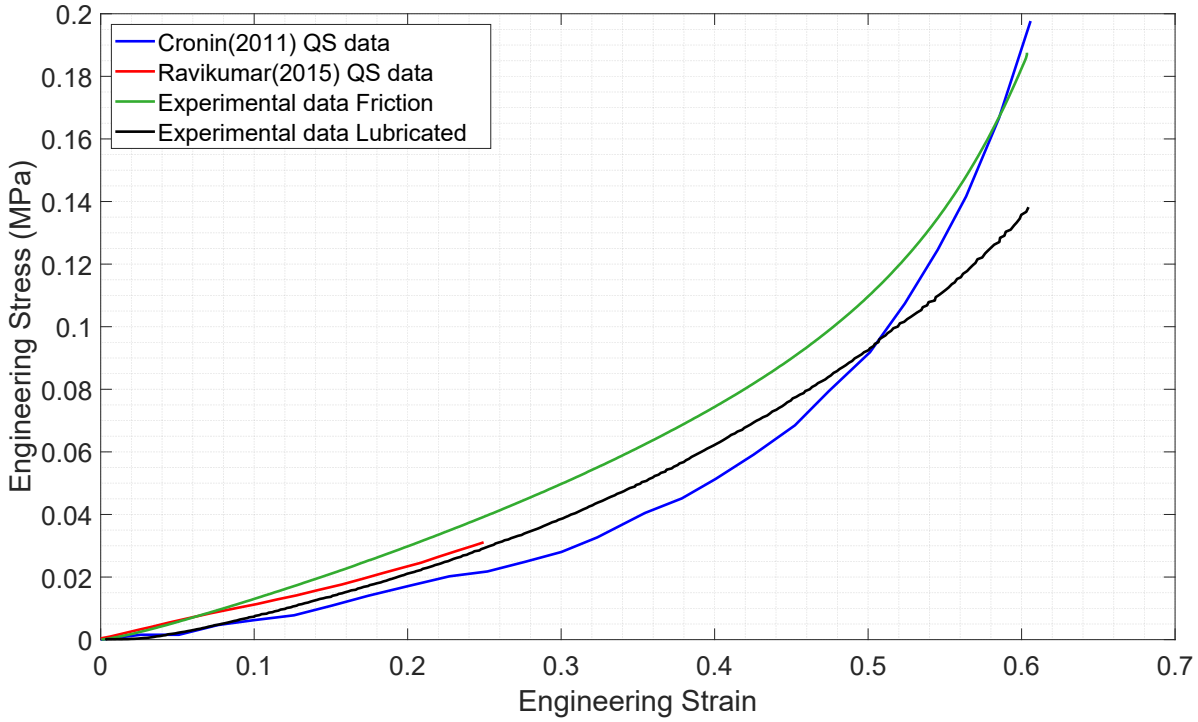

Figure 3.11: Stress-strain results from initial experiments compared to Cronin and Falzon (2011) and Ravikumar et al. (2015).

3.1.5 Implications for Final Specimen Design and Manufacture

This section summarises the important steps needed to manufacture the final specimens that were used in the following sections (Section 3.2 and 3.3). The custom aluminium mould described previously was used to produce ballistic gelatine cylinder specimens with a 25 mm diameter and 25 mm length. The gelatine was dyed white using epoxy resin dye to facilitate the use of DIC. This created a contrasting background for the speckle pattern. Before the specimens were removed from the mould, the top surface was cut using the hot-wire cutter to achieve a flat surface. This was done carefully to avoid a rough finish. Finally, the speckle pattern was applied to the gelatine by rolling the specimen over an inked DIC stamp. Care was taken to avoid smudging the speckle pattern.

3.2 Final Experimental Arrangement

A Shimadzu universal compression machine was used for all the uniaxial compression tests. A diagram depicting the side and plan view of the testing arrangement is shown in Figure 3.12. Tests were conducted at strain rates of 0.01 s^{-1} and 0.1 s^{-1}. These strain rates were chosen as they were used by both Cronin (2011) and Ravikumar (2015) in their studies, allowing for a comparison between organic and synthetic gelatine with more than one data source. These strain rates were set by setting a constant cross-head velocity, and the tests were stopped when 60% strain was reached. Digital image correlation (DIC) was facilitated in this work by using two high-resolution, 5Mpx stereo cameras. The arrangement of these cameras can be seen in the plan view in Figure 3.12. To increase the image clarity, a polarised blue light was directed at the gelatine specimen. The cameras were also fitted with polarised lenses, which reduced the glare from the reflective gelatine surface. The cameras were calibrated to the speckle pattern by taking a series of images of the calibration targets with a known pattern. This allows the camera focus and position to be set–up before the test. The size of the dots in the speckle pattern affects the accuracy of the DIC results (Curry, 2017). IDIC guidance recommends a pattern feature size of 5 pixels (iDICs, 2018). However, the final speckle pattern achieved a feature size of 10 - 15 pixels. This was the smallest speckle stamp size available, and using a stamp ensured a more consistent feature size across the specimen. Therefore, a consistent speckle pattern on the specimen surface and between different specimens was prioritised over achieving the optimal feature size. The speckle pattern used had a dot size of 0.18 mm, as stated earlier.

Technique used	3D stereo image correlation	Speckle size	0.18mm
Camera type	Correlated Solutions, 5Mpx	Frame rate	5
DIC software	VIC3D - Correlated Solutions	Subset size	105

Table 3.1: DIC hardware and analysis parameters.

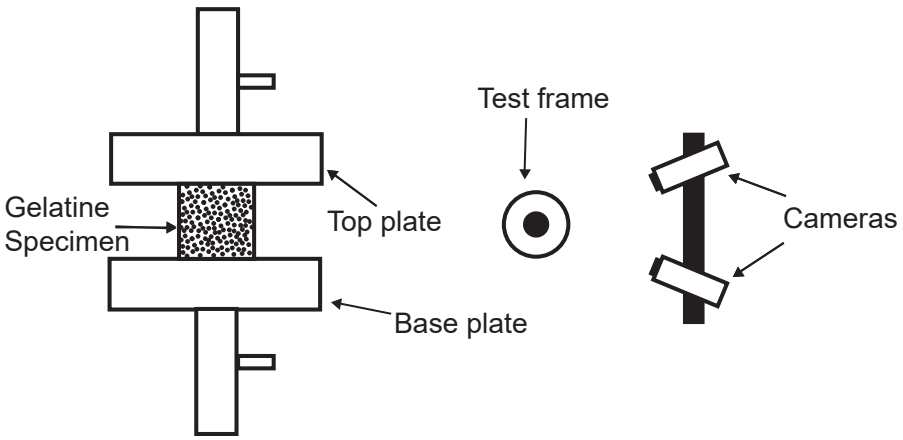

Figure 3.12: Diagram of DIC set-up.

3.3 Experimental Results

The use of DIC in this work allowed the movement of the gelatine to be measured in three directions. This means that the lateral or horizontal movement of the gelatine can be measured

in addition to the vertical displacement recorded by the universal compression machine. Figure 3.13 shows two 3D displacement plots, looking side-on at the specimen. These plots display the horizontal displacement of the gelatine as the specimen is compressed vertically. The plot on the top displays the specimen before the compression has started, and the plot on the bottom shows the specimen at 45% strain. As the gelatine compresses vertically, the specimen begins to move horizontally, as indicated by the change in colour on the contour plot. However, because of friction between the loading plates and the gelatine, the lateral movement is not linear, and the specimen starts to form a curved shape. The curved shape is indicated by the colour change across the specimen in Figure 3.13.

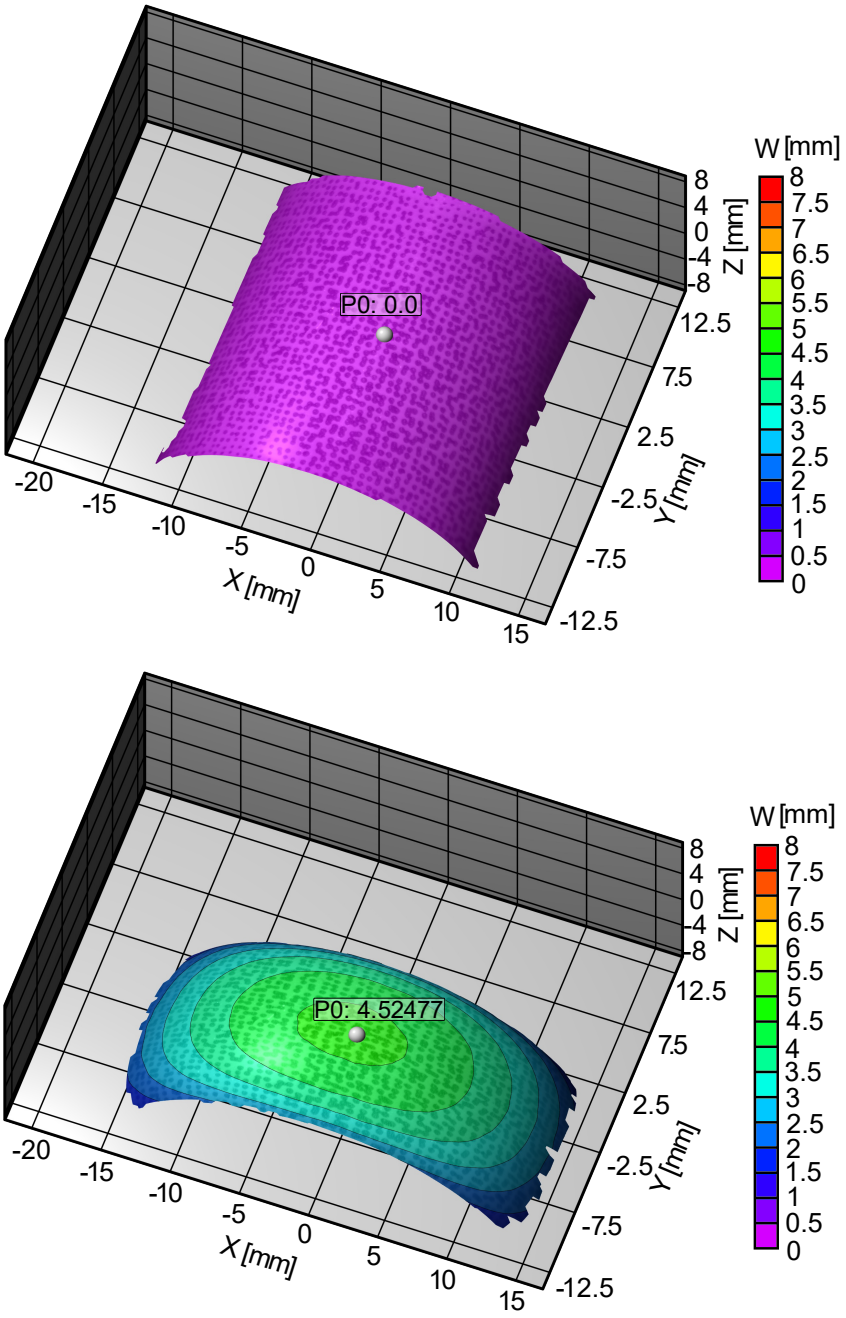

Figure 3.13: 3D displacement plots from the DIC data of the gelatine at the start of the compression test (top) and at 45% strain (bottom).

To investigate the shape of the specimen further, a line slice of data points was taken along the length of the specimen. The diagram in Figure 3.14 illustrates where the data points were extracted from. The data collected from the line slice was used to plot the displacement of the specimen over the duration of the experiment, Figure 3.15. Each line/curve displayed in Figure 3.15 represents a different time step in the experiment, with time increasing from left to right. Every time step in the experiment is not depicted here, so the graph is not too crowded. The increased barrelling of the specimen over the test duration can be clearly seen in this graph, with the lines becoming more curved as you move from left to right.

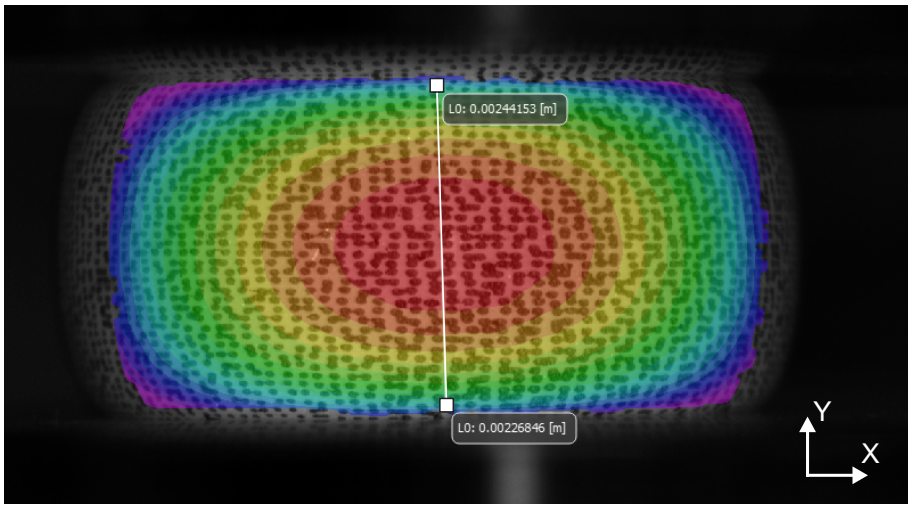

Figure 3.14: Diagram showing the line slice used to extracted data points from the DIC data.

The effect of friction between the gelatine and the loading plates was explored by lubricating some specimens. Figure 3.16 displays a line slice plot showing the horizontal displacement of a lubricated specimen over the duration of the test. The lines highlighted in red in both Figure 3.15 and Figure 3.16 show the horizontal displacement of the gelatine at 40% engineering strain and clearly show that increasing the friction increases the curvature of the specimen.

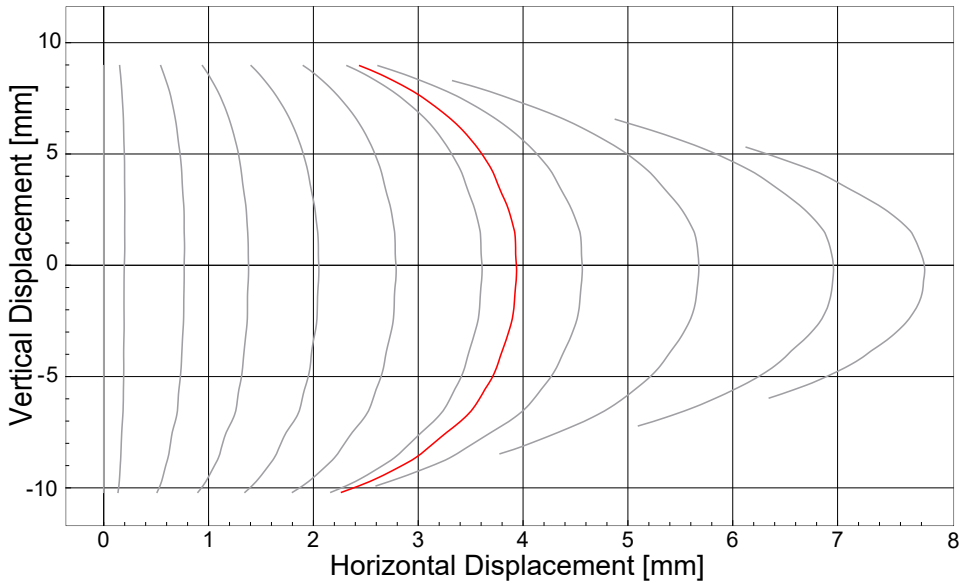

Figure 3.15: Horizontal displacement of gelatine specimen with no lubrication (red line: 40% strain).

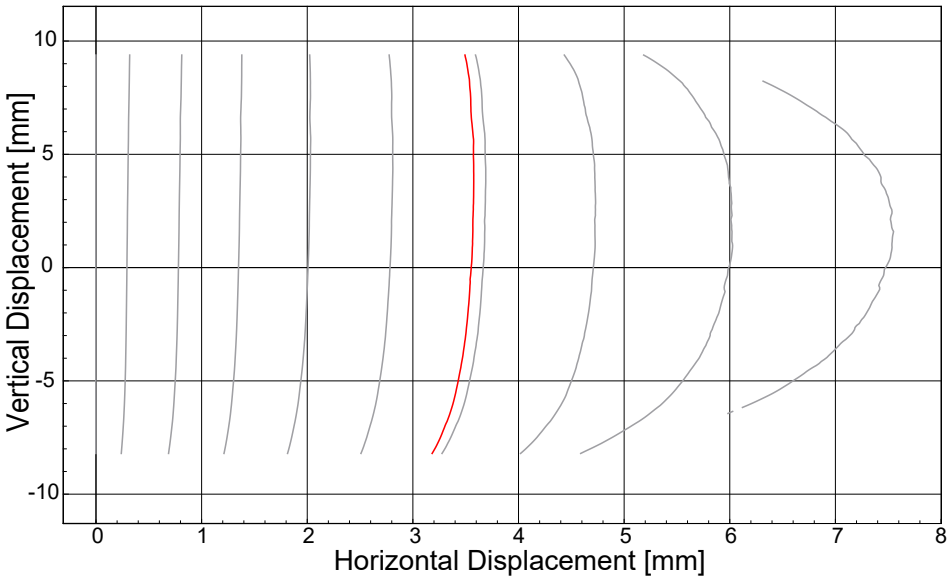

Figure 3.16: Horizontal displacement of the gelatine specimen with lubrication (red line: 40% strain).

The stress-strain relationship for synthetic gelatine can be calculated from the force-displacement data collected in these experiments. The two strain rates tested are plotted in Figure 3.17, and the strain rate is seen to affect the behaviour of the material. Figure 3.17 shows that test-to-test repeatability was very high. This repeatability is a result of improvements made to the specimen preparation that was developed in this work.

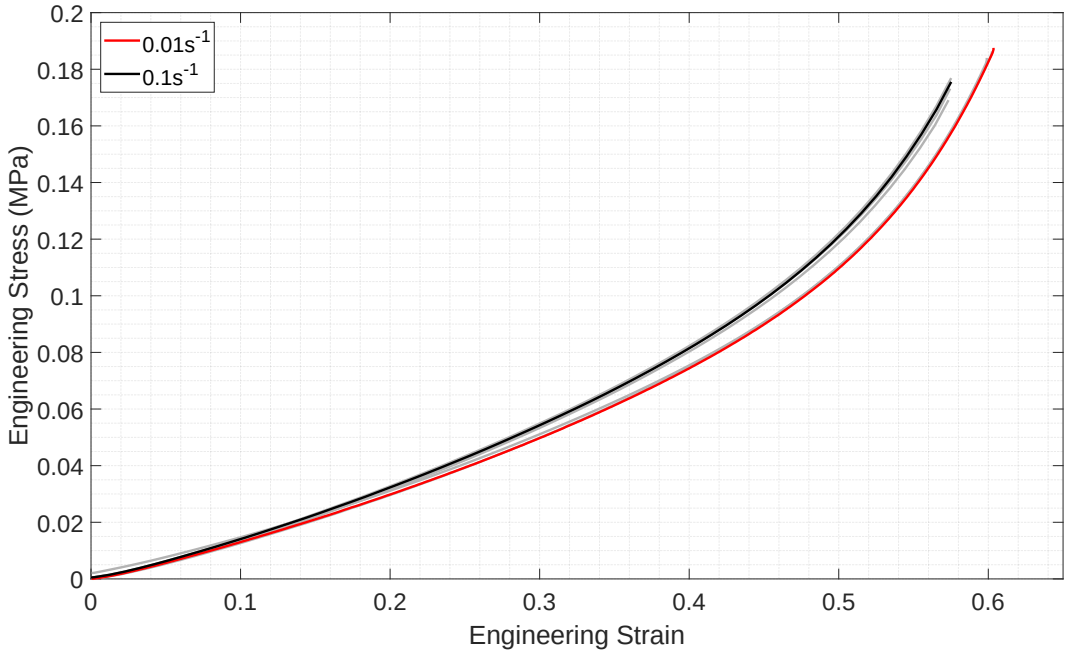

Figure 3.17: Engineering stress-strain graph for strain rates of 0.1 and 0.01 s^{-1}.

More tests were conducted at a strain rate of 0.01 s^{-1} with the loading surface being lubricated. Figure 3.18 displays the engineering stress-strain relationship of synthetic gelatine for lubricated and friction specimens. Figure 3.18 shows how increasing the friction between the specimens and the loading plates increases the gradient of the stress-strain curves. An increase in the gradient corresponds to an increase in the material stiffness.

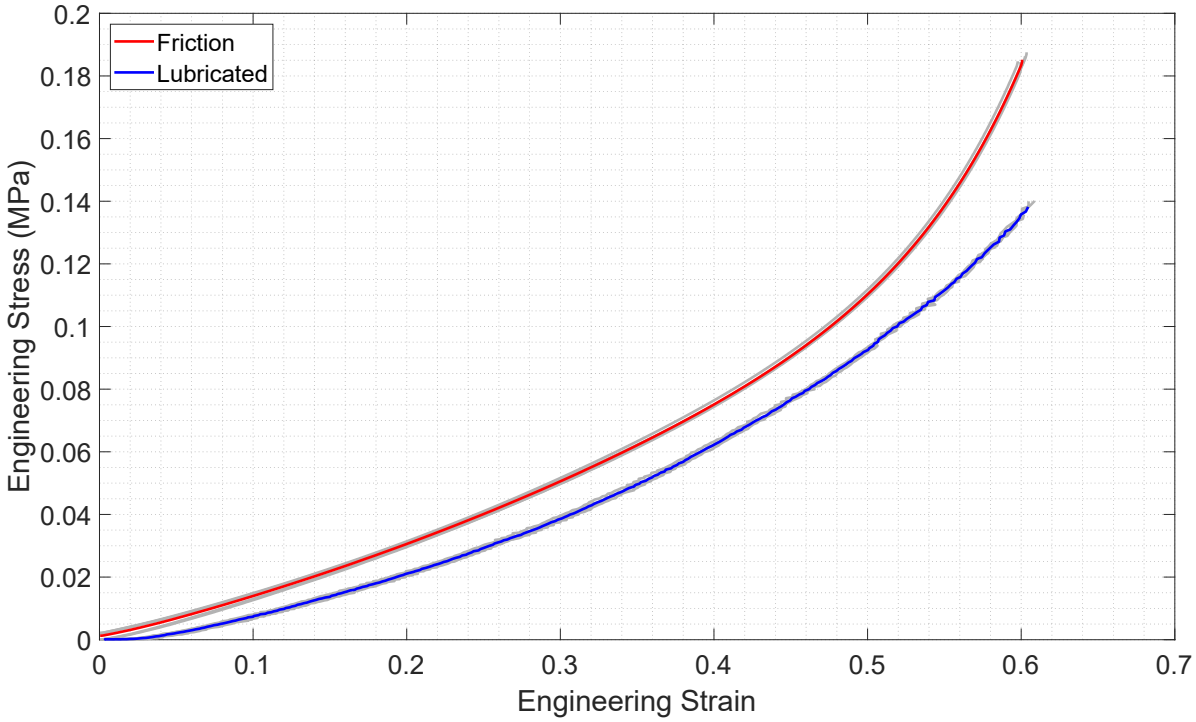

Figure 3.18: Engineering stress-strain graph comparing lubricated and friction specimens.

3.4 Insights from Simulations

3.4.1 Model Description

The software LS Dyna was utilised to simulate the behaviour of synthetic gelatine in the quasi-static compression experiment described above. LS Dyna is a multipurpose explicit and implicit finite element program capable of simulating the response of materials to short periods of severe loading. This allows it to simulate complex events such as blast loading. For the quasi-static simulation, the gelatine was modelled using a 2D axis-symmetric rectangular Lagrangian mesh of dimensions 12.5 mm and 25 mm in the x and y directions, respectively. In a Lagrangian description, each node of the finite mesh is deformed together, allowing the deforming material's shape to be determined. A symmetry boundary was defined about the y-axis, creating a cylinder when the mesh is revolved. The nodes at the base of the mesh were fixed in the y direction to represent the fixed bottom plate of the test machine. Finally, a constant velocity was applied to the top nodes to represent the moving top plate. This velocity determines the strain rate. The setup and geometry of the numerical model are detailed in Figure 3.19.

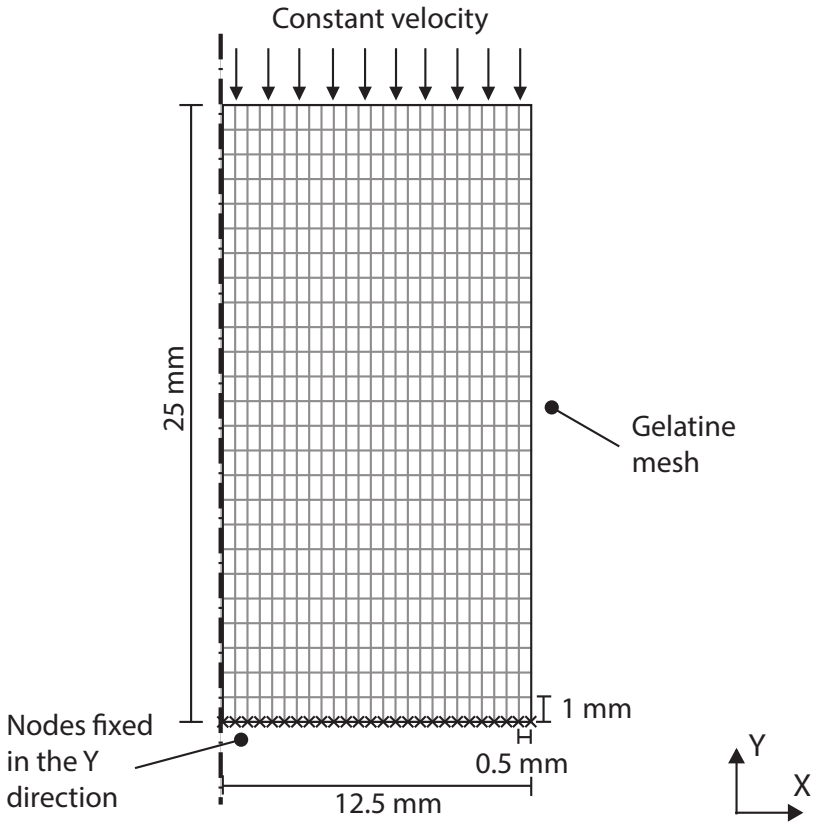

Figure 3.19: Geometry of the numerical model.

Different discretisations of the gelatine mesh were trialled to optimise the model. This numerical model is modelling compression, so the mesh size vastly affects the stress-strain results. This is because the compression could cause the mesh to become distorted and cause the simulation to terminate prematurely. However, selecting an appropriate mesh size is a trade-off between accuracy and running time. Four different mesh sizes were trialled: element size 1.04 mm by 1 mm, 0.5 mm by 0.5 mm, 1.04 mm by 2 mm and 0.5 mm by 1 mm. Figure 3.20 indicates the engineering stress-strain results for the different mesh sizes. The results are compared to the data collected in the experiments.

Decreasing the element size and increasing the number of elements in the mesh increased the running time of the model, Figure 3.21. Changing from a 1 mm square element to a 0.5 mm square element resulted in 8 times the termination time. However, this only resulted in a 9% increase in the final strain, at which point the simulation prematurely terminated, Figure 3.20. Through trial and error, the most effective mesh arrangement was a rectangular element size of 0.5 mm in the x-direction and 1 mm in the y-direction. This mesh design can be seen in Figure 3.19. The choice of rectangular elements resulted in a higher final strain at which the simulation terminated for less increase in the termination time, as shown in Figures 3.20 and 3.21.

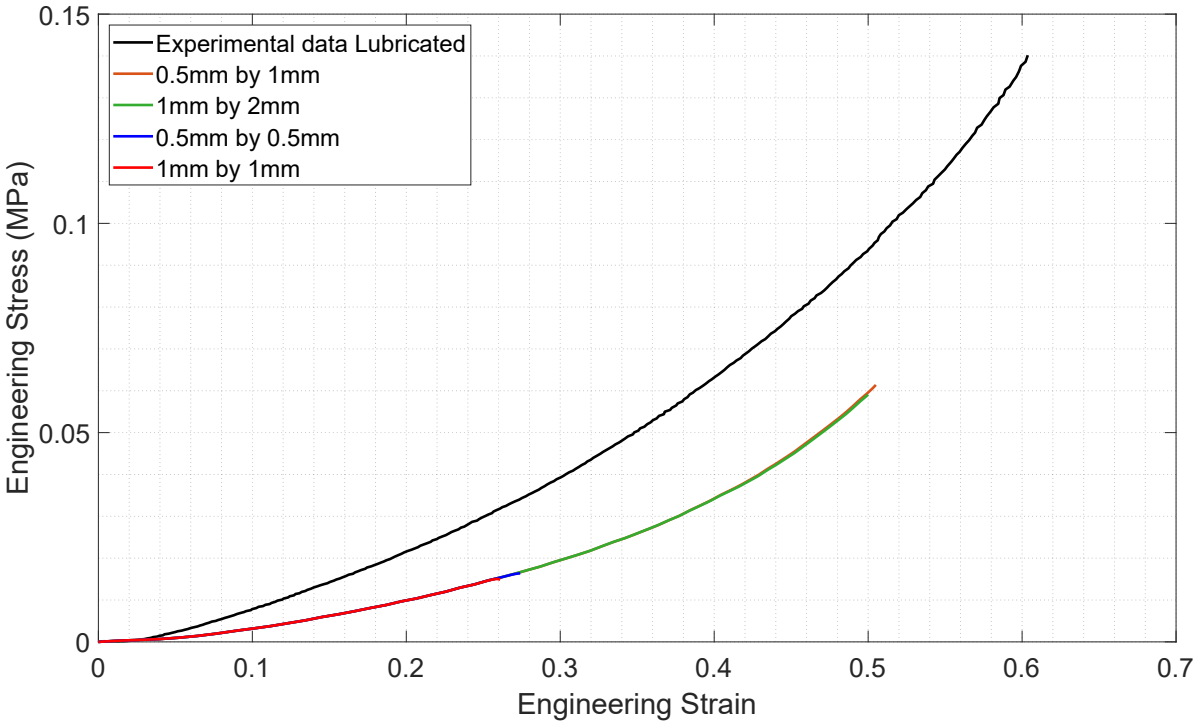

Figure 3.20: Engineering stress-strain results for different mesh sizes.

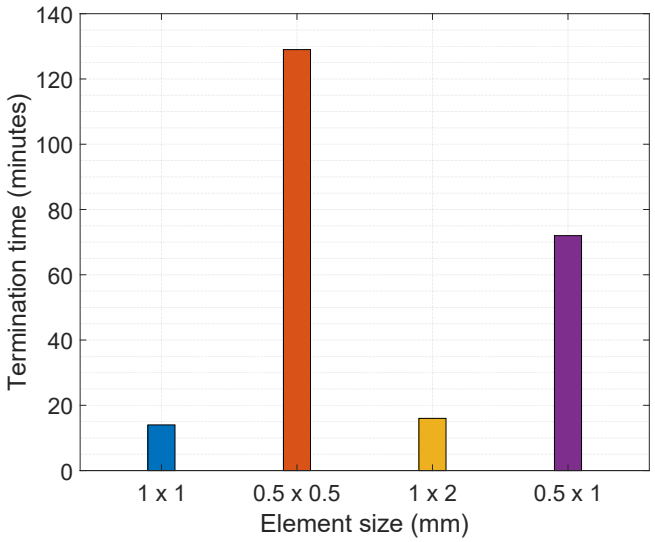

Figure 3.21: Simulation termination time vs mesh dimensions.

3.4.2 Influence of Constitutive Modelling Approach

As was identified in the literature review, many different material models have been used to simulate the behaviour of gelatine. In this study, four different material models were trialled to model the behaviour of gelatine under quasi-static compression. These material models were Elastic-Plastic, Linear Elastic, hyper-elastic Mooney-Rivlin and Simplified Rubber/Foam. The stress-strain curve from each model was compared with experimental data from Cronin and Falzon (2011) and Ravikumar et al. (2015) on organic gelatine and the experimental data reported in Section 3.3.

Linear Elastic

The Linear Elastic material model was investigated first. This material model is based on the Young's modulus relationship, Equation 3.1,

$$\sigma = E\epsilon \tag{3.1}$$

where σ is engineering stress, ϵ is engineering strain and E is Young's modulus. As shown in Figure 3.22, the results from the Elastic model initially agree with the gradient of the experimental data. However, this model fails to capture the non-linearity seen experimentally at higher strains.

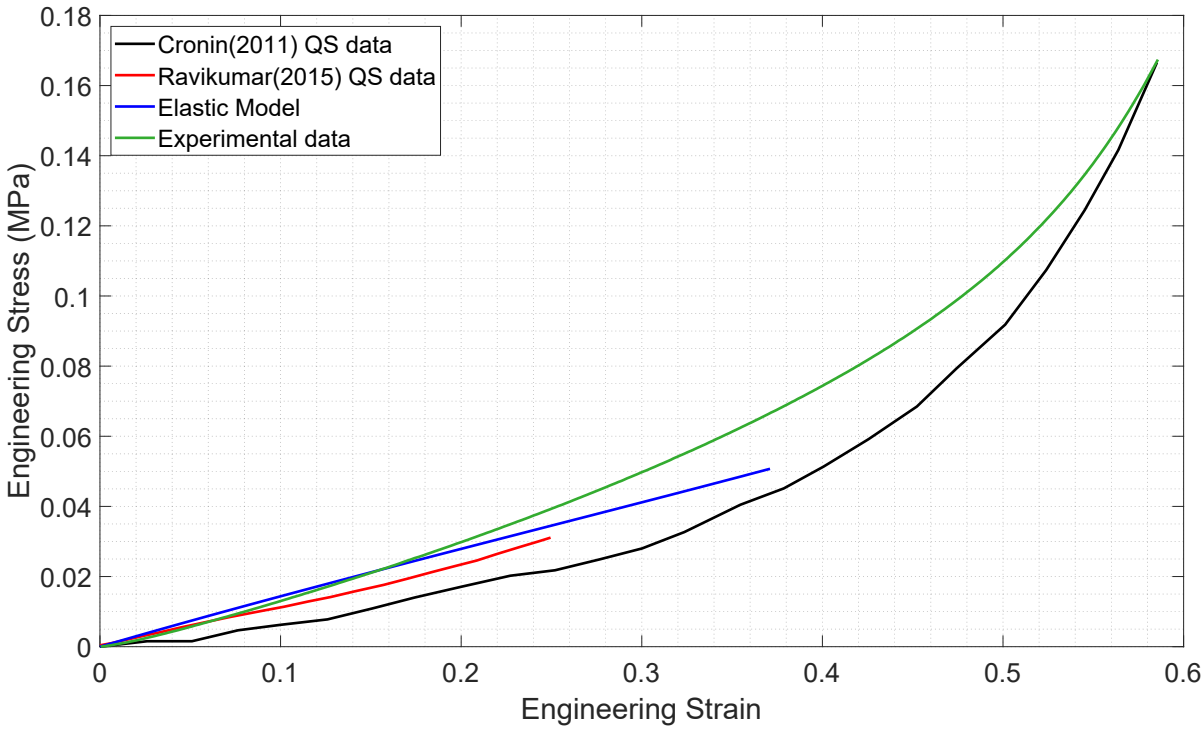

Figure 3.22: Stress-strain results from Linear Elastic material model compared to Cronin and Falzon (2011) and Ravikumar et al. (2015).

Elastic - Plastic

The Elastic-Plastic material model utilised by Gilson et al. (2016) to simulate the behaviour of ballistic gelatine allows complex hardening behaviour to be accurately represented (LST, 2012). This material model can also erode mesh elements once they reach a set failure strain, reducing mesh distortion and early termination of the simulation. An equation of state is required for this material model, and the linear polynomial was used here to define the thermodynamic state of the material. This material model requires the Plastic hardening modulus, Equation 3.2,

$$E_h = \frac{E_t E}{E - E_t} \tag{3.2}$$

where E is Young's modulus and E_t is the tangential Young's modulus. These were determined from the experimental data reported in Section 3.3. The Elastic-Plastic material results are compared to the experimental data and data by Cronin and Falzon (2011) and Ravikumar et al. (2015). Figure 3.23 displays how the initial elastic behaviour is captured well; however, once the model reaches higher strains, the mesh experiences larger distortion and the stress is reduced. This may be the result of the elastic hardening modulus being negative for gelatine because the tangential Young's modulus is higher than the Young's modulus.

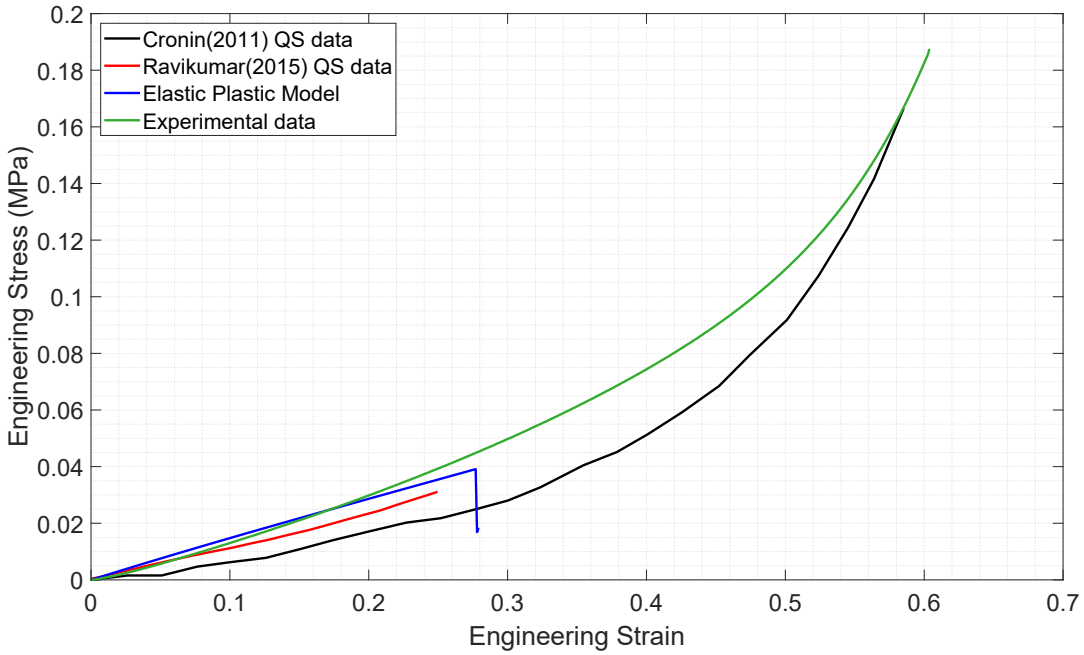

Figure 3.23: Stress-strain results from Elastic-Plastic material model compared to Cronin and Falzon (2011) and Ravikumar et al. (2015).

Mooney - Rivlin Rubber

The Mooney-Rivlin rubber model has been used in past studies to successfully predict the behaviour of hyperelastic materials at high strain rates (Ramezani et al., 2009). The Mooney-Rivlin model states that for an incompressible material, the energy density can be described as a combination of the linear terms of the power series, Equation 3.3. For uniaxial compression, this model can be expressed in terms of the stretch ratio and differentiated with respect to the extension to find the true stress of the material, Equation 3.4 (Mooney, 1940).

$$w = C_1(I_1 - 3) + C_2(I_2 - 3) \tag{3.3}$$

$$\sigma_{true} = (2C_1 + \frac{2C_2}{\lambda})(\lambda^2 - \frac{1}{\lambda}) \tag{3.4}$$

This equation can be used to find the Mooney-Rivlin constants for a material by curve fitting to experimental data. Figure 3.24 shows the Mooney-Rivlin curve fitted to the experimental data. These constants were used in an LS Dyna model, and the corresponding results can be seen in Figure 3.24. The results from the Mooney-Rivlin model showed no correlation to the experiments or the literature results, and obtaining the constants proved difficult as the stress-strain relationship exhibited by the gelatine specimens appears to be exponential.

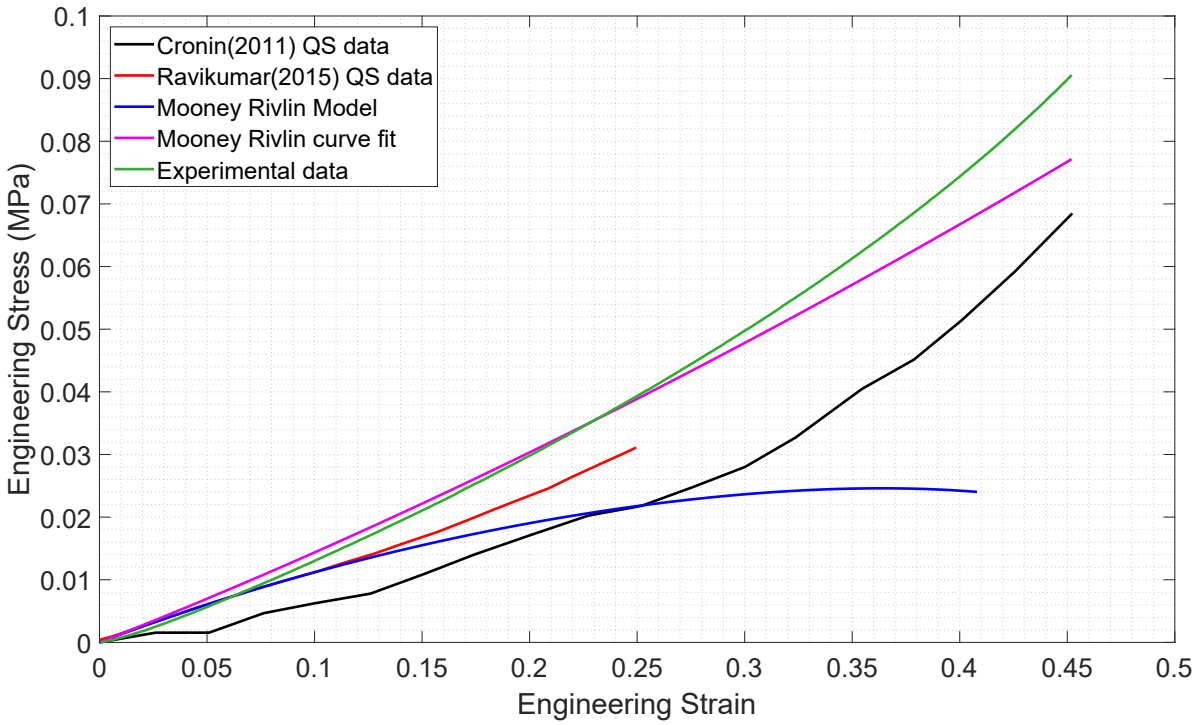

Figure 3.24: Stress-strain results from Mooney-Rivlin material model compared to Cronin and Falzon (2011) and Ravikumar et al. (2015).

Simplified Rubber/Foam

The final material model considered was the Simplified Rubber/Foam model. This material is used in Toyota's total human model of safety (THUMS) LS Dyna model to define the tendons and soft tissue. The Simplified Rubber/Foam model is a tabulated version of the hyper-elastic Ogden material law. The Ogden material law is a visco-hyperelastic constitutive single-term model, the same approach used by Ravikumar to simulate the behaviour of gelatine in the software Abaqus (Ravikumar et al., 2015). In Ogden's law, the elastic isochoric strain energy is defined in terms of the shear modulus and the stretch ratio in Equation 3.5,

$$W_{iso}^{E}(\lambda_1, \lambda_2, \lambda_3) = \sum_{i=1}^{N_H} \frac{\mu_i}{\alpha_i^2}(\lambda_1^{\alpha_i}, \lambda_2^{\alpha_i}, \lambda_3^{\alpha_i} - 3) \tag{3.5}$$

and the volumetric strain energy is defined in terms of the initial bulk modulus, Equation 3.6

$$W_{vol}(J) = \frac{K_0}{2}(J-1)^2. \tag{3.6}$$

A uniaxial load curve from experimental tests, bulk modulus and Poisson's ratio, are defined in the LS Dyna material card. Figure 3.25 shows a better correlation between the simulation and the literature results, with the average gradient of the model being only 6% higher than Cronin's data. The higher stiffness of the experimental data is thought to be linked to the friction between the gelatine surface and the loading plates. This frictional force is not simulated at this stage but is explored later in this chapter.

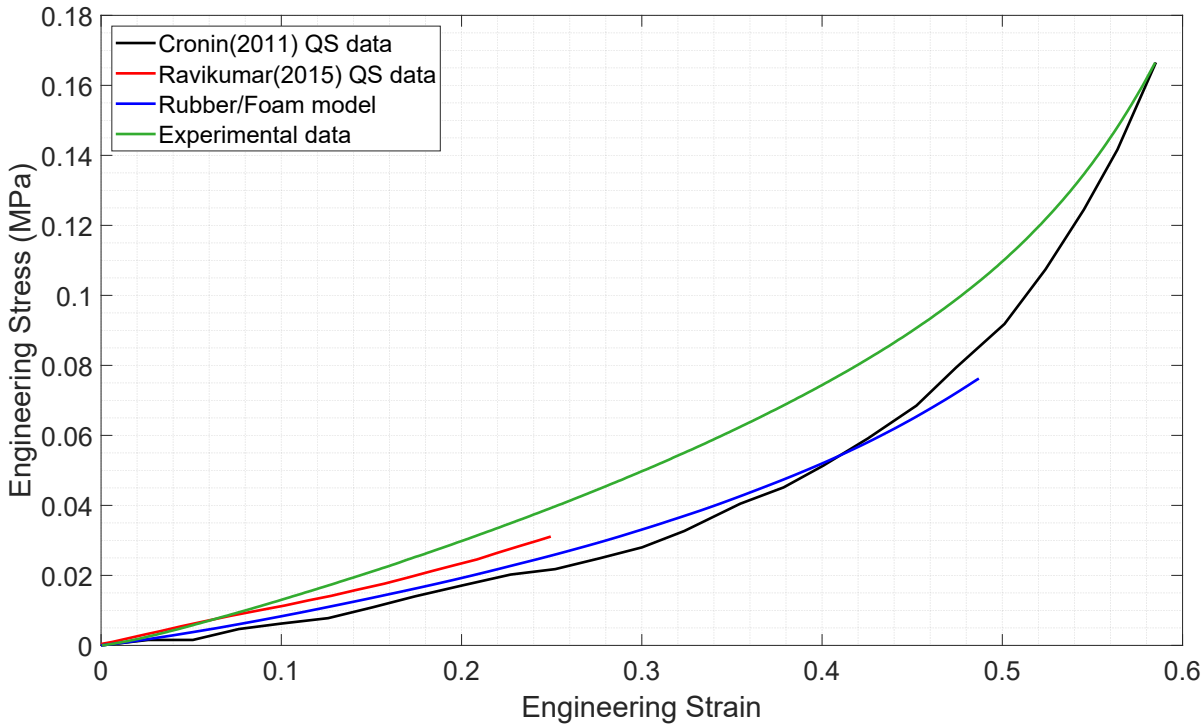

Figure 3.25: Stress-strain results from Simplified Rubber/Foam material model compared to Cronin and Falzon (2011) and Ravikumar et al. (2015).

The Simplified Rubber/Foam material model was chosen for the final numerical model as results from this model aligned closely with the experimental data. The relevant properties

required for the material card were calculated from our experimental data and the experimental data was also used as the load curve for the model.

	Bulk modulus (MPa)	Poisson's ratio
Input values	0.75	0.49

Table 3.2: Initial material properties for synthetic gelatine.

3.4.3 Extracting Material Properties

To investigate the volumetric material properties of gelatine, the change in volume and shape needs to be quantified. Calculating the volume was made possible through the use of DIC. Using the side-on displacement data collected from the line slice plots in Section 3.3, the volume of the specimen at each time step can be estimated, see Figure 3.26. The equation for the volume of a cylinder was utilised to calculate the volume of gelatine. To account for the barrelling of the gelatine, the volume was calculated in segments and summed up to find the entire volume.

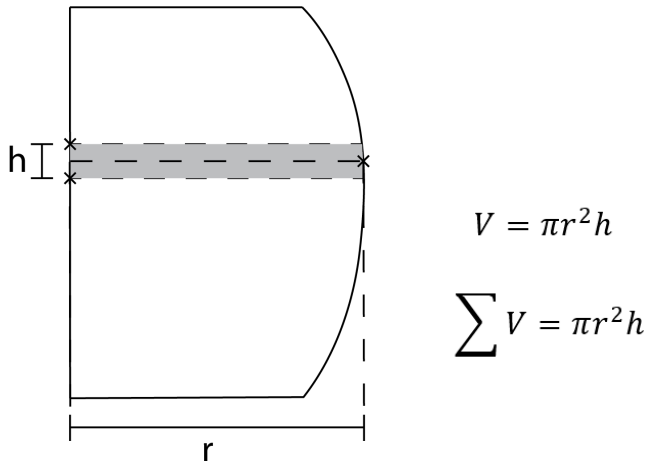

Figure 3.26: Diagram illustrating how the volume of gelatine was calculated.

This data was then used to calculate the volume change and subsequently used to calculate the volumetric strain. The volumetric strain was calculated using Equation 3.7,

$$\epsilon_v = \frac{\Delta V}{V_0} \tag{3.7}$$

where ΔV is the change in volume and V_0 is the initial volume. True stress needs to be calculated also to calculate the bulk modulus. This was calculated by taking the force recorded by the uniaxial compression machine and dividing that by the cross-sectional area at each time step, Equation 3.8.

$$\sigma_T = \frac{F}{A_i} \tag{3.8}$$

and bulk modulus is given by Equation 3.9

$$K = \frac{\sigma_T}{\epsilon_v}. \tag{3.9}$$

The volumetric strain and bulk modulus are plotted over the duration of the tests in Figure 3.27 and 3.28.

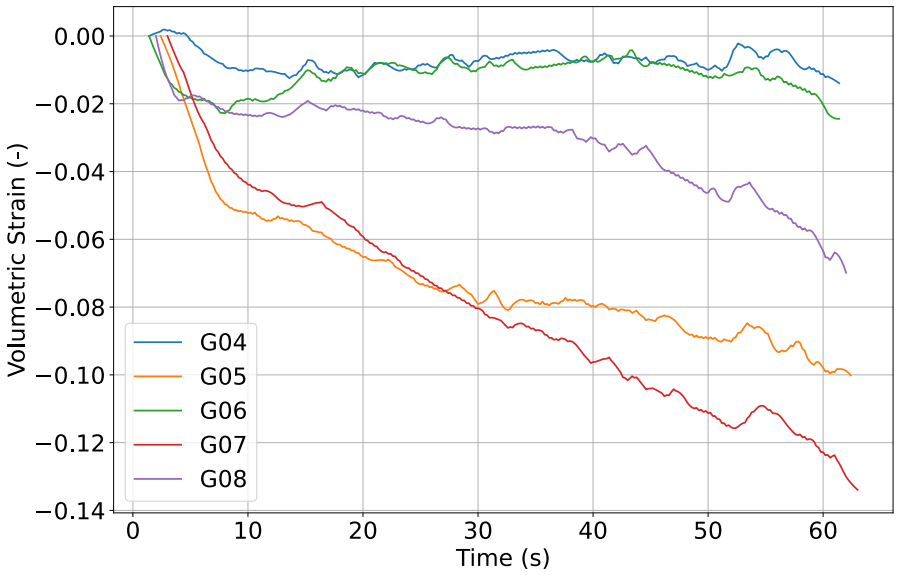

Figure 3.27: Volumetric strain results.

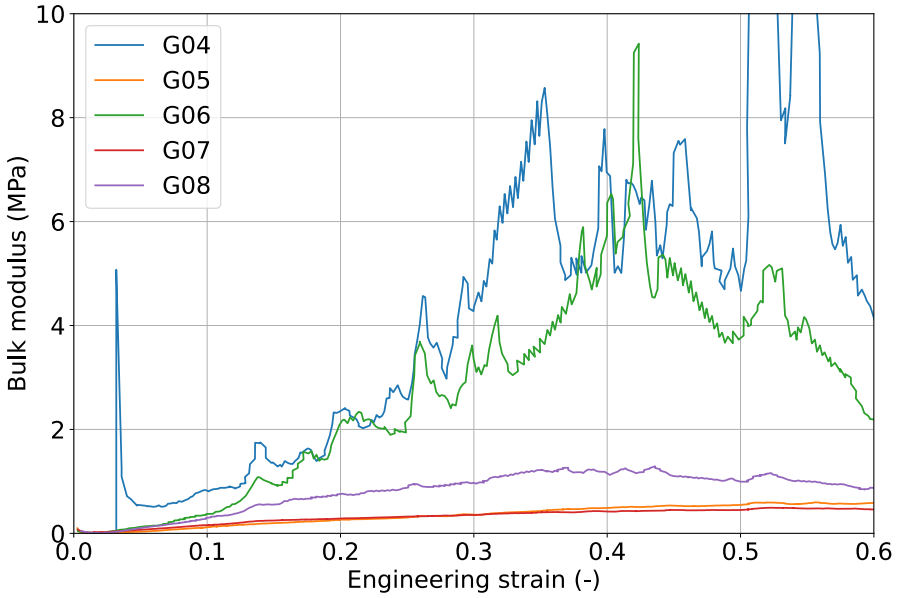

Figure 3.28: Bulk modulus results.

Poisson's ratio was calculated by utilising the relationship between Young's modulus, bulk modulus (Equ 3.9), Equation 3.10.

$$\nu = 0.5 - \frac{E}{6K} \tag{3.10}$$

where Young's modulus E is the engineering stress divided by the linear strain,

$$E = \frac{\sigma_E}{\epsilon_x}. \tag{3.11}$$

The engineering stress σ_E is given by,

$$\sigma_E = \frac{F}{A_0} \tag{3.12}$$

and the linear strain ϵ_x is the change in height divided by the initial height of the specimen,

$$\epsilon_x = \frac{\Delta l}{l_0}. \tag{3.13}$$

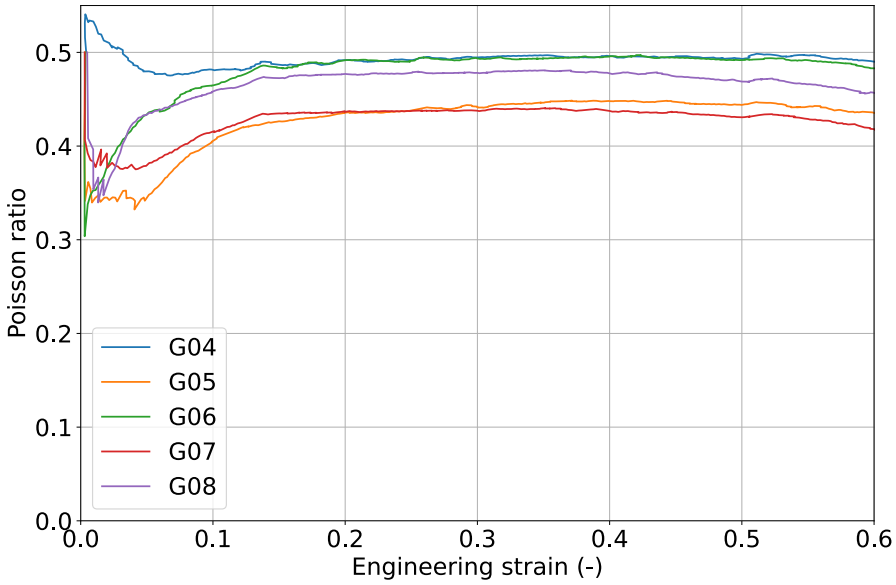

Figure 3.29: Poisson's ratio results.

The bulk modulus of synthetic gelatine was determined by taking the average of the maximum value from tests 5, 7 and 8. Tests 4 and 6 showed minimal change in volume over the experiment, resulting in bulk modulus values rising to infinity by dividing by close to zero. This caused the calculated bulk modulus values for tests 4 and 6 to be highly variable. For Poisson's ratio, two distinct groups of curves are seen. During the early investigation of this material model, Poisson's ratio was found to have a significant effect on the model's stiffness. To account for this, three Poisson's ratio values will be compared. These values are the average of the maximums from tests 5 and 7, the average of the maximums from tests 4, 6 and 8 and the average of the maximums from all the tests. The values used in the material model for gelatine can be seen in Table 3.3.

	Bulk modulus (MPa)		Poisson's ratio	
		Tests 5 & 7	All Tests	Tests 4, 6 & 8
Input values	0.793	0.445	0.475	0.495

Table 3.3: Material properties for synthetic gelatine from DIC analysis.

3.4.4 Results from no Friction Model

The values for bulk modulus and Poisson's ratio identified in Section 3.4.3 were input into the numerical model, along with the experimental load curves. The numerical model was run with the load curve from the lubricated experiments and then the one from the experiments with friction. Firstly, the results from using the three different values for Poisson's ratio are

compared. The results from each of the load curves are displayed in Figures 3.30 and 3.31. The gradient of the exponential curve increases as the value of Poisson's ratio increases. The increase in gradient shows an increase in material stiffness. The stiffness is increasing because Poisson's ratio tends towards incompressibility, 0.4999. The curves where Poisson's ratio is 0.495 show the closest match to the curvature of the experimental curves.

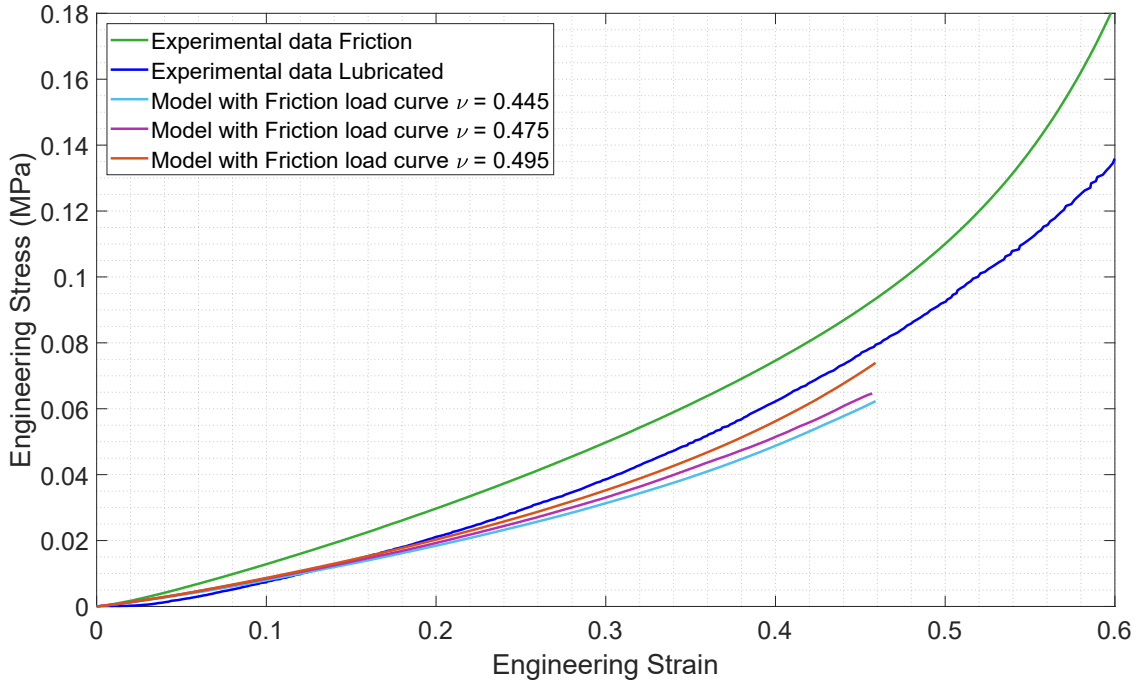

Figure 3.30: Results from numerical model with friction load curve.

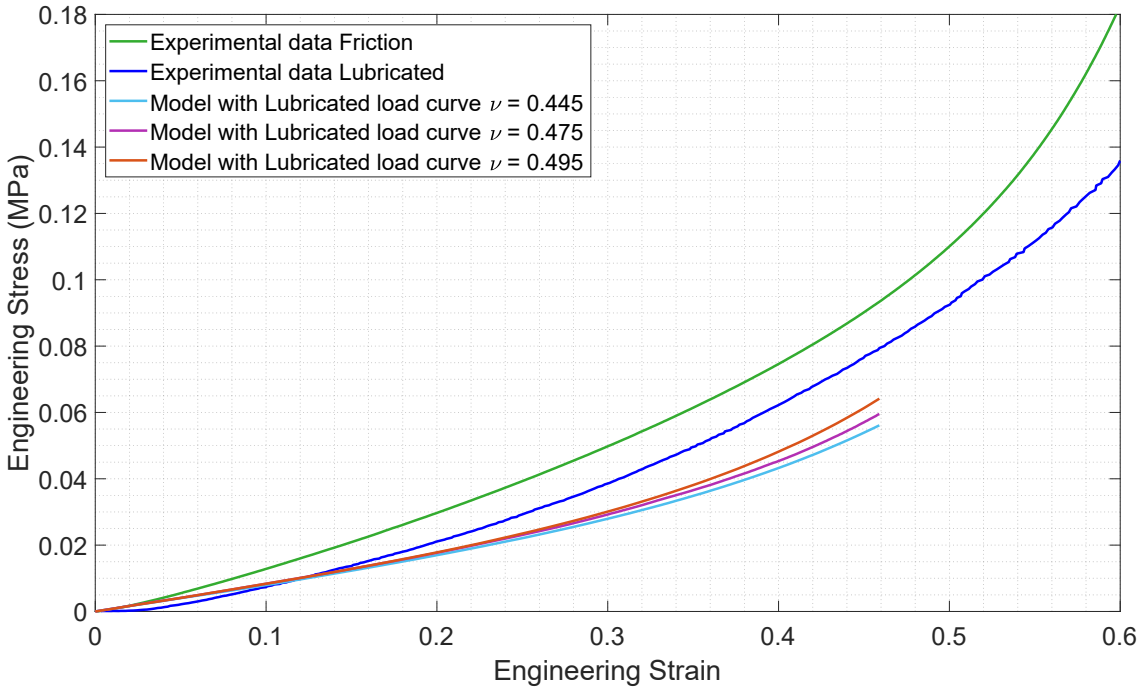

Figure 3.31: Results from numerical model with lubricated load curve.

The results from the model using Poisson's ratio of 0.495 are repeated in Figure 3.32 to compare the friction and lubricated load curves. Both model curves follow a similar exponential shape to the experimental data, with the gradient increasing as strain increases. The variation in the stiffness of the four curves is thought to be caused by friction between the gelatine and the loading plate. The models are lower than the experimental data because the loading plates are not present in the simple numerical model. The variation in stiffness between the two models is linked to the variation in the load curves' stiffness.

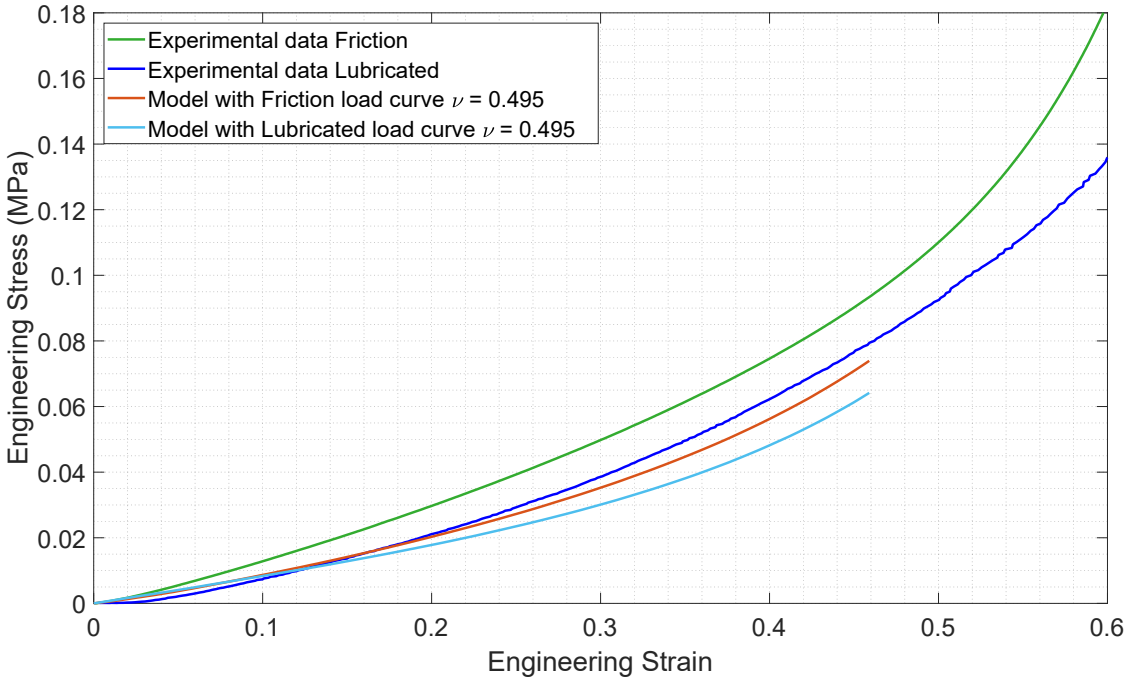

Figure 3.32: Results from numerical model with no friction factors.

3.4.5 Determining the Friction Coefficient

Previously, gelatine was modelled during a quasi-static compression test, assuming no friction was present at the top and bottom of the specimen. This assumption reduces the complexity of the numerical model; however, it was highlighted that friction between the loading plates and the specimen significantly affects the response. The mesh geometry was modified to try and replicate the friction between the loading plates and the specimen in the numerical model, Figure 3.33. Two rigid parts were added to the model at the top and bottom of the specimen. The mesh was designed to align the nodal points for the gelatine and loading plates. Mesh sensitivity analysis performed in Section 3.4.1 displayed that the mesh was insensitive to material stiffness, so the size was unaltered here (see Figures 3.20 and 3.21). The frictional contact can then be defined by defining the type of contact surface. The contact between the gelatine and the loading plates was simulated with the keyword file automatic surface-to-surface contact. The gelatine surface was defined as the slave part, and the loading plates were the master parts.

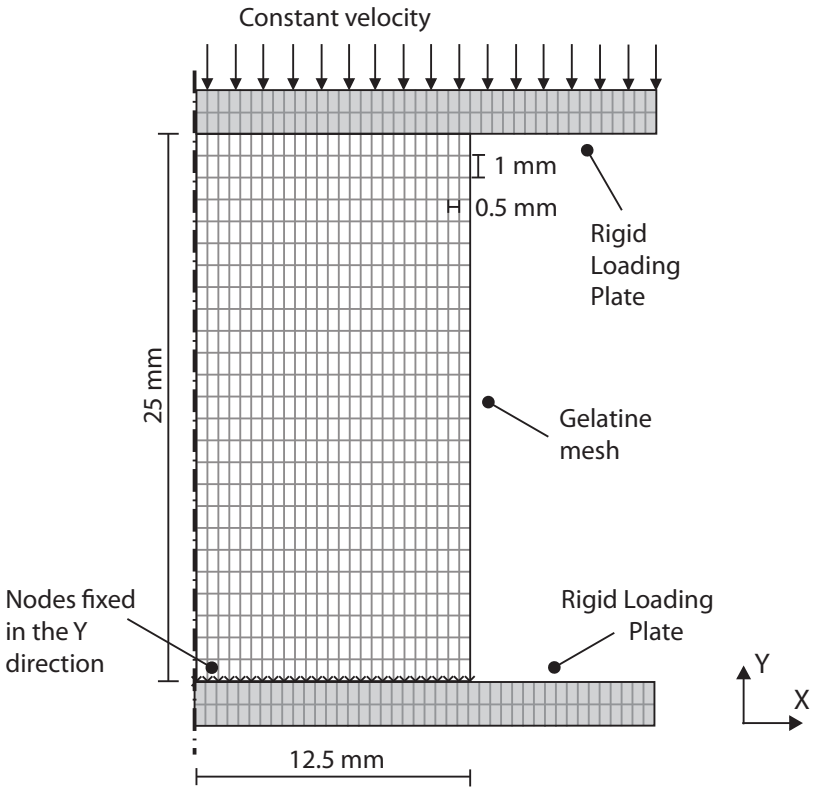

Figure 3.33: Geometry of the numerical model with the loading plates added.

A range of static friction factors were applied to both contact surfaces in the numerical model. Both set-ups of the model were considered, using both load curves. Figure 3.34 displays the results by assigning a friction factor of 0.1, 0.2 and 0.3 to the model with the lubricated load curve. Figure 3.35 shows the results by assigning friction factors of 0.1, 0.2, 0.3, 0.4, and 0.5 to the model using the friction load curve. The figures display how, as the friction factor is increased, the gradient of the stress-strain curve increases. A friction factor of 0.3 has the least gradient difference to the lubricated experimental data, with a 7% difference. However, after 0.35 strain, the gradient increases at a higher rate than in the experiment, causing the curves to diverge from the experiment. The higher gradient could be linked to increased mesh distortion in the model, increasing the stress.

For the friction load curve model, a friction factor of 0.1 aligns closely with the lubricated

experimental data, with only a 4% difference in the gradient, highlighting the inbuilt friction of the friction load curve. A friction factor of 0.3 has the least gradient difference to the friction experimental data, with a 12% difference. However, a similar increase in stress is seen after 0.4 strain due to mesh distortion. As seen in Figure 3.35, increasing the friction factor beyond 0.3 causes little difference in the strain-stress results.

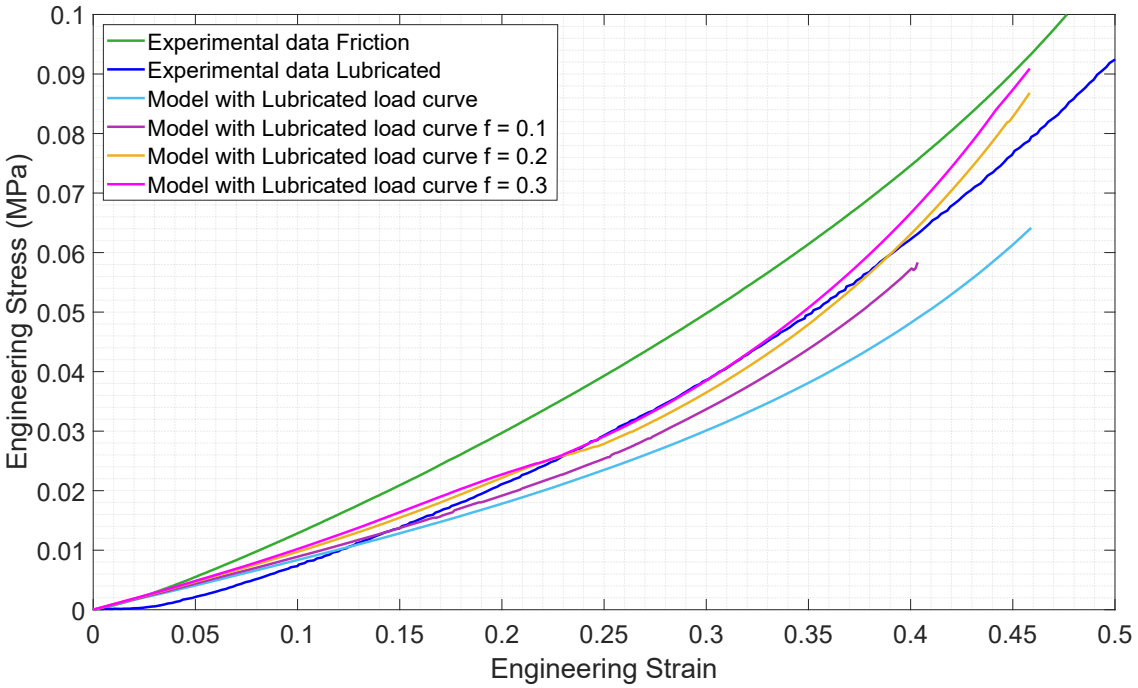

Figure 3.34: Results from numerical model with lubricated load curve with different friction factors.

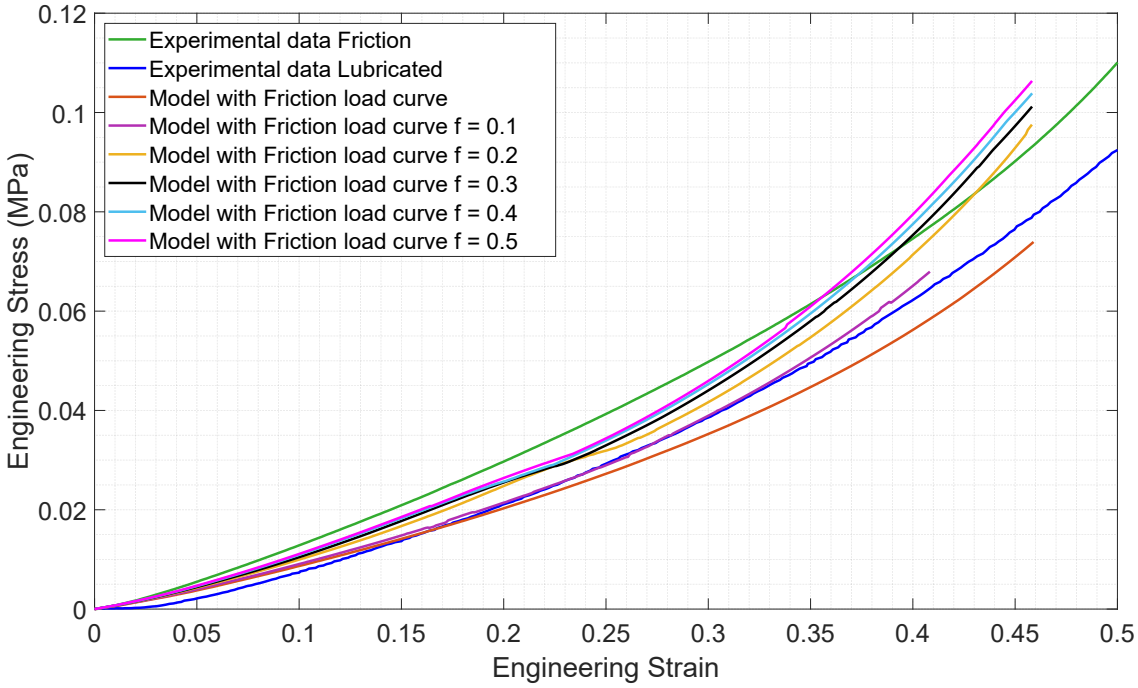

Figure 3.35: Results from numerical model with friction load curve with different friction factors.

3.5 Summary of Findings

This chapter refined the process of manufacturing gelatine specimens for quasi-static compression tests to produce repeatable results. The surface finish on the top and bottom of the gelatine specimens considerably affected the repeatability of these experiments. A speckle pattern was successfully applied to the gelatine to facilitate DIC. The gelatine was dyed white with epoxy resin dye and speckled with an ink pad. The stress-strain results from these experiments were compared with the literature data from Cronin and Falzon (2011) and Ravikumar et al. (2015) and synthetic gelatine was found to respond similarly to organic gelatine under compressive loading. After this was verified, more experiments were conducted where the surfaces of the gelatine were lubricated to explore the effect of friction on the stiffness. These experiments highlighted that friction increases the stiffness of gelatine in compression. The results from the high-speed video were processed using DIC to estimate key material properties required to develop a numerical model for gelatine. Initial simulations found that the Simplified Rubber/Foam material model in LS Dyna most closely matched the experimental data. Bulk modulus and Poisson's ratio were estimated for gelatine by calculating the volume change of the specimens over the test duration. The bulk modulus was 0.793 MPa, and Poisson's ratio was 0.495. With these properties defined, the numerical model displayed a stress-strain relationship similar to the experimental data. The effect of friction between the loading plates and gelatine was also explored in the simulation, and increasing the friction factor was found to increase the model's stiffness, as expected.

Chapter 4

Behaviour of Synthetic Gelatine under High Strain-Rate Loading

This chapter explores the behaviour of synthetic gelatine during dynamic loading. The strain-rate sensitivity of the material seen in Chapter 3 is investigated at high strain rates, and the material model previously developed for gelatine is tested at higher strain rates.

4.1 Experimental Testing

4.1.1 Specimen Design and Manufacture

To study the behaviour of synthetic gelatine under high-strain rate loading, split-Hopkinson pressure bar (SHPB) experiments were carried out. As discussed in Chapter 2, previous studies have used specimens of a wide range of sizes for SHPB experiments on organic gelatine. When testing gelatine, it is recommended to use a specimen with a small diameter-to-length ratio to minimise inertial and friction/barrelling effects during the test (Salisbury and Cronin, 2009). Thin samples are also used in SHPB testing to ensure stress equilibrium across the sample. The size chosen for this study was circular specimens with a diameter of 12 mm and a thickness of 3 mm. A diameter of 12 mm was selected to reduce the extrusion of the material from the Hopkinson bars as it was compressed. As in Chapter 3, an aluminium mould was manufactured to cast the gelatine into the desired dimensions. The mould consisted of a 3 mm deep aluminium block with 12 mm diameter circular holes drilled through. This was attached to the same base plate used for the quasi-static specimens to allow for easy removal of the gelatine specimens.

The specimens were produced following Clear Ballistics remoulding guidelines. Pieces of gelatine were removed from the premade block and carefully weighed to the correct mass. The gelatine was then heated in the mould to 125°C for 4 hours and left to cool overnight. Due to the higher diameter-to-thickness ratio of these specimens compared to the quasi-static specimens, a meniscus did not form on the top of the specimens. As a result, the samples did not need to be cut down after cooling. During the remoulding process, the synthetic gelatine was dyed white to contrast the clear Hopkinson pressure bars. The synthetic gelatine was dyed using epoxy resin dye, as used in Chapter 3.

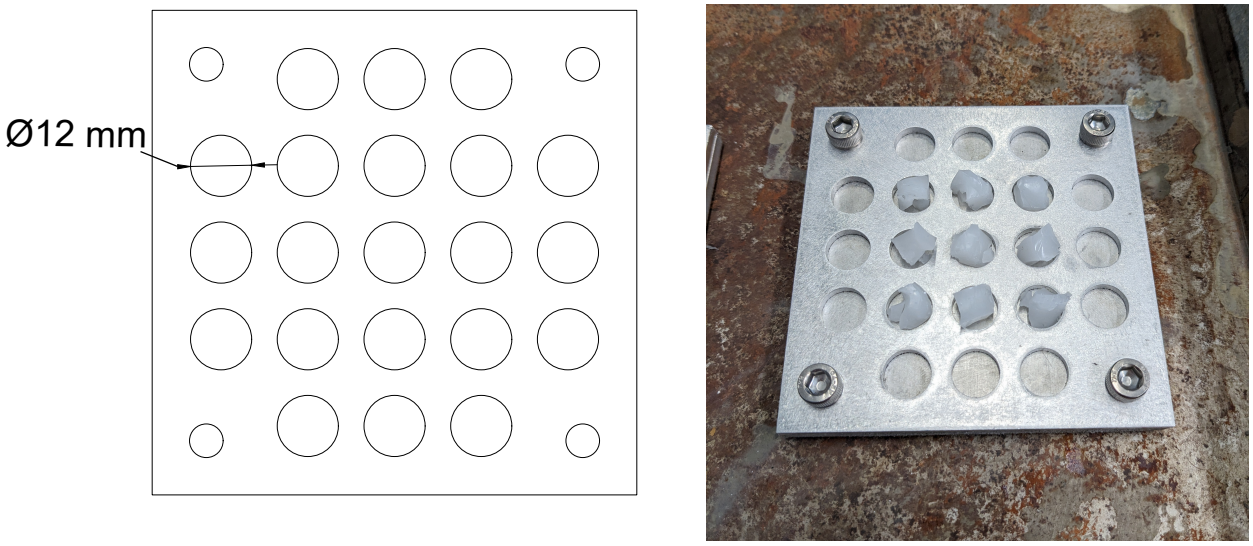

Figure 4.1: Drawing of gelatine mould and gelatine weighted out and ready to go in the oven.

4.1.2 Test Arrangement

As discussed, a SHPB apparatus was used to conduct high-strain-rate gelatine testing. For this testing, polymeric pressure bars were used to reduce the impedance mismatch between the soft gelatine and the pressure bars. This ensures the stress wave passes into the specimen rather than being reflected at the sample boundary. The polymer utilised for this SHPB set-up was polycarbonate, as previous research by Curry (2011) found it to have a small amount of dispersion and attenuation compared to other polymers like nylon and PMMA. Also, the wave speed calculated by Curry (2011), 1436 m/s, is close to the estimated wave speed for gelatine, which is 1500 m/s (Cronin and Falzon, 2011).

The striker bar was fired using a gas gun, which allowed a controlled amount of nitrogen gas to be pressurised in a sealed reservoir. The striker bar is inserted down the gas gun at a predetermined distance to achieve a consistent desired impact velocity for all tests, see Tables 4.1 and 4.2. A speed trap mechanism was installed on the gas gun's barrel to record the striker's velocity. The light gates in the speed trap were 50 mm apart and connected to the TiePie Handyscope oscilloscope, so the velocity can be calculated using Equation 4.1,

$$v_s = \frac{l_s}{t_b - t_f} \tag{4.1}$$

where v_s is the striker velocity, the speed trap distance (50 mm) is l_s and t_b–t_f is the time the striker takes to travel between the light traps. With the polycarbonate being transparent, the striker bar was spray-painted white, so the light trap was blocked when the bar passed through it. The experimental setup consisted of 1-inch diameter polycarbonate incident and transmitter pressure bars and a 20 mm diameter polycarbonate striker bar with 2400, 2400, and 190 mm lengths, respectively. The bars were arranged in a typical SHPB arrangement, and the incident and transmitter bar lengths were chosen to match Salisbury and Cronin's (2009) polymeric SHPB arrangement. The striker bar dimensions were selected to reduce the bar's weight so a low impact velocity of 5 m/s could be achieved. One set of strain gauges was mounted halfway along the incident bar, and the other was mounted at 300 mm along the transmitter bar. This distance for the transmitter bar strain gauge was chosen to reduce the attenuation of the signal. The arrangement is shown in Figure 4.2.

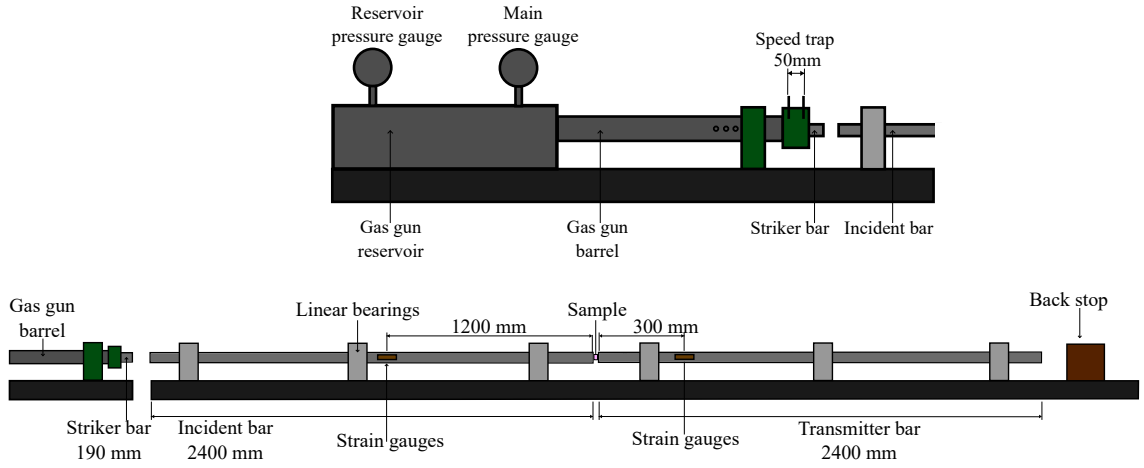

Figure 4.2: Diagram of the gas gun and SHPB apparatus.

The SHPB is impacted by a polycarbonate striker bar on one end fired by a gas gun, causing a compressive stress pulse to propagate through the system. The pressure bars are calibrated by comparing the theoretical strain caused by the striker to the recorded strain in the bar. For a known striker velocity, the theoretical strain in the bar is given by the relationship in Equation 4.2,

$$\epsilon_j = \frac{V}{2c_b} \tag{4.2}$$

where ϵ_j is the theoretical strain in the bar, V is the velocity of the striker bar, and c_b is the longitudinal wave speed of the bar. The longitudinal wave speed in the bar can be calculated using Equation 4.3 to compare the incident and reflected pulse at a strain gauge location. Using textbook values for the wave speed is not advised in literature (Nemat-Nasser, 2000).

$$c_0 = \frac{2l}{t} \tag{4.3}$$

Two strain gauges were installed on opposing sides of the pressure bars and connected to a TiePie Handyscope four-channel digital oscilloscope to record the pulse caused by the impact of the striker bar. The sampling rate used was 1 MHz. The strain gauges used were Kyowa KFP-2-350-C1-65L3M2R semiconductor gauges, which were arranged on opposite sides of the bar to eliminate strain caused by bending, so only longitudinal strain was recorded. The strain gauges were configured as a half Wheatstone bridge with two variable resistors to balance out temperature-induced strain; the layout is shown in Figure 4.3. The signal from the strain gauges was amplified by 100 to allow the true signal to be differentiated from noise. The recorded voltages from the incident and transmitter pressure bars can be processed to calculate the bar strain using Equation 4.4,

$$\epsilon_b = 2\frac{V_o}{FV_i} \tag{4.4}$$

where V_i and V_o are the input and output voltages across the Wheatstone bridge, and F is the gauge factor. The gauge amplification is applied to the input voltage, and the gauge factor is determined by comparing the recorded bar strain with the theoretical strain during calibration.

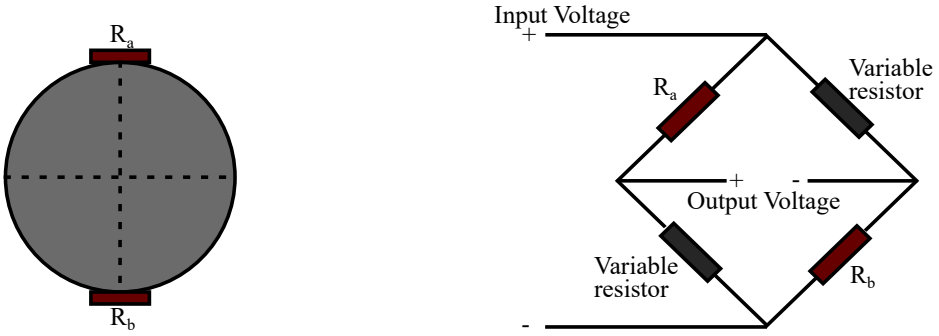

Figure 4.3: Right is strain gauge poition on the bars and left is the half Wheatstone bridge.

4.1.3 Results and Discussion

Tap tests were performed using a 25 mm long cylinder of nylon that was impacted on the end of each bar. The nylon provided a sharp pulse, allowing for high accuracy when measuring the time difference between the incident and the reflected pulse. These tap tests were used to calculate the wave speed in the polycarbonate pressure bar using Equation 4.3. The graph in Figure 4.4 shows an example of the signal recorded in the tap tests. The wave speed for the polycarbonate bars was found to be 1455 m/s. This is similar to the wave speed Curry (2011) reported of 1436 m/s. A series of 'bar together' tests were conducted to determine the gauge factors for the strain gauges. These tests are conducted by placing the incident and transmitter bars together and firing the striker at desired velocities, see Table 4.1. The theoretical bar strain is then compared with the recorded signal to determine the gauge factor.

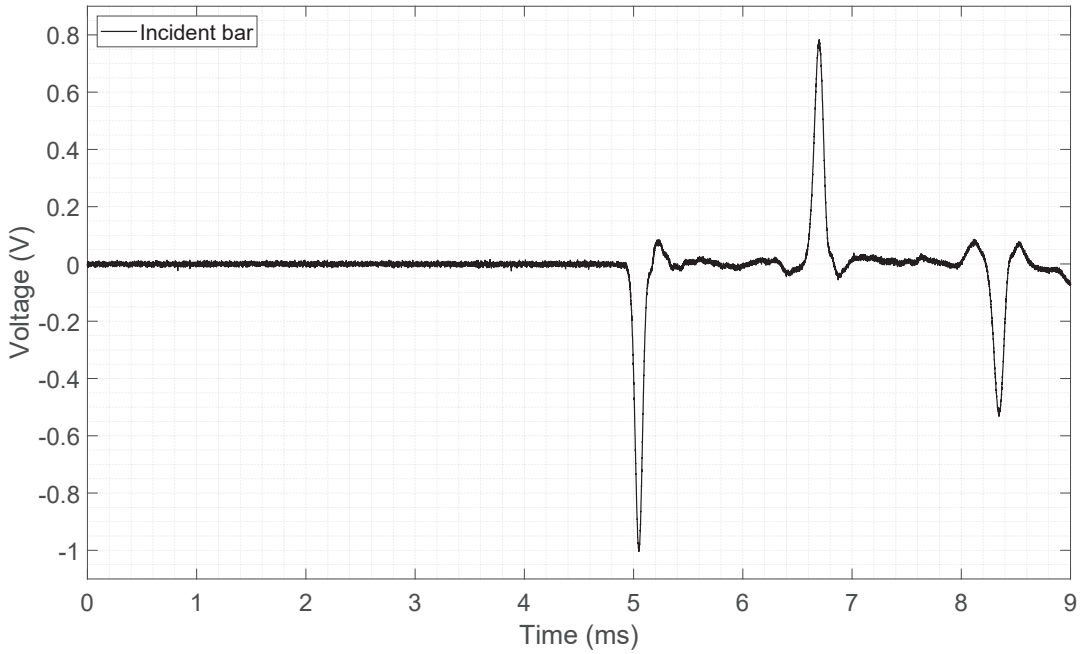

Figure 4.4: Strain gauge signal from nylon tap test; time from striker impact.

SHPB experiments were conducted at three different striker velocities to provide a range of strain rates. When selecting striker velocities, the strain rate in the specimen caused by a certain velocity can be calculated by Equation 4.5,

$$\dot{\epsilon} = \frac{V}{l} \tag{4.5}$$

where V is the striker velocity, and l is the length of the specimen. The strain rate in the specimen will change over the test as it is compressed, but this quick calculation is a good estimate for velocity selection. The velocities chosen for these experiments were 5, 7 and 9 m/s. Pulse shaping was conducted by placing BlueTac on the first end of the incident bar, this removed the oscillations from the incident pulse. More BlueTac was added until the high frequency oscillations were removed; this was 0.015 g of BlueTac. Figure 4.5 shows a strain gauge signal without pulse shaping and Figure 4.6 shows a signal that was pulse shaped.

Test number	Barrel length (mm)	Pressure (psi)	Velocity (m/s)
1	200	15	9.139
2	200	15	9.139
3	200	15	9.139
4	100	20	5.173
5	100	20	5.317
6	100	20	5.004
7	200	12	7.518
8	200	12	7.518
9	200	12	7.445

Table 4.1: List of SHPB calibration experiments.

Test number	Barrel length (mm)	Pressure (psi)	Velocity (m/s)
10	100	20	5.224
11	100	20	5.004
12	100	20	5.138
13	200	12	7.230
14	200	12	7.518
15	200	12	6.723
16	200	15	9.363
17	200	15	9.030
18	200	15	9.479

Table 4.2: List of SHPB experiments with gelatine specimens.

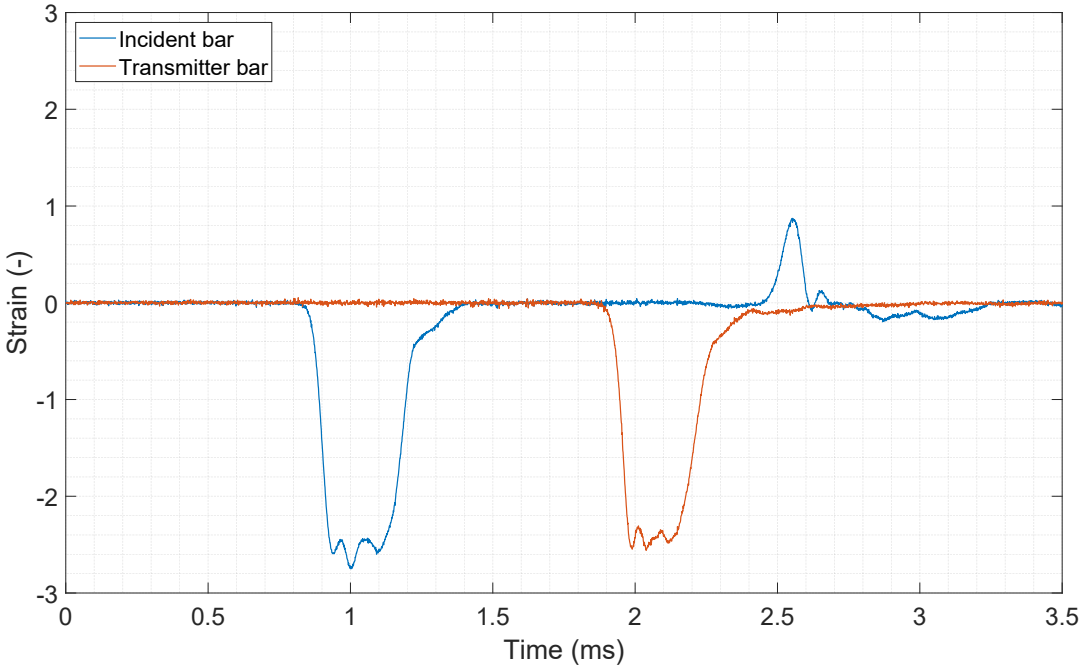

Figure 4.5: Strain gauge signal without pulse shaping; time from striker impact.

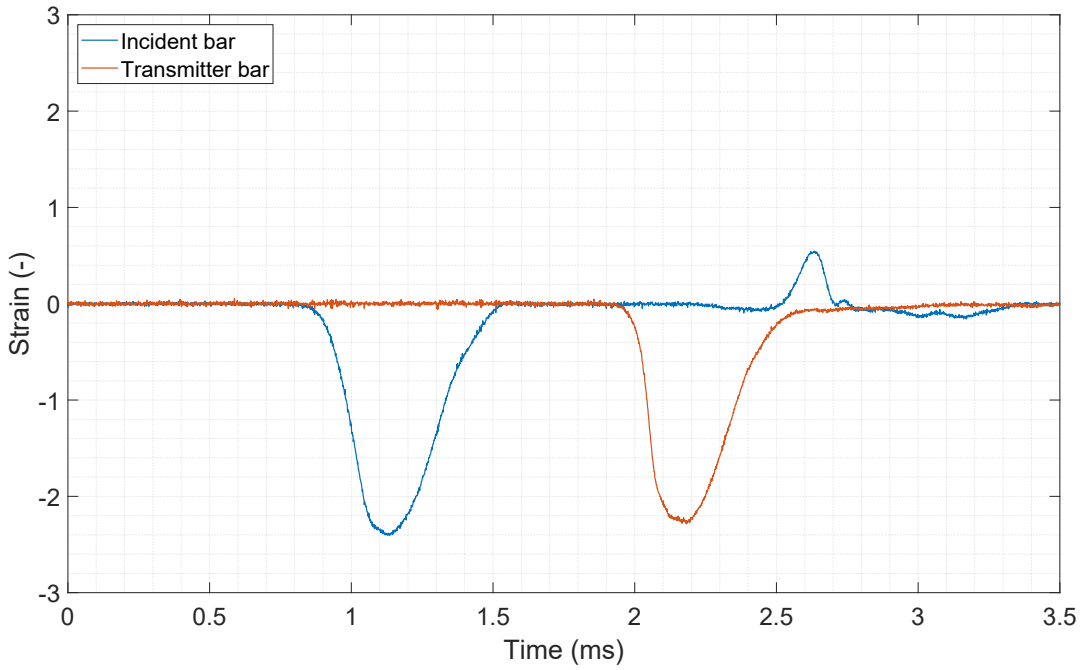

Figure 4.6: Strain gauge signal with pulse shaping; time from striker impact.

The data collected from the strain gauges is shifted in time to find the response of the specimen. This is done by using the wave speed of the bars calculated earlier. Signal shifting was trialled using Bacon's method (Bacon, 1998) to account for the visco-elasticity of the bars; however, this was unsuccessful. The incident signal is shifted 1.2 m down the bar to find the front stress, and the transmitted signal is shifted back 300 mm to find the back stress. The average between these is known as the mid-stress, which is the stress the specimen experiences in the experiment. This is plotted against the specimen strain to observe the stress-strain behaviour of gelatine at different strain rates. The strain rate for each test was plotted in Figures 4.7 - 4.9. The strain-rate classification of a particular SHPB experiment is determined differently throughout the literature, and the method of classification is often not reported. For the experiments conducted in this PhD, the strain rate was taken at a specimen strain of 0.3. This point was chosen as it was after any initial pulse oscillations had dissipated. These gave strain rates of 2200, 3000 and 4200 s^{-1}, respectively.

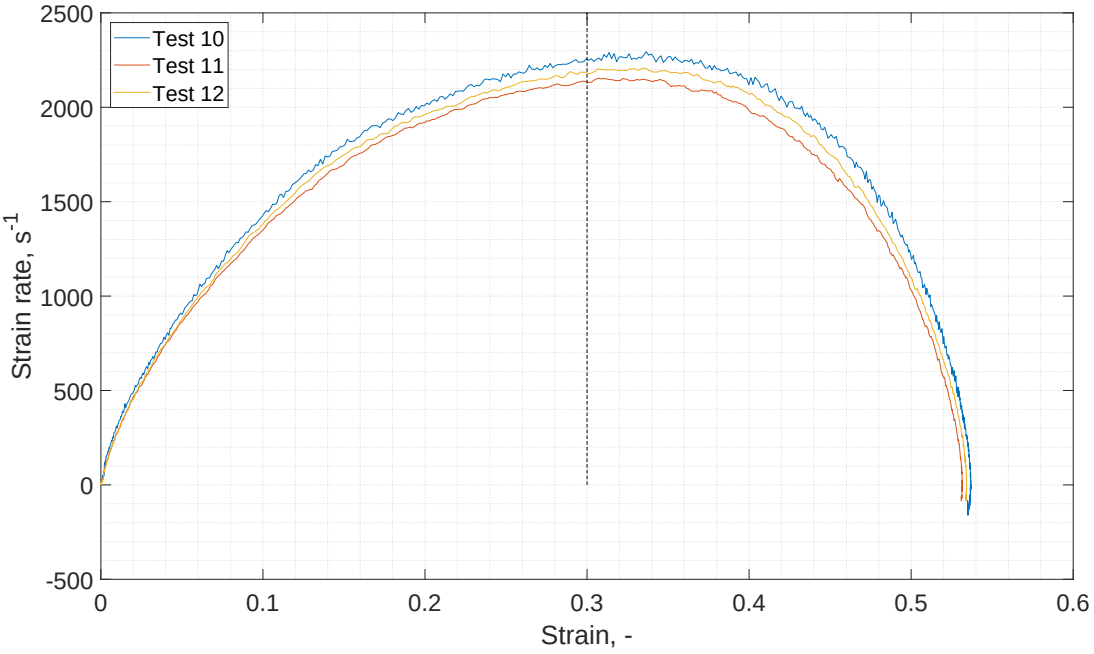

Figure 4.7: Strain rate against specimen strain for a striker velocity of 5 m/s.

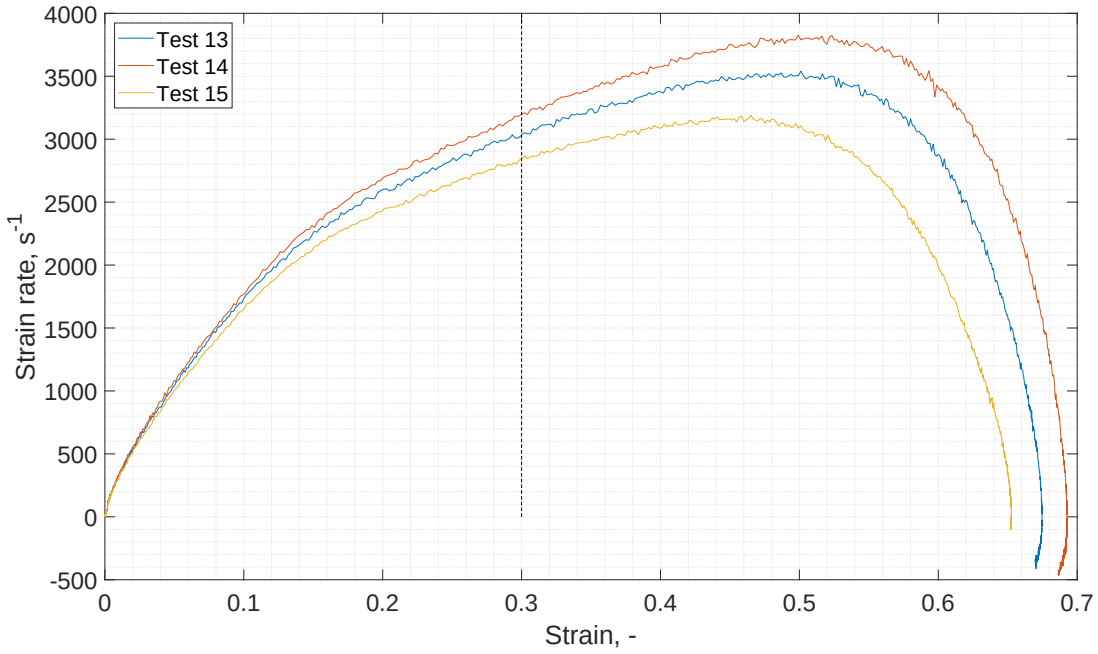

Figure 4.8: Strain rate against specimen strain for a striker velocity of 7 m/s.

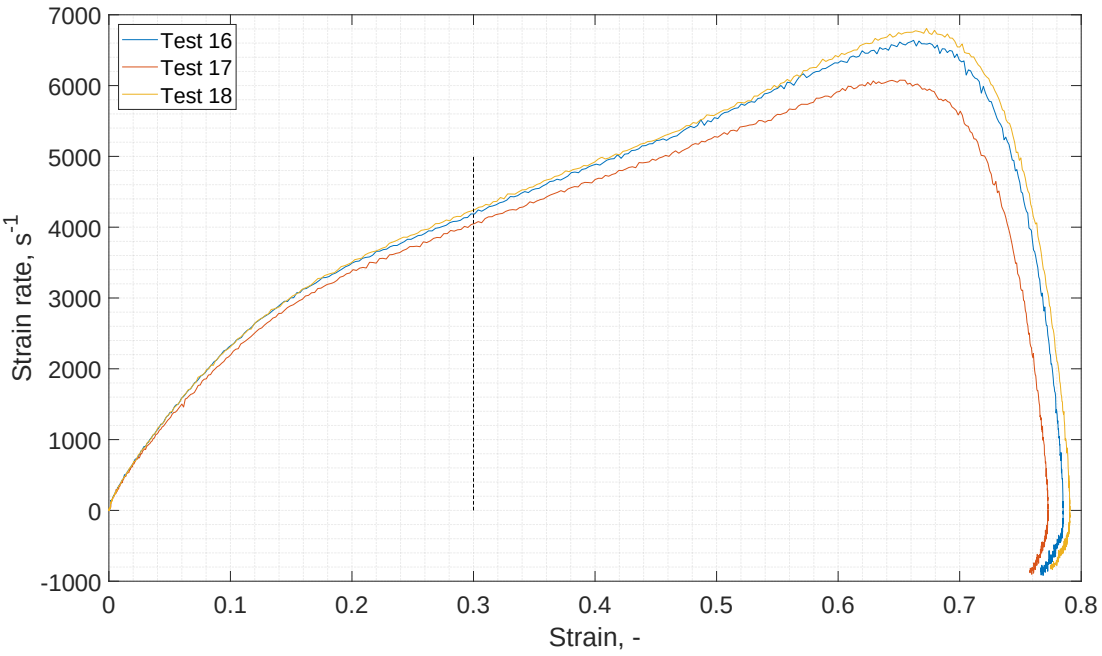

Figure 4.9: Strain rate against specimen strain for a striker velocity of 9 m/s.

Figures 4.10 – 4.12 include the front and back stress for each SHPB test conducted, allowing stress equilibrium to be discussed. Stress equilibrium in the specimen is reached when the front and back stresses are equal. Figure 4.10 displays the data from a striker velocity of 5 m/s and shows that stress equilibrium was reached for Test 10 by 0.7 ms, but Test 11 and 12 only reached equilibrium at the end of the compression. Conducting SHPB tests at this strain rate proved difficult, as increasing the pulse length may have helped reach equilibrium, but that would require a longer striker bar. This longer striker bar would not be able to travel at such low velocities because of the increased weight. Figures 4.11 and 4.12 illustrate that the rest of the experiments did reach equilibrium.

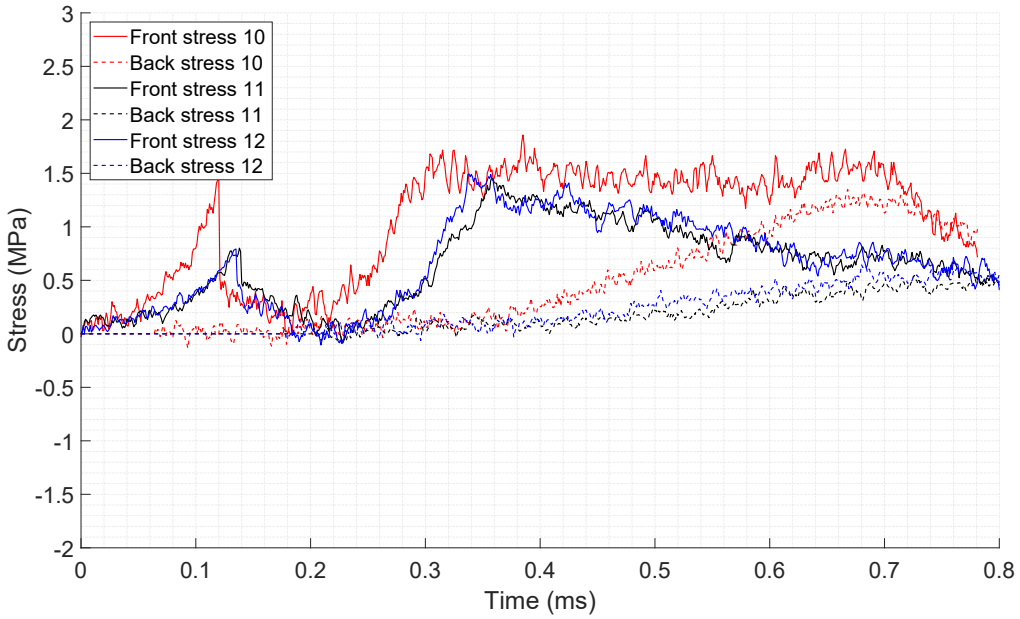

Figure 4.10: Front and back stress for a striker velocity of 5 m/s; time from specimen impact.

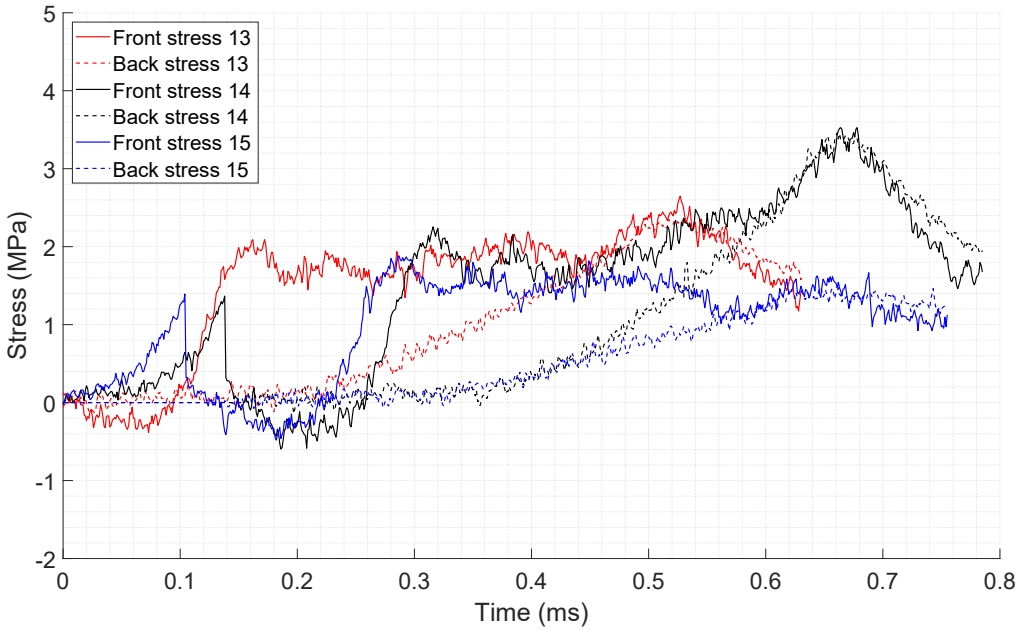

Figure 4.11: Front and back stress for a striker velocity of 7 m/s; time from specimen impact.

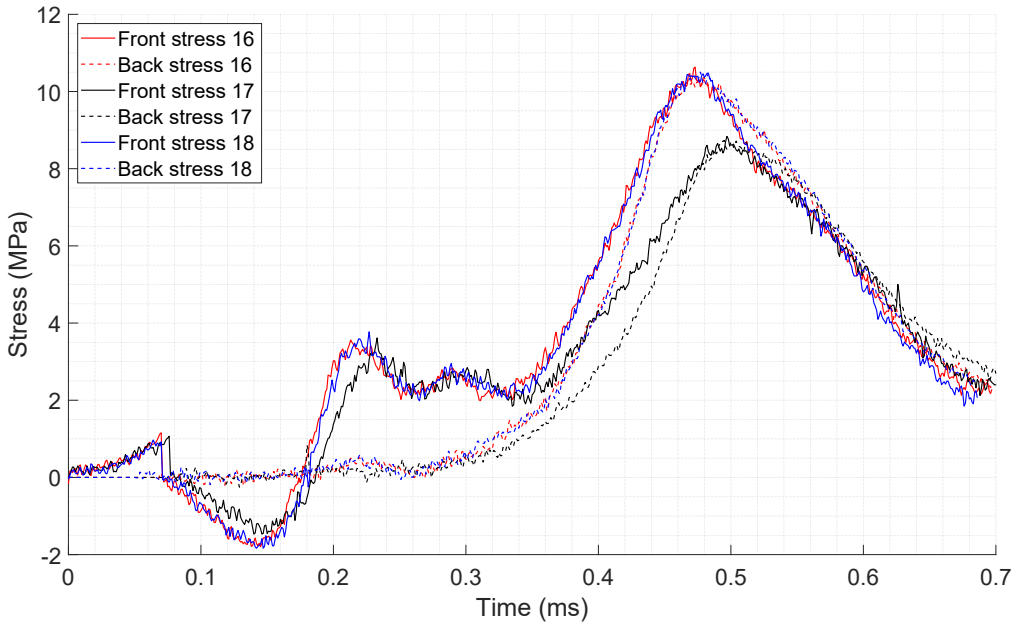

Figure 4.12: Front and back stress for a striker velocity of 9 m/s; time from specimen impact.

The mid stress is plotted against the specimen strain for each of the experiments in Figure 4.13 - 4.15, and three repeats were conducted at each striker velocity. The tests showed fairly good repeatability, and a similar response was observed for each strain rate. The oscillation at the start of the response between 0 and 0.2 strain is thought to be caused by the lubricant being compressed out from the gelatine-bar interface during the initial compression. Or, possibly due to the samples not being completely flat, as the oscillation evens out at similar strains for all the tests. After this, an exponential relationship is seen. Figure 4.13 shows less repeatability than the higher strain rates due to two tests not reaching equilibrium. Figure 4.16 compares the response for each of the striker velocities. The final stress increases as the strain rate of the experiment increases. Also, the final strain reached increases with increasing velocity, corresponding to higher velocities causing a higher amount of compression of the gelatine, as would be expected.

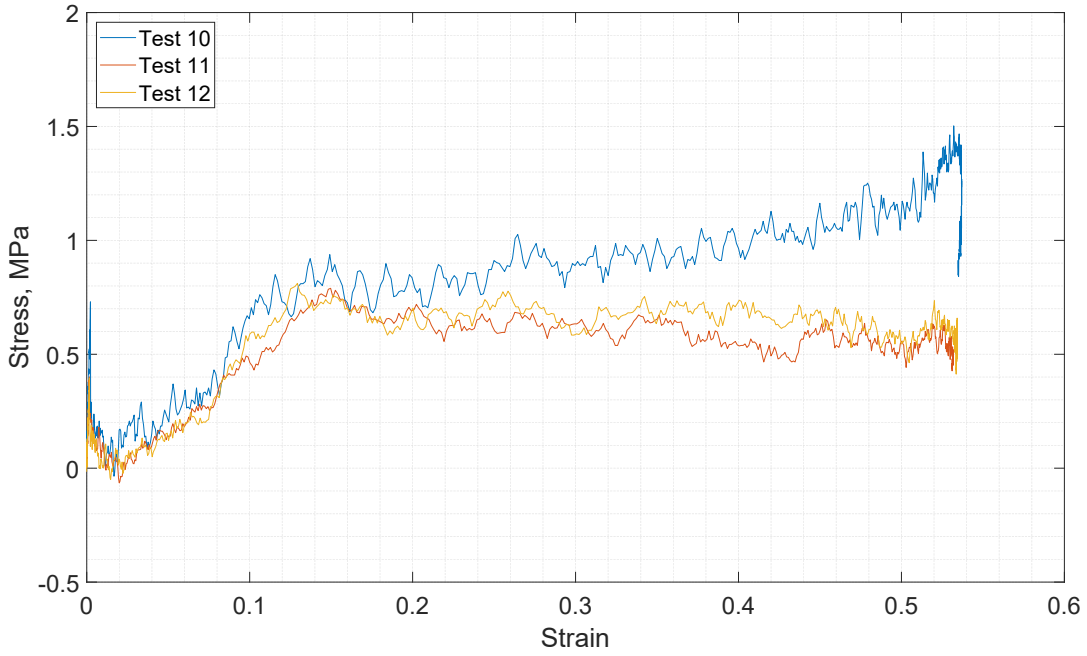

Figure 4.13: Stress - strain behaviour for a striker velocity of 5 m/s.

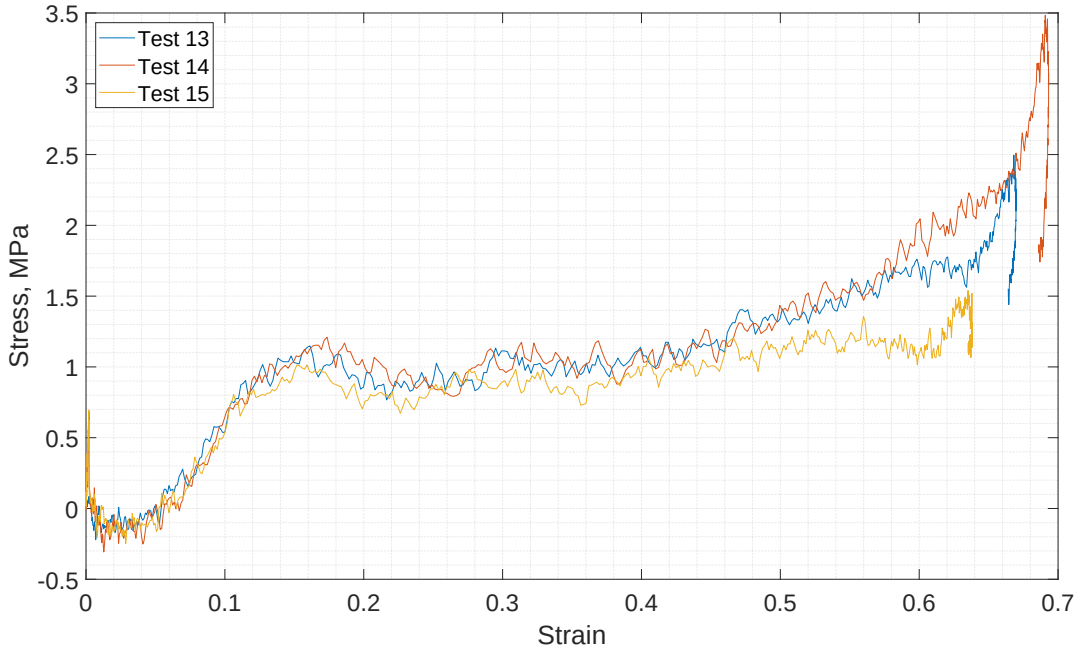

Figure 4.14: Stress - strain behaviour for a striker velocity of 7 m/s.

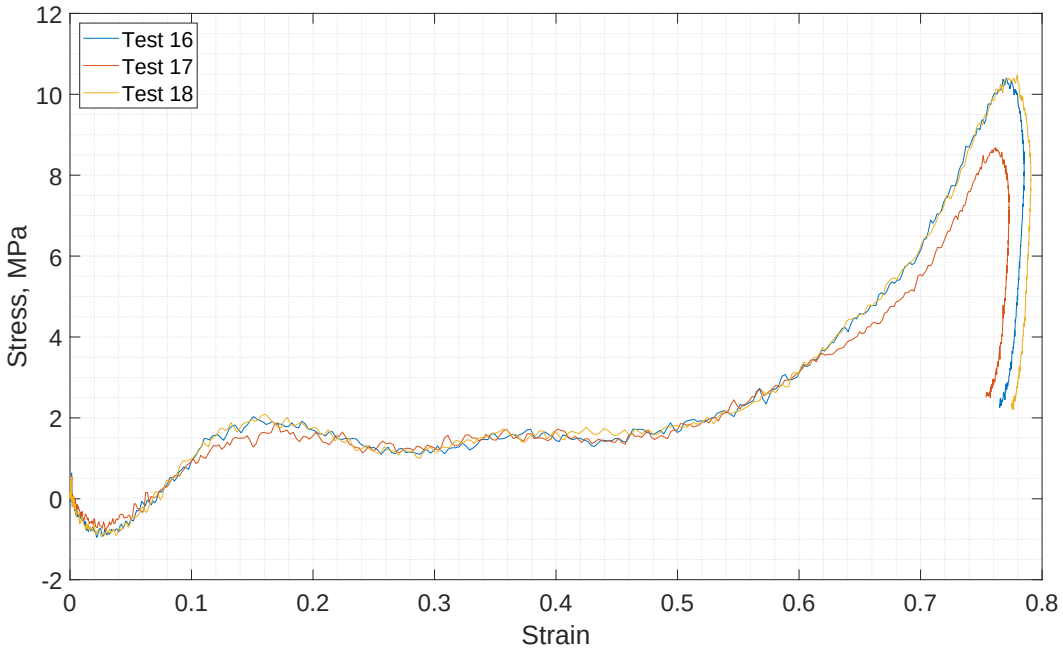

Figure 4.15: Stress - strain behaviour for a striker velocity of 9 m/s.

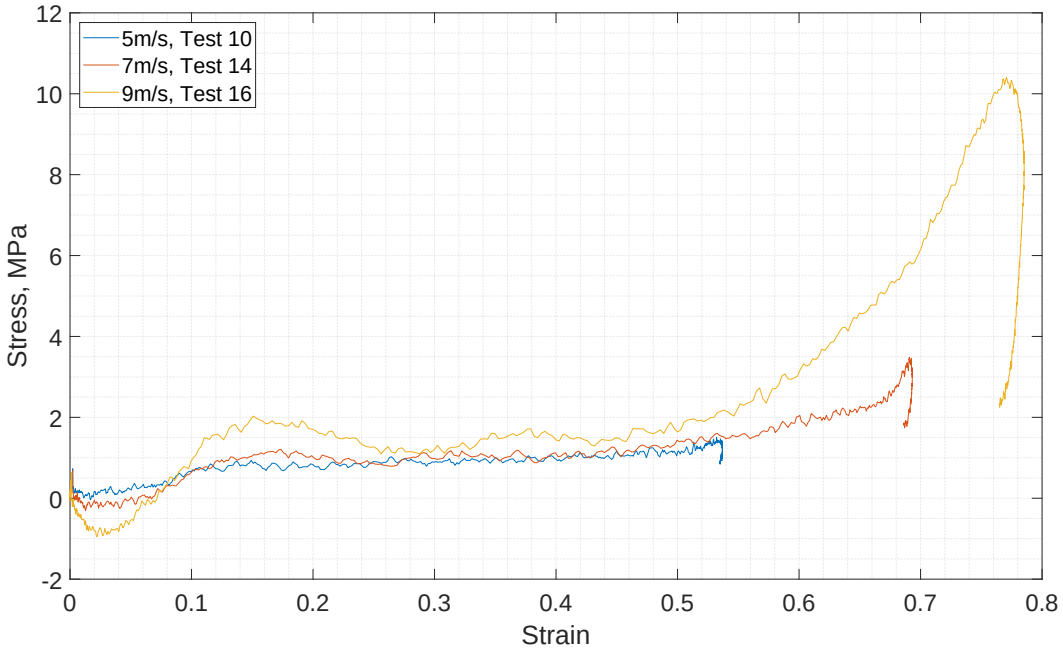

Figure 4.16: Stress - strain behaviour for all strain rates tested.

4.2 Numerical Analysis

4.2.1 Numerical Model Set-up

A 2D axisymmetric numerical model was produced in LS Dyna to simulate the SHPB experiments. Each part of the experimental set-up was modelled as separate Lagrangian meshes with a mesh size of 2.5 mm. The gas gun was simulated by applying a velocity curve to the striker bar nodes. To account for the pulse shaping conducted in the experiment, the velocity curve was defined as a parabolic curve, gradually loading and unloading the striker bar. This meant that the stress in the incident bar perfectly matched the data processed from the strain gauge on the incident bar, Figure 4.17. The bars were modelled with the Elastic material model to reduce model complexity. The compressive strength of polycarbonate is 80 MPa, which is much higher than the stresses seen in these experiments. As a result, visco-elastic effects are thought to be low. The gelatine was modelled with a smaller 0.6 mm mesh size to reduce mesh distortion when the gelatine experiences the large deformations expected. The Simplified-Rubber/Foam material model was again used to model the gelatine's behaviour. The same material properties determined in Chapter 3 were selected for gelatine in this model, but the stress-strain data from the SHPB experiment was used to calculate the load curve. The load curve is shown in Figure 4.18; the data at the very start of the curve was altered, so it started at 0,0 and gradually joined the data. This reduces sudden jumps in the load curve, which is difficult for the model to interpret.

	Bulk modulus (MPa)	Poisson's ratio
Input values	0.793	0.495

Table 4.3: Material properties for synthetic gelatine.

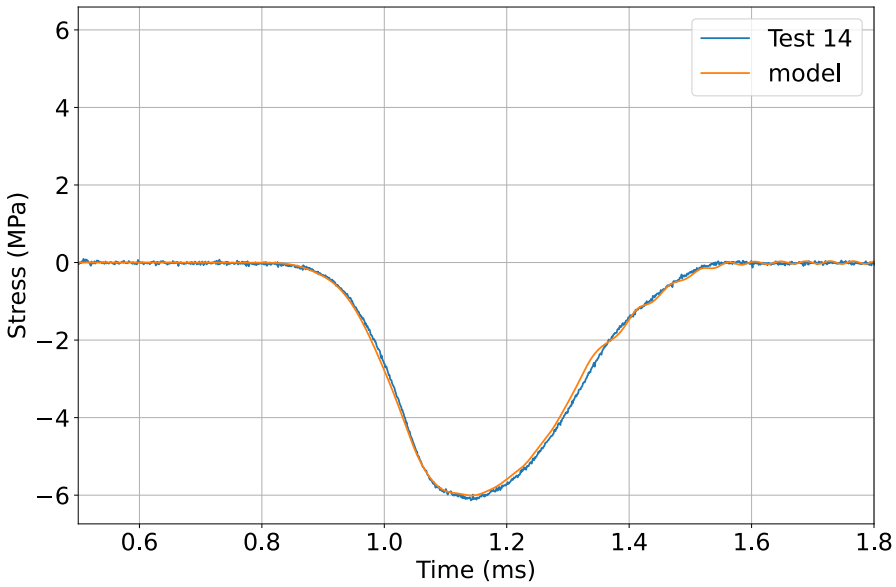

Figure 4.17: Stress in the incident pressure bar and the first gauge location for striker velocity of 7 m/s; time from striker impact.

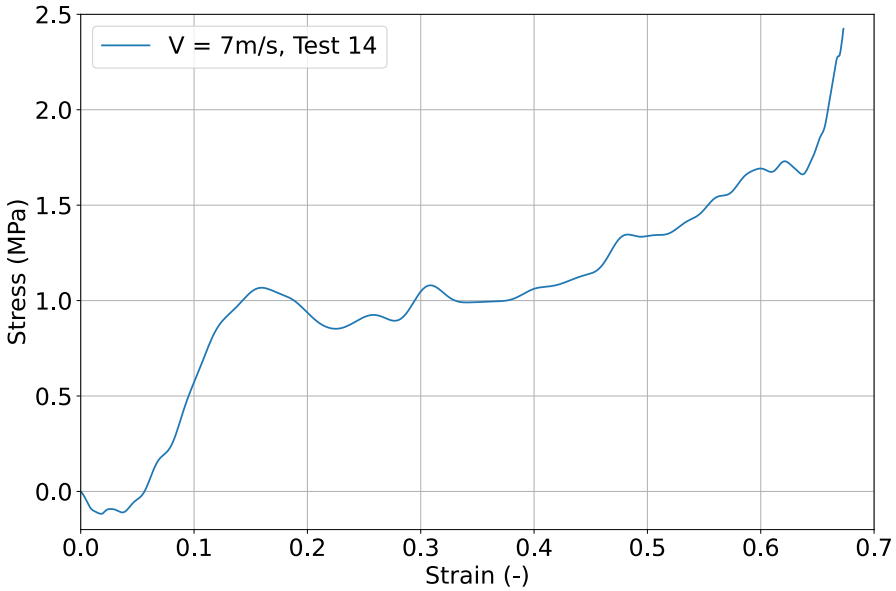

Figure 4.18: Stress-strain load curve for numerical model.

4.2.2 Results and Discussion

The front and back stress is the stress at the bar-specimen interfaces; in the experiment, this is found by shifting the gauge signals. In the model, this was directly extracted from the elements. The front and back stress are plotted together for the numerical model in Figure 4.19 and show that stress equilibrium was reached in the model at approximately 0.45 ms. Figures 4.20 and 4.21 compare the front and back stress to Test 14, and good agreement is seen between the experimental data and the model, with both curves following a similar shape. This illustrates that stress wave propagation is simulated well by the numerical model.

Figure 4.22 plots the stress in the middle of the gelatine (mid-stress). In the experiment, this is found by taking an average of the front and back stress, whereas this can be directly extracted in the numerical model. A good correlation in the mid-stress is seen in Figure 4.22, implying that the stress propagation in the gelatine is simulated well by the material model used. The engineering stress-strain data is plotted together for the experiment and the numerical model, shown in Figure 4.23. The curves show similar behaviour; the difference in shape may be due to how the gelatine mesh was compressed in the model, affecting the strain of the specimen. This modelling shows that the material properties of gelatine (bulk modulus and Poisson's ratio) can be determined in quasi-static conditions, and the rate effects can be simulated by defining a series of stress-strain load curves. This supports the use of this material model to investigate the influence gelatine has on the loading from an explosion.

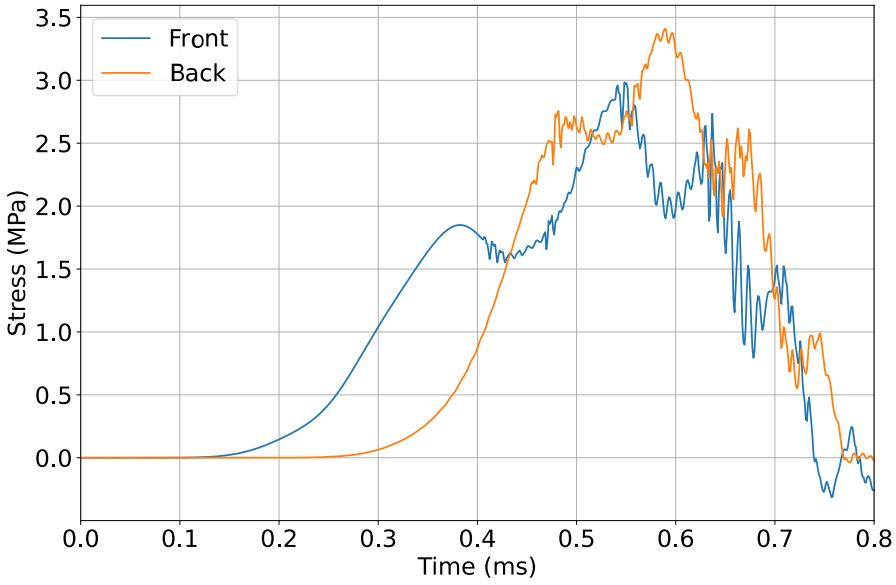

Figure 4.19: Front and back stress for the numerical model; time from specimen impact.

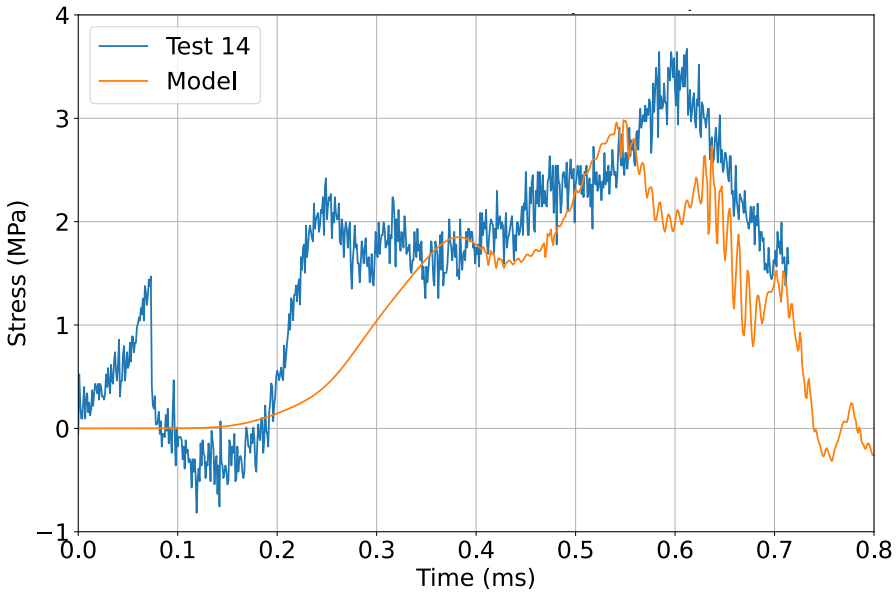

Figure 4.20: Front stress in the experiment and numerical model; time from specimen impact.

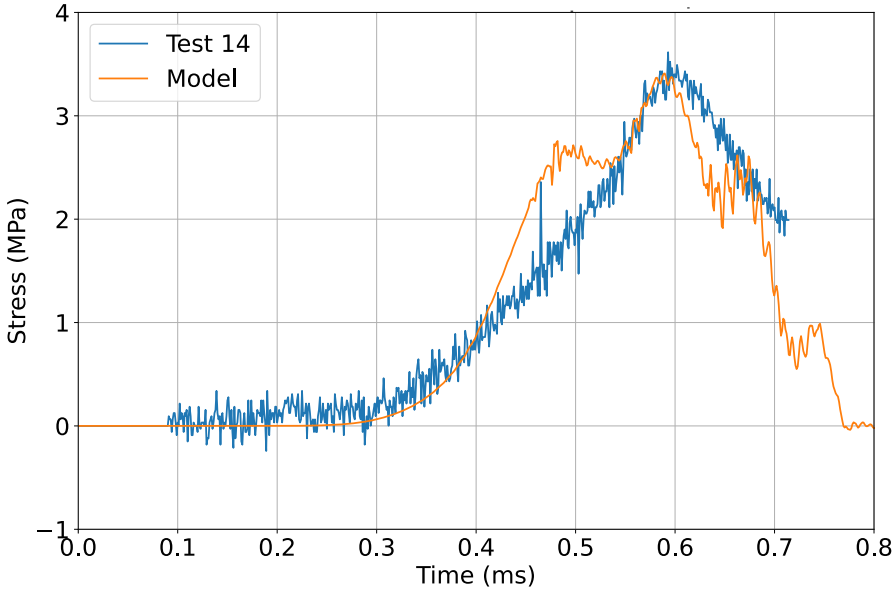

Figure 4.21: Back stress in the experiment and numerical model; time from specimen impact.

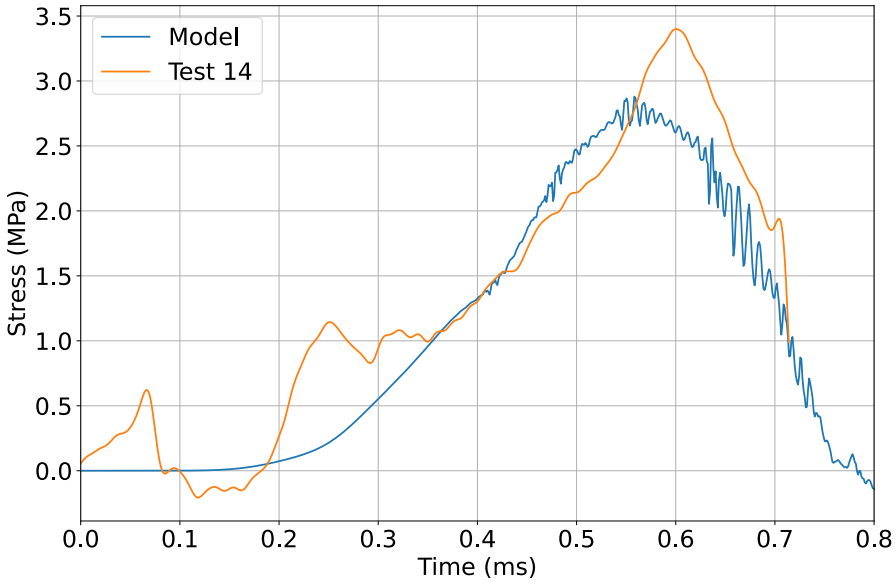

Figure 4.22: Mid-stress in the experiment and numerical model; time from specimen impact.

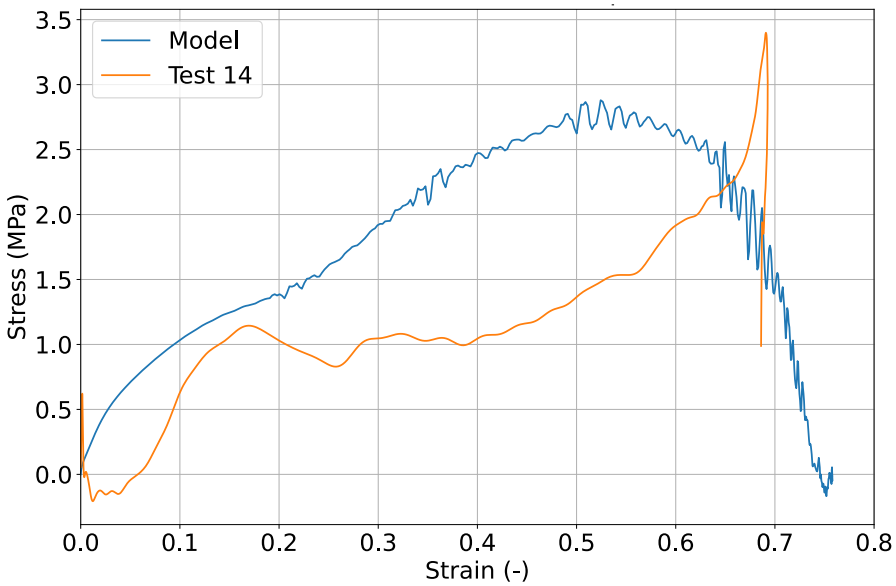

Figure 4.23: Stress vs strain in the experiment and numerical model.

4.3 Summary of Findings

This chapter investigated the behaviour of synthetic gelatine at dynamic strain rates using SHPB experiments. Polycarbonate pressure bars were utilised to reduce the impedance mismatch between the pressure bars and gelatine. The experiments proved challenging at low velocities, with stress equilibrium not always being reached. The experiments found that the final stress increased as the strain rate of the experiment increased. Also, the final strain increased with increasing impact velocity, causing a higher amount of compression of the gelatine, as would be expected. These experiments were modelled in LS Dyna to assess the suitability of the material model used for gelatine in Chapter 3 for higher strain rates. The numerical model was found to correlate well with the experimental data. This modelling shows that the material properties of gelatine (bulk modulus and Poisson's ratio) can be determined in quasi-static conditions, and the rate effects can be simulated by defining a series of stress-strain load curves.

Chapter 5

Behaviour of Synthetic Gelatine in an Explosion

5.1 Design of the Experiment

5.1.1 Experimental Layout

One of the objectives of this thesis is to obtain insight into the response and blast transmission of synthetic gelatine when undergoing air-blast loading. This chapter reports the methods and results from air-blast experiments with hybrid aluminium alloy/synthetic gelatine panels. A literature review of past work in this area (see Chapter 2 for further details) highlighted significant problems encountered in previous experimental investigations, namely high levels of noise obscuring true data signals, issues mounting pressure sensors and challenges of preventing air bubble pockets from affecting the measurements. A new approach was developed for this thesis.

An existing testing arrangement at the University of Sheffield, called Appliqué, was modified to implement this investigation (Fuller, 2018). Appliqué is a reinforced and re-instrumented version of the HITSss rig (Clarke et al., 2015). The transient deformation of the target plates was recorded using crush blocks, and photogrammetry was used to measure residual deformation. The HITSss rig was originally designed to measure impulse from a buried explosion using a free-flying reaction. Figure 5.1 shows a side-on view of the modified Appliqué testing arrangement, which allows for a clamped target plate to be mounted above an explosive charge. The modifications to the rig included adding a steel beam to allow high-speed cameras to be mounted above the clamped plate. Also, a new clamping frame was manufactured to clamp the smaller target plates; details of the clamping frame are in Section 5.1.4

5.1.2 Threat

After conflicts have finished, small anti-personnel landmines and explosive remnants of war (ERW) are often left behind, which can cause injuries to civilians. Previous research has looked closely at the resulting primary injuries to the lower leg of civilians from explosions (Cronin et al., 2011) (Karahan et al., 2018) (Elgy et al., 2020) (Singh and Basri, 2022). However, limited research has looked at the effect the blast wave has on the upper leg as it transmits through the tissue. To focus on the effect the blast wave has on the synthetic gelatine, the target plate was placed at 0.650m away from the charge. This distance allowed the loading from the blast wave to be investigated away from the fireball and target the upper leg area of the human body.

There are a large number of different anti-personnel landmines that are used in conflicts. For this research, the charge size was based on small anti-personnel landmines to focus on the blast wave effect rather than primary injuries. These types of landmines cause primary injuries

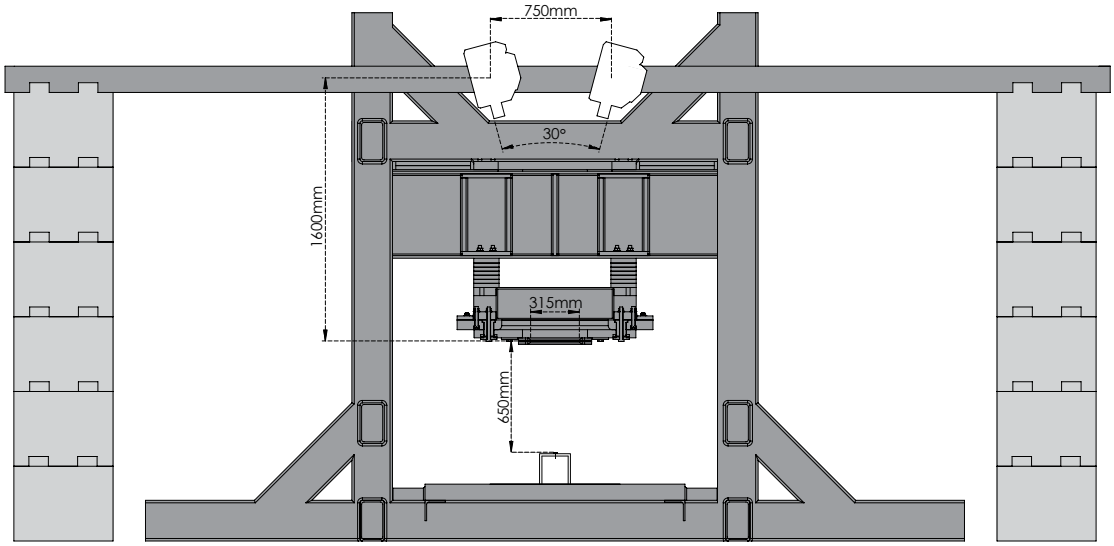

Figure 5.1: Engineering drawing of the Appliqué testing arrangement.

to the foot area only. A typical small anti-personnel landmine is an M-14 mine, which is 28.3 g Tetryl (1.07 TNT equivalent (Dobratz and Crawford, 1985)), this was converted to PE4 using Equation 5.1,

$$\begin{aligned}(Mass_{Tetryl} \times TNTeq_{(Tetryl)}) \div TNTeq_{(PE4)} &= Mass_{PE4} \\ (28.3 \times 1.07) \div 1.2 &= 25.2\ g.\end{aligned} \tag{5.1}$$

This roughly equals 25 g of PE4 explosive, the threat context chosen for this project. The 25 g charge was shaped into a 3:1 cylinder with a diameter of 39 mm and a height of 13 mm. A cylinder was chosen so a direct comparison could be made to future buried charge experiments. All charges were detonated from the bottom in this test series, as previous testing has shown this to reduce noise in the results (Clarke et al., 2014). Scaled distance is often used to classify whether a blast experiment is near or far field. The scaled distance Z is given by Equation 5.2,

$$Z = \frac{R}{\sqrt[3]{W}} \tag{5.2}$$

where R is the distance from the centre of the explosive, and W is the charge mass expressed as an equivalent mass of TNT. Scaled distances of less than 1 m/kg$^{1/3}$ are considered near-field; this experimental set-up has a scaled distance of 2.09 m/kg$^{1/3}$, so it is considered a far-field experiment. The charge size and layout can be seen in Figure 5.2.

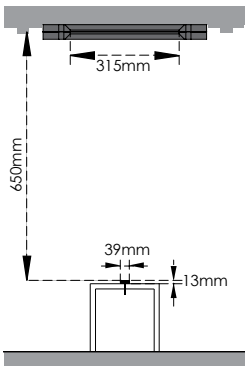

Figure 5.2: Charge dimensions and stand-off distance to the clamping frame.

5.1.3 Measurement Technique

The novel experimental method proposed in this project utilised the digital image correlation (DIC) measurement technique. The DIC set-up consisted of two high-speed Photron SA-Z cameras mounted above the target plate on a steel beam supported on concrete blocks (Figure 5.1), which made them independent of the main testing frame. Figure 5.3 shows a photograph of the cameras mounted to the testing frame. Mounting the cameras independently from the main testing frame reduced their movement during testing. The cameras were 1600 mm above the back of the target plate, at a stereo-angle of 30° (15° to the vertical). The choice of stereo-angle was based on Reu (2013), who advises an optimum angle of between 15 - 35 degrees, with wider angles improving the accuracy of out-of-plane results. By placing the cameras 1600 mm above the target plate, a camera view of the entire width of the plate was achieved, with an image size of 640 x 280 px. Lighting was used to illuminate the back of the target plate, and a frame rate of 100,000 fps was achieved. The dimensions of the camera positions and the viewing area can be seen in Figures 5.1 and 5.3.

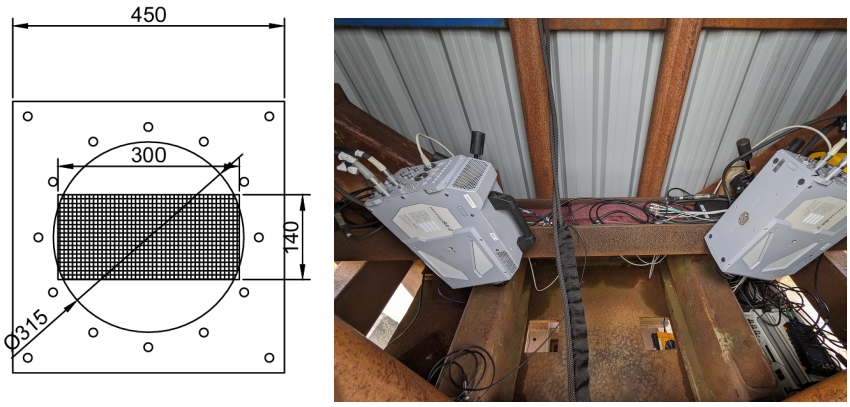

Figure 5.3: Dimensions in mm of the camera's view and photograph of the cameras mounted to the testing frame.

5.1.4 Design of Clamping Frame

An adaptor plate was used to allow the smaller clamping frame design used previously by Curry and Langdon (2017) to be fitted to Appliqué. This clamping frame size helps reduce the amount of gelatine needed. Some adaptations were required to the clamping frame's dimensions to accommodate the gelatine specimens. Firstly, the mould size chosen for the gelatine specimen was 12" or 305 mm in diameter, as this was easy to obtain. Secondly, a 5 mm clearance was needed between the edge of the gelatine specimen and the clamping frame. This clearance allowed for easier assembly of the clamping frame around the gelatine. As a result, the clamping frame was manufactured with a diameter of 315 mm. The full dimensions of the clamping frame can be seen in Figure 5.4.

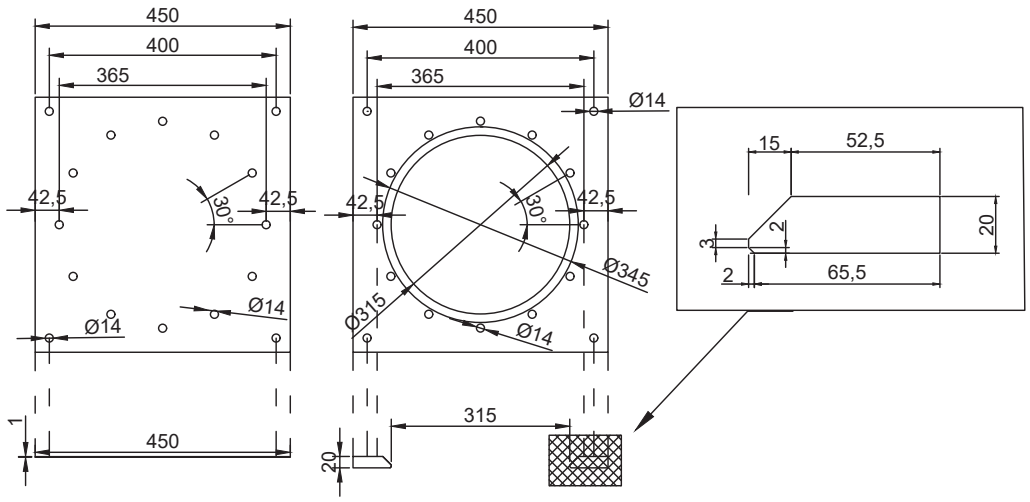

Figure 5.4: Dimensions in mm of the clamping frame (right) and the target plates (left).

5.2 Specimen Design and Manufacture

Specimen manufacture involved the preparation of the target plates and the gelatine specimens. As in the previous chapters, the gelatine specimens were made from 10% synthetic gelatine from Clear Ballistics. A mould with a 305 mm, 12" diameter and a removable bottom was used to create the test specimens. The specimens were produced following Clear Ballistics remoulding guidelines. Pieces of gelatine were removed from the block and carefully weighed to the correct mass. Then, the gelatine was heated in the mould to 125°C for 4 hours and left to cool overnight. Once the gelatine is cooled thoroughly, the specimen is removed from the mould and glued to the aluminium target plate with polyurethane resin (clear Gorilla glue). Three thicknesses of synthetic gelatine were produced for this testing: 10 mm, 30 mm and 50 mm. The thickness of the gelatine was varied to investigate the effect gelatine has on the loading transferred to the target plate. Images of the manufacturing process and finished specimen can be seen in Figures 5.5.

The 450 mm by 450 mm square target plates were laser cut from 1 mm thick 1050-H24-grade aluminium. The thickness and grade of aluminium were selected because of its low strength and high ductility, which allowed for a considerable amount of plate deflection at the large charge stand-off distance. The target plates were spray-painted white and then speckled using a DIC speckle roller from Correlated Solutions to facilitate DIC. The roller was passed over the plates three times at 0°, 90° and 45° to achieve the desired speckle density. The speckle size chosen for this testing had a diameter of 2.54 mm. This speckle size was selected following guidance from the DIC manual that a speckle should be between 10 – 15 pixels across (iDICs, 2018). These target plates were clamped into the steel clamping frame, leaving an exposed circular area. Images of the target plates can be seen in Figure 5.6.

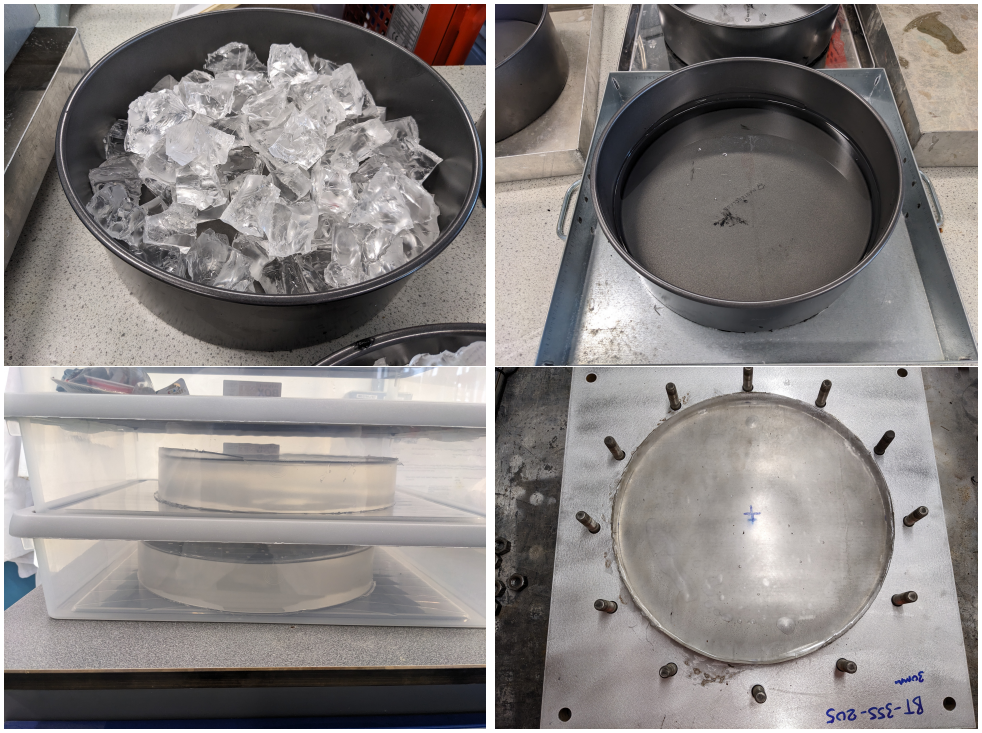

Figure 5.5: Manufacturing process for gelatine specimens; top is moulding process, bottom is final specimens and glueing to the plates.

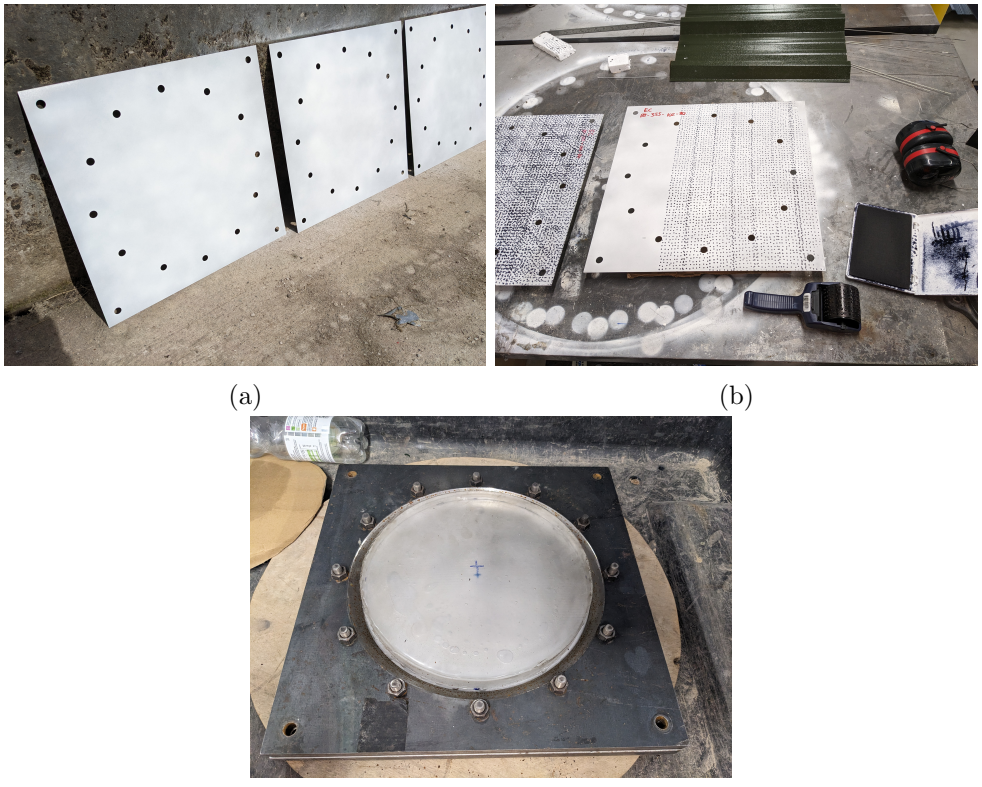

(a) (b)

(c)

Figure 5.6: Preparation of target plates; a) white spray paint, b) applying the speckle pattern and c) clamped plate with gelatine.

5.3 Experimental Results

5.3.1 Test Series

A total of 21 free-air blast tests were conducted at the University of Sheffield's blast and impact laboratory in Buxton. The tests were performed on aluminium alloy target plates with different thicknesses of synthetic gelatine on the front surface. Four test series were conducted: bare plates (without gelatine), and plates with gelatine of 10 mm, 30 mm and 50 mm thickness. The distance between the plate and the charge was constant for all tests (650 mm). A table detailing all the tests conducted in this test series is shown below (Table 5.1). For each test, 10,000 images were captured at a frame rate of 100,000 frames per second, which allowed us to record data across the plate every 0.01 millisecond. The cameras were triggered using a break-wire that was embedded in the charge. Before the cameras were mounted, a pop test was conducted to ensure the clamped target plate would not fail due to the loading from the charge and damage to the cameras.

The equipment had to be set up and packed away on each day of testing because the testing frame was outside and exposed to the elements. A dummy target plate with a crosshair on the centre was used to align the cameras and set the focus so the images were sharp. The dummy target plate was removed once the cameras were positioned and focused correctly. Next, the calibration board from Correlated Solutions was held where the target plate would be, and a series of images were captured on both cameras. The best results were achieved when the calibration board was positioned in multiple directions. This process was repeated each time the equipment was set up to ensure high-quality images of the testing were recorded.

A forklift was used to position the clamped plate in the Appliqué test frame, as it was unsafe for personnel to lift it in place. The charge was positioned on a polystyrene bridge to create a non-reflective surface condition. A laser level was used to position the charge in the centre of the clamped target plate. Great care was taken with the charge positioning to increase the repeatability of the experiment.

Test Type	No.	Explosive Type	Charge Mass (g)	Stand-off Distance (mm)	Gelatine Thickness (mm)	Test No.
Bare Plate	9	PE4	25	650	0	001, 002, 102, 104, 105, 203, 204, 206, 208
Gelatine 10	4	PE4	25	650	10	106, 108, 111, 114
Gelatine 30	4	PE4	25	650	30	109, 112, 205, 207
Gelatine 50	4	PE4	25	650	50	003, 107, 110, 113

Table 5.1: Test series for free air blast experiments.

After the experiments, the high-speed camera images were processed using the DIC software called VIC-3D by Correlated Solutions. Firstly, the calibration images and the images of the clamped target plate are loaded into the software. Next, the calibration images are analysed to correlate the cameras. After calibration, an area of interest is drawn around the target plate, so the software only focuses on surfaces with a speckle pattern, not places like the clamping frame. Next, the subset size for the digital image correction is selected to achieve a mean error of less

than 0.0099 (pixel error). Finally, the VIC-3D analysis is run to calculate the displacement and velocity data across the plate.

5.3.2 Bare Plates

After the high-speed camera images have been processed, the displacement and velocity data across the surface of the plates can be explored. This data can be extracted in the x, y and z directions because 3D DIC was used. Figures 5.7 - 5.8 display an example of the displacement for a bare target plate. Figure 5.7 shows the out-of-plane displacement profile across the plate as it rises to its peak displacement at four different time steps. The x and y axes are the target plate coordinates, and the z-axis depicted by the colour bar is the out-of-plane displacement, W. The plate is initially loaded uniformly and then starts moving upwards away from the charge from the edge first, which travels towards the centre over time. The plate rises to its peak displacement at the centre of the plate.

By taking a line slice across the middle of the plate (see Chapter 3), the out-of-plane displacement can be observed across the total time of the experiment. The line slices taken of the target plate at each time step are plotted together on the contour graph in Figure 5.8a. The y-axis is the x coordinates of the target plate, and the colours of the contours are used to depict the out-of-plane displacement, W. The figure focuses on the plate's movement in the first 2 ms after detonation. This figure shows how the shape of the plate develops over time. By selecting a series of time steps, Figure 5.8b is created. This figure shows a side-on view of the plate as it rises to its peak displacement. The x-axis is the x coordinates of the target plate, and the y-axis is the out-of-plane displacement of the plate. The figure again displays how the target plate is firstly loaded uniformly and then moves upwards from the edge. Between 1.00 ms and 1.10 ms, Figure 5.8b demonstrates how the centre of the plate seems to accelerate and 'pop' through to reach the peak transient displacement at 1.15 ms.

These previous graphs (Figures 5.7 and 5.8) have displayed an example of the data collected from the bare target plates, which is an effective way of observing the full plate's behaviour. So a comparison between repeat tests can be made; the out-of-plane displacement at the centre of the plate is plotted in Figure 5.9 for each bare target plate test. Figure 5.9 displays the sharp rise in displacement of the plates as the explosion impacts them. The graph also illustrates how the plate rises to a maximum transient displacement and then relaxes and oscillates until it rests at its permanent displacement. The test results appeared to be categorised into two behaviour groups. Tests within each group showed repeatability; 2% variability in the higher group and 5% in the lower group.

One theory of how these two distinct groups of data have formed is due to the shape of the target plate before the impact of the explosion. By observing the shape of the plate at the start of the test, it was found that if the target plate was concave, the displacement result fell in the lower group of data. Conversely, it was found that if the target plate was convex, the displacement results fell in the higher data group. The convex starting condition causing a higher displacement could be due to the centre of the plate "popping" through and accelerating the plate to a higher displacement, seen by a divergence in the gradient of the two data groups after 0.75 ms. The exception to this rule was Test 208, where the results lay in the middle, possibly due to improvements in clamping the plate flat. The thinness of the target plate could be causing the plate to be so sensitive to its clamping condition.

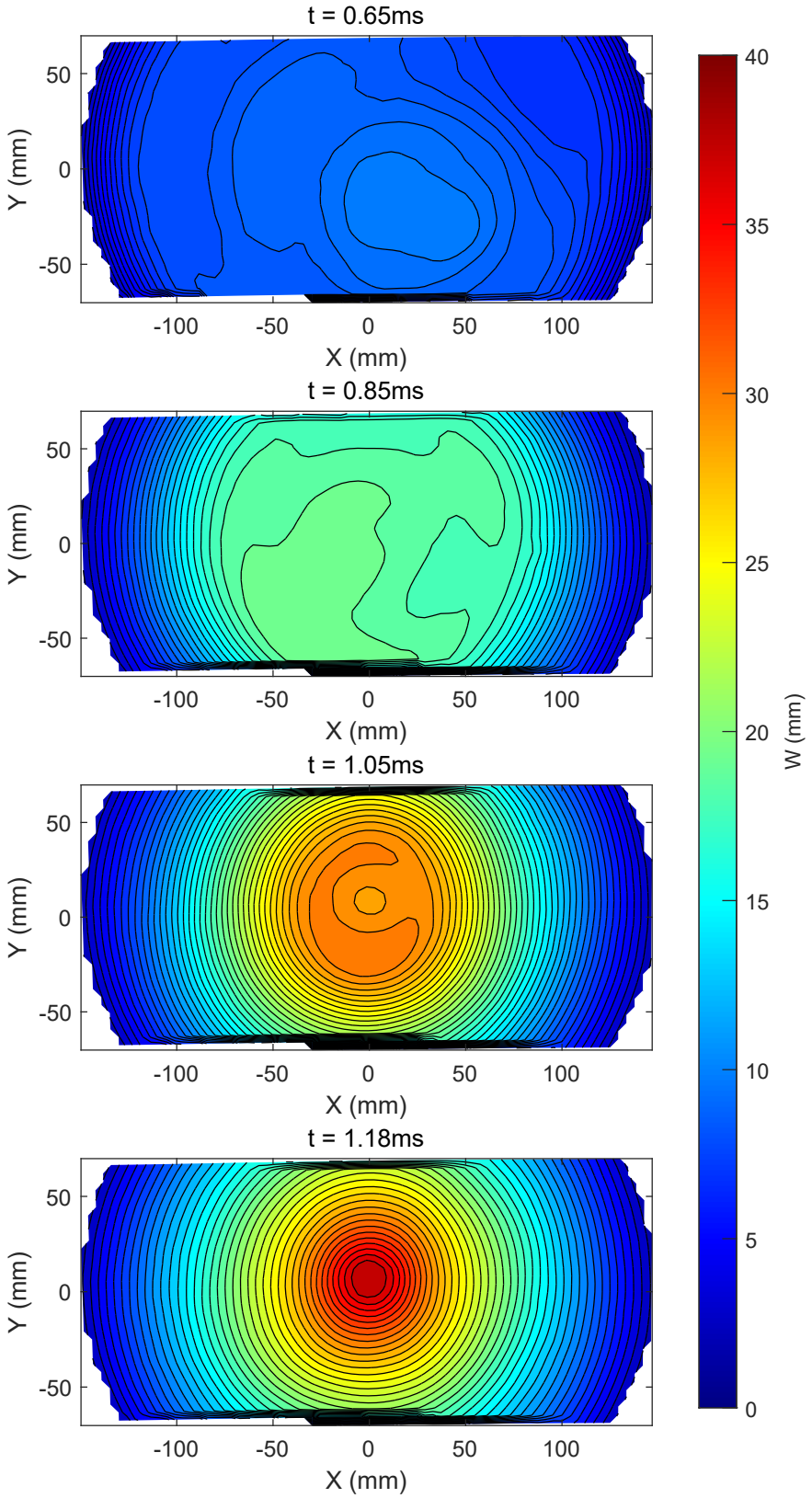

Figure 5.7: Full plate displacement over time of a bare plate.

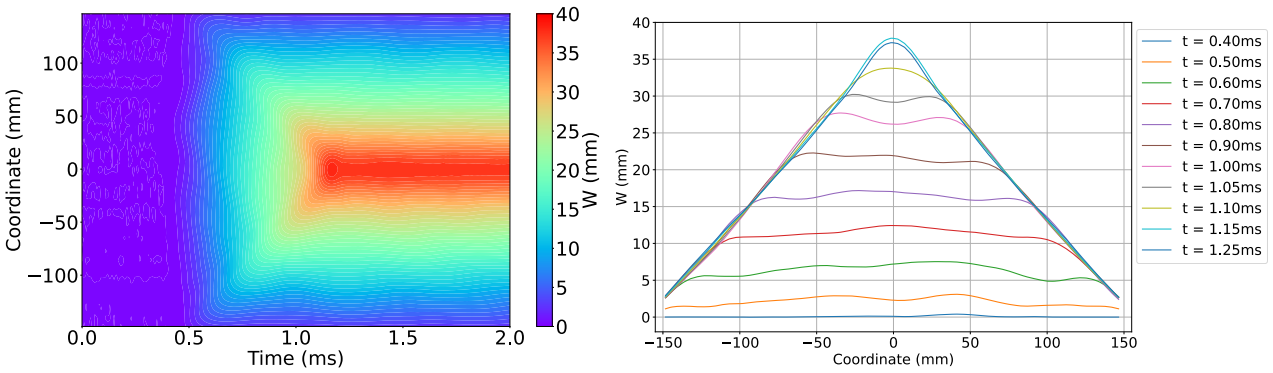

(a) (b)

Figure 5.8: Displacement over time across the width of the plate for a bare plate test.

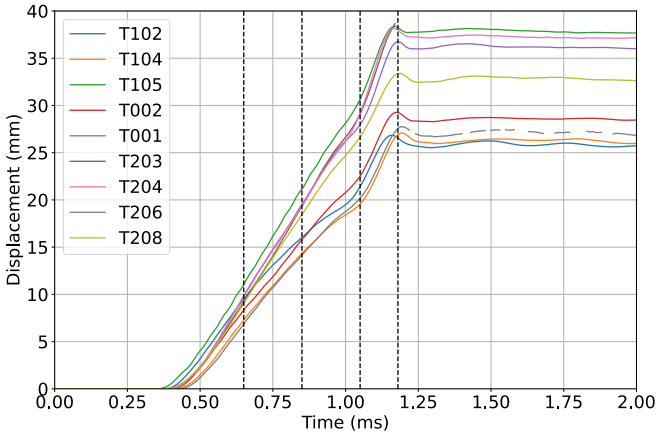

Figure 5.9: Midpoint displacement for the bare plates.

As stated previously, the velocity of the target plate can also be explored. The line slices taken of the target plate at each time step are plotted together on the contour graph in Figure 5.10a. The y-axis is the x coordinates of the target plate, and the colours of the contours are used to depict the velocity of the target plate, dW/dt. This figure helps to illustrate how the plate is initially loaded uniformly and then moves away from the charge from the edges of the plate first. This movement is seen in the velocity data as higher velocities at the edges of the plate. This higher velocity travels across the target plate, meeting at the centre of the plate, causing a peak velocity at the centre. The figure also shows how the target plate rebounds after the peak velocity, demonstrated by the negative velocity on the graph.

Figure 5.10a is an example of data from a bare target plate test; Figure 5.10b shows the velocity at the plate's centre for each test. The data depicts a sudden rise in velocity as the explosion initially loads the plate. This velocity then oscillates until the centre of the plate receives the velocity that was travelling in from the edges, seen in Figure 5.10a, resulting in a sharp increase in the velocity.

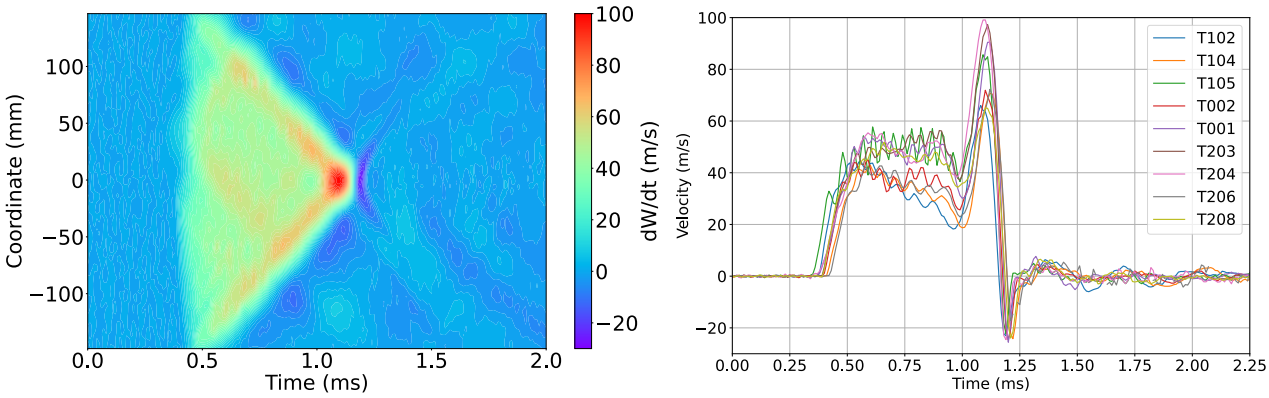

(a) (b)

Figure 5.10: a) Velocity over time across the width of the plate and b) midpoint velocity for the bare plates.

5.3.3 10 mm Gelatine Plates

Figures 5.11 - 5.13 display an example of the displacement for a target plate with a 10 mm thickness of synthetic gelatine glued to the front face. The contour graphs depicted in Figure 5.11 illustrate the out-of-plane displacement of the back surface. The images to the left show the plate moving away from the explosion to its peak at the centre (t = 1.95 ms). The plate moves similarly to the bare plates and travels up to a peak displacement at the centre of the plate. On the right, it shows how the target plate moves downwards towards the charge after reaching its transient peak displacement. The target plate elastically rebounds from the edges first, gradually inverting the plate. However, there isn't enough momentum to pull the centre through, leaving it in the opposite direction from the rest of the plate.

The target plate profile over time is shown in Figure 5.13, which uses line slices of the midline across the plate at the different times displayed in the legend. Figure 5.13a shows how the shape of the plate develops, rising to a peak transient displacement in the centre of the plate after 2 ms. Figure 5.13b shows how the plate displacement then decreases after the initial transient peak. The plate displacement decreases from the edges first, and the out-of-plane displacement reverses direction (moving towards the blast) due to elastic rebound. The final displacement of the plate centre is in the direction opposite to that expected. The contour plot in Figure 5.12 is created by potting all the line slice data together, which helps to describe the shape of the plate. This figure helps show the gradual downward movement of the plate after reaching its peak transient displacement.

To compare the test to test repeatability, the out-of-plane midpoint displacement is plotted in Figure 5.14 for each of the 10 mm gelatine tests. Figure 5.14a shows the displacement over the first 10 ms to focus on the maximum and minimum displacements. The results show high repeatability, apart from one test where the plate rebound was slightly lower. Figure 5.14b illustrates that the plate oscillations continue long after the initial elastic rebound. The oscillations of the plate are also quite similar from test to test. The noise in Test 114 is thought to be caused by water on the plate, which caused overexposure in the DIC data. While preparing for this test, there was an unexpectedly large downpour of rain, which splashed water onto the plate. Overexposed areas were seen in the data because the water was accelerated by the plate and illuminated by the lights.

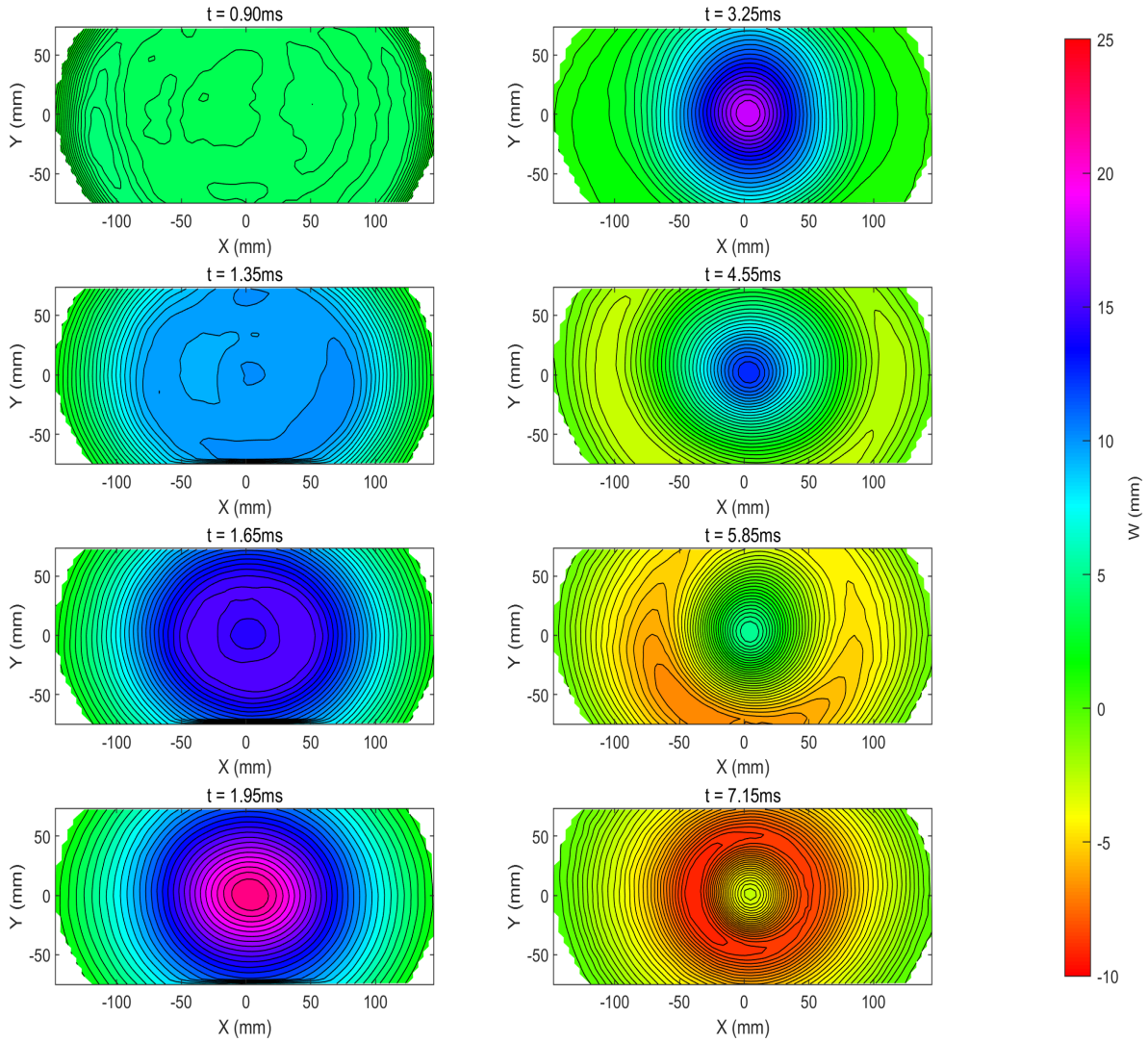

Figure 5.11: Full plate displacement over time of a plate with 10 mm of gelatine in front.

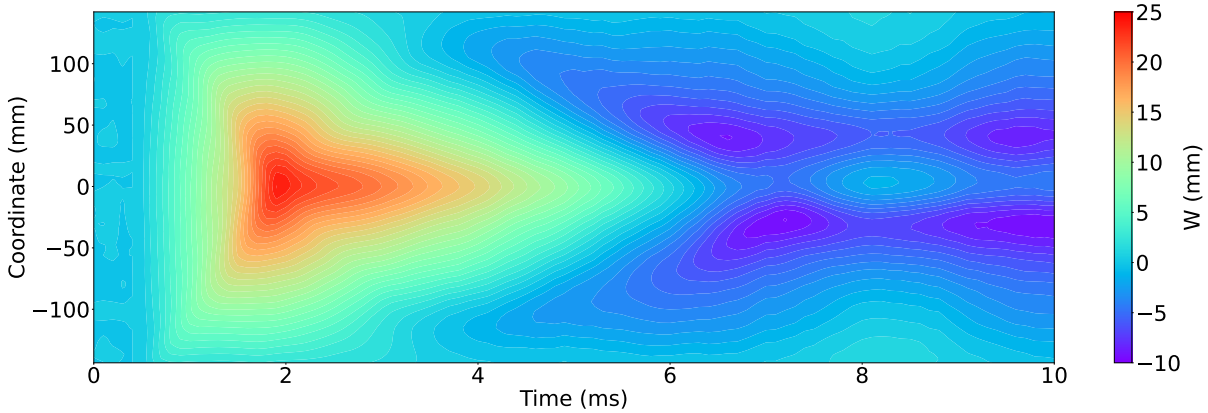

Figure 5.12: Displacement over time across the width of a plate with 10 mm of gelatine in front.

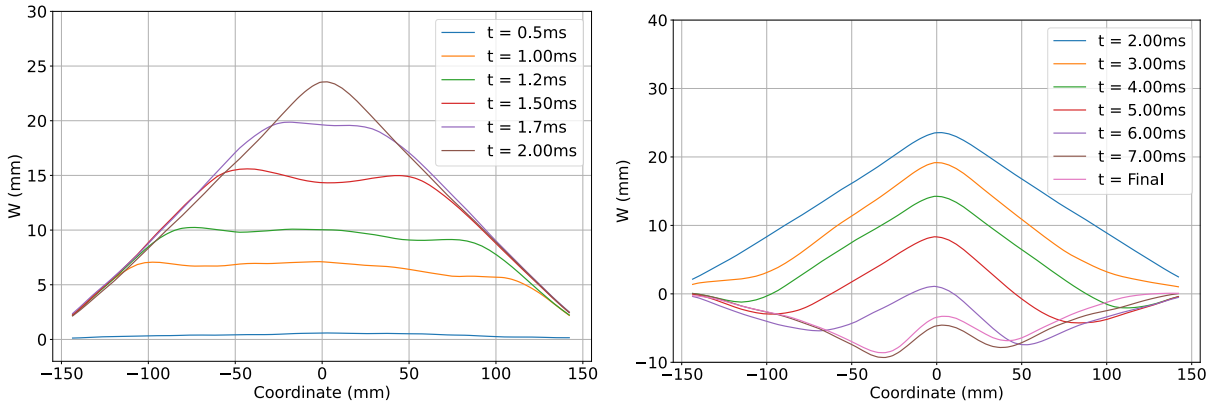

(a) (b)

Figure 5.13: Displacement profile of a plate with 10 mm of gelatine in front.

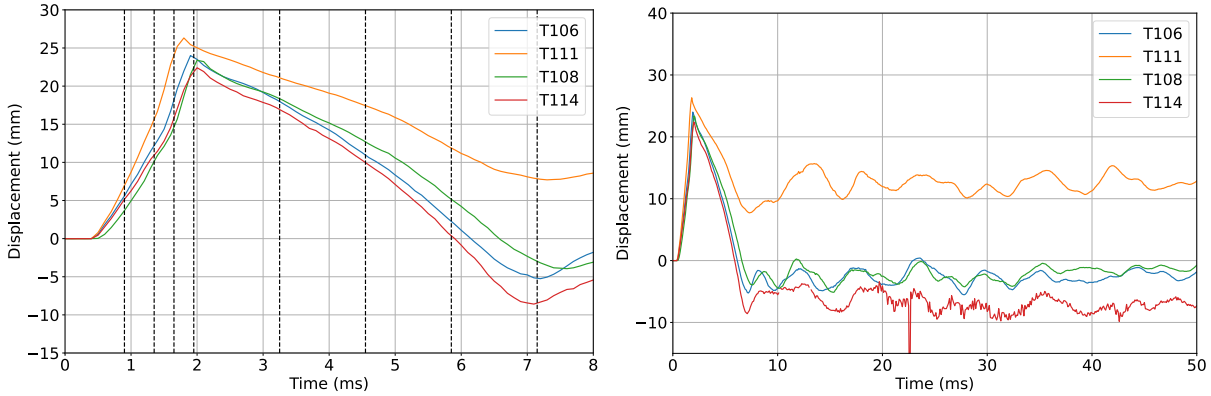

(a) (b)

Figure 5.14: Midpoint displacement for the plates with 10 mm of gelatine in front.

The line slices taken of the velocity of the target plate at each time step are plotted together on the contour graph in Figure 5.15. This figure helps to illustrate how the plate is initially loading uniformly across its width. Then, higher velocities are seen at the edges of the plate. This higher velocity travels across the target plate, which also seems to experience oscillations. The highest velocity is experienced in the middle of the target plate. The figure also shows how the target plate travels downwards from the edges first after the peak velocity, demonstrated by the negative velocity on the graph.

Figure 5.15 is an example of data from a test with 10 mm of gelatine in front of the target plate; Figure 5.16 shows the velocity at the centre of the plate for each of the tests conducted. The data depicts a sudden rise in velocity as the explosion initially loads the plate. This velocity then oscillates until the centre of the plate receives the velocity that was travelling in from the edges, seen in Figure 5.15, increasing the velocity. Shortly after this peak, a sudden decrease in velocity is seen.

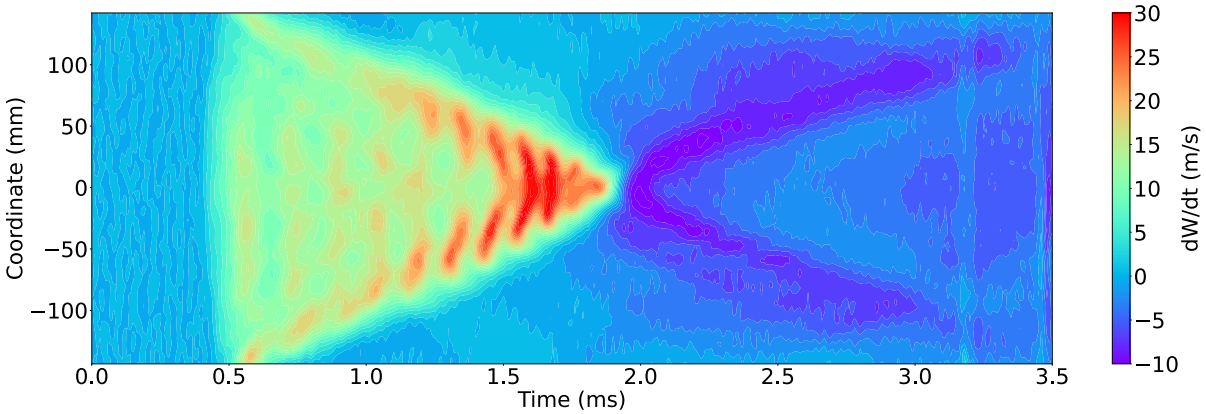

Figure 5.15: Velocity over time across the width of a plate with 10 mm of gelatine in front.

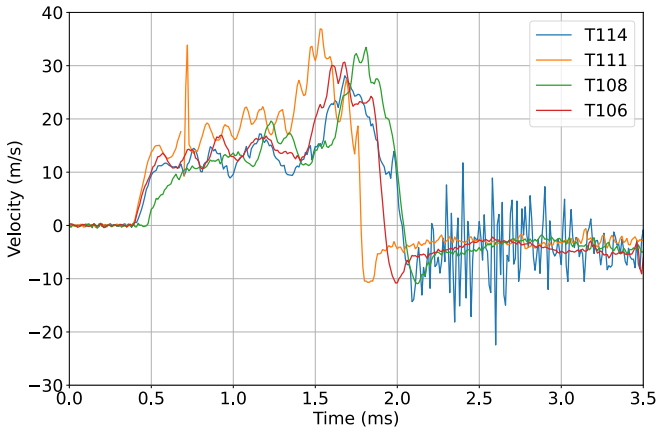

Figure 5.16: Midpoint velocity for the plates with 10 mm of gelatine in front.

5.3.4 30 mm Gelatine Plates

Figures 5.17 - 5.19 display an example of the displacement for a target plate with a 30 mm thickness of synthetic gelatine glued to the front face. The contour graphs depicted in Figure 5.17 illustrate the out-of-plane displacement of the back surface of the target plate caused by the impact of the explosion. The contour graphs on the left show the plate rise away from the blast to a central peak transient displacement. The contour graphs on the right show how the plate elastically rebounds after reaching its peak. The target plate moves towards the charge from the edges first, gradually inverting the plate entirely.

Figure 5.19 show line slice data taken across the width of the plate, allowing the shape of the plate to be viewed from side-on. The figure illustrates how the target plate travels much like the 10 mm gelatine tests, reaching its peak transient displacement at the middle of the plate. The elastic rebound motion of the target plate is displayed in Figure 5.19b, where the target plate travels towards the charge from the edges first. The plate eventually inverts fully, and the centre of the plate 'pops' through. The contour plot in Figure 5.18 is created by plotting all the line slice data together, which helps to describe the shape of the plate. The figure clearly shows the movement of the plate as the explosion loads it and highlights the maximum and minimum peak transient displacements at the centre of the plate.

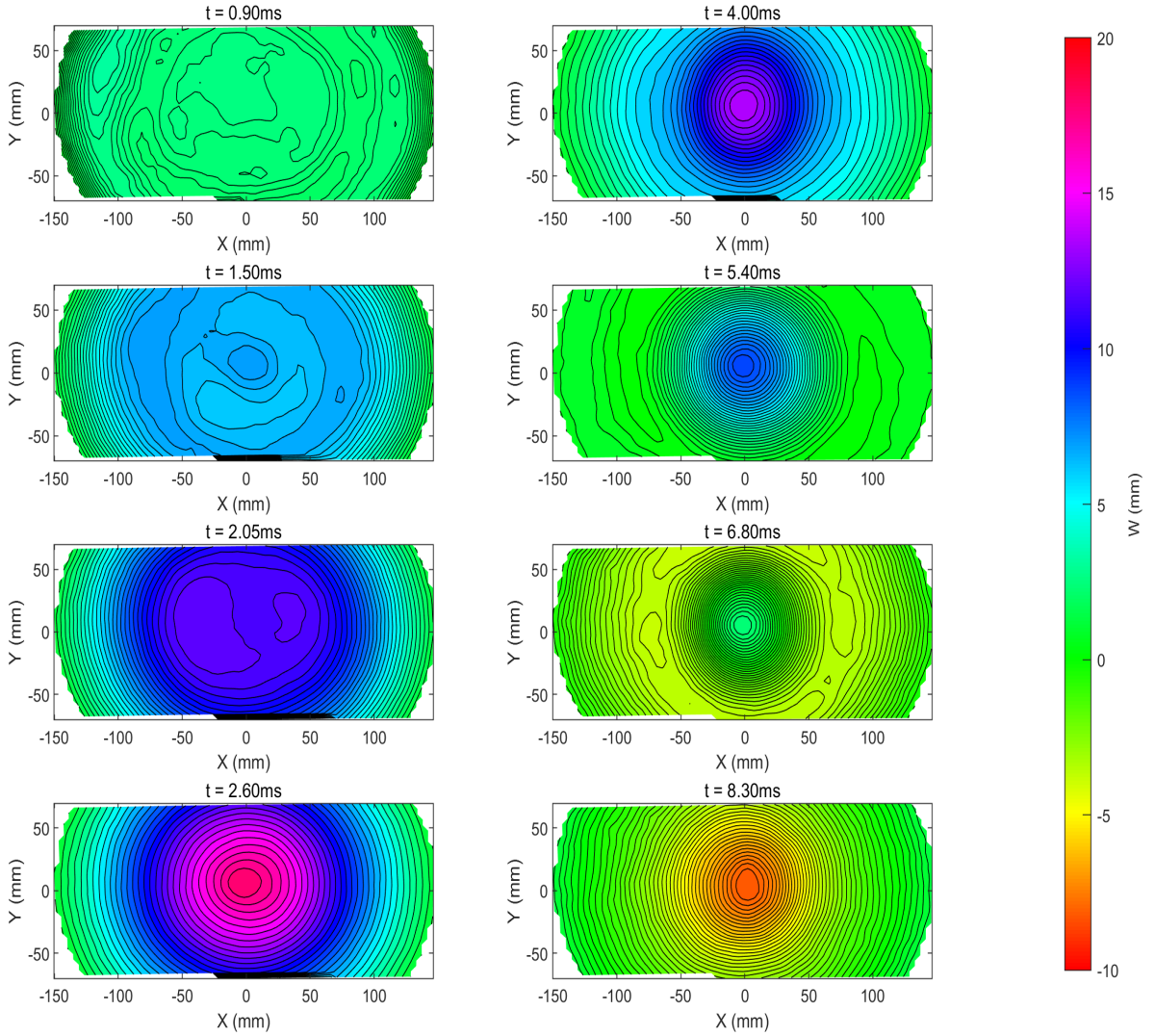

Figure 5.17: Full plate displacement over time of a plate with 30 mm of gelatine in front.

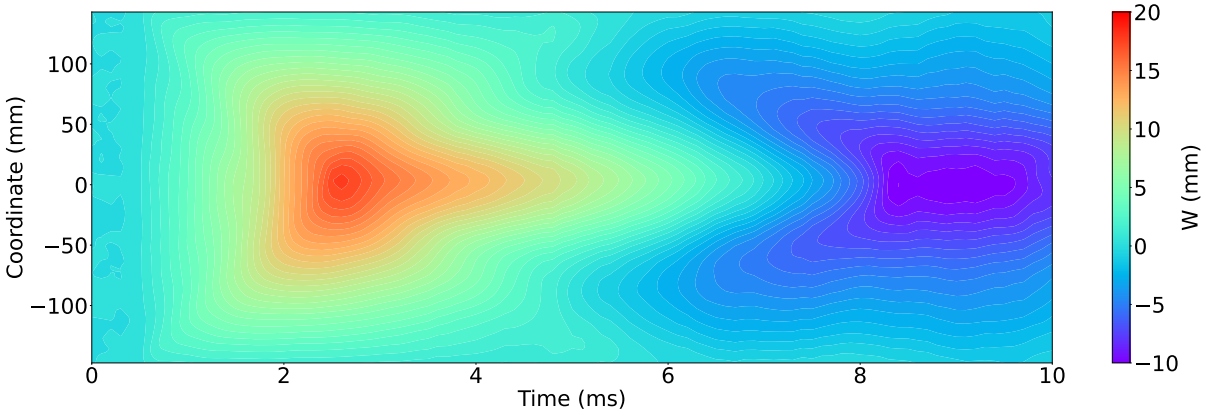

Figure 5.18: Displacement over time across the width of a plate with 30 mm of gelatine in front.

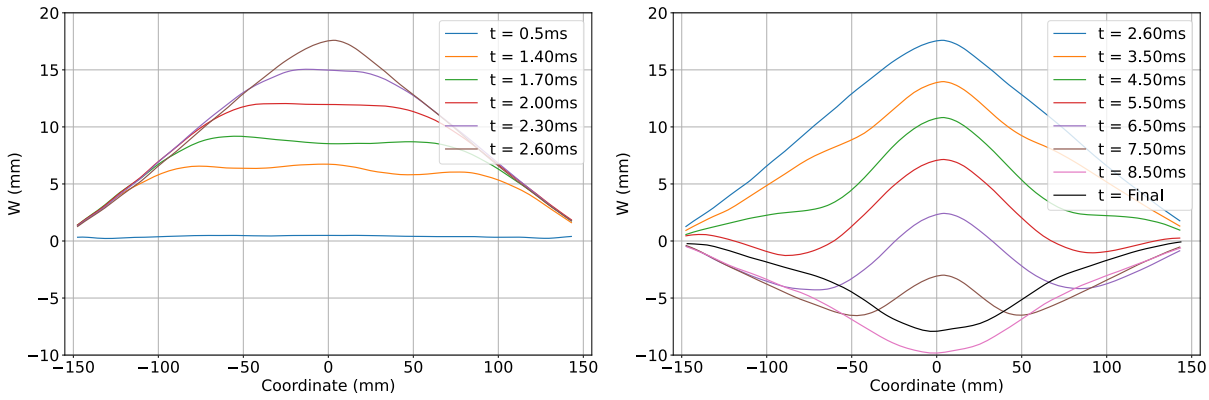

(a) (b)

Figure 5.19: Displacement profile of a plate with 30 mm of gelatine in front.

The out-of-plane displacement at the centre of the plate is plotted in Figure 5.20 for each of the 30 mm gelatine tests. Figure 5.20a focuses on the initial loading of the plate and is similar for all the tests up to the peak out-of-place displacement (approx t = 2.60 ms). After the peak, all the plates exhibit similar unloading and elastic rebound behaviour, with displacements reversing direction. There is some divergence in Test 207 for the magnitude of the peak displacement and the time to first rebound in post-peak behaviour. It also shows a large secondary positive peak after approx 12 ms in Figure 5.20b.

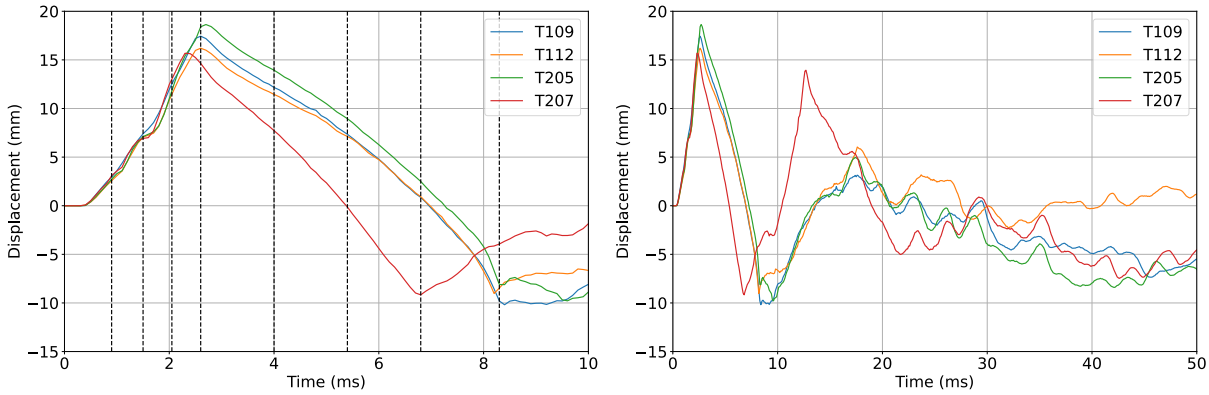

(a) (b)

Figure 5.20: Midpoint displacement for the plates with 30 mm of gelatine in front.

The line slices taken of the target plate at each time step are plotted together on the contour graph in Figure 5.21. The figure shows a ridge of higher velocity at the edges of the plate that travels towards the centre over time. When this wave meets at the centre of the target plate, an increase in velocity is seen. The figure displays how the plate oscillates over time as the velocity increases overall. After the peak velocity, the sharp elastic rebound can be seen, demonstrated by the negative velocity on the graph.

Figure 5.22 shows the velocity at the centre of the plate for each of the tests conducted with 30 mm of gelatine. The graph shows an initial rise in velocity as the explosion loads the plate. The plate then experiences some oscillating; the intensity of this oscillation seems to vary between tests. Then, the centre receives the velocity that was travelling in from the edges, seen in Figure 5.21, increasing the velocity. After the peak velocity passes, a sudden decrease is seen where the plate is travelling towards the charge.

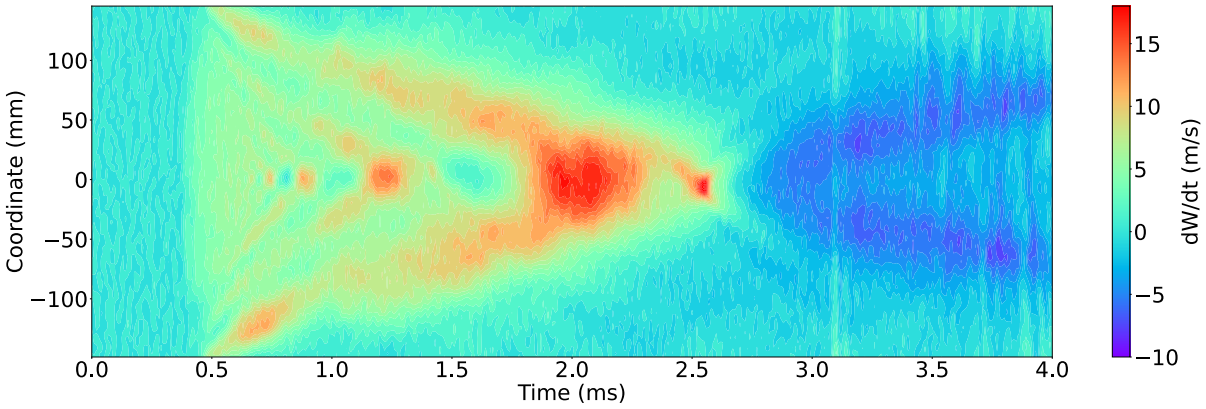

Figure 5.21: Velocity over time across the width of a plate with 30 mm of gelatine in front.

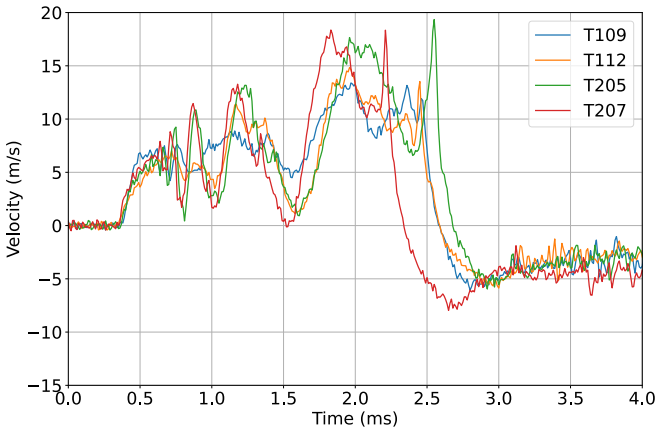

Figure 5.22: Midpoint velocity for the plates with 30 mm of gelatine in front.

5.3.5 50 mm Gelatine Plates

Figures 5.23 - 5.25 display an example of the displacement for a target plate with a 50 mm thickness of synthetic gelatine glued to the front face. The contour graphs depicted in Figure 5.23 illustrate the out-of-plane displacement of the back surface of the target plate caused by the impact of the explosion. The contour graphs on the left show how the plate travels away from the charge to a central peak transient displacement. The contour graphs on the right show how the plate elastically rebounds after reaching its peak, similar movement to the tests with 30 mm of gelatine.

Figure 5.25 show the side-on displacement data for a 50 mm gelatine test. The figure illustrates similar movement to the other experiments, reaching its peak transient displacement at the middle of the plate. The downward motion of the target plate is displayed in Figure 5.25b, where the target elastically rebounds. The plate eventually inverts fully, and the centre of the plate 'pops' through. The contour plot in Figure 5.24 is created by potting all the line slice data together. The figure shows the movement of the plate as the explosion loads it and highlights the large area of elastic rebound after the maximum transient displacement.

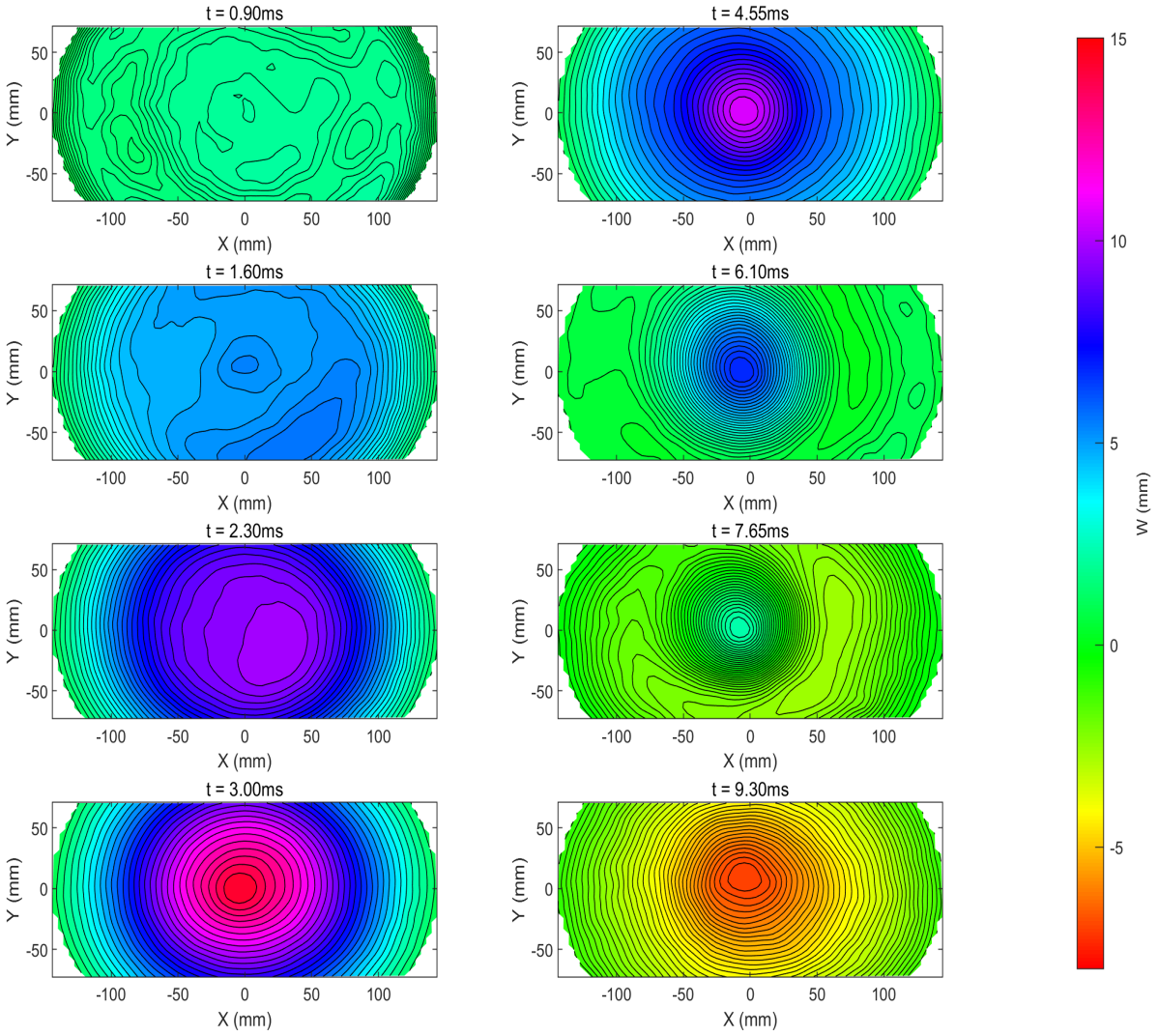

Figure 5.23: Full plate displacement over time of a plate with 50 mm of gelatine in front.

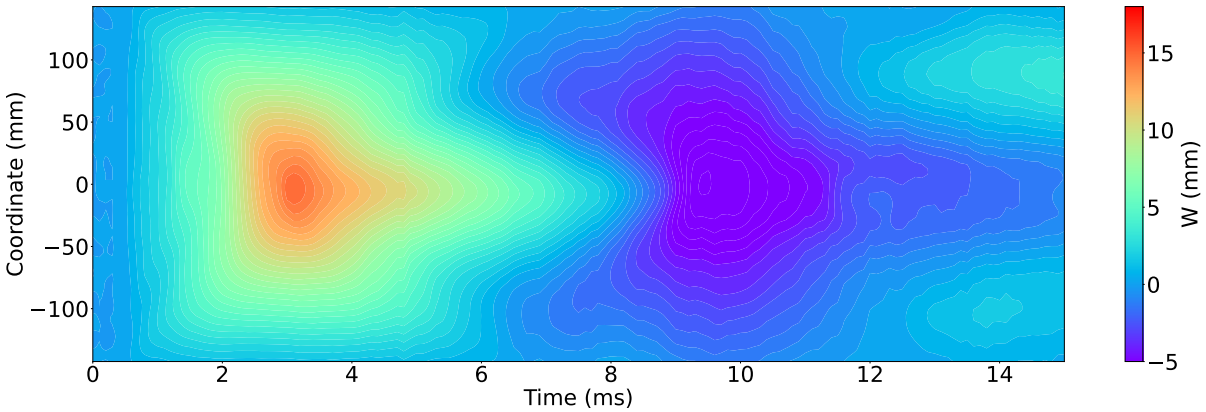

Figure 5.24: Displacement over time across the width of a plate with 50 mm of gelatine in front.

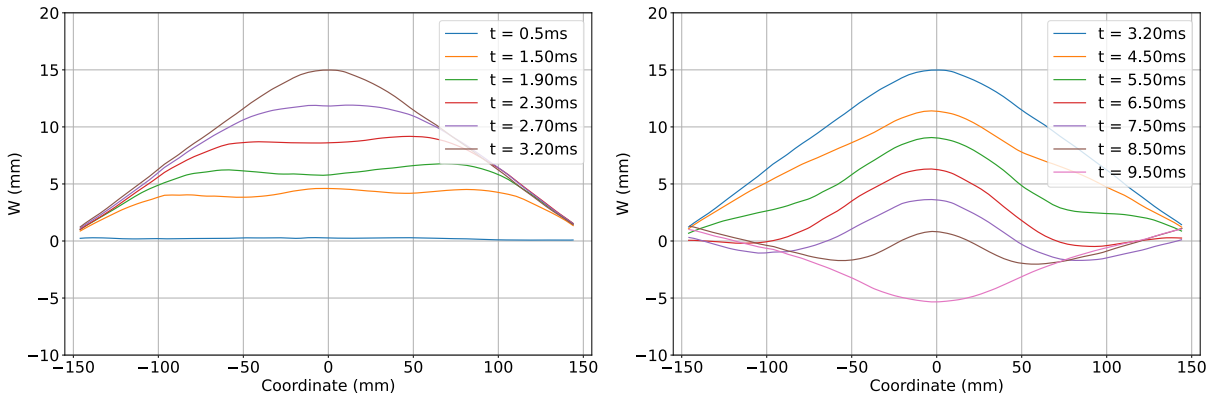

(a) (b)

Figure 5.25: Displacement profile of a plate with 50 mm of gelatine in front.

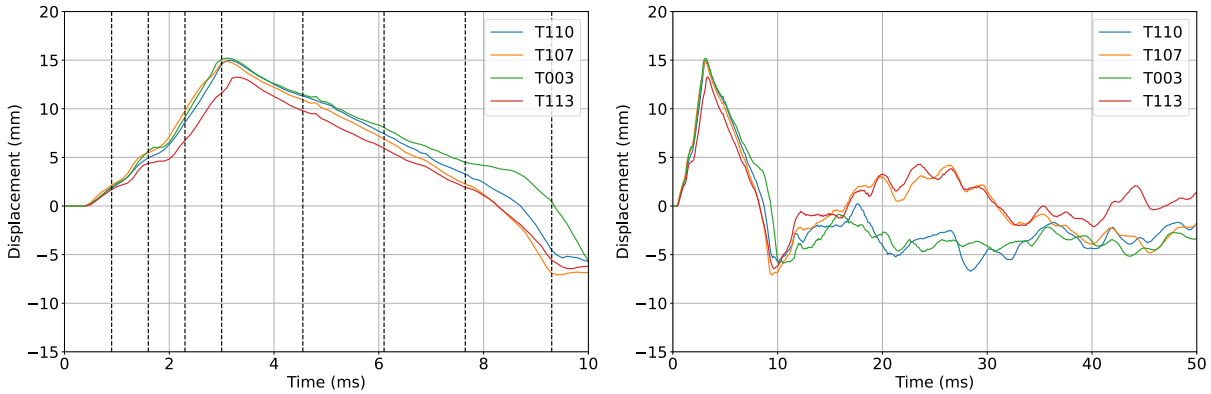

(a) (b)

Figure 5.26: Midpoint displacement for the plates with 50 mm of gelatine in front.

Figure 5.26 compare the test to test repeatability for each of the 50 mm gelatine tests. Figure 5.26a focuses on the initial loading of the plate and shows high repeatability between tests, with no variation in peak transient displacement apart from one outlier. These tests with 50 mm of gelatine show the highest repeatability out of the four types of tests that were conducted. This is most likely caused by the increase in mass of the overall clamped specimens. The bare plate had a mass of 210 g, and the gelatine specimens with the addition of a plate had masses of 816 g, 2020 g and 3226 g from each gelatine type. Therefore, the mass of the 50 mm gelatine specimens was 15 times greater than the bare plate experiment. The data in Figure 5.26b displays how the plate continues to move long after the initial loading, continuing to oscillate.

The line slices taken of the target plate at each time step are plotted together on the contour graph in Figure 5.27. The figure shows a ridge of higher velocity at the edges of the plate that travels towards the centre over time. When this wave meets at the centre of the target plate, an increase in velocity is seen. The figure also shows how the plate oscillates over time as the velocity increases overall.

Figure 5.28 shows the velocity at the centre of the plate for each of the tests conducted. The graph shows an initial rise in velocity as the explosion loads the plate. The plate then experiences some oscillating; the intensity of this oscillation seems well repeated between tests.

Then, the centre receives the velocity that was travelling in from the edges, seen in Figure 5.27, increasing the velocity. The plate experiences this peak velocity for about 1 ms, after which a sudden spike is seen, followed by a sudden decrease where the plate elastically rebounds.

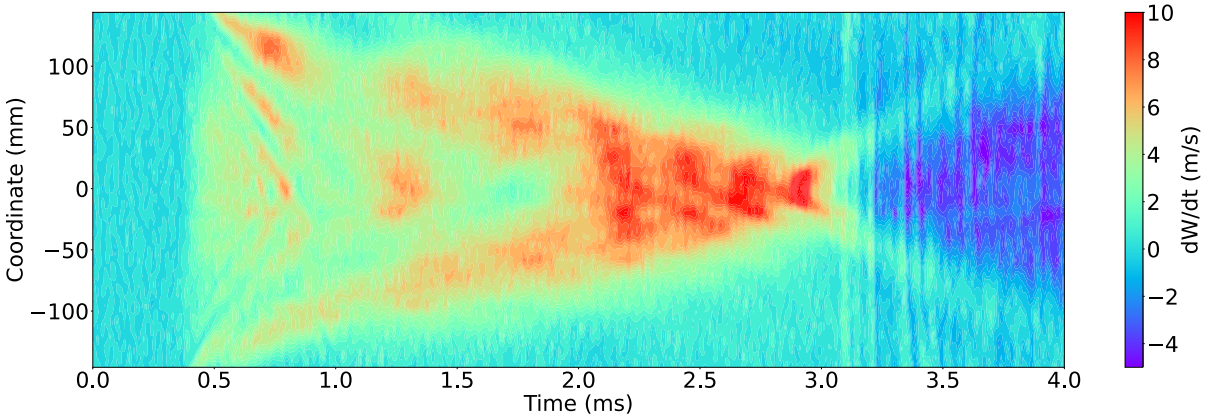

Figure 5.27: Velocity over time across the width of a plate with 50 mm of gelatine in front.

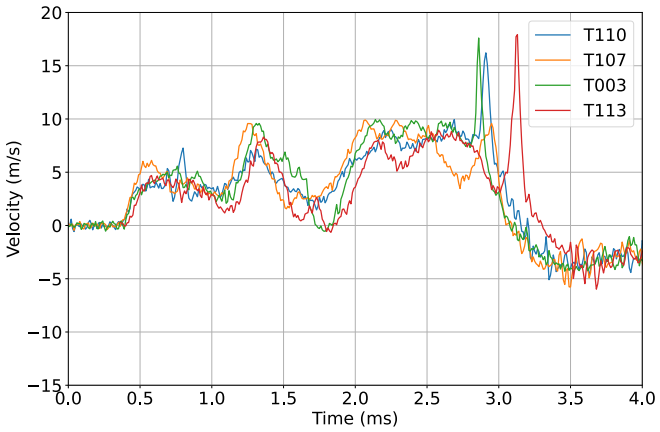

Figure 5.28: Midpoint velocity for the plates with 50 mm of gelatine in front.

5.4 Discussion

5.4.1 Post Test Photos

Figure 5.29 displays post-test images from each experiment type conducted. Figures 5.29a and 5.29b are photos of a bare plate test and show the permanent deformation caused to the plate, creating a uniform domed shape. Figures 5.29c – 5.29e include photos of each gelatine experiment in size order: 10 mm, 30 mm and 50 mm. The images show that the specimens were completely intact after the experiment, with only slight discolouration from the charge soot. Figure 5.29c displays how the centre of the 10 mm gelatine remained inverted in the opposite direction to the rest of the plate, as seen in the DIC. The 30 mm and 50 mm gelatine specimens have a uniformly doomed negative permanent deflection, which was also seen in the DIC data.

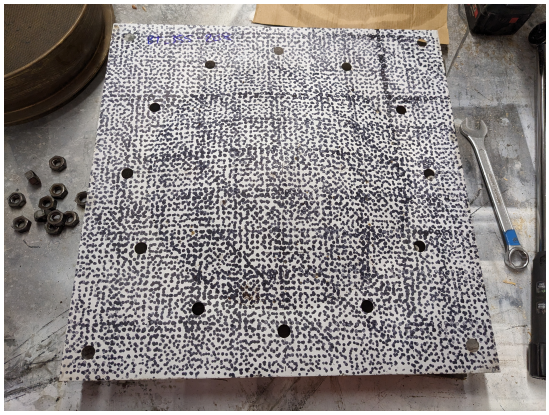

(a)

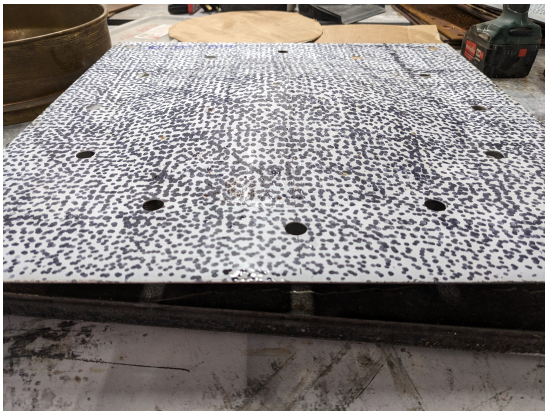

(b)

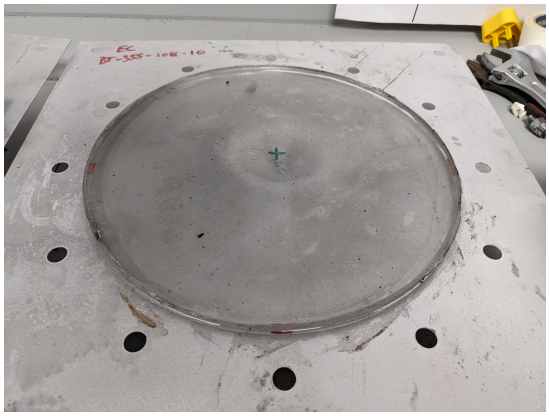

(c)



(d)



(e)

Figure 5.29: Post-test photos of a bare plate and 10 mm gelatine, 30 mm gelatine and 50 mm gelatine experiments

5.4.2 Effect of Gelatine Thickness

The contour plots used in the previous section to discuss the shape of the plates as the explosion loads them are compared here for a bare plate and plates with 10 mm, 30 mm and 50 mm of synthetic gelatine in front. These four contour plots are displayed in Figures 5.30 - 5.33; the data is plotted on the same colour bar scale. The figures illustrate that the overall shape of the plate deformation is similar for each test with gelatine. However, it is also apparent that the displacement decreases in magnitude as the amount of gelatine increases. Also, the time to peak transient displacement increases with increasing gelatine thickness. This is probably due to the attenuation of the energy by the gelatine from the explosive loading or by the higher

inertia of the large amounts of gelatine attached to the plates.

These contour graphs help to visualise how the deformation develops across the plate's width, Figures (5.30 - 5.33). The shape of the plate as it rises up to its peak transient displacement is similar across all four test types. The plates are initially loaded uniformly and then start moving away from the explosion from the edges first, propagating towards the centre over time. These contour graphs also show how the plates with gelatine attached behave very differently from the bare plate after the transient peak displacement is reached. The bare plate relaxes slightly and remains at a permanent positive displacement, whereas the plates with gelatine in front all elastically rebound to a much smaller final displacement. As with the initial positive displacement, the time it takes for the plate to decrease in displacement increases with increased gelatine thickness. The contours also show how the centre of the 10 mm gelatine plate remains in the positive direction, whereas the 30 mm and 50 mm gelatine plates reach a negative displacement at their centre.

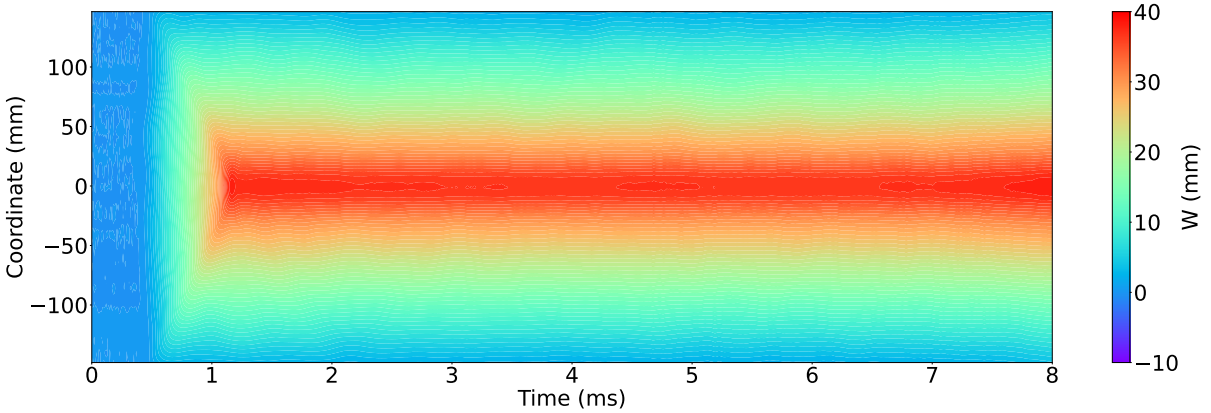

Figure 5.30: Displacement over time of a bare plate.

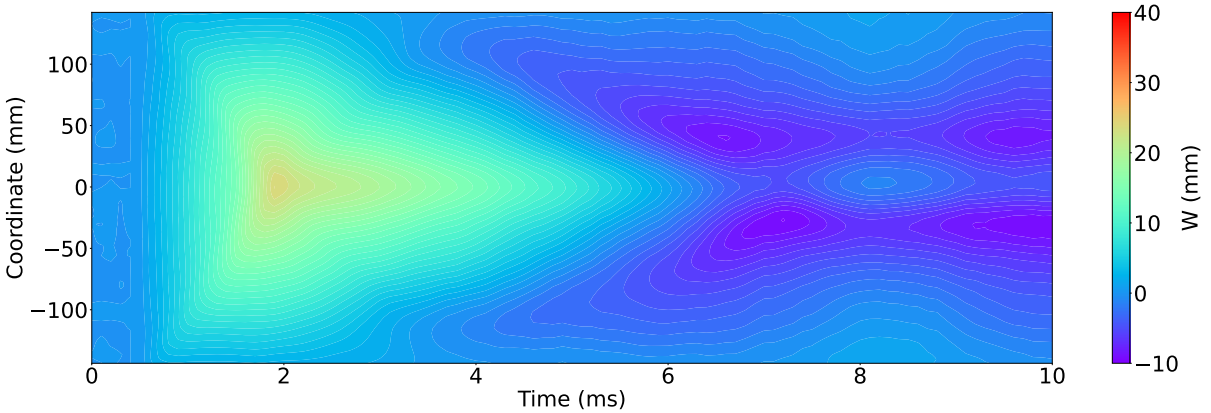

Figure 5.31: Displacement over time of a plate with 10 mm of gelatine.

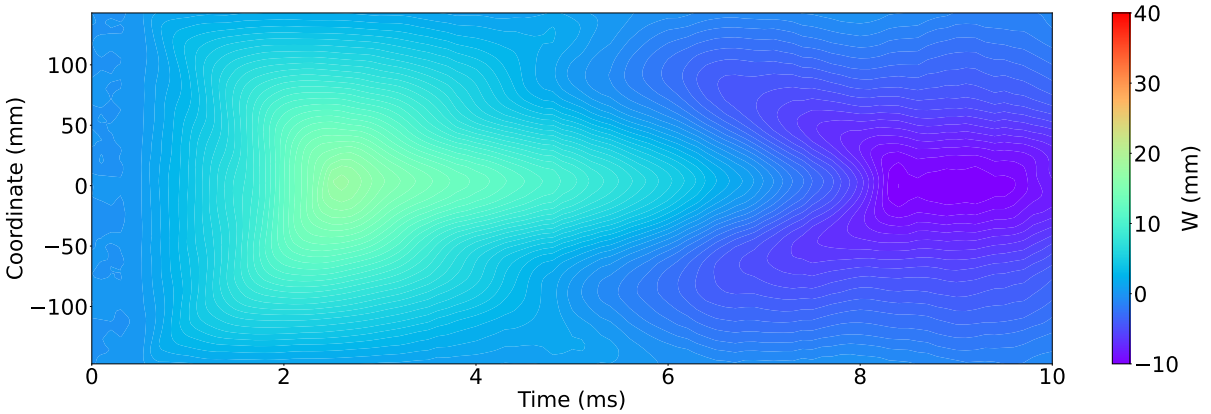

Figure 5.32: Displacement over time of a plate with 30 mm of gelatine.

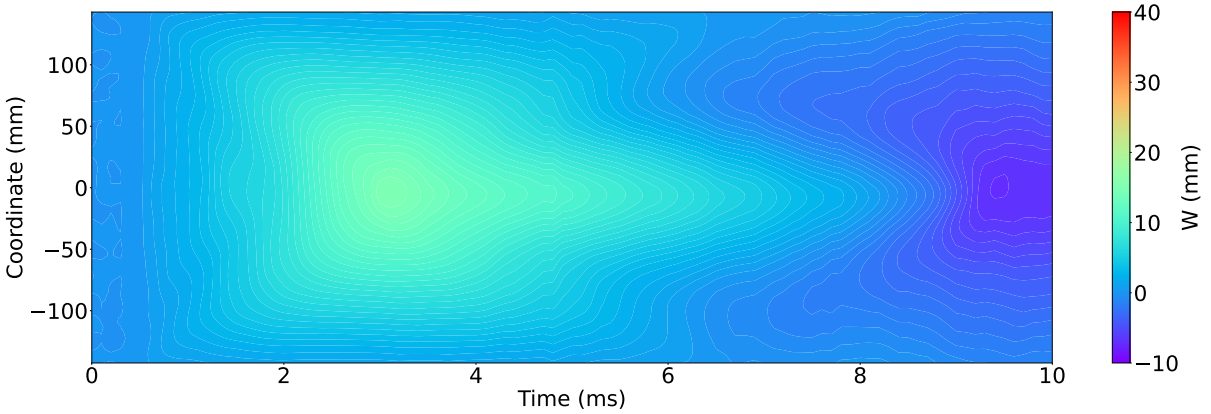

Figure 5.33: Displacement over time of a plate with 50 mm of gelatine.

The plots in Figure 5.34 display the out-of-plane midpoint displacement for each specimen type, plotted on the same scale vertical axes. Figure 5.34 shows that both the peak transient displacement decreases and the time to peak increases with increasing gelatine thickness. These graphs also illustrate the improved response repeatability in the tests with gelatine covering the target plate.

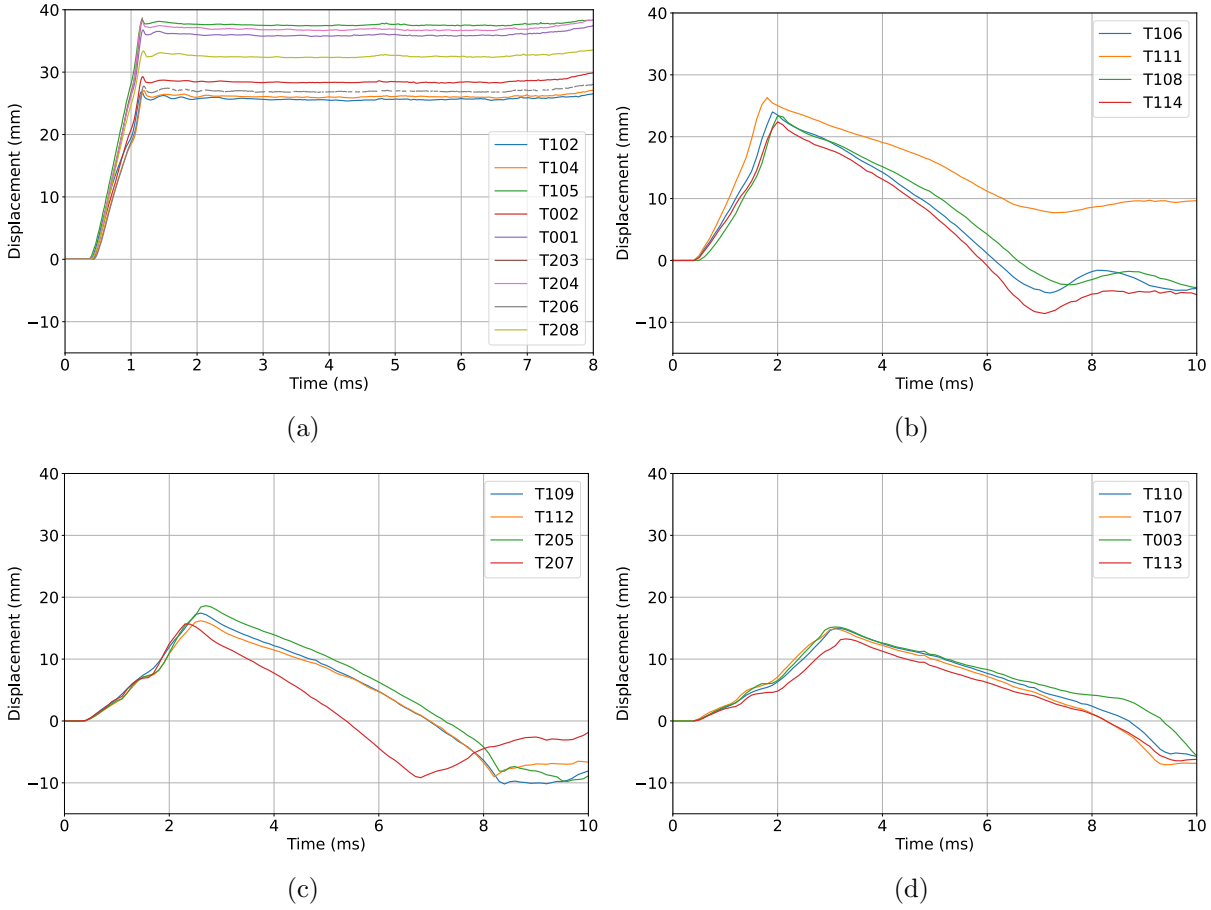

Figure 5.34: Midpoint displacement for a bare plate and 10 mm, 30 mm and 50 mm of gelatine.

Figures 5.35 - 5.38 show normalised velocity contour plots across midline slices of the plates as time progresses. The data is normalised to the maximum velocity for each test to focus on the overall behaviour rather than the magnitude. The graphs show how, after the initial loading, the plates have a higher velocity at the edge that travels into the centre over time. In all cases, the peak velocity of the target plate attained during the response was located at the plate centre. As the time to the peak velocity increases, the thickness of the gelatine attached to the plates increases. The bare plate experiences a sharp spike in velocity at the centre of the plate, whereas the gelatine plates spread out this large velocity over time; it takes longer as the thickness of gelatine increases. The bare plate and 10 mm gelatine plate display similar "ripples" in the velocity across the plates as the plate is loading, whereas the 30 mm and 50 mm gelatine plates show different responses across the plates.

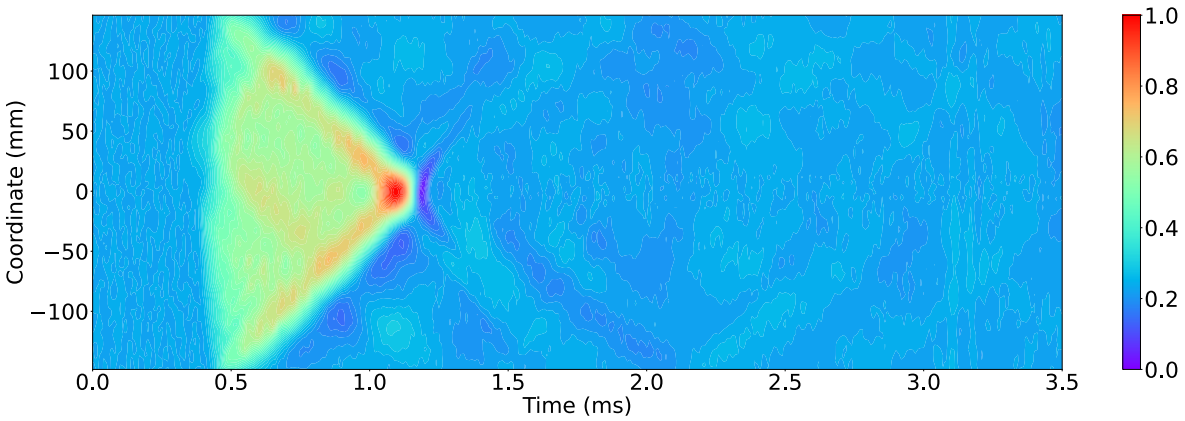

Figure 5.35: Velocity over time of a bare plate, velocity scale normalised.

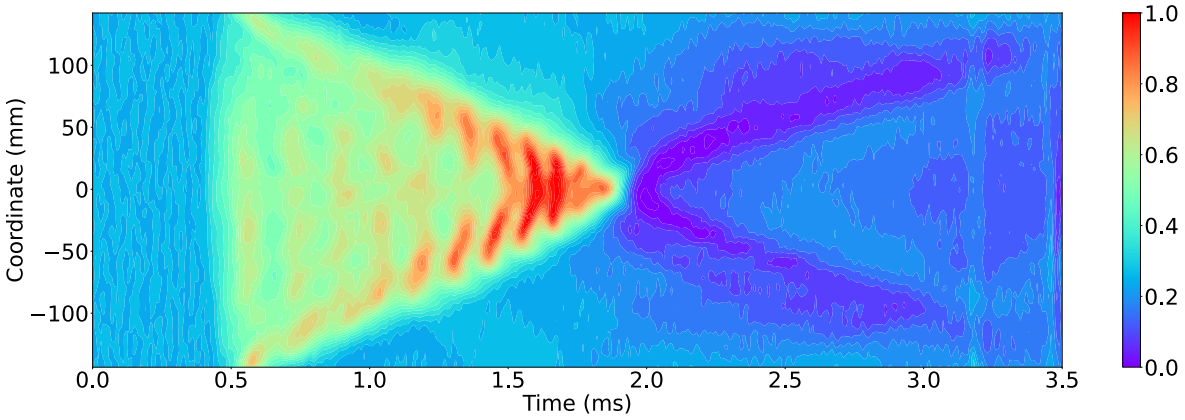

Figure 5.36: Velocity over time of a plate with 10 mm of gelatine, velocity scale normalised.

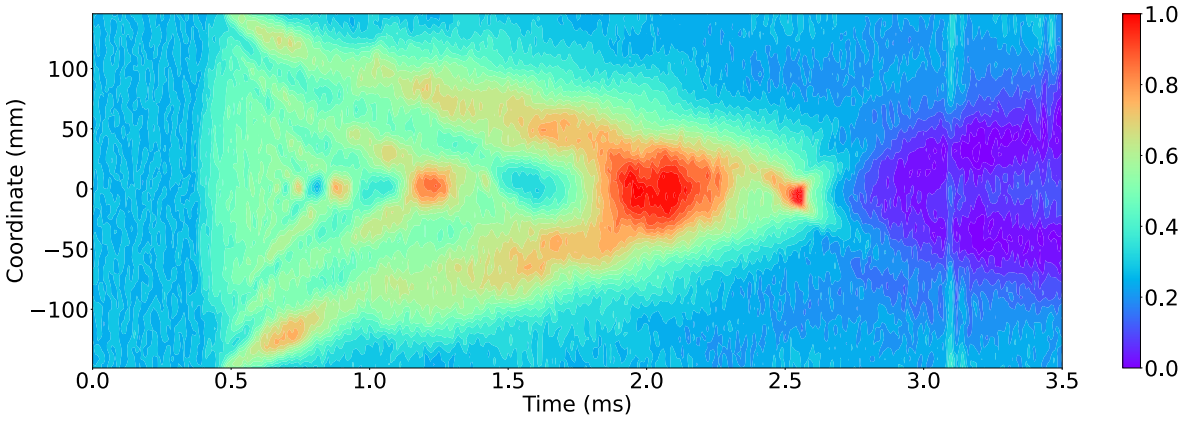

Figure 5.37: Velocity over time of a plate with 30 mm of gelatine, velocity scale normalised.

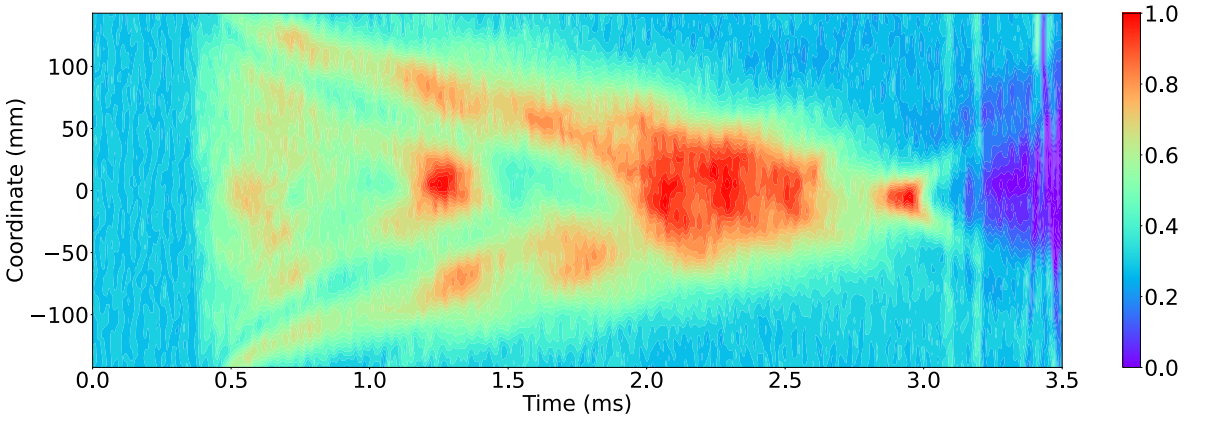

Figure 5.38: Velocity over time of a plate with 50 mm of gelatine, velocity scale normalised.

Figure 5.39 shows transient midpoint velocity-time histories for each sample type, plotted on the same scale for ease of comparison. They illustrate that the time to peak velocity increased with increasing gelatine thickness. These graphs also include the magnitude of the velocity experienced by the plates and show that as the thickness of gelatine is increased, the velocity of the plate decreases. Having gelatine in front of the target plate significantly influences the plate velocity, with 10 mm of gelatine reducing the peak velocity from approximately 80 m/s to 35 m/s.

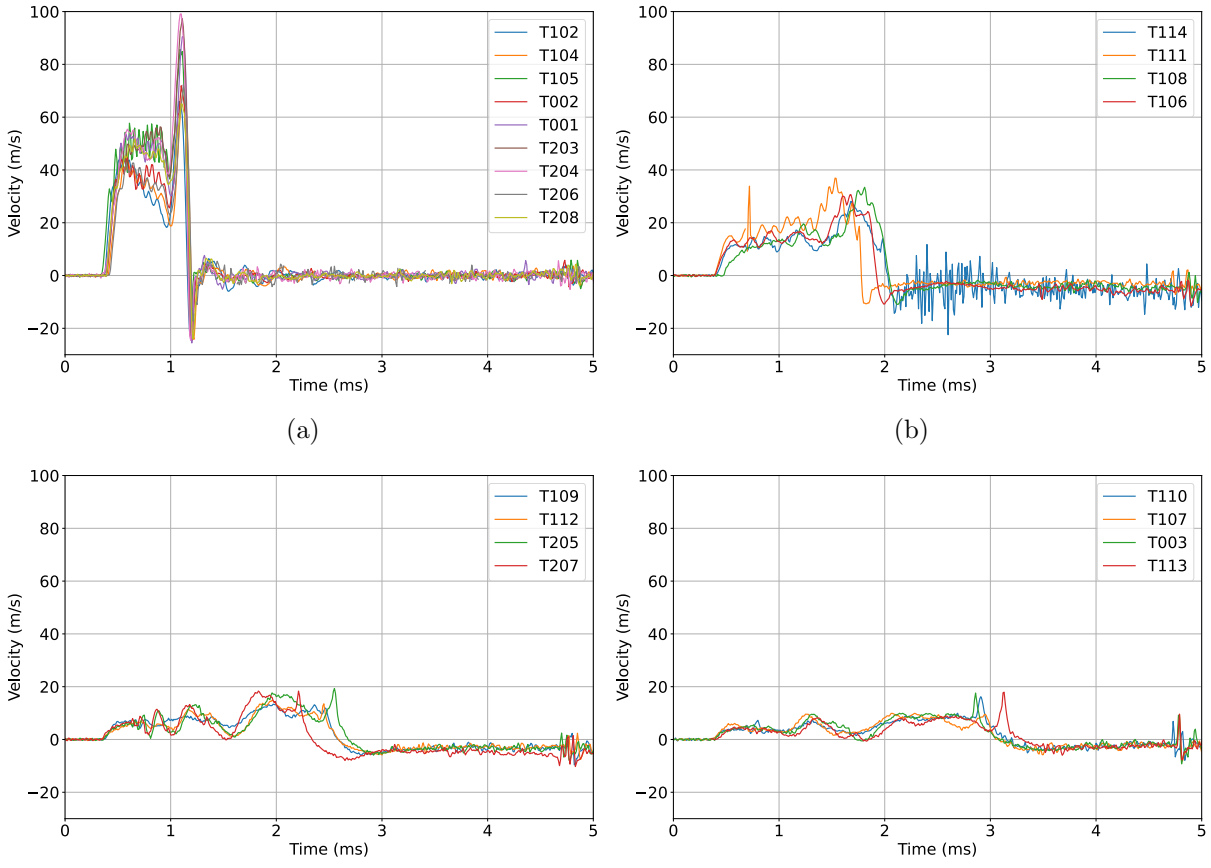

Figure 5.39: Midpoint velocity for a bare plate and 10 mm, 30 mm and 50 mm of gelatine.

The explosive loading causes the initial response of the plate. The plate also experiences loading in response to the fixed clamping boundary condition. Figure 5.40a displays the velocity of a bare target plate over the time of the test at the centre and 50 mm, 100 mm and 145 mm from the centre. The y-axis is the velocity of the plate, and the x-axis is time. The graph initially shows at roughly 0.4 ms the sudden loading from the explosive that is uniform across the plate width. The explosive loading has finished at 0.5 ms, shown in the 145 mm trace, and the plate oscillates. Then, at 0.7 ms at a distance of 100 mm from the plate's centre, a velocity peak is seen. This increase in velocity is seen to travel towards the centre of the plate over time, with another peak at 50 mm. When this velocity reaches the centre, it causes a sharp rise in velocity. This response in the plate is probably caused by a velocity wave travelling into the centre of the plate.

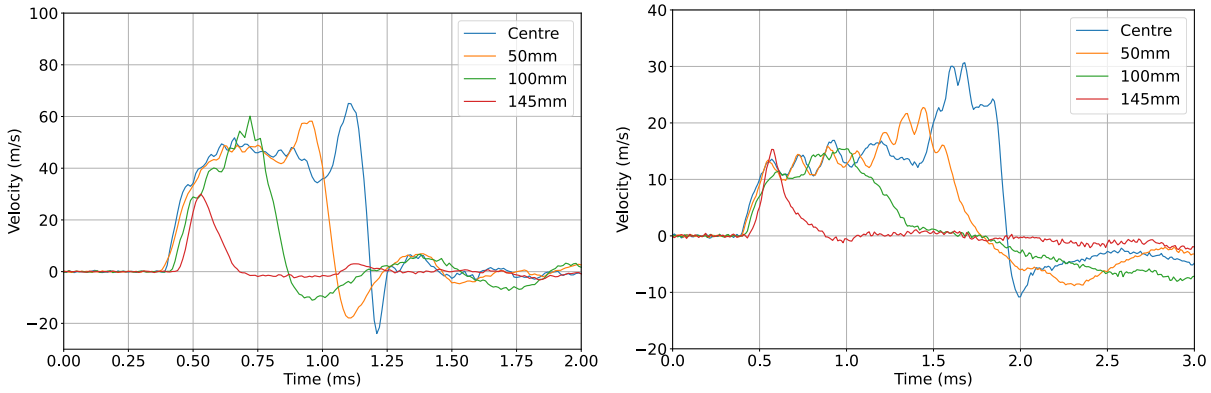

(a) (b)

Figure 5.40: Velocity for a bare plate and 10 mm gelatine plate.

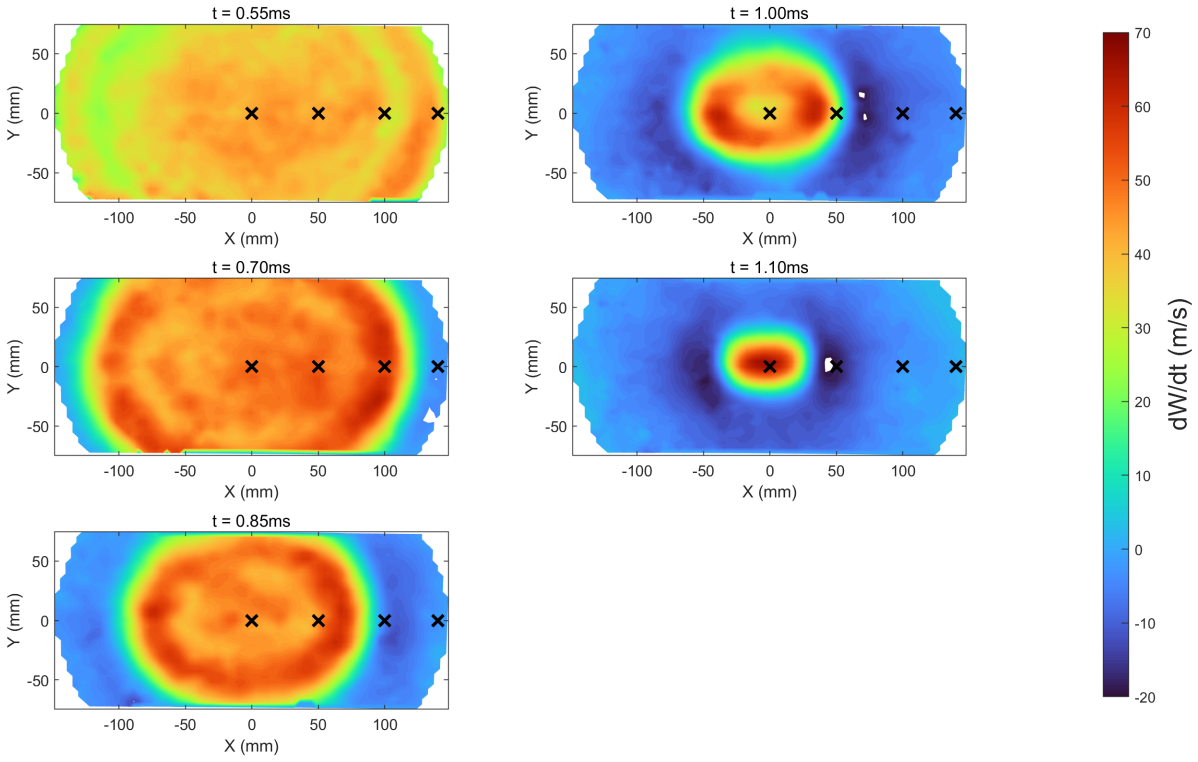

Figure 5.41: Full plate velocity for a bare plate.

The path of the velocity wave can be seen in the whole plate graphs in Figure 5.41. Figure 5.41 illustrates the velocity of the back surface of the target plate from 0.55 ms to 1.10 ms. The location of the data points used in Figure 5.40a is marked on these graphs for clarity. The red ring progressing into the centre over time illustrates this velocity wave travelling in.

A similar response mechanism was also seen in the tests where 10 mm of gelatine was placed in front of the target plate. Figure 5.40b displays the velocity of a plate with 10 mm of gelatine at the centre and 50 mm, 100 mm and 145 mm from the centre of the plate. The graph shows how the plate is initially loaded uniformly across the four points and then begins to oscillate. A higher velocity is seen between 0.8 ms and 1.1 ms at a distance of 100 mm from the centre of the plate. This behaviour is similar to that seen in the bare plate; however, the peak in the velocity is spatially more distributed. This increase in velocity is seen to travel towards the centre of the plate over time, with another peak at 50 mm. When this velocity reaches the centre, it causes a larger increase in velocity. The path of the velocity wave can be seen in the whole plate graphs in Figure 5.42 below. The progression of the velocity wave towards the centre can be seen here. The velocity ring is spatially more distributed than the response of the bare plate.

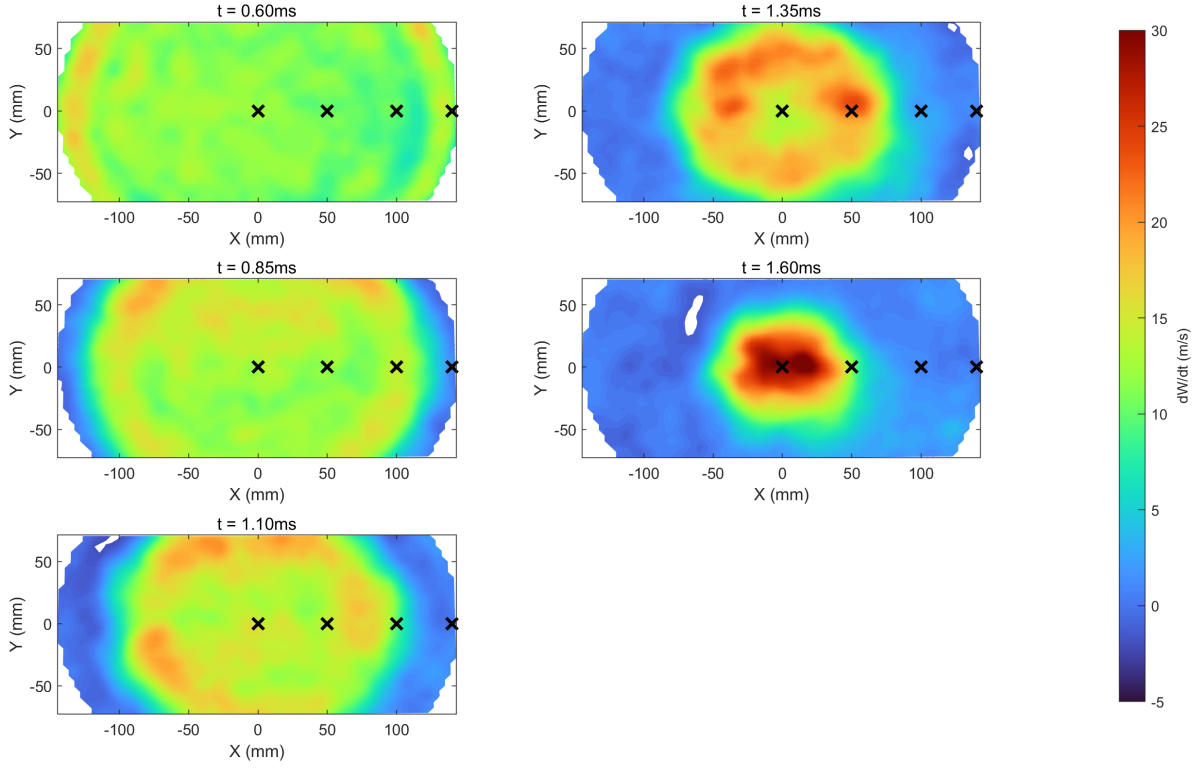

Figure 5.42: Full plate velocity for a 10 mm gelatine plate.

More complex velocity wave behaviour is seen in the experiments where 30 mm of gelatine is placed in front of the target plate. Figure 5.43a displays the velocity of a plate with 30 mm of gelatine at the centre and 50 mm, 100 mm and 145 mm from the centre of the plate. The graph depicts how the centre of the target plate receives two velocity waves at the centre of the plate. The full plate graphs in Figure 5.44 display the progression of the velocity waves as they propagate to the centre. Two orange rings are seen to progress towards the centre of the plate, causing the two peaks in the velocity data at the centre. The behaviour from the 30 mm experiments is also seen in the experiments where 50 mm of gelatine was placed in front of the target plate. Figure 5.43b shows the velocity of the plate with 50 mm of gelatine at the centre and 50 mm, 100 mm and 145 mm from the centre of the plate and displays the first wave arriving at the centre of the plate at 1.25 ms. The full plate graphs in Figure 5.45 display the progression of the velocity waves as they propagate to the centre. The double velocity wave may be caused by stress waves travelling laterally through the gelatine after reflecting off the free side surface. The behaviour change observed when moving from 10 mm thick gelatine to 30 mm thick gelatine could be attributed to the increased thickness, which enlarges the size of the free surface on the side of the specimen. Propagation in the 10 mm thick gelatine is minimal due to its reduced thickness. The velocity wave in the final two graphs is spread over a broader area in the 50 mm experiments compared to the 30 mm ones. This could be causing the centre velocity to remain high for longer in the 50 mm experiments.

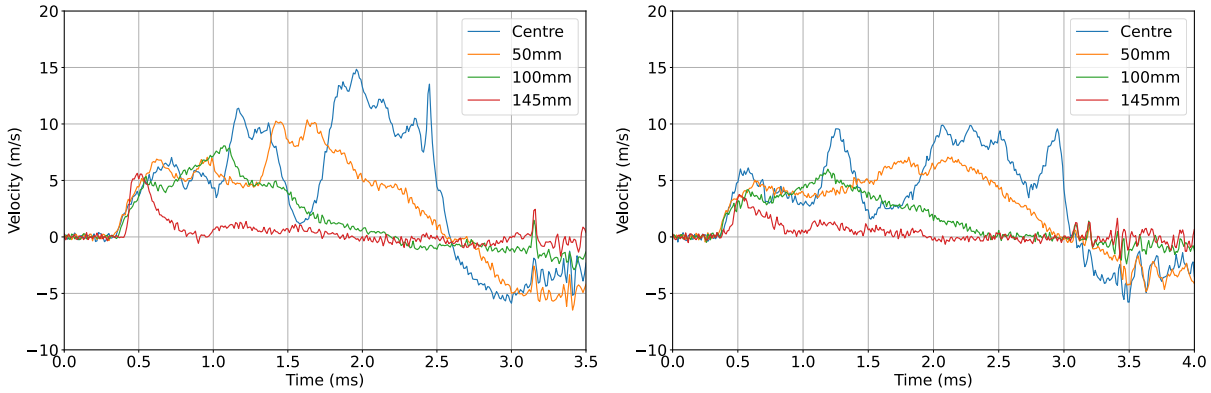

(a) (b)

Figure 5.43: Velocity for a 30 mm and 50 mm gelatine plate.

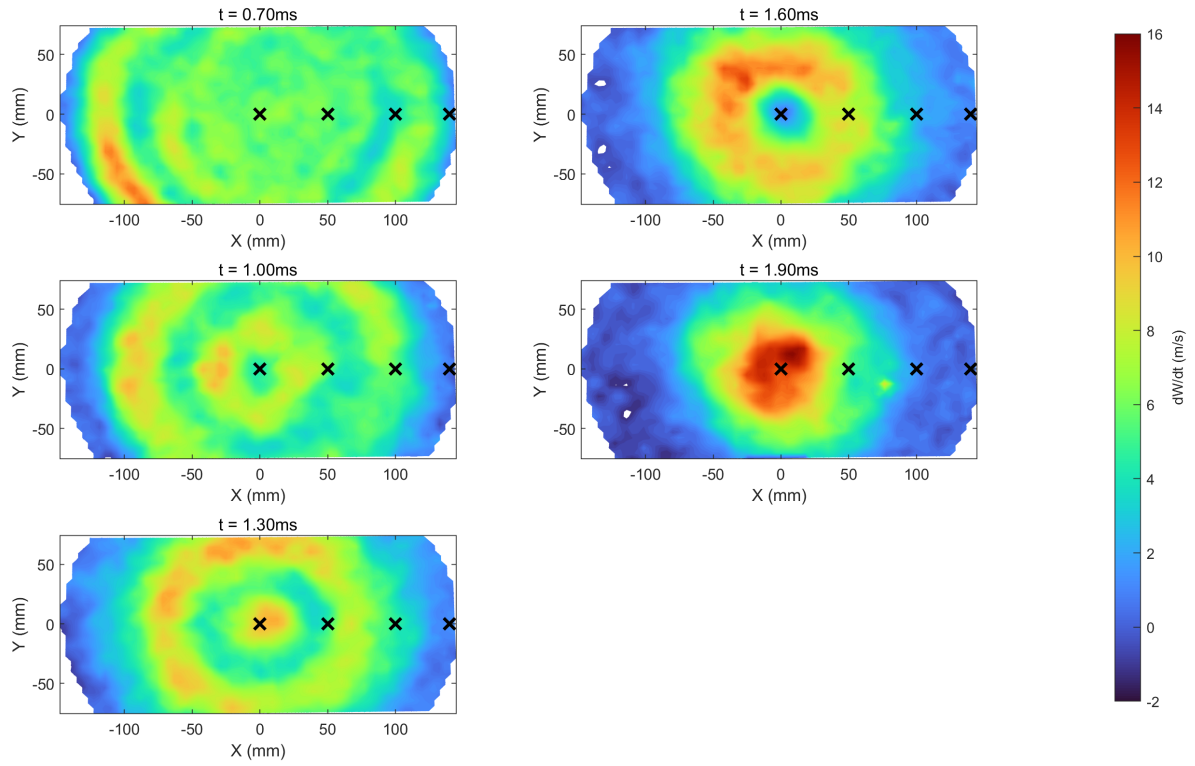

Figure 5.44: Full plate velocity for a 30 mm gelatine plate.

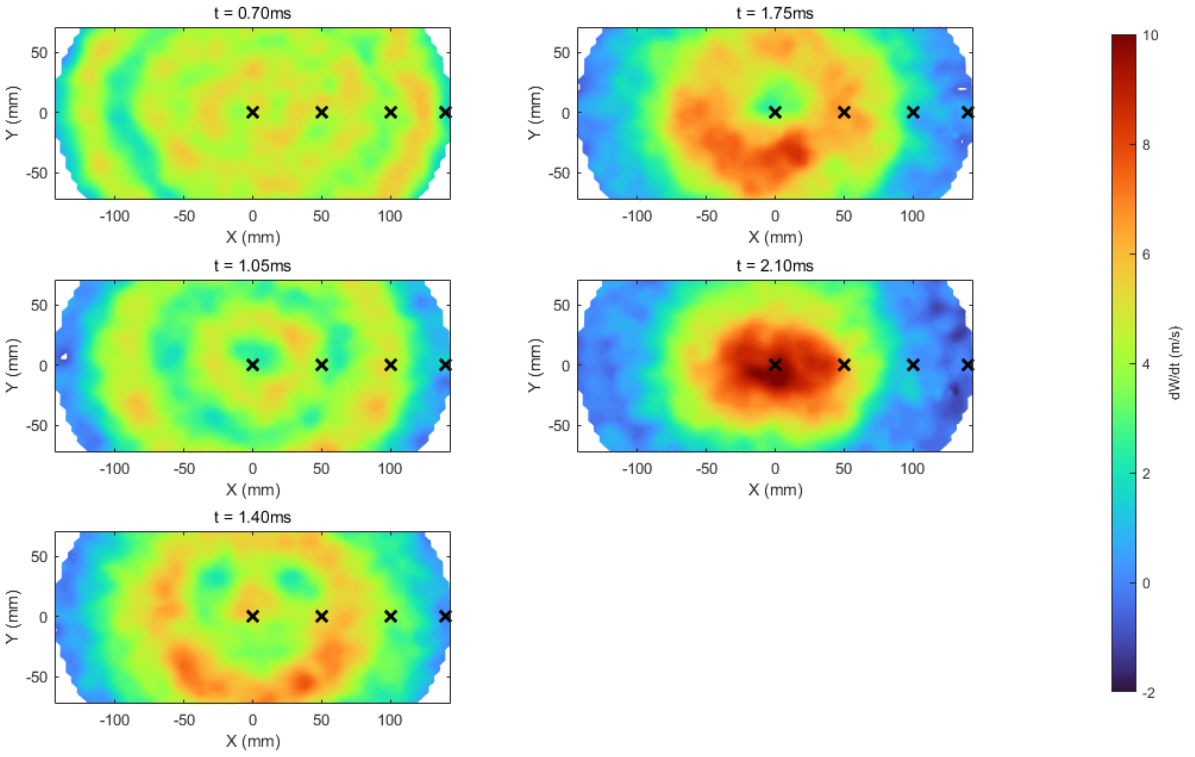

Figure 5.45: Full plate velocity for a 50 mm gelatine plate.

5.5 Numerical Analysis

LS Dyna was chosen for this PhD project as it specialises in high strain rate non-linear structural dynamics and can model rapid compression and movement of gasses (Reay, 2014). Two different methods have been used in the literature to simulate blast loading. The first uses an Arbitrary Lagrangian Eulerian (ALE) formulation with the appropriate equations of state to model the expansion of the blast wave from detonation. This method is computationally costly because a mesh of the entire area of interest is needed, and a high mesh density near the detonation point and interactions with Lagrangian bodies are required. Alternatively, the load can be prescribed to elements with energy or pressure time histories. This reduces the geometry of the mesh needed. However, full spatial pressure loading is required to fully model a spherical blast wave.

Here, a Multi-Material Arbitrary Lagrangian Eulerian solver (MMALE) was utilised to simulate the explosion. This method can simulate the movement of the gases for the explosion. Pressure time histories for this charge could not be predicted using the Kingery and Bulmash equations as this charge is a cylinder.

5.5.1 Initial Geometry

A finite element model was created in LS Dyna with the same geometry as the blast experiments, so the influence of synthetic gelatine on the loading could be interrogated. The blast experiment was modelled as a 3D quarter axisymmetric mesh. A 3D model was chosen to visualise the spatial movement of the synthetic gelatine and visualise any non-symmetric movement that would not be captured in a 2D model. The model consisted of an air domain defined by a 225 x 225 x 800 mm mesh of solid elements. After trialling a few different sizes, an element size of 5 mm was chosen. Reducing the element size increased the accuracy of the loading magnitude and arrival time predictions, however, when the element size was reduced to less than 5 mm, this improvement was reversed. Hence, an element size of 5 mm was used. The explosion was modelled within this mesh using the keyword file Initial-Volume-Fraction-Geometry. This method 'fills' the air mesh with the explosive material from the detonation point and modelled the propagation of the pressures. The charge cylinder had the same dimensions as the experiment: 39 mm diameter and 13 mm height. The layout of the air domain and charge can be seen in Figure 5.46.

A quarter of the clamping frame was modelled with 4 mm solid elements with dimensions to match the experiment, see Figure 5.46. The bolts were modelled with spring elements to simulate the clamping force on the plate. These allowed the compression forces of the clamping bolts and the confinement of the target plate to be simulated. The friction forces between the clamps and the target plate caused by the bolts were simulated by defining Automatic-Contact-Surface-To-Surace with static and dynamic friction factors for aluminium-to-steel contact. Initially, the target plate was modelled with 5 mm thin shell elements with a thickness of 1 mm. The element size was chosen to match the size of the air elements to limit the leakage of explosive parts through the plate. The interaction between the explosive and the plate was described by the Constrained-Lagrange-In-Solid formulation. This formulation applies penalty coupling forces to both the ALE and Lagrangian elements if the ALE part penetrates the Lagrangian material. The card has different options to control this interaction, and the user manual's advice was followed.

X and y symmetry planes were described along the front two faces to account for only a quarter of the domain being simulated. The top surface of the top clamp was fixed for translations in the z-direction (vertical) to include the restriction of the rest of the test frame. Another

spring element was defined in the far corner of the clamp to model where the clamping frame was mounted to the rest of the test frame. The nodes above this spring element were fixed in all directions to create a simplified simulation of how the clamping frame was attached to the test frame.

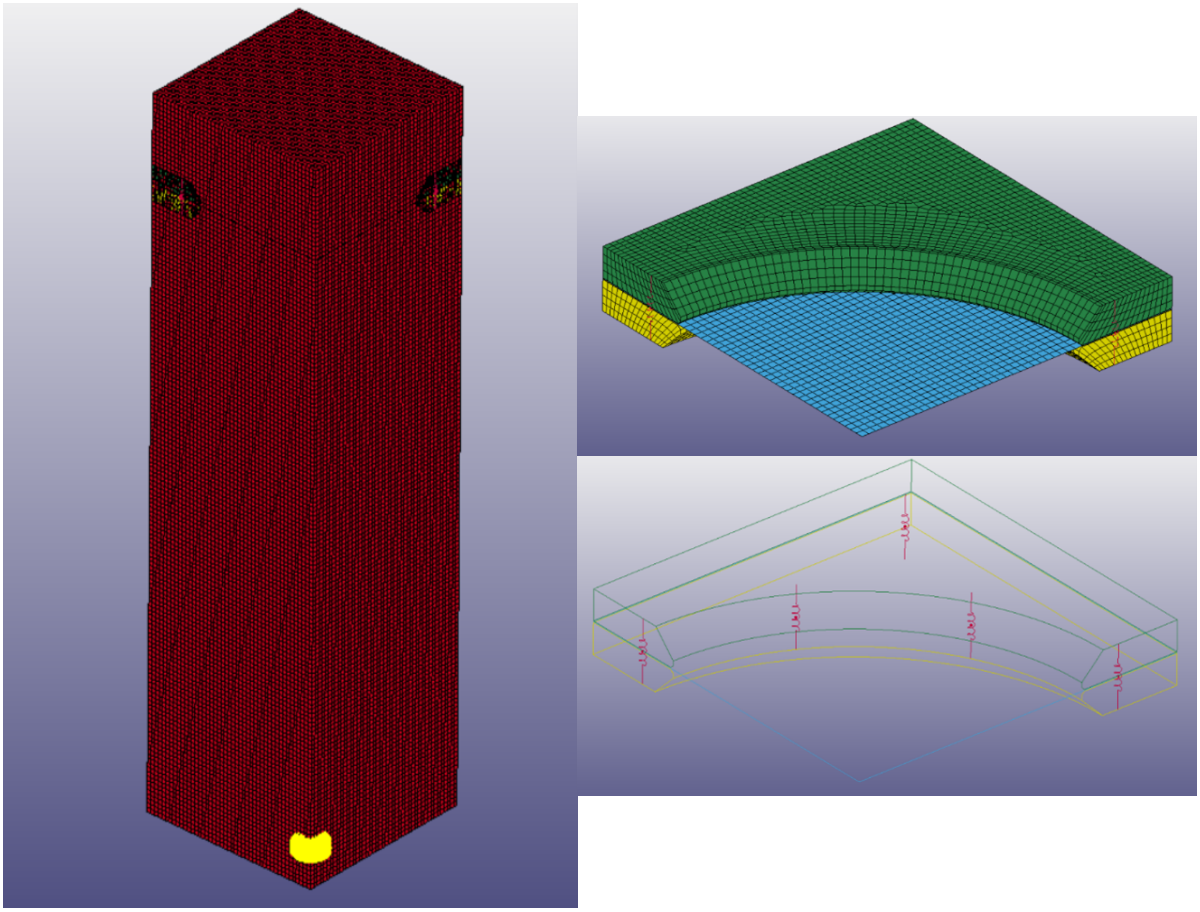

Figure 5.46: Numerical model layout; left is the full domain, right is the clamp and plate with an outline version to view spring locations.

5.5.2 Material Model and Equation of State

The properties of the air were described as an ideal gas using the MAT-Null material model and Linear-Polynomial equation of state. The pressure in the system is characterised by Equations 5.3 and 5.4,

$$p = C_0 + C_1\mu + C_2\mu^2 + C_3\mu^3 + (C_4 + C_5\mu + C_6\mu^2)E \tag{5.3}$$

$$\mu = \frac{\rho}{\rho_0} - 1 \tag{5.4}$$

where C_0 to C_6 are constants, E is the specific internal energy, and μ is a volumetric parameter defined by current and initial density.

The explosive properties were modelled using keyword files MAT-High-Explosive-Burn and JWL equation of state. The material model controls the programmed detonation of the explosive. The pressure-volume-energy relationship of the explosive products is given by Equation 5.5,

$$p = A(1 - \frac{\omega}{R_1 V})e^{-R_1 V} + B(1 - \frac{\omega}{R_2 V})e^{-R_2 V} + \frac{\omega E}{V} \tag{5.5}$$

where A, B, R_1, R_2 and ω are constants, V is the volume, and E is the specific internal energy.

Values for these were taken for Rigby et al. (2018), who also modelled PE4 explosives, where the modelling was shown to be in agreement with physical testing. The parameters for the air and the explosive are included in Tables 5.2 and 5.3.

MAT-Null			
Parameter	ρ (kg/mm^3)		
Value	$1.255e^{-9}$		
MAT-High-Explosive-Burn			
Parameter	ρ (kg/mm^3)	D (m/s)	P_cj (Pa)
Value	$1.601e^{-6}$	8193	$28.0e^9$

Table 5.2: Material model properties for air and PE4.

EOS Linear-Polynomial								
Parameter	C_0 (Pa)	C_1 (Pa)	C_2 (Pa)	C_3 (Pa)	C_4 (-)	C_5 (-)	C_6 (-)	E_0 (Pa)
Value	0.0	0.0	0.0	0.0	0.4	0.4	0.0	$253.40e^3$
EOS JWL								
Parameter	A (Pa)	B (Pa)	R_1 (-)	R_2 (-)	Ω (-)	E_0 (Pa)		
Value	$609.77e^9$	$12.95e^9$	4.50	1.40	0.25	$9.00e^9$		

Table 5.3: Equation of state model properties for air and PE4.

The clamping frame was modelled with Johnson-Cook material parameters for mild steel (Vedantam et al., 2006). This allowed the compression forces of the clamping bolts and the confinement of the target plate to be simulated. The clamps were modelled with the Simplified-Johnson-Cook keyword card to reduce computational time, as the behaviour of the steel was not the main focus of this PhD. The aluminium target plate was modelled using the Johnson-Cook parameters reported by Spranghers et al. (2013*b*) as these parameters correlated well with their experiment, and they used the same hardening type of aluminium as was used here. The Johnson-Cook parameters for both these materials are included in Table 5.4.

Johnson-Cook parameters						
Parameter	ρ (kg/mm^3)	E (GPa)	ν (-)	A (GPa)	B (GPa)	n (-)
EN AW-1050A H24	$2.71e^{-6}$	69	0.33	0.110	0.150	0.360
Mild Steel	$7.90e^{-6}$	210	0.27	0.217	0.2337	0.6428
Parameter	C (-)	m (-)	T_m (K)	C_p (J/kg K)		
EN AW-1050A H24	0.014	1.0	918.15	899		
Mild Steel	0.0756					

Table 5.4: Material model properties for aluminium and mild steel.

5.5.3 Initial Results and Discussion

Figure 5.47 displays the displacement and velocity of the back surface of the target plate from the numerical model and experimental Test 208. The numerical model was compared to Test 208 because this test lay in the middle of the range of bare test results and was deemed a typical bare plate experiment. The different colours in the figures depict different radial distances across the width of the plate. The figures show that the model does not capture the plate's entire behaviour. The velocity data in Figure 5.47b shows that at the centre of the plate, the initial velocity has minimal variation from the experiment. However, after 0.7 ms, the velocity drops off, and the model does not see the velocity wave arrive at 1.10 ms, as previously discussed in the experimental data and shown most clearly in the blue central trace here. The velocity data at 50 mm from the centre initially follows a similar shape to the experiment but with a 5% lower magnitude. The velocity at this point also drops off after the initial loading.

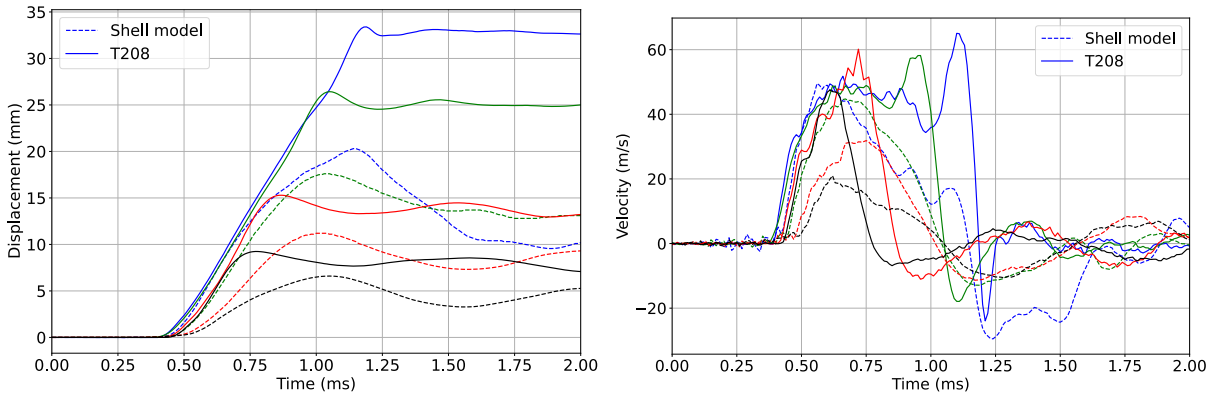

(a) (b)

Figure 5.47: a) Displacement and b) velocity for the shell plate model compared to Test 208 at the midpoint (blue), 50 mm (green), 100 mm (red) and 125 mm (black) across the plate.

The reason that the plate does not receive the later loading from the velocity wave can be explained by looking at the behaviour further out from the centre. As discussed in the experimental section, the velocity wave is thought to be caused by the loading from the edge of the plate propagating towards the centre. In the experiment, the plate initially responded uniformly to the loading from the explosion, seen by the similar initial velocity across the plate. This suggests the blast wave from the explosion is almost planar in shape when it arrives at the plate. This makes sense because with the charge of 25 g being 650 mm away from the target plate, the scaled distance is 2.09 m/kg$^{1/3}$ and the explosion is not near-field. In the numerical model, the velocity of the plate at 125 mm from the centre is less than half that of the experiment. Pressure readings were taken in the air mesh located just in front of the plate, and the pressure at the edge of the plate was 10% of the pressure at the centre. Also, the blast wave arrival is delayed at the edge compared to the experiment. These findings suggest LS Dyna cannot fully model the behaviour of this charge shape. The magnitude of the blast wave is believed to be correct at the centre, but the loading is curved and reduces considerably as you move out from the centre. LS Dyna has been seen to have trouble with modelling cylinder charges before, as seen in Rigby et al. (2018).

The velocity contour plots in Figure 5.48 show the velocity across the plate's surface for the experiment and the numerical model at five timesteps. These graphs support the findings discussed above that the initial response of the plate in the experiment is uniform and staggered in the model, time = 0.55 ms. Later in the experiment, the velocity wave can be seen progressing towards the centre, the red band on the contour plot, but this is not evident in the numerical

model.

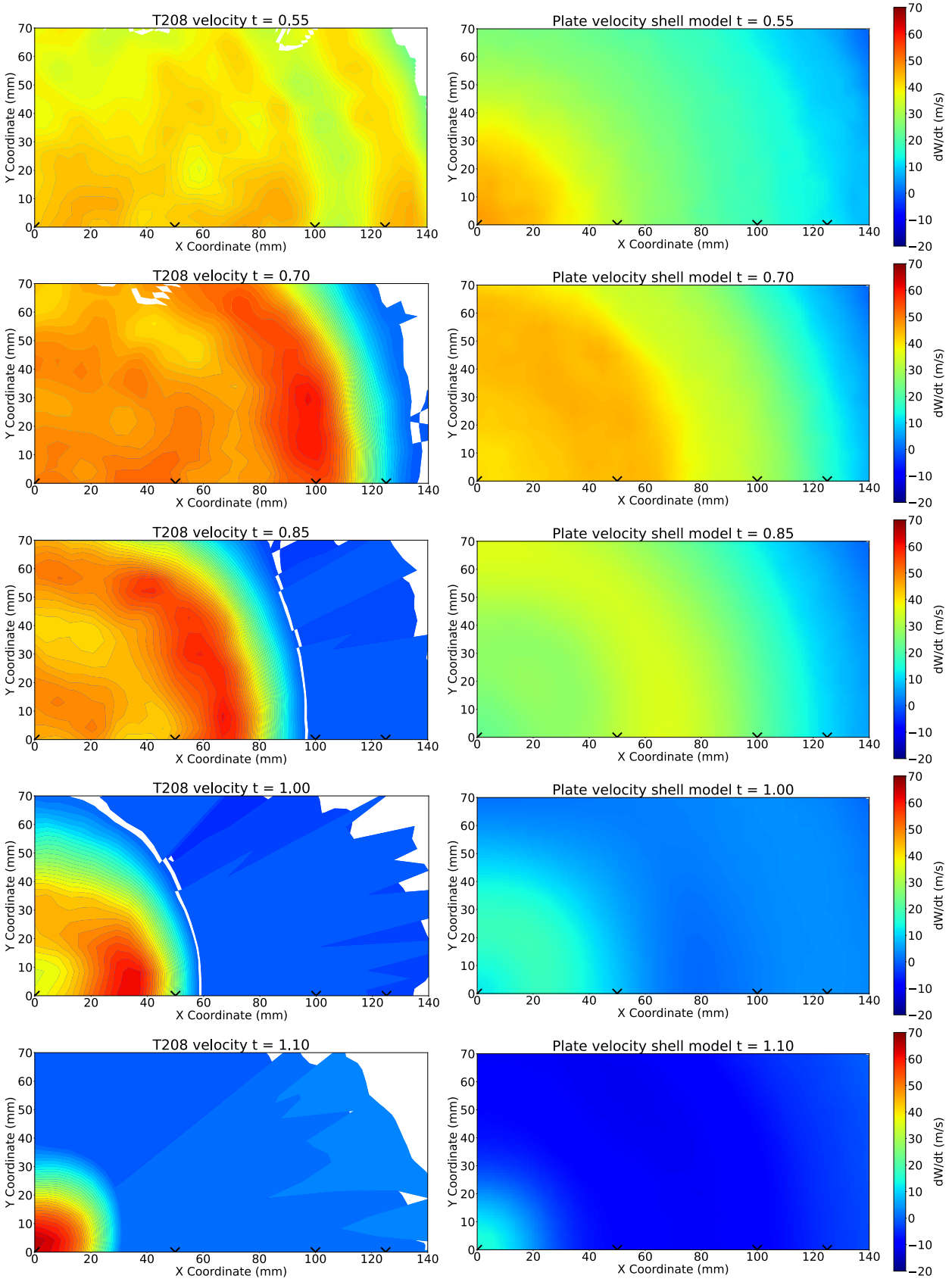

Figure 5.48: Velocity for a quarter of the plate for the shell plate model compared to Test 208.

5.5.4 Final Model Set-up

A different approach was taken to model the explosion to improve the numerical model. As the blast wave can be assumed to be almost planer at this stand-off distance and the initial velocity of the plate agreed well at the centre of the plate, the central pressure was used as a point load across the plate. A separate model with an ALE air domain with a reflective boundary at 650 mm from the charge, recording the pressure at the central element, was created to collect the pressure data. So the pressure point loading could be applied to the plate, the plate was changed to solid elements. The arrival time of this point load was staggered across the plate's width to reflect the response times in the experiments. The slight delay in the arrival time of the loading reflects the statement that the blast wave is almost planar. This was divided into three sections to reduce model complexity. Nodes between the centre and 50 mm radius were loaded at the central experimental loading time (0.39 ms). Nodes between 50 and 100 mm were loaded at the 100 mm experimental loading time (0.42 ms). Nodes between 100 mm and the edge of the plate were loaded at the 125 mm experimental loading time (0.44 ms). By applying the loading in this manner, any variations between the experiment results and the numerical model will be linked to the simulation of the plate behaviour rather than how the explosion is modelled.

The displacement and velocity results from the back surface of the target plate from the numerical model and experimental Test 208 are plotted in Figure 5.49. These results are for the numerical model with the plate simulated with solid elements and the explosion applied as load time histories to each node. Minimal variation is seen in both the displacement and velocity data at the 100 mm and 125 mm data points. The velocity data shows that the initial velocity across the plate has very low variation from the experiment. Now that the behaviour towards the edge of the plate is well simulated, the velocity wave is seen to arrive at the midpoint in Figure 5.49b. The velocity wave arrives earlier and is approximately 5% lower than in the experiment, which explains why the displacement at the midpoint and 50 mm is 7.5% lower than in the experiment. Velocity contour plots across the plates are included in Figure 5.50 for the solid plate numerical model and the experiment. These plots show that the numerical model highly correlates with the experiment across the plate.

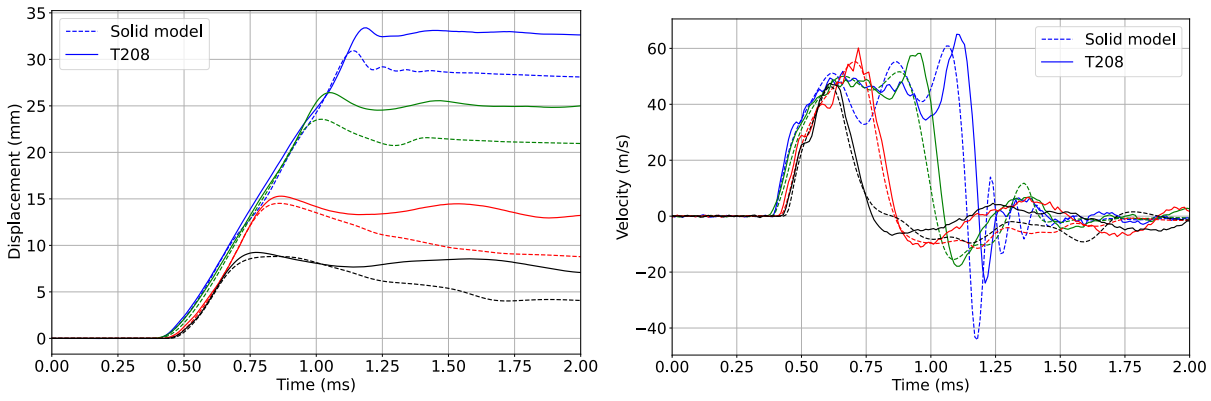

(a) (b)

Figure 5.49: a) Displacement and b) velocity for the solid plate model compared to Test 208 at the midpoint (blue), 50 mm (green), 100 mm (red) and 125 mm (black) across the plate.

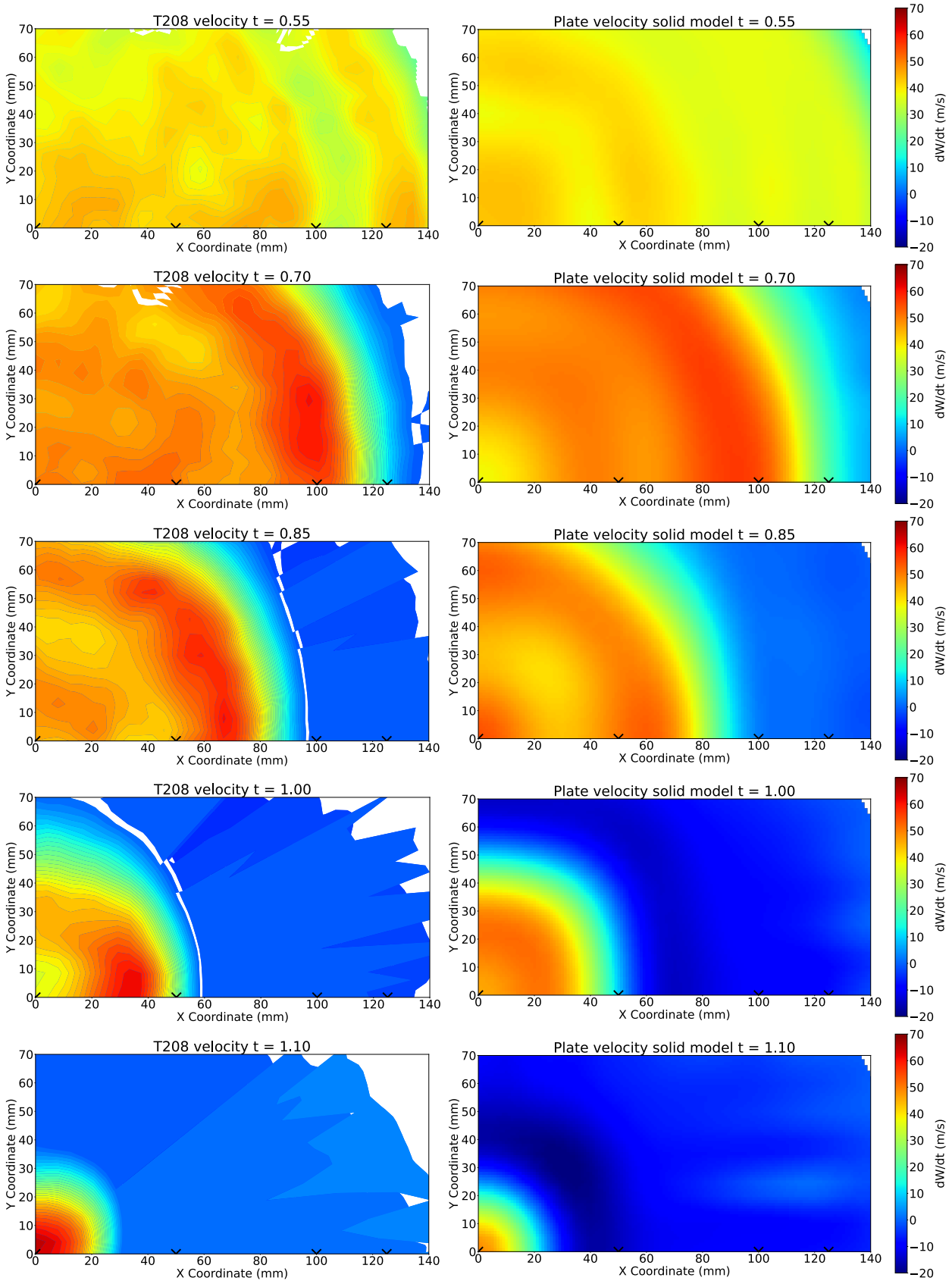

Figure 5.50: Velocity for a quarter of the plate for the solid plate model compared to Test 208.

A mesh sensitivity study was performed, investigating the effect of the number of elements on the side of the plate on the plate response and wave propagation from the boundary. The number of elements in the thickness of the plate was increased from 1 to 2, 3 and 5 elements. Figure 5.51a displays the displacement across the width of the plate for each of the models and the experimental data from Test 208. The displacement of the new models shows no variation from the original solid model up to peak transient displacement. However, the latest models improve on the original model for the post-peak behaviour. For example, at 1.5 ms, the magnitude of the displacement is closer to Test 208 by 2% at the centre, 10% at 50 mm, 14% at 100 mm and 17% at 125 mm. Also, the timing of post-peak oscillations is improved in the new models.

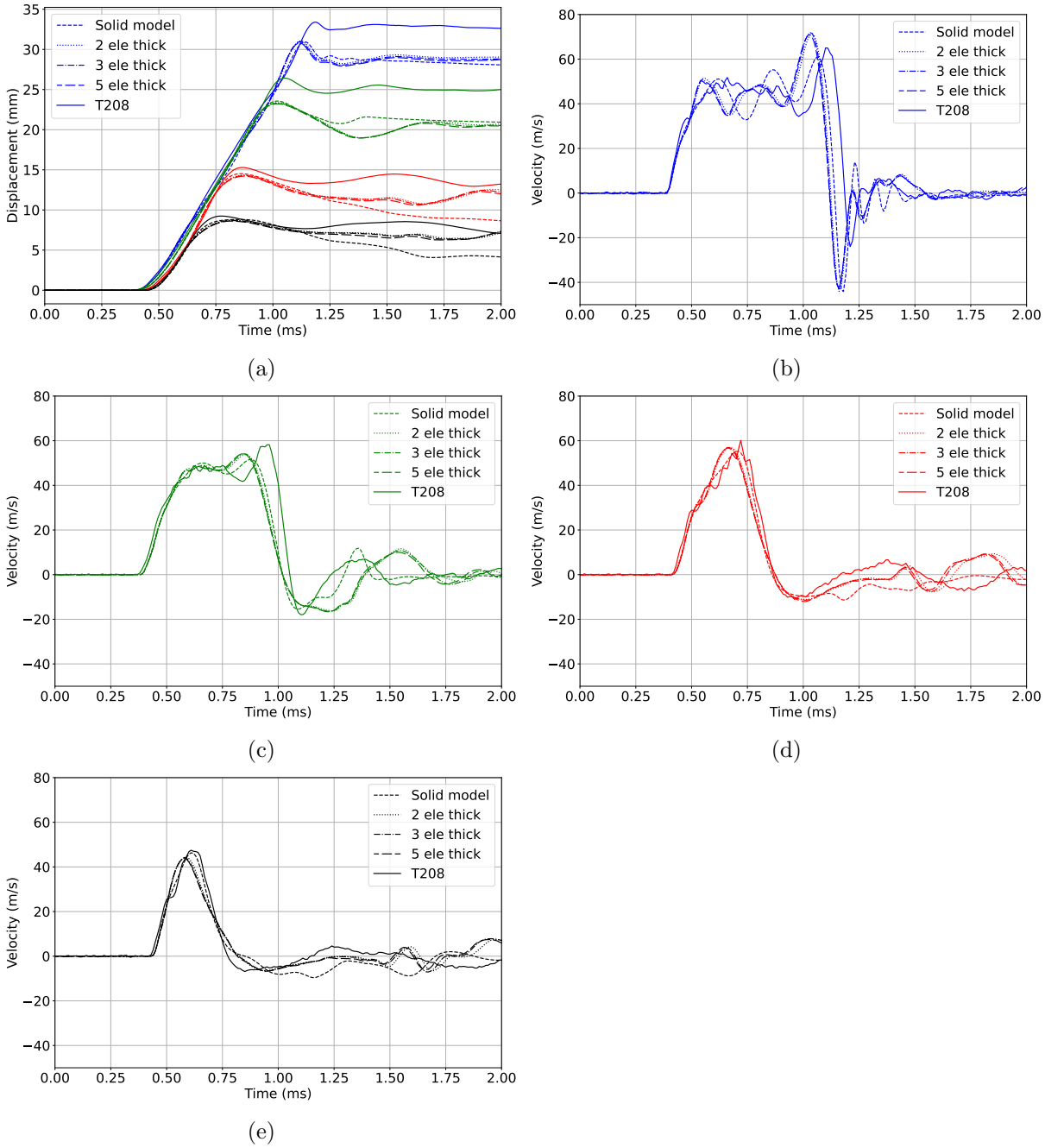

Figure 5.51: Displacement and velocity for different number of elements in plate thickness compared to Test 208 at the midpoint (blue), 50 mm (green), 100 mm (red) and 125 mm (black) across the plate.

Figures 5.51b - 5.51e show the velocity at each plate location. They display similar improvements in the post-peak oscillation behaviour of the plate, both magnitude and timing. However, the new models show deviations in the initial loading and peak response. The initial loading of the plate at 125 mm and 100 mm locations, which was modelled with minimal variation by the original model, shows 7% and 9% percentage differences from Test 208. At the centre of the plate, the initial loading peaks 12% earlier than the experiment. Also, the final peak velocity from the velocity wave arrives earlier and is 10% higher than the experiment.

As this work focuses on the initial loading from the explosion and the peak behaviour, the model will remain with one element thickness for the gelatine model. The reduced correlation of the earlier behaviour outweighs the improvements made to the post-peak behaviour. Also, no difference was seen between the 2, 3 and 5 element models.

5.5.5 Hybrid Gelatine/Aluminium Model

A hybrid gelatine/aluminium model was created and compared to the experiment where 50 mm of the gelatine was placed in front of the target plate. The solid plate model from the previous section was used for this. The gelatine mesh was added to the model below the target plate, and the glued surface nodes were tied together to simulate the glue. This method was chosen to simulate the connection between the gelatine and the plate because, at the end of the experiment, the gelatine was still glued to the plate. Also, this reduced the complexity of the numerical model. A new ALE domain with a reflective boundary at 600 mm from the charge was created to collect the pressure load curve data needed to apply the point loads to the gelatine surface. The Simplified-Rubber/Foam material model used to model gelatine in previous chapters was utilised again here. A table of load curves was created to include the data from the three SHPB experiments. The strain rates recorded for these load curves were 2200, 3000, and 4200 s^{-1}. The image in Figure 5.52 shows the addition of the gelatine mesh to the solid plate model.

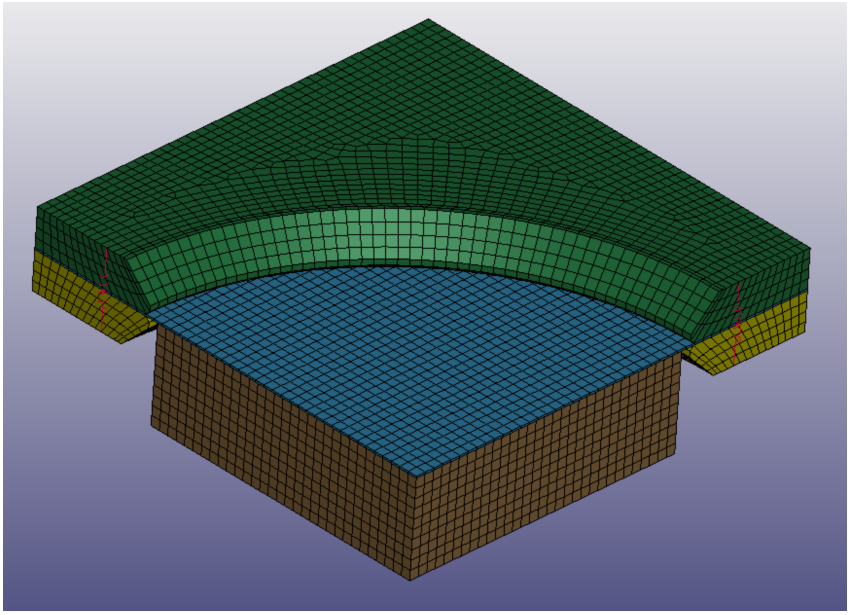

Figure 5.52: Numerical model layout with 50 mm of gelatine.

The displacement and velocity results from the back surface of the target plate from the numerical model and experimental Test 110 are plotted in Figures 5.53 and 5.54. The different colours in the figures depict different radial distances across the width of the plate. The displacement data shows how the numerical model displays behaviour similar to the experiment, with the plate displacing away from the charge and then elastically rebounding back on itself. The plate responds to the loading at a very similar time to the experiment, which means the simulation captures the time for the blast wave to travel through the gelatine well. However, the peak displacement arrived earlier and was 25% lower than in the experiment.

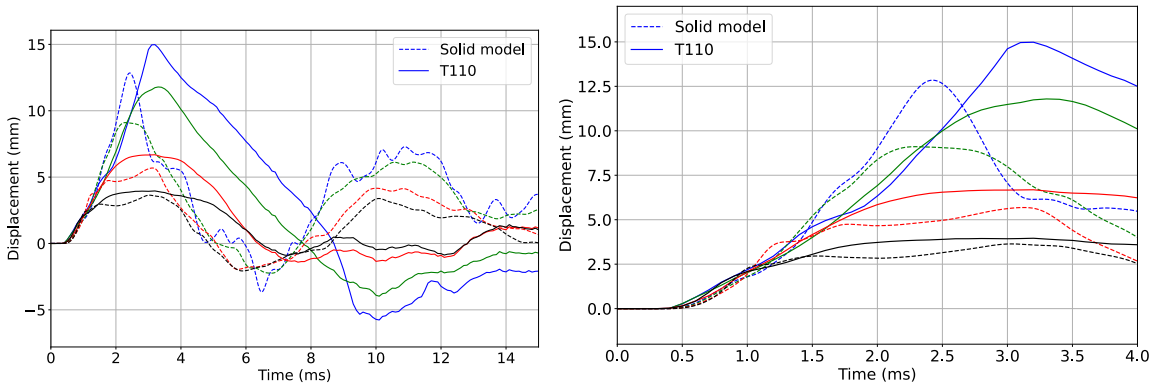

(a) (b)

Figure 5.53: Displacement for the gelatine model compared to Test 110 at the midpoint (blue), 50 mm (green), 100 mm (red) and 125 mm (black) across the plate; a) 15 ms, b) 4 ms.

Figure 5.54 display the velocity of the plate with each of the radial distances on separate graphs for more straightforward comparisons. A good correlation can be seen as the velocity oscillates, with the velocity peak at similar time steps; however, the model sometimes overestimates the magnitude. These higher velocity oscillations are likely causing the gradient of the plate displacement to be higher. The second peak in velocity at 2 ms at the centre of the plate is not sustained in the model as in the experiment, which is causing the peak displacement to be 25% lower and rebound earlier.

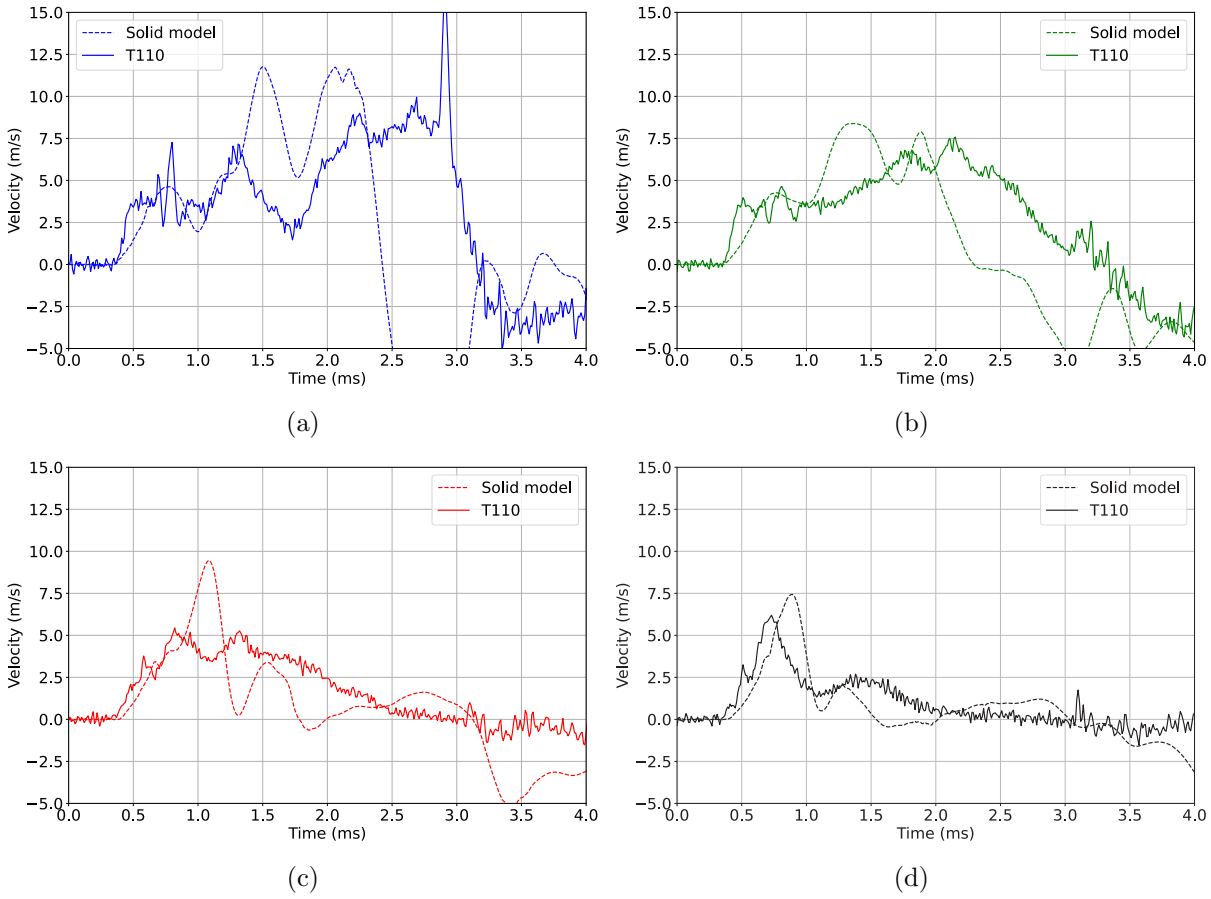

Figure 5.54: Velocity for the gelatine model compared to Test 110 at the midpoint (blue), 50 mm (green), 100 mm (red) and 125 mm (black) across the plate.

To gain some insight into how the gelatine behaves during the blast experiment, the vertical stress in the gelatine was extracted from the numerical model. Figures 5.55 – 5.56 are screenshots of stress contour data produced in LS Dyna at various time steps, displaying a side-on view of the model. Figure 5.55 shows as the explosion initially loads the gelatine, stresses propagate through the gelatine and across its width. Figure 5.56 includes images with larger time steps and shows that the stress that propagated toward the free edge of the gelatine reflects back. This stress wave propagates across the width of the gelatine back to the centre. The time that the stress wave reaches the centre aligns with the first velocity peak seen in the plate response at a time of 1.5 ms. Later, the propagation of the velocity wave from the constraint of the clamped boundary conditions can be seen in the red regions of the plate. This supports the theory stated in the previous chapter that the double velocity wave seen in the 30 mm and 50 mm gelatine experiments could be caused by stress reflected off the free end of the gelatine and propagating back across to the centre.

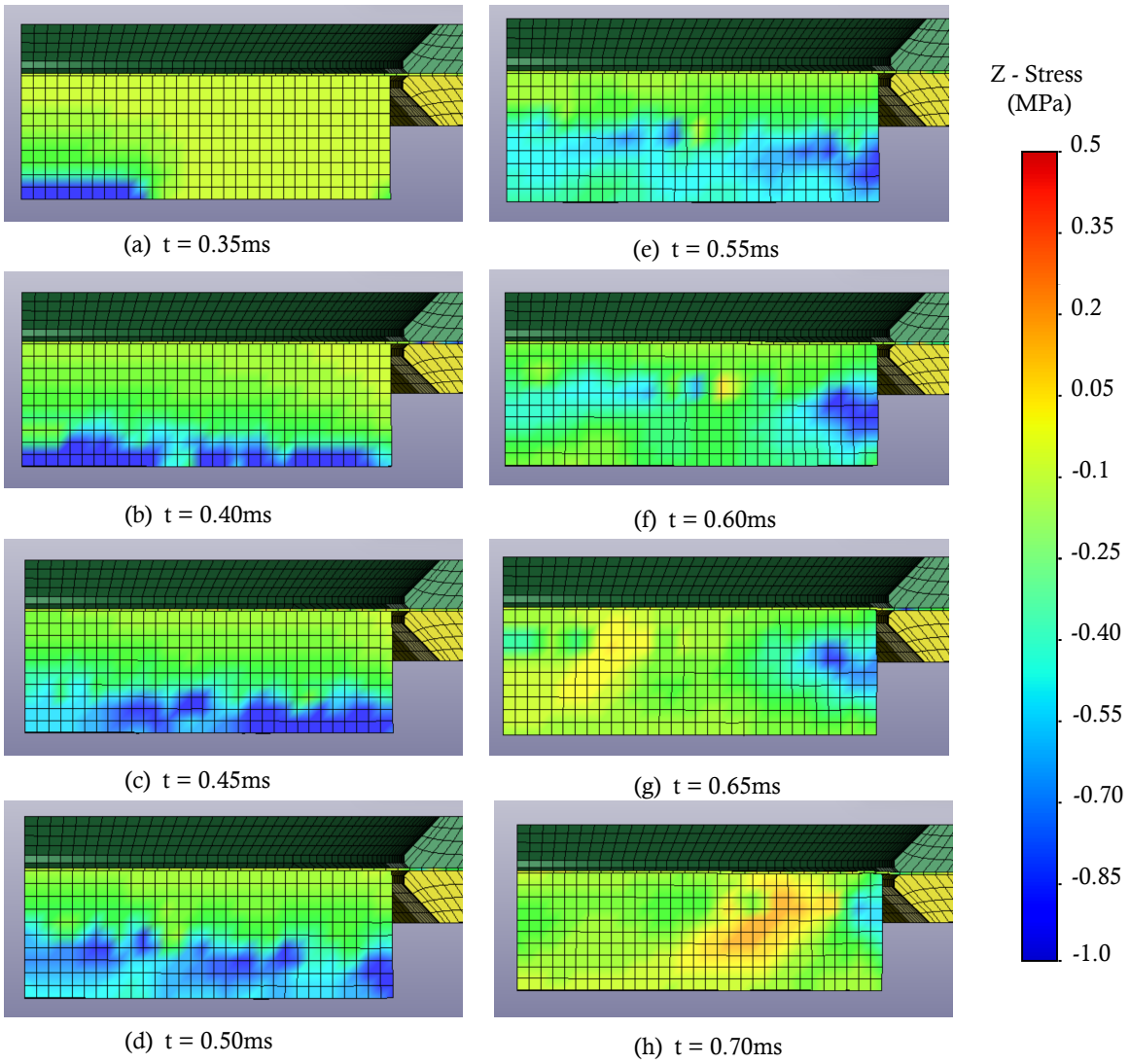

Figure 5.55: Vertical stress data from the numerical model; t = 0.35 ms - t = 0.70 ms.

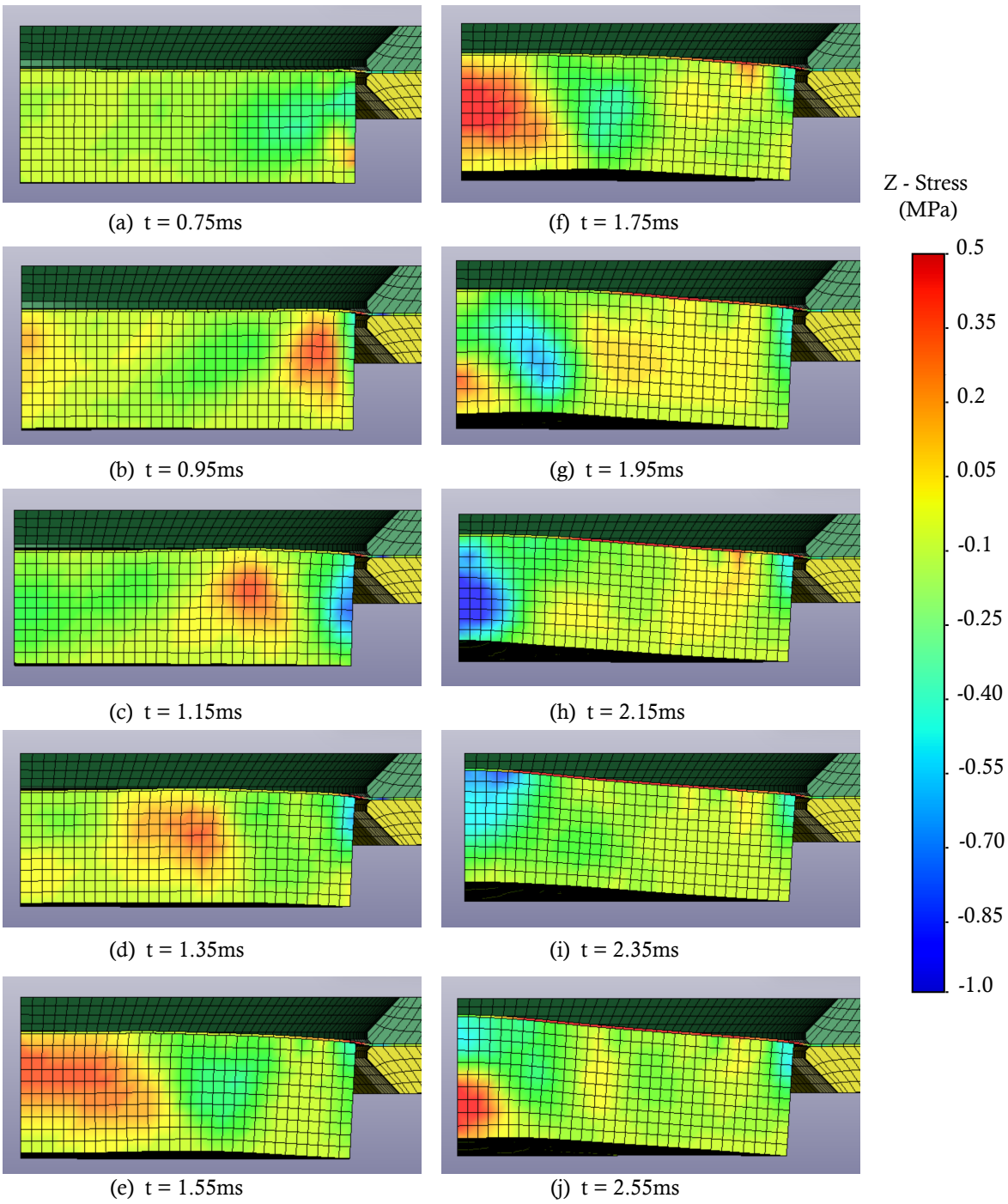

Figure 5.56: Vertical stress data from the numerical model; t = 0.75 ms - t = 2.55 ms..

5.6 Summary of Findings

In this chapter, a novel experimental setup was developed to measure the effect synthetic gelatine has on the response of a clamped plate to an explosion. This involved adapting an existing apparatus to facilitate stereo-imaging to measure the response of clamped aluminium plates. Different thicknesses of synthetic gelatine were attached to the front of these plates to determine the effect gelatine has on the loading. The addition of gelatine reduced the peak displacement and velocity of the target plate. It was also found to increase the time to peak displacement and velocity. The gelatine was found to cause a lot of oscillates of the plate long after the loading had finished, lasting over 50 ms. Efforts were made to develop a numerical model to simulate the experimental setup. The model for the bare plate set-up was found to correlate very well with the experimental data. A numerical model was created to simulate the 50 mm gelatine experiments, and similar behaviour was observed. Stresses were found to propagate across the width of the gelatine, possibly causing the complex oscillations seen in the plate velocity data from the blast experiments with 30 mm and 50 mm of gelatine. This numerical model is a step towards understanding how a blast wave from an explosion propagates through synthetic gelatine.

Chapter 6

Behaviour of Synthetic Gelatine in a Buried Explosion

Up to this point, the influence of gelatine on the response of air-blasted plates has been considered. While explosions often occur in air, many anti-personnel landmines are buried in shallow ground. As such, it would be useful to ascertain the influence of gelatine in the context of a buried charge detonation. This chapter reports results from similar tests to those in Chapter 5, but in these tests, the explosive was buried in sand at a depth of 28 mm prior to detonation. The geometry of the test plates, gelatine layers, PE4 charge and the overall stand-off distance were kept constant. The target plates and gelatine specimens were manufactured the same way as they were for the previous free air experiments; however, only bare plates and 50 mm gelatine plates were tested. The 25 g PE4 charge was buried in 5% moisture content Leighton Buzzard sand to simulate a landmine, Figure 6.1. This soil was chosen because it is widely available and commonly found worldwide. Great care was taken in the soil preparation to ensure repeatable results. Preparation methods developed by Rigby et al. (2016) and Clarke et al. (2015) were used as they have been shown to produce highly repeatable results.

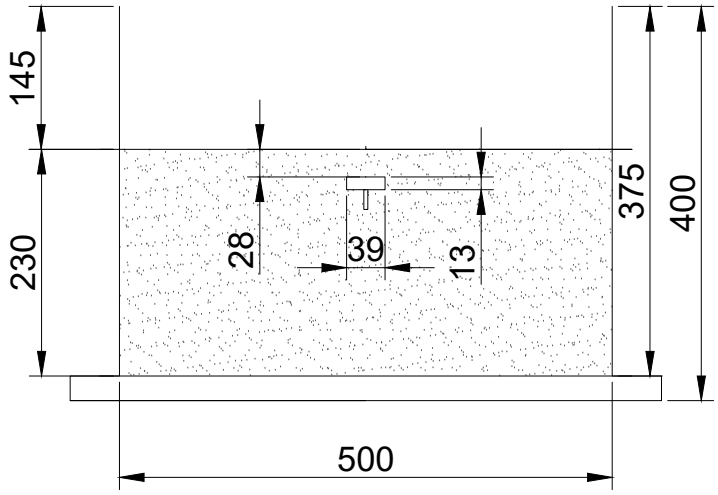

Figure 6.1: Sand bin dimensions, mm.

6.1 Soil Preparation

The sand bins for this series of tests were filled to a depth of 230 mm to achieve the required stand-off distance to the plate. The sand was prepared in two batches of 37 kg each. Firstly, 37 kg of sand was accurately weighed out and loaded into a mixer, Figure 6.2c. Next, a sample of this soil is weighed and dried to calculate the delivered moisture content. The mass of water needed to achieve 5% moisture content is calculated and added to the mixer. The mixer is allowed to run for 5 minutes to mix the sand and water thoroughly. Another soil sample was weighed and dried to check if the correct moisture content was achieved. The soil was then transferred to the sand bin and compacted to the required density of 1.60 Mg/m^3. This process is repeated for another 37 kg of sand to fill the sand bin to the required 230 mm depth. The image in Figure 6.2a shows a finished sand bin. An average moisture content of 5.01% + - 0.2% and soil density of 1.615 Mg/m^3 + - 0.025 Mg/m^3 was achieved across the 9 sand bins. The sand bins were then sealed to retain the moisture content, Figure 6.2b. Before testing, the charge is carefully buried in the sand at a burial depth of 28 mm, Figure 6.2d.



(a) (b)

(c) (d)

Figure 6.2: Photos of the sand bin preparation process; a) finished sand bin, b) sealed sand bin, c) mixing the sand, d) positioning of the charge.

6.2 Experimental Process

A total of seven buried blast tests were conducted at the University of Sheffield's blast and impact laboratory in Buxton. These tests comprised of four bare target plate tests and three tests with 50 mm of synthetic gelatine on the target plate. A table detailing all the tests conducted in this test series is shown in Table 6.1. As in Chapter 5, two high-speed cameras were used to record the back surface of the target plates. For each test, 10,000 images were captured at a frame rate of 100,000 frames per second, which allowed data to be recorded across the plate every 0.01 millisecond. The cameras were triggered using a break-wire that was embedded in the charge. Before the cameras were mounted, a "pop" test was conducted to ensure the clamped target plate would not fail due to the loading from the soil and damage the cameras. A third camera was positioned side-on to the test apparatus to record the explosion. This third camera allowed the break out of the soil and the arrival of the shock wave/soil ejecta to be captured. The data obtained from the side-on camera was used to interpret some of the full field transient displacement and velocity data obtained using DIC from the stereo-imaging of the target plate.

A dummy target plate with a crosshair on the centre was used to align the DIC cameras and set the focus, prior to each experiment, to ensure that the images were sharp. The calibration board from Correlated Solutions was held where the target plate would be to calibrate the cameras, and a series of images were captured on both cameras. The best results were achieved when the calibration board was positioned in multiple directions, such as by slightly tilting the angle of the board. This process was repeated each time the equipment was set up to ensure high-quality images of the testing were recorded.

The charge was buried shortly before testing. A forklift positioned the sand bin first and then positioned the clamped target plate as done in Chapter 5. Once the clamped target plate was bolted in place, final adjustments were made to the position of the sand bin using a laser level to ensure the charge was centred under the target plate. Great care was taken with the charge positioning to increase the repeatability of the experiment.

Test Type	No.	Explosive Type	Charge Mass (g)	Stand-off Distance (mm)	Buried depth (mm)	Gelatine Thickness (mm)
Bare Plate	4	PE4	25	650	28	0
Gelatine 50	3	PE4	25	650	28	50

Table 6.1: Test series for the buried blast experiments.

The third side-on camera was used to confirm the arrival time of the shock wave and the soil ejecta. This information gave insight into some of the behaviours seen in the DIC data. The camera was positioned side-on to the test apparatus with a view of the sand bin and the side of the clamping frame. An example of the camera view can be seen in Figure 6.3. The background in the raw image is the grass bank behind the apparatus. A zebra board was not available for this testing setup. The camera was triggered by a breakwire from the explosion and recorded at 80,000 frames per second. This resulted in a time step between images of 0.0125 ms, and a total of 256 frames were saved to give roughly 3 ms of video.

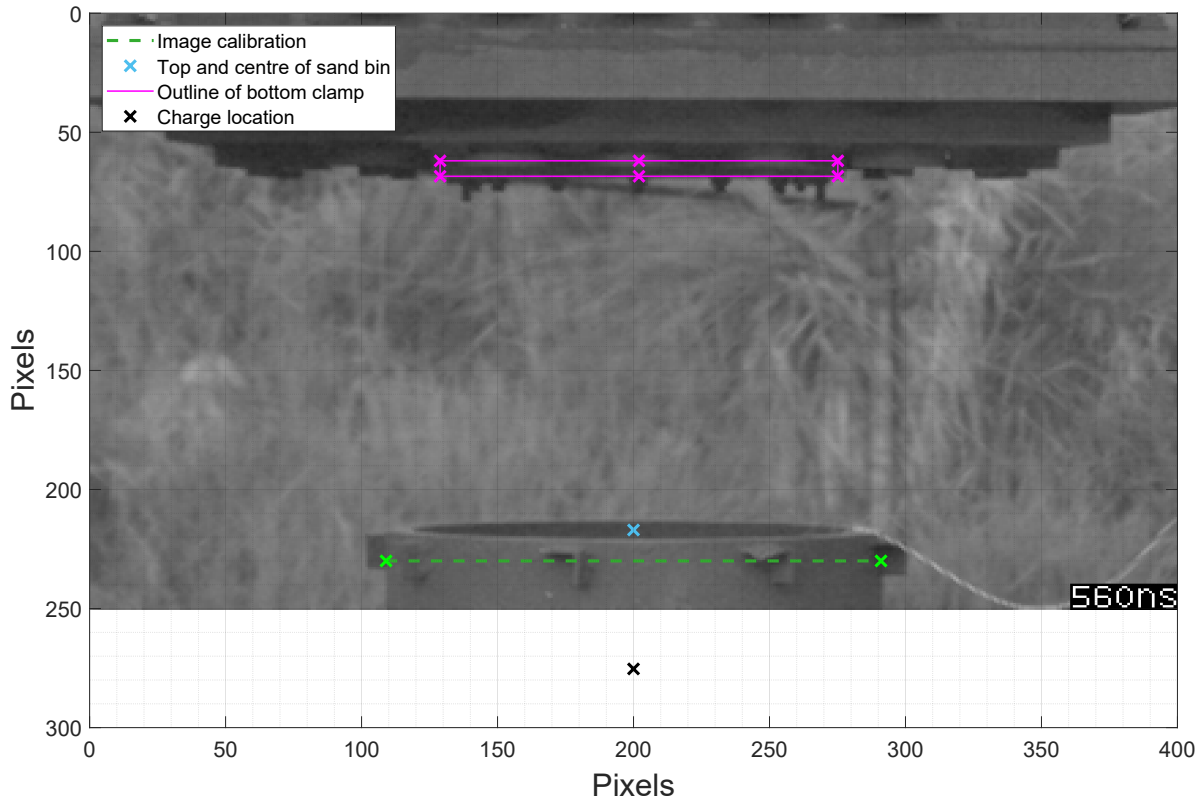

Figure 6.3: Image showing calibration points used to measure pixel size.

Before the arrival of the shock wave or soil could be tracked, distances in the image need to be calibrated to the pixel size. The width of the sand bin was used to calculate the size of a pixel in millimetres, as the position of this was clear in the image and in line with the charge and plate. Firstly, the x-pixel position of the sand bin edges is determined from the image, green crosses in Figure 6.3. Next, the sand bin width (560 mm) is divided by the number of pixels between the edges of the sand bin. This information was then used to mark on the image the location of the bottom clamping frame. This was done by taking the centre and top of the sand bin and using the relative stand-off distance to the clamp to determine the pixel position of the clamp. The outline of the bottom clamp is included in Figure 6.3 and lines up well with the clamp bolts seen in the image. A similar approach was taken to locate the position of the charge in the image, as indicated by the black cross in Figure 6.3. Now that the position of the clamp is determined, the arrival time of the shock wave and soil can be found by seeing when the two cross paths.

6.3 Experimental Results

6.3.1 Bare Plate Tests

After the high-speed camera images have been processed, the displacement and velocity data across the surface of the plates can be explored. Figures 6.4 & 6.5 display an example of the out-of-plane displacement of a bare target plate for the buried charge tests. Figure 6.4 shows the out-of-plane displacement profile across the plate as it rises to its peak displacement at four different time steps. The plate increases to its peak transient displacement at the centre of the plate similarly to the free air experiments.

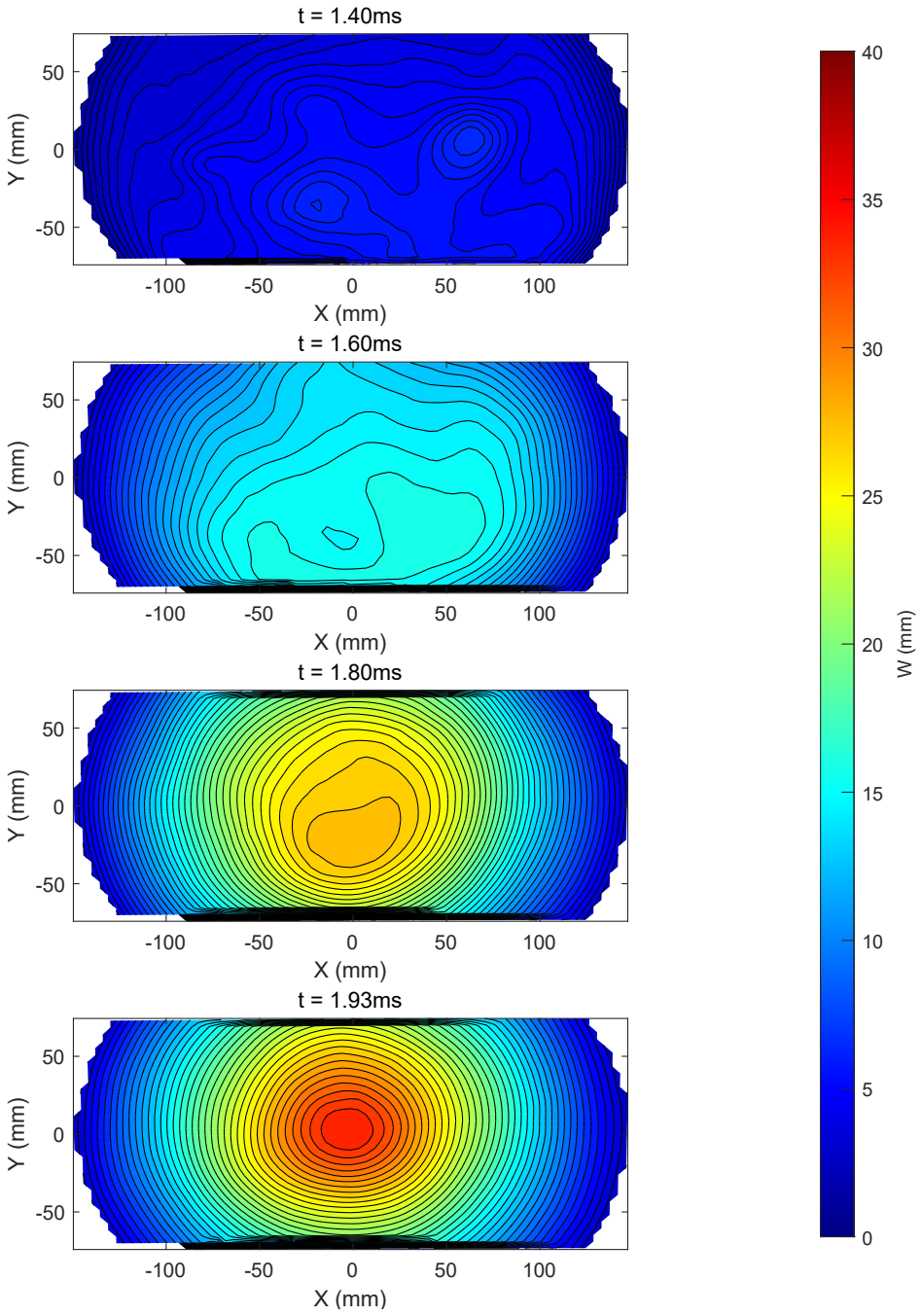

Figure 6.4: Full plate displacement for a bare plate for a buried charge.

The line slices taken of the target plate at each time step are plotted together on the contour graph in Figure 6.5a. The figure focuses on the plate's movement in the first 1 to 3 ms after detonation. This figure shows how the plate is initially loaded uniformly and then rises to its peak displacement at the centre of the plate. Figure 6.5b shows a side-on view of the plate as it rises to its peak displacement. After the initial uniform loading (up to 1.3 ms), the plate starts to ripple at a coordinate of approximately -25 mm. This was thought to be caused by the soil loading after the shock wave. The out-of-plane displacement at the centre of the plate is plotted in Figure 6.6 for each bare target plate tested. Figure 6.6 displays an initial gradual rise, increasing in gradient as the plate is fully loaded. Test-to-test repeatability is good, but there are some variations in the arrival time.

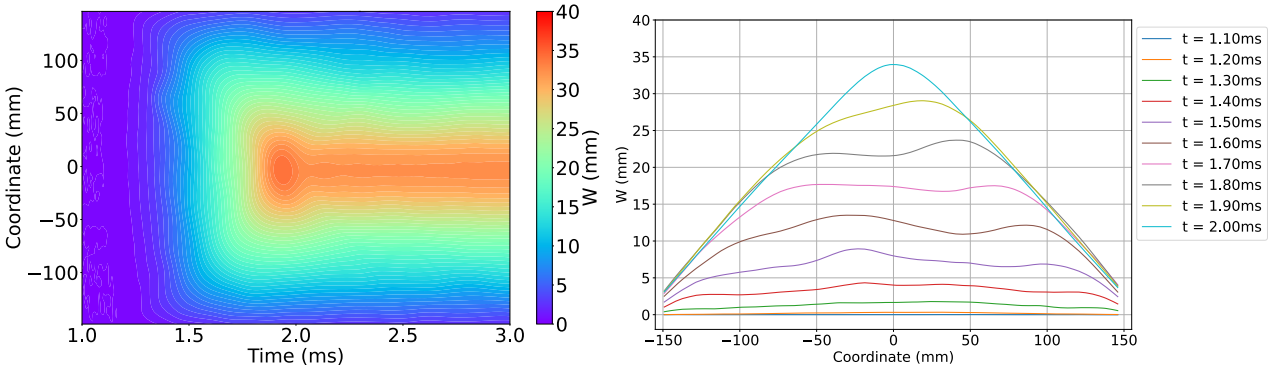

(a) (b)

Figure 6.5: Displacement over time of a bare plate for a buried charge.

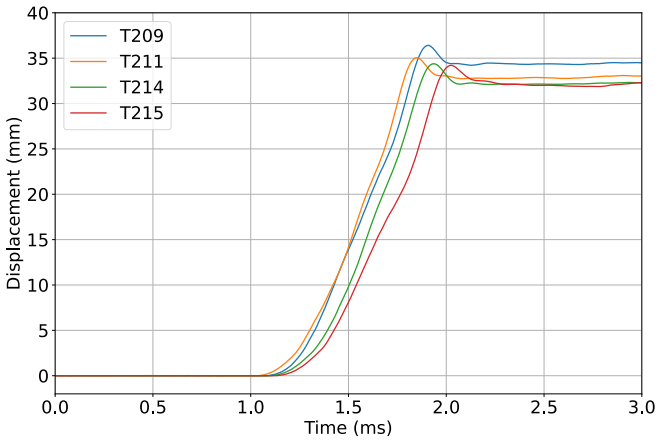

Figure 6.6: Midpoint displacement for a bare plate for a buried charge.

Figure 6.7a illustrates how the plate is initially loaded uniformly and then experiences a higher velocity across the plate that oscillates. This second loading is thought to be from the soil ejecta that arrives later than the shock wave. The plate reaches a peak velocity at the centre of the plate. The figure also shows how the target plate rebounds after the peak velocity, demonstrated by the negative velocity on the graph. Figure 6.7b shows the velocity at the plate centre for each test and shows good repeatability. The data depicts a sudden rise in velocity as the explosion initially loads the plate. This sudden rise has two distinct parts with different gradients. This velocity then oscillates until the centre of the plate receives another sharp increase in velocity. Shortly after the peak velocity, a sharp decrease in velocity is seen as the plate decelerates.

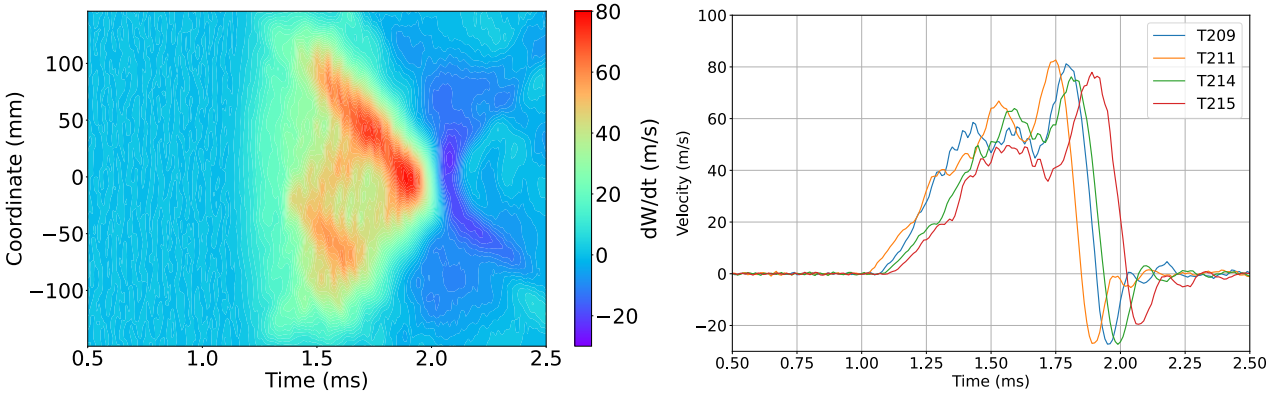

(a) (b)

Figure 6.7: a) Velocity over time and b) midpoint Velocity of a bare plate for a buried charge.

6.3.2 50 mm Gelatine Tests

Figures 6.8 - 6.11 display an example of the displacement for a target plate for the buried charge with a 50 mm thickness of synthetic gelatine glued to the front face. The contour graphs depicted in Figure 6.8 illustrate the out-of-plane displacement of the back surface. The images to the left show a rise in displacement to its peak at the centre (t = 3.70 ms). On the right, the figure shows how the target plate elastically rebounds after reaching its transient peak displacement. However, there was not enough momentum to pull the centre through, leaving it in the opposite direction from the rest of the plate.

Figure 6.9 show line slice data taken across the width of the plate. It illustrates how the target plate travels away from the charge uniformly, reaching its peak transient displacement at the middle of the plate. The elastic rebound of the target plate is displayed in Figure 6.9b. The plate continues to travel towards the charge, slowly inverting the plate. However, the centre of the plate does not fully invert when it reaches its minimum transient displacement at a time equal to 12.7 ms. The final position of the plate is shown by the black line with a positive displacement of 10 mm at the centre.

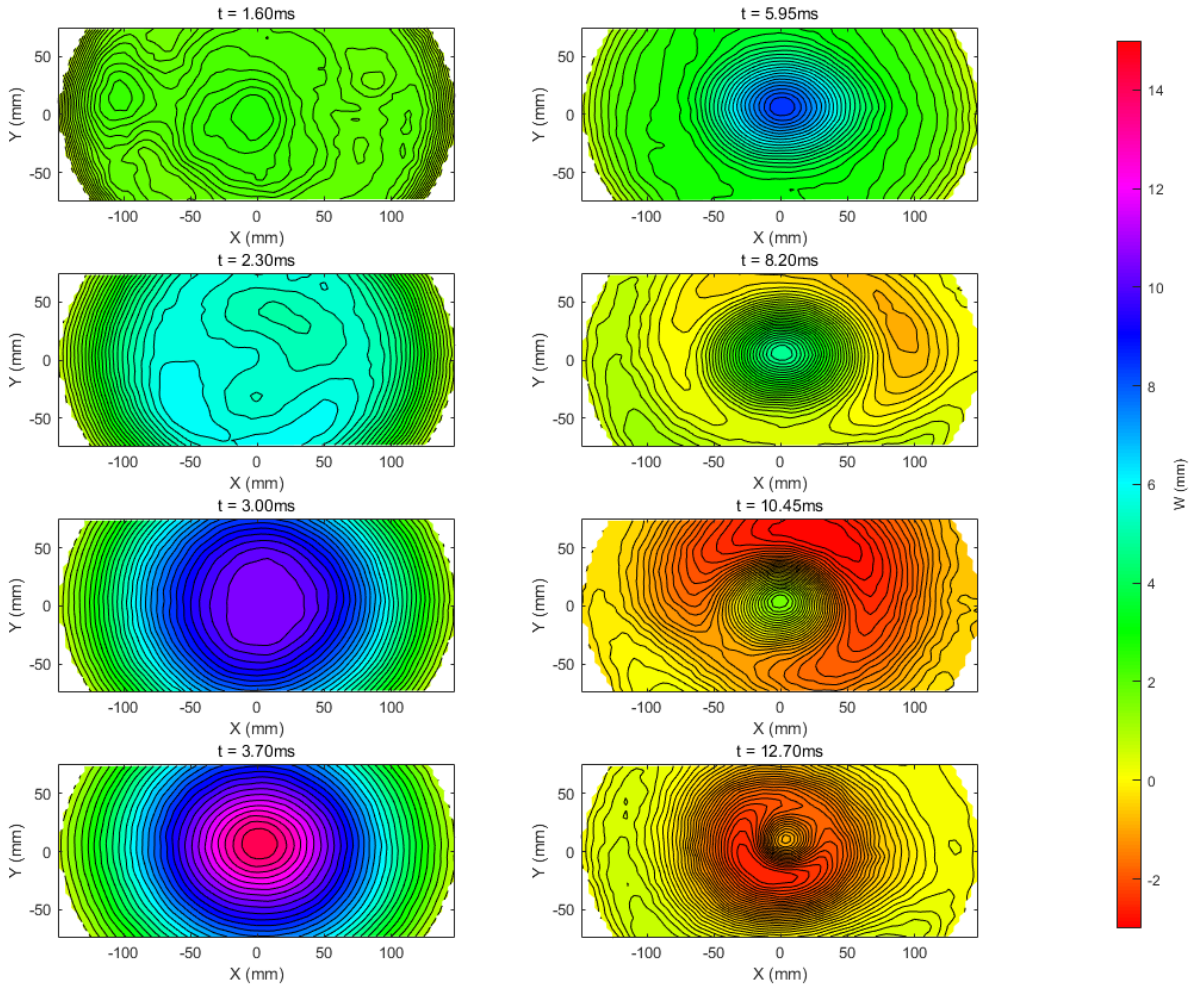

Figure 6.8: Full plate displacement for a plate with 50 mm of gelatine in front for a buried charge.

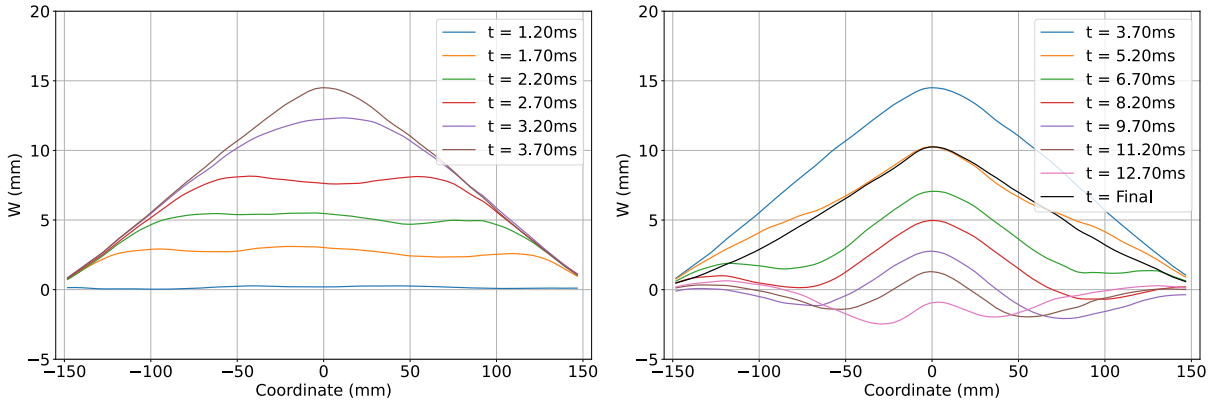

(a) (b)

Figure 6.9: Plate displacement profile of a plate with 50 mm of gelatine in front for a buried charge.

Figure 6.10 displays the displacement across the plate for the first 15 ms of the response, whereas Figure 6.11 shows the response for the full 100 ms recorded. Figure 6.10 clearly shows the movement of the plate as the explosion loads it and highlights the maximum and minimum transient displacements at the centre of the plate. The data in Figure 6.11 shows how the plate continues to move after reaching its minimum transient displacement. At a time of roughly 70 ms, the plate starts to translate upwards, resulting in its final displacement shape.

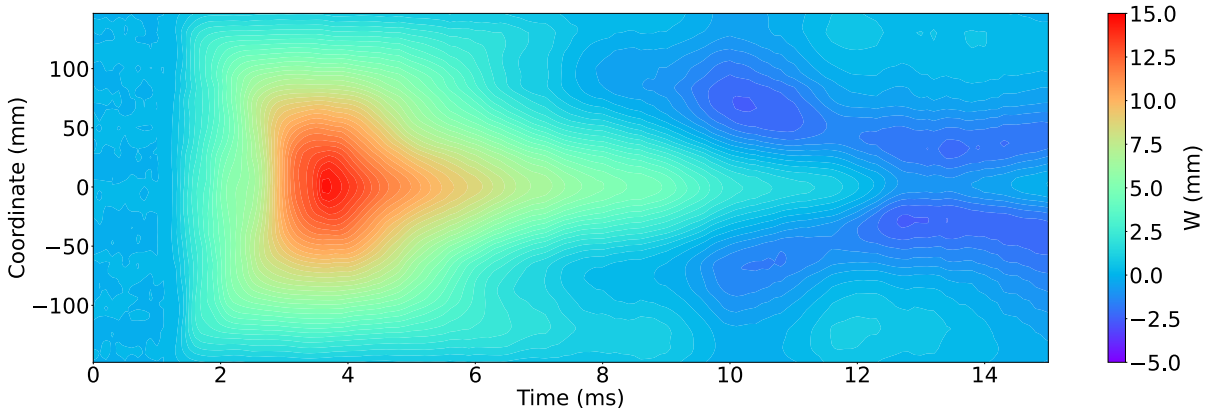

Figure 6.10: Displacement over time of a plate with 50 mm of gelatine in front for a buried charge, 15 ms.

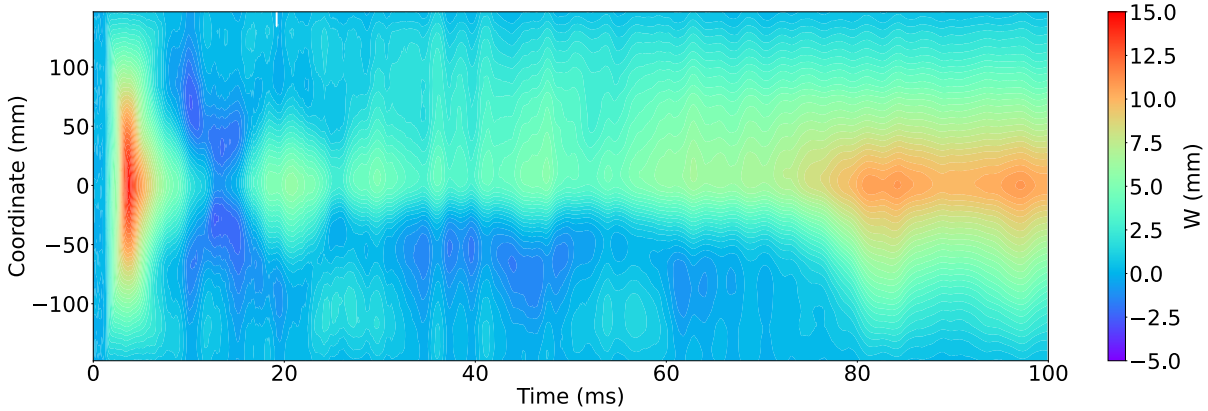

Figure 6.11: Displacement over time of a plate with 50 mm of gelatine in front for a buried charge.

The out-of-plane displacement at the centre of the plate is plotted in Figure 6.12. Figure 6.12a shows the displacement of the plates for the first 15 ms of the response and displays fairly repeatable results with similar peak transient displacements at the centre. Figure 6.12b shows how the plates start to diverge from each other after 20 ms, showing large variates in the midpoint displacements. Tests 202 and 213 display similar responses from 20 ms to 100 ms but are mirror images of each other, whereas Test 210 records a higher minimum transient displacement and minimal movement between 20 ms and 100 ms.

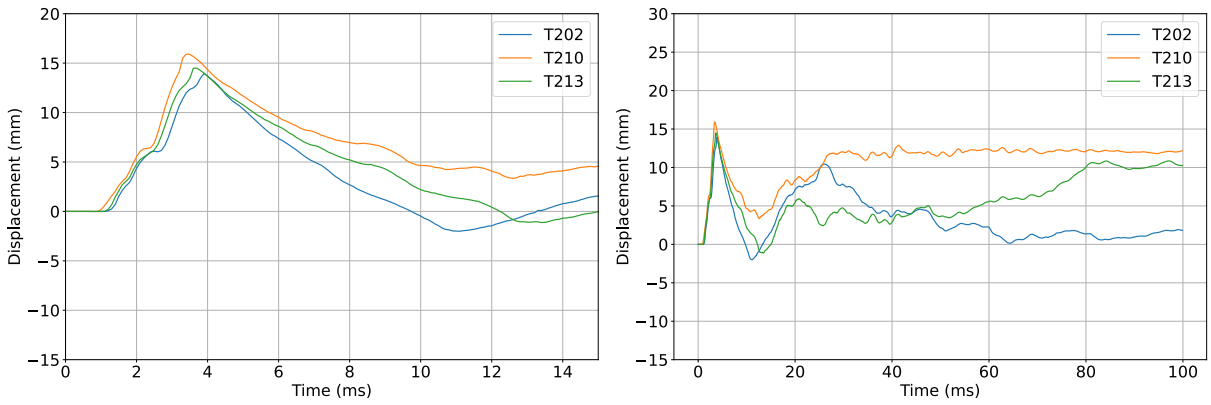

Figure 6.12: Midpoint displacement for a plate with 50 mm of gelatine in front for a buried charge.

Figure 6.13 shows the velocity across the width of the plate and illustrates how the plate is initially loaded fairly uniformly and then experiences high velocities at the centre and edges, which oscillate. The plate reaches a peak velocity at the centre of the plate, which is spread across 0.5 ms. There is a gap of 0.5 ms before the plate receives a second sharp rise in velocity, and shortly after, the target plate rebounds, demonstrated by the negative velocity on the graph. Figure 6.14 shows the plate velocity at the centre for each test. The figure shows a sudden rise as the explosion loads the plate. The velocity-time histories are fairly similar for all three tests with gelatine. There are small differences in the times of initial rises and when the sharp second peak occurred, but the overall shape was similar.

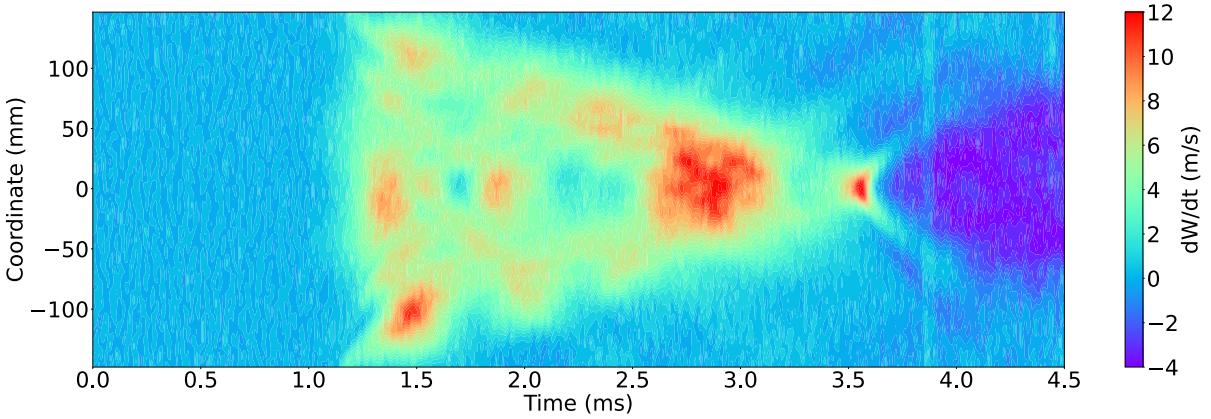

Figure 6.13: Velocity over time of a plate with 50 mm of gelatine in front for a buried charge.

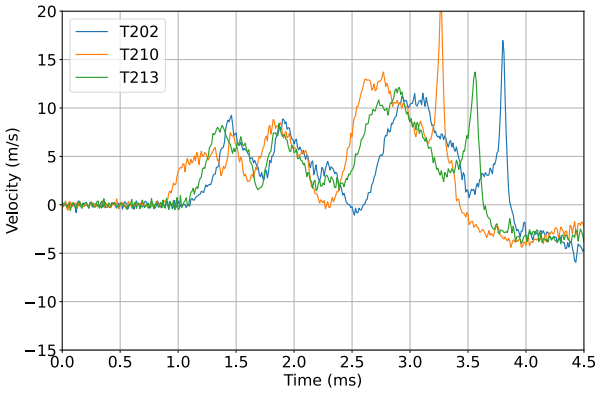

Figure 6.14: Midpoint velocity of a plate with 50 mm of gelatine in front for a buried charge.

6.3.3 Shock Wave and Soil Ejecta Tracking

The image difference method was used to track the movement of the shock wave from the third side-on camera (Farrimond et al., 2022). This worked by calculating the difference between the greyscale pixels in each time step. This produced a grid for pixel data for each time step where lighter pixel colours indicated movement in the image. Hence, the shape of the shock wave and the soil particles were highlighted when the image was plotted, Figure 6.15. The shape of the shock wave was determined by extracting several data points from the image and fitting a polynomial curve to them. The results of this method can be seen in Figure 6.16, where the shock wave had been mapped out at a time of 1.113 ms for Test 215. At this time step, the shock wave has passed the bottom face of the clamp and is close to arriving at the plate.

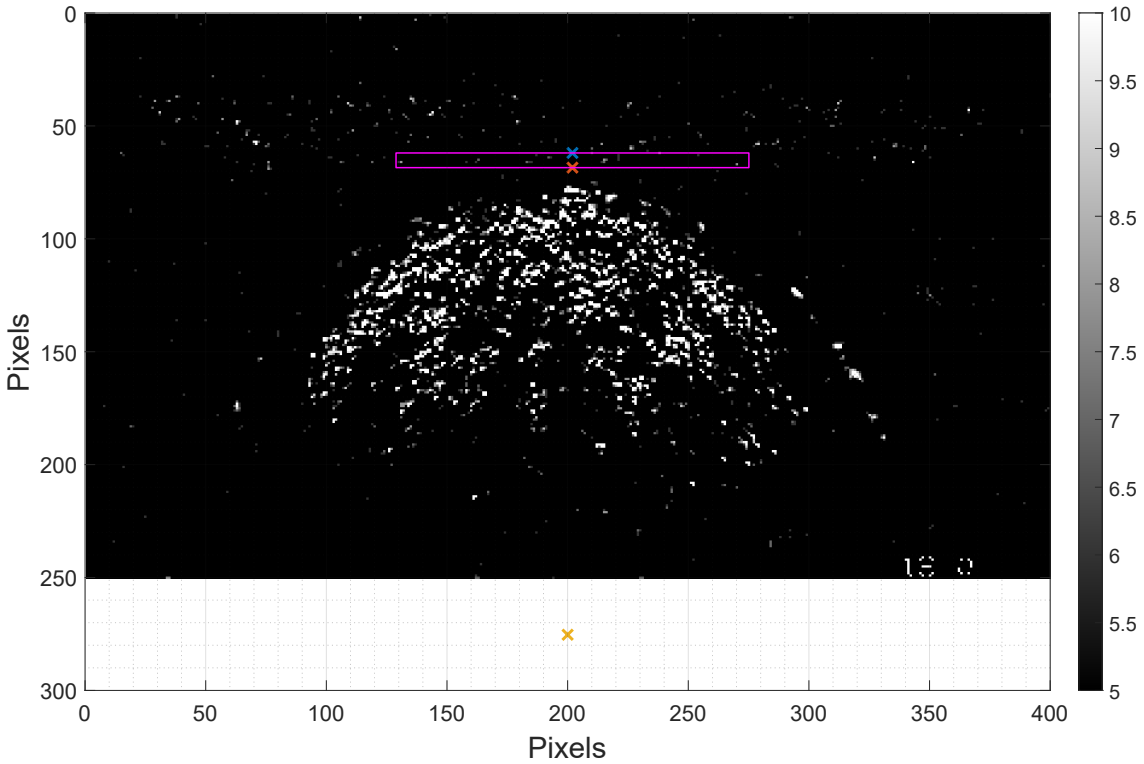

Figure 6.15: Image difference plot where the lighter pixel correspond to movement in the video.

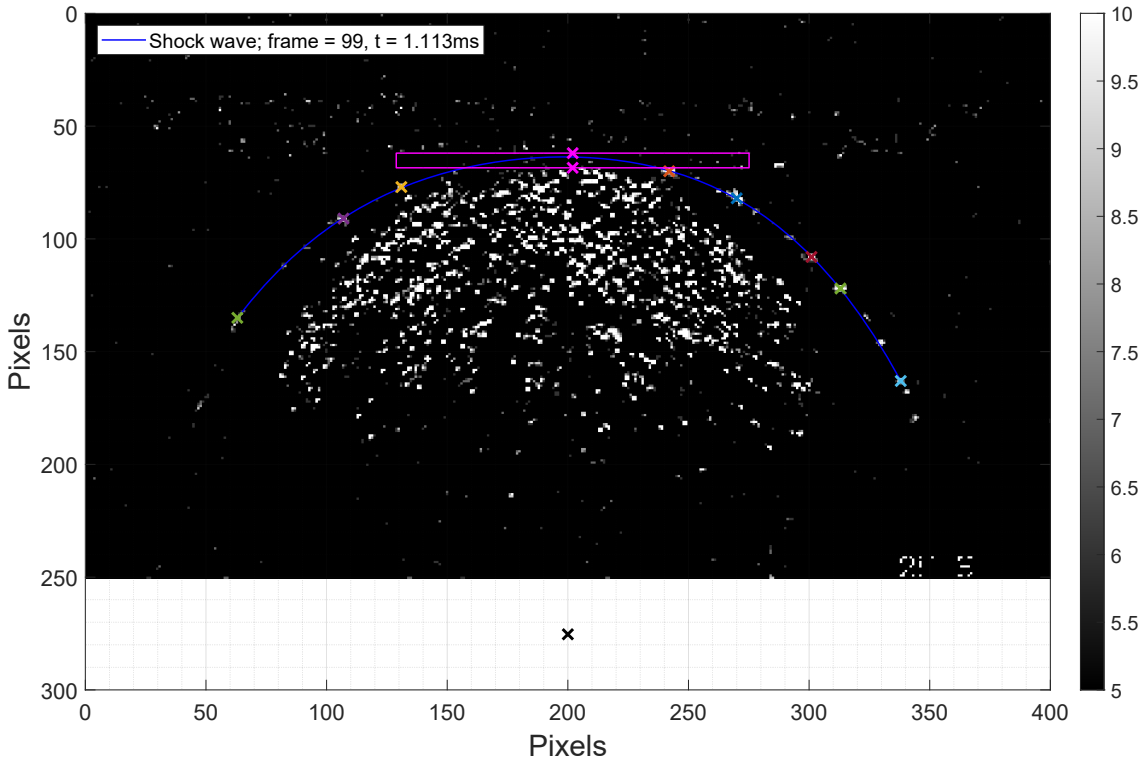

Figure 6.16: Image difference plot with polynomial of the shock wave at t = 1.113 ms for Test 215.

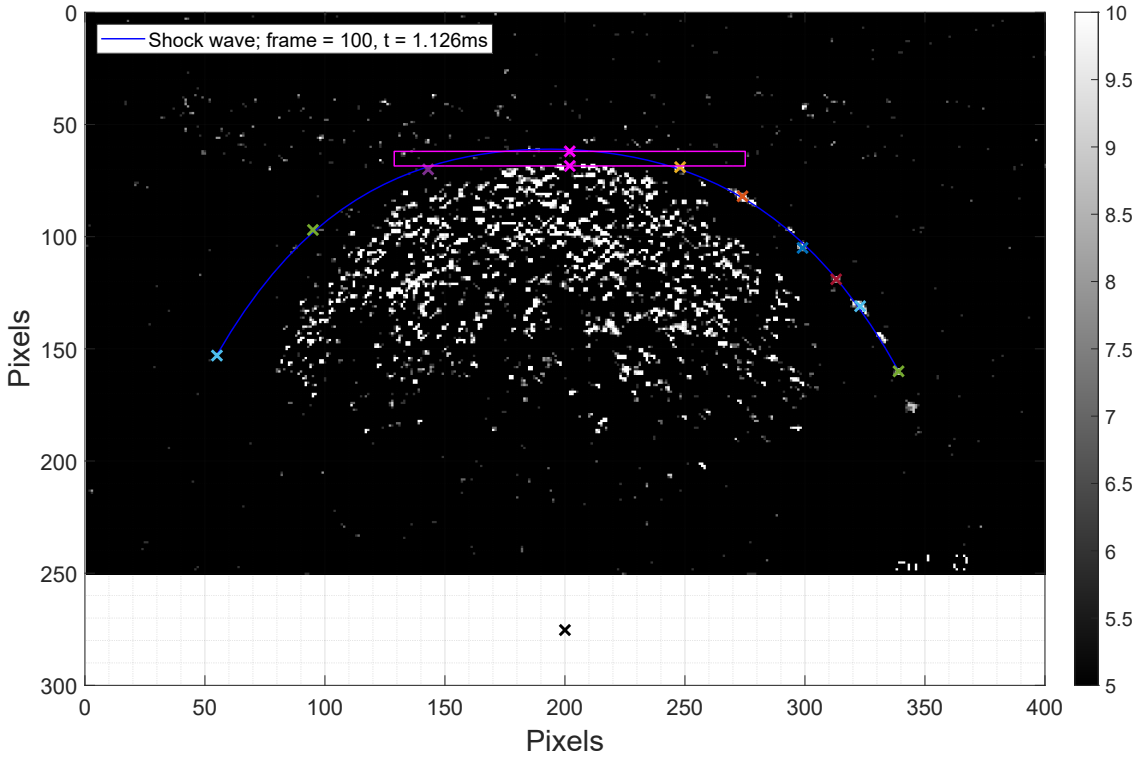

Figure 6.17: Image difference plot with polynomial of the shock wave at t = 1.126 ms for Test 215.

The same approach was applied to the next time step of t = 1.126 ms, Figure 6.17, where the plotted curve of the shock wave has passed the surface of the plate, indicating the shock wave has hit the plate by this point. This information was compared with the data recorded from the back surface of the target plate, and the arrival times were closely aligned with each other, see Figure 6.18a.

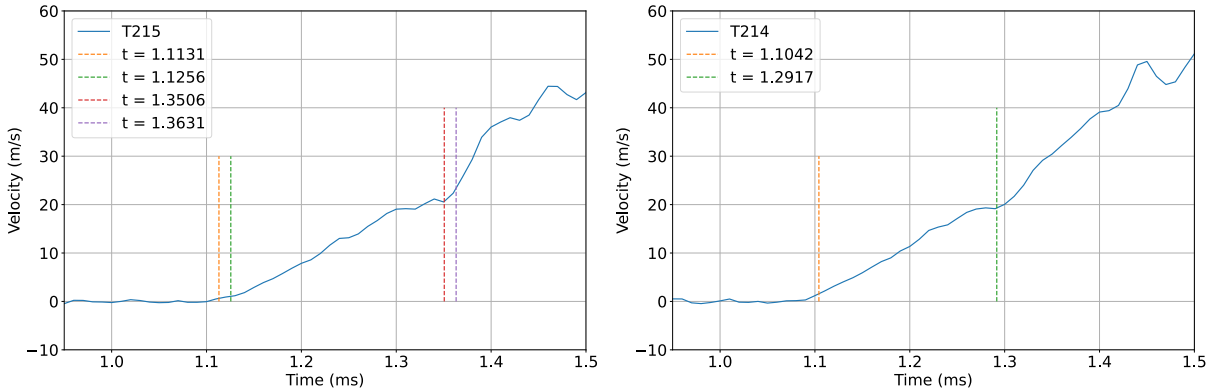

Figure 6.18: Midpoint velocity for Tests 215 and 214 with the arrival time of the shock wave and soil ejecta indicated.

The next step was to determine the arrival time of the soil ejecta and see if this time explained any behaviour indicated by the DIC signal. However, the same method used to visualise the shock wave could not be used to view the soil ejecta front. This is because when the explosion accelerates the relatively dry soil, some particles break out of the main mass of ejecta. These particles are picked up on the image difference plot, causing the edge of the main body of soil to not be visible. This is evident when the raw image is compared with the image difference plot for the shock wave arrival, Figure 6.17 and 6.19. The image difference plot in Figure 6.17 appears to show the soil arriving at the bottom clamp; however, by viewing the raw image in Figure 6.19, we see that these light parts are caused by individual particles that have separated from the main body of soil. The front of the main body of soil is visible in the raw image as darker areas, with the top at this time step being approximately y = 90 pixels. With this in mind, the curve fitting process was carried out on the raw images to track the soil arrival time.

The arrival time of the soil ejecta was found to be between the time of 1.351 ms and 1.363 ms; the curve fits are shown in Figures 6.20 & 6.21. There is a level of uncertainty in the true shape of the soil front due to the method of fitting a perfect polynomial. These time steps are also plotted in Figure 6.18a, showing the midpoint velocity data of the plate. The arrival time of the soil ejecta coincides with a change in the gradient of the velocity data. This supports the theory that the two-stage loading seen in the buried DIC data is caused by the soil arriving later than the shock wave. The same process for tracking the shock wave and the soil ejecta was also implemented on Test 214, another bare plate test, and the arrival times of the shock wave and the soil are plotted on the midpoint velocity in Figure 6.18b. This process was not performed for the other two bare plate tests as these tests were not performed with the third camera.

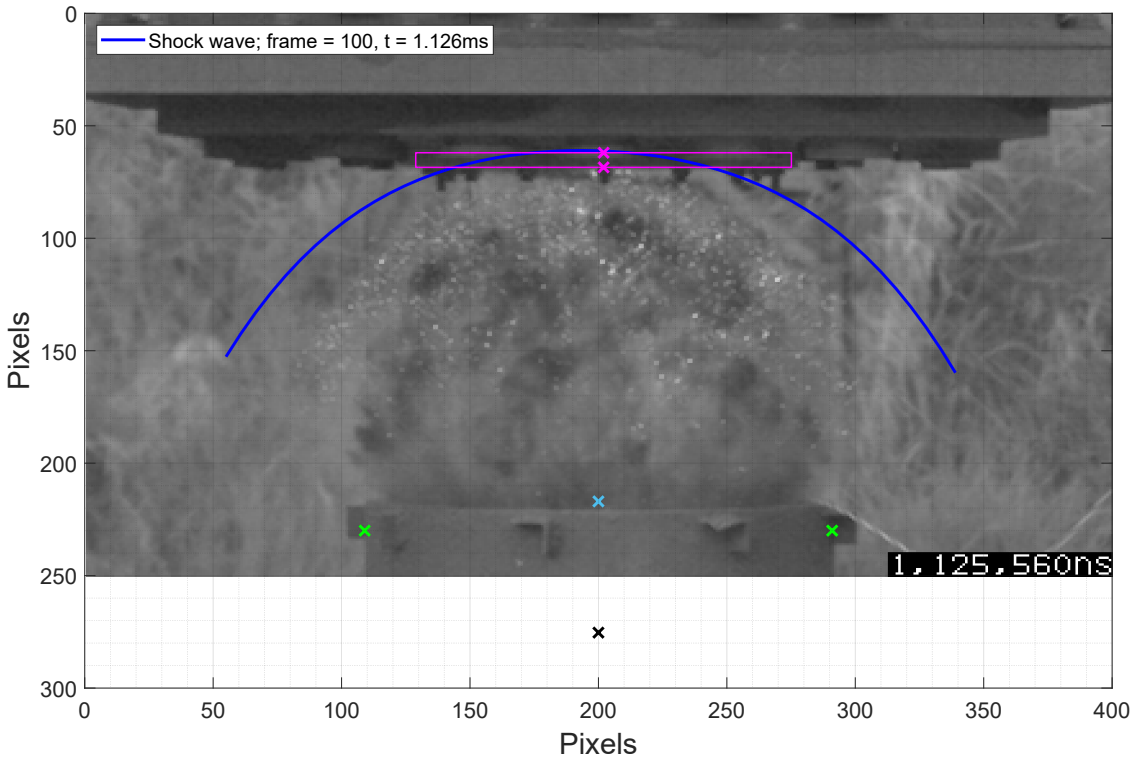

Figure 6.19: Raw image plot with polynomial of the shock wave at t = 1.126 ms for Test 215.

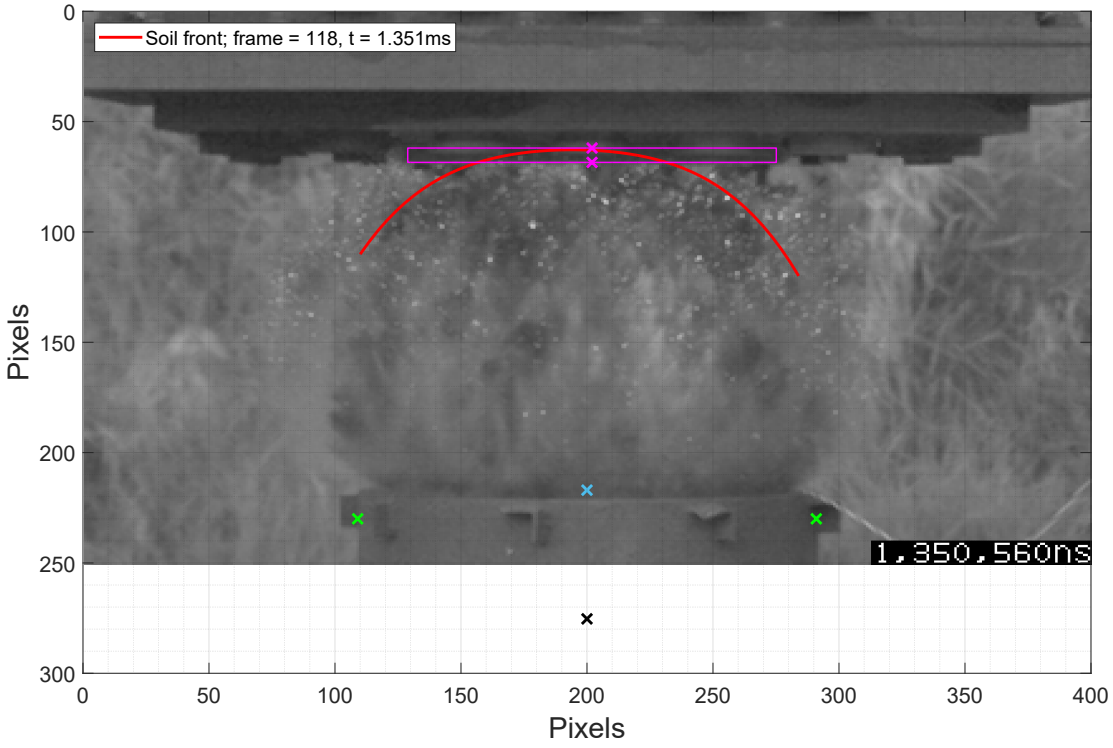

Figure 6.20: Raw image plot with polynomial of the soil ejecta at t = 1.3506 ms for Test 215.

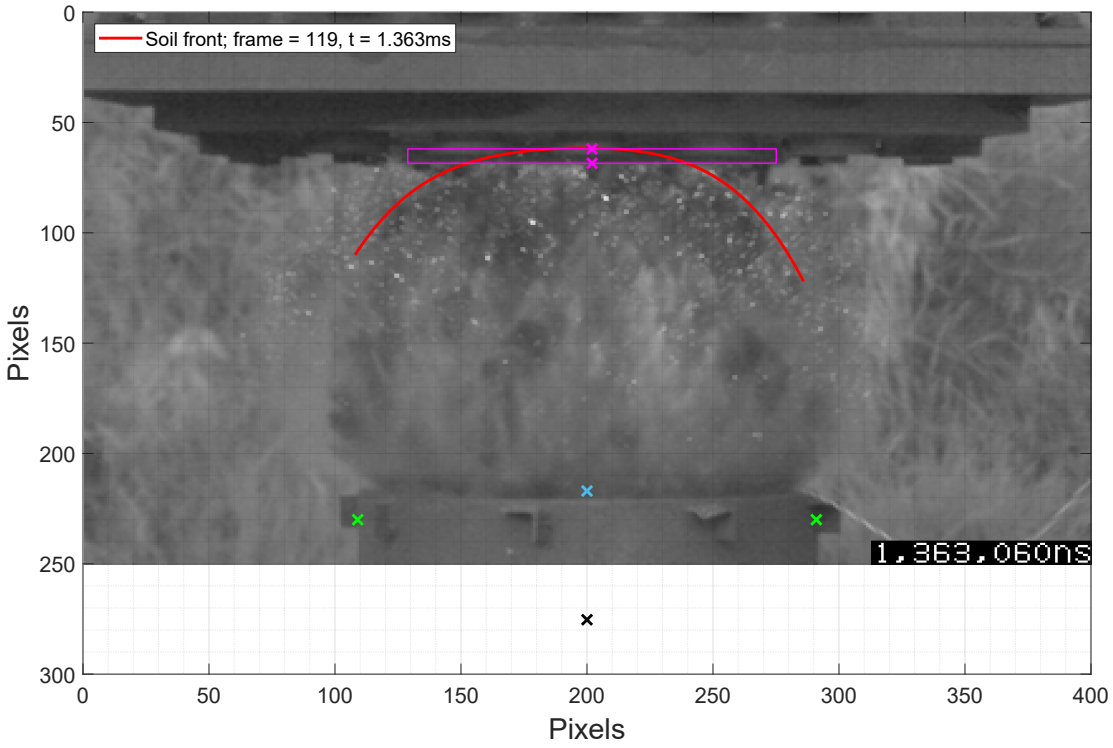

Figure 6.21: Raw image plot with polynomial of the soil ejecta at t = 1.3631 ms for Test 215.

This information about where and when the soil impacted the plate was compared to the displacement profile of the plates from the DIC data. The curve-fit data from video tracking was plotted onto the plate displacement profile. Figure 6.22 shows the plate displacement for Test 215; the x-axis is the x coordinates of the target plate, and the y-axis is the out-of-plane displacement of the plate. Plotted in red is the curve fit of the soil at a time step of 1.363 ms. The figure shows how the soil hits the plate slightly off-centre and causes a ripple in the plate profile in subsequent time steps. Figure 6.23 displays the plate displacement and soil curve fit for Test 214 and indicates that the soil's position may cause a ripple in the plate. The pixel size in the side-on video was calculated to be approximately 3 mm, which will cause some uncertainty in the position of the soil.

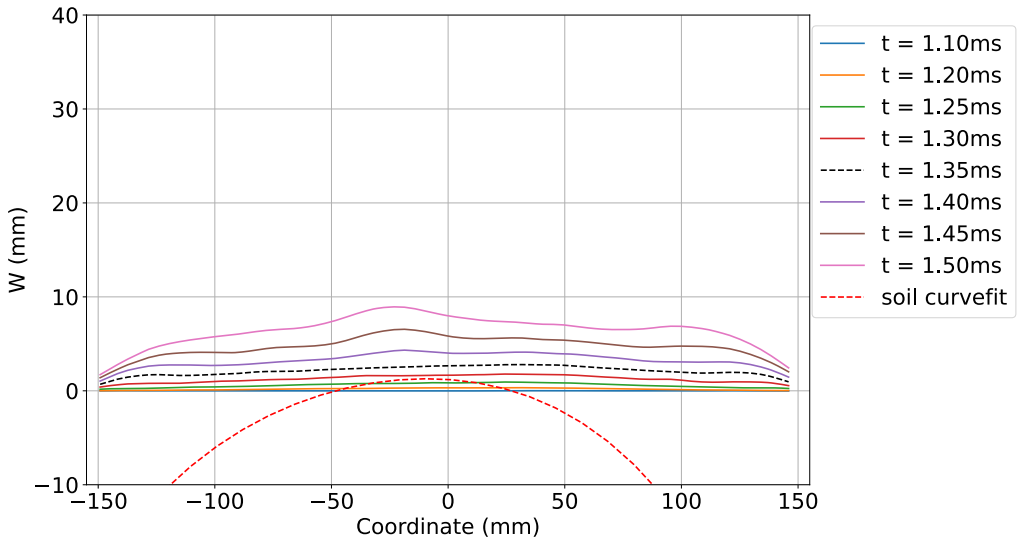

Figure 6.22: Plate displacement profiles for Test 215 plotted with the soil front curve fit at t = 1.36 ms.

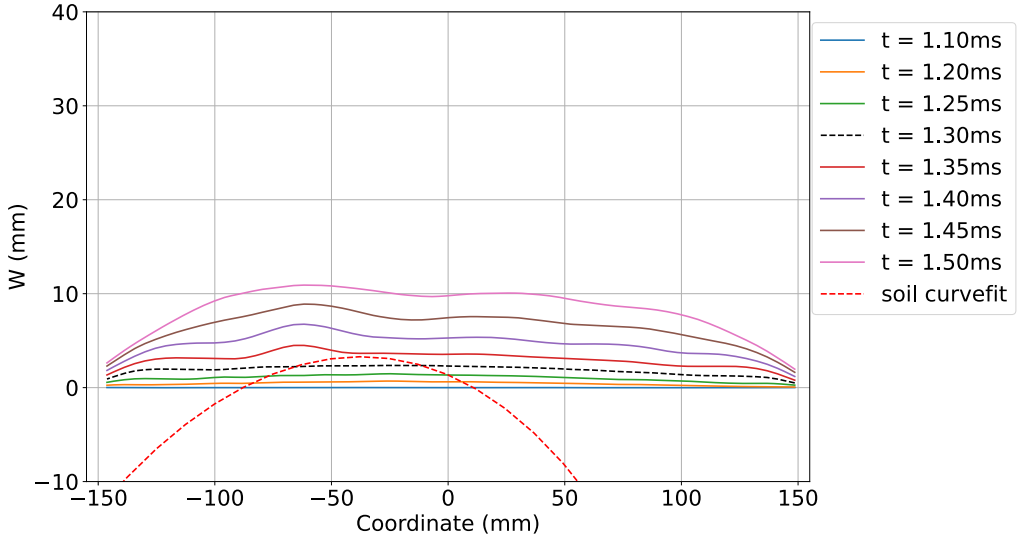

Figure 6.23: Plate displacement profiles for Test 214 plotted with the soil front curve fit at t = 1.29 ms.

For Tests 210 and 213, which had 50 mm of gelatine in front of the plate, the arrival time of the shock wave on the gelatine surface was investigated. The same curve-fitting approach was adopted here to find the arrival time of the shock wave. Figure 6.24 shows the curve fitting results for Test 213, and the shock wave curve is plotted in Figure 6.25 on the raw image where the gelatine can be seen. This time step is compared to the start of the movement from the DIC data in Figure 6.26a. There is a time difference of 0.156 ms between the shock wave arriving at the gelatine and the plate responding to the loading.

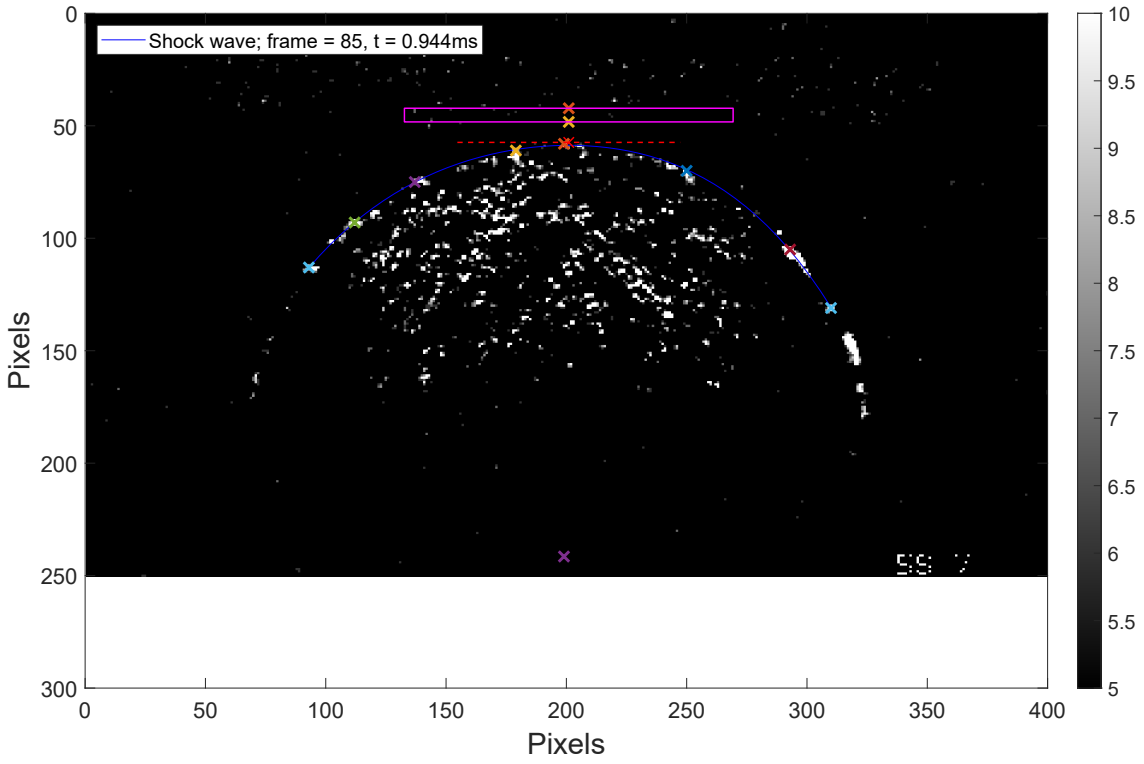

Figure 6.24: Image difference plot with polynomial of the shock wave at t = 0.944 ms for Test 213.

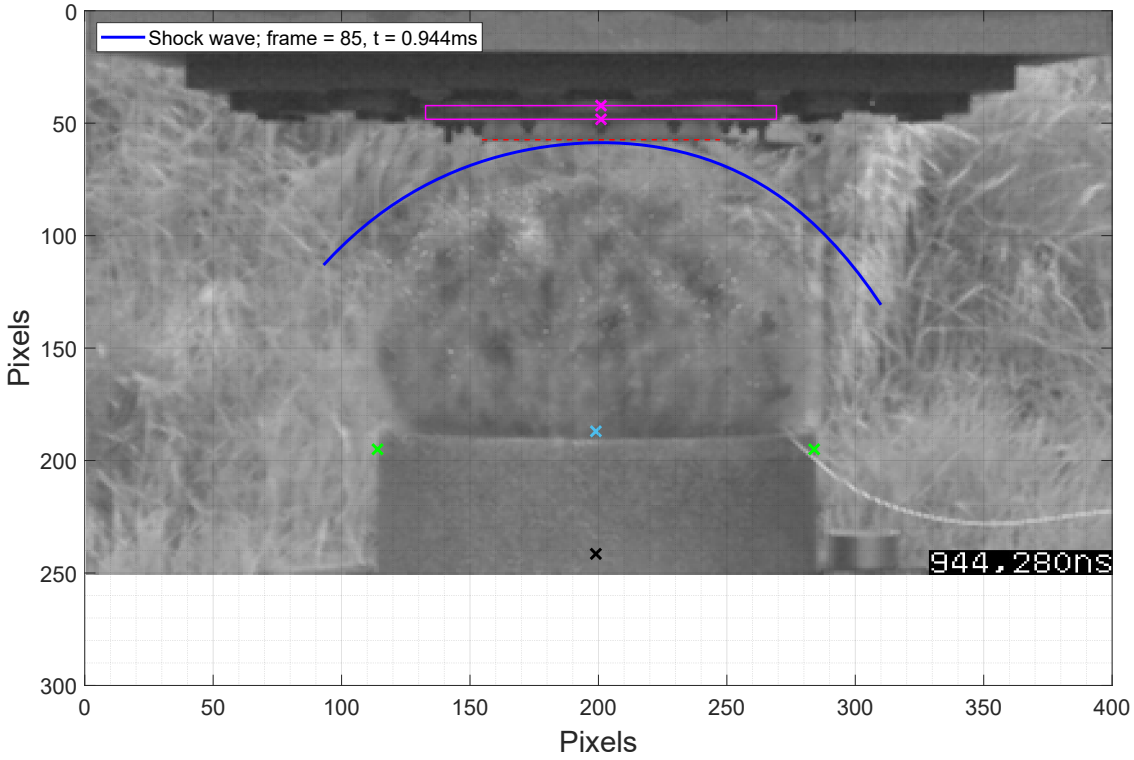

Figure 6.25: Raw image plot with polynomial of the shock wave at t = 0.944 ms for Test 213.

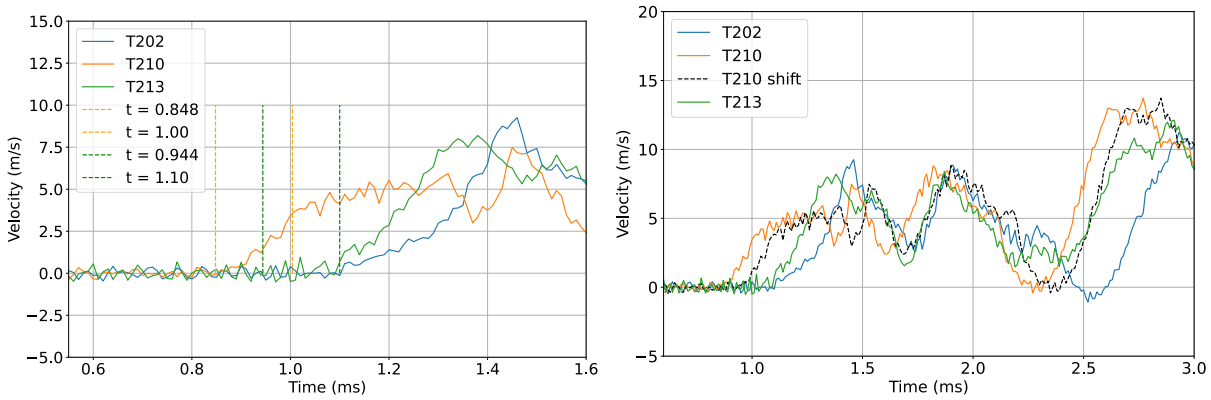

Figure 6.26: a) Midpoint velocity for the 50 mm gelatine tests with the arrival time of the shock wave indicated, b) midpoint velocity for the 50 mm gelatine tests with Test 210 shifted.

The DIC midpoint velocity data for Test 210 arrives earlier and has a different gradient from the other tests. The arrival time of the shock wave was investigated from the side-on video, and the shock wave was found to arrive on the gelatine surface at t = 0.848 ms, see Figure 6.27. If the assumption is made that there is a 0.156 ms time gap between the shock wave at the gelatine and the arrival at the plate, Test 210's arrival time should be 1.004 ms, shown in Figure 6.26a. Suppose the midpoint velocity data for Test 210 is shifted to arrive at 1.004 ms, see Figure 6.26b. In that case, the data from Test 210 aligns closer with the other two gelatine tests, following similar oscillations.

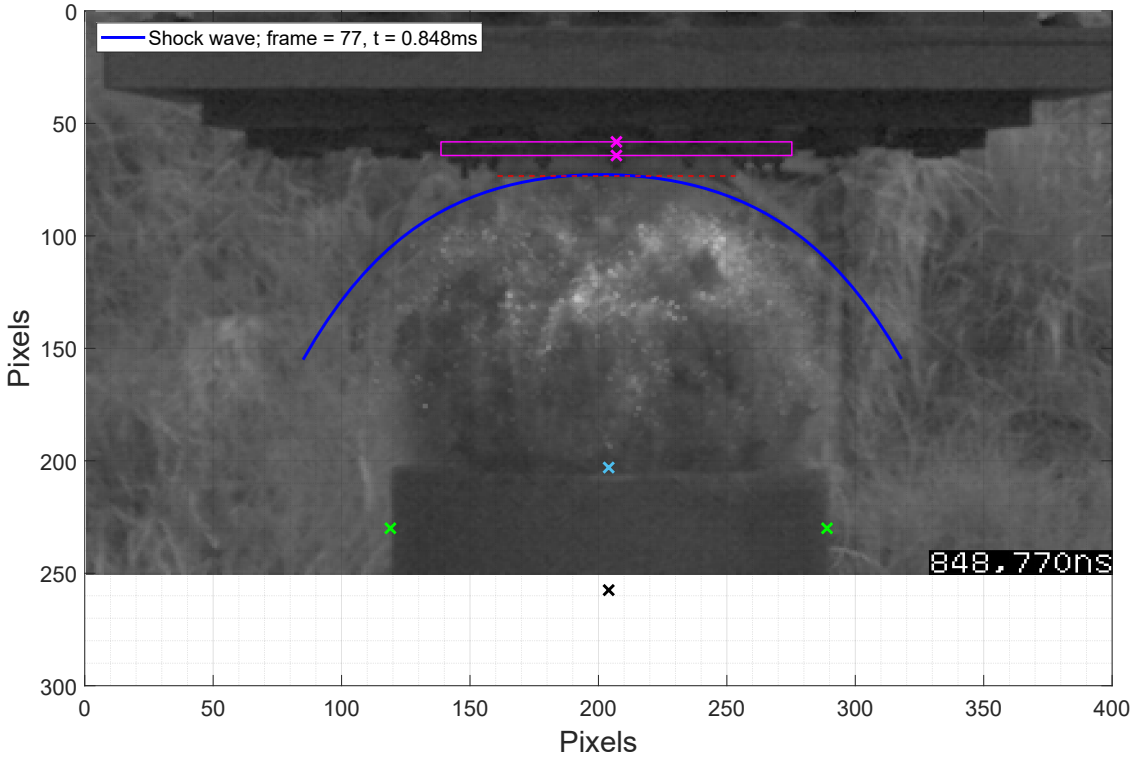

Figure 6.27: Raw image plot with polynomial of the shock wave at t = 0.848 ms for Test 210.

6.4 Discussion

6.4.1 Post Test Photos

In Figure 6.28, photos of a bare plate after testing can be seen. The images show the permanent deformation caused to the plate, creating a uniform domed shape. Figure 6.28a shows the front surface of the plate, which has sand and soot from the explosion on the plate surface. The close-up photos in Figures 6.28c and 6.28d display the indentations from the sand particles impacting the plate.

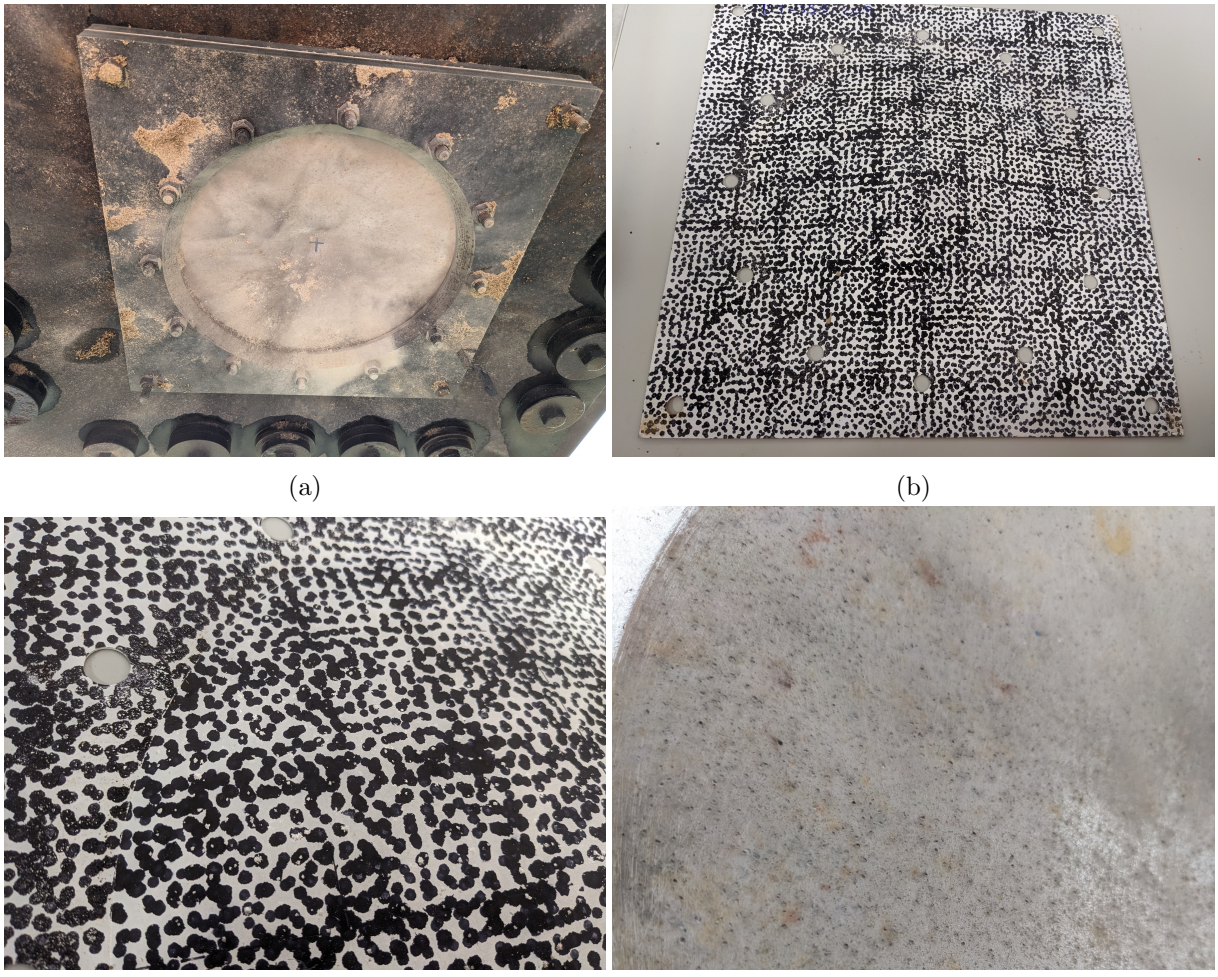

(a) (b)

(c) (d)

Figure 6.28: Post-test photos of a bare plate for a buried charge experiment.

Figure 6.29 displays post-test images of a 50 mm gelatine experiment. The photo in Figure 6.29a shows the gelatine shortly after the explosion, which is coated in sand and soot from the explosion. Figures 6.29b and 6.29c show the gelatine specimen after the surface was wiped clean of any loose particles. Surface damage and permanent discolouration from the ejecta impact are evident here. Finally, Figure 6.29d shows a close-up side-on view of the gelatine. Part of the gelatine has been cut away to allow a clear view of the sand particles embedded in the gelatine.

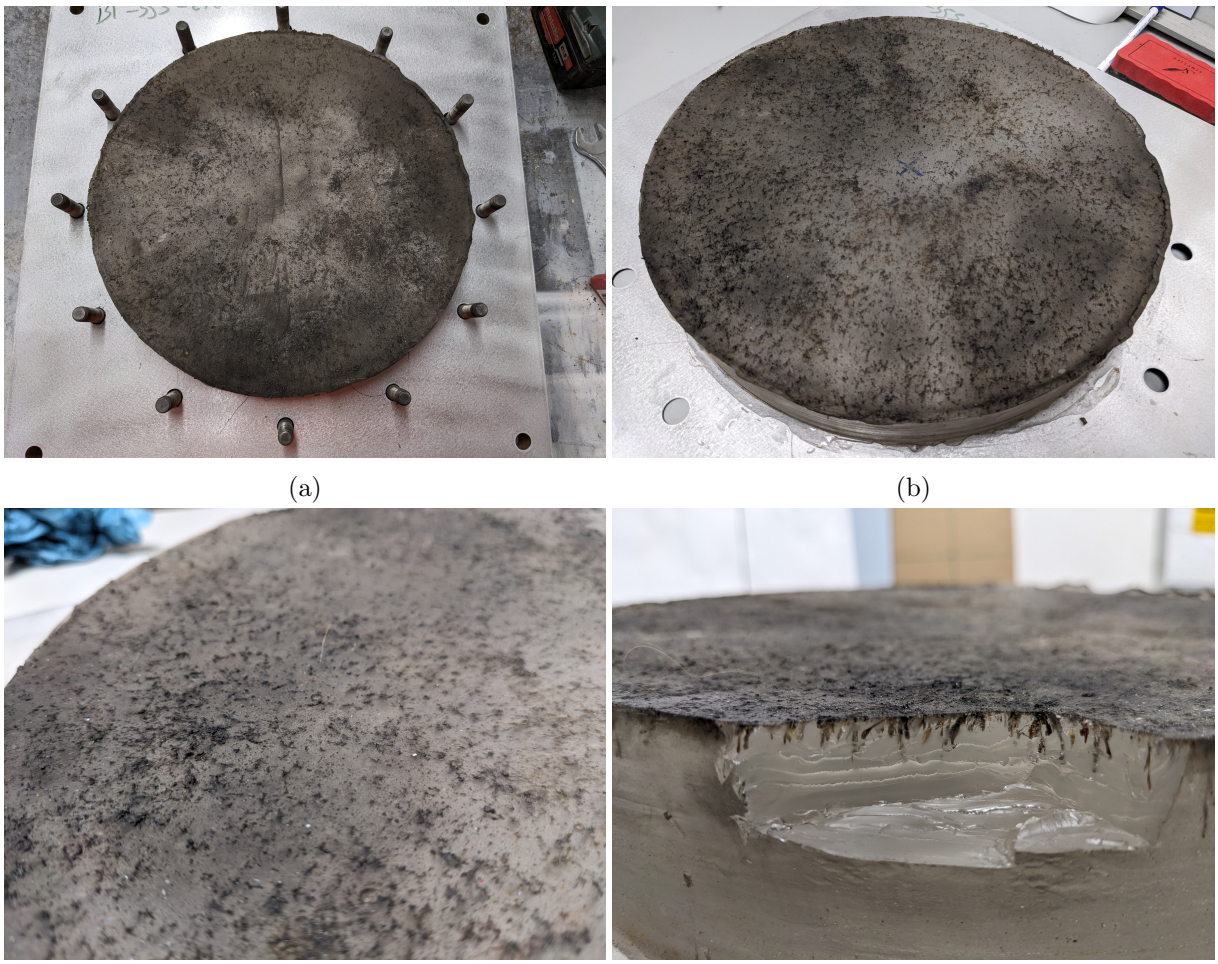

(a) (b)

(c) (d)

Figure 6.29: Post-test photos of a plate with 50 mm of gelatine for a buried charge experiment.

6.4.2 Comparison Between Free-air and Buried Data

Bare Plates

The graphs in Figure 6.30 show the out-of-plane displacement of the target plate for both a free-air charge and a buried charge. The plate response in the buried charge test is delayed by 1 millisecond compared to the free air charge. However, the response once the loading arrives is similar. The plates are initially loaded uniformly and then rise to their peak displacement at the centre of the plate. After the peak displacement, the plates rebounds to a residual cone shape.

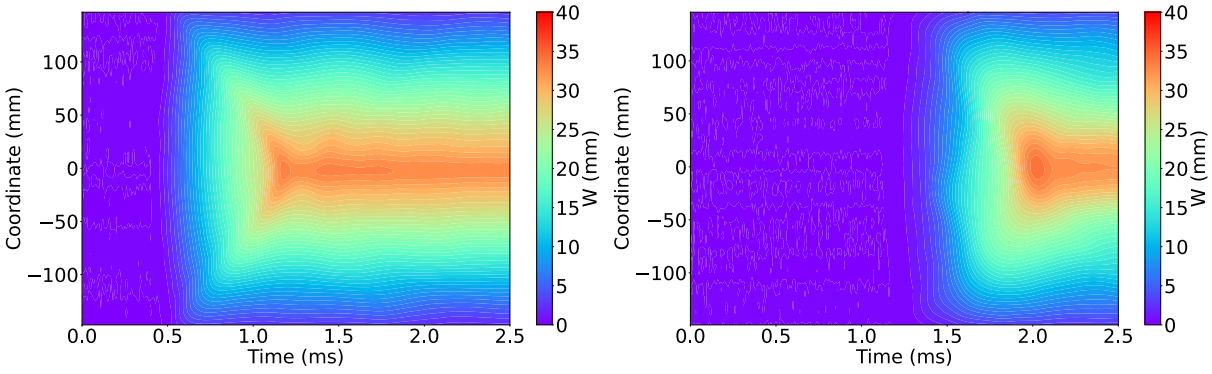

(a) (b)

Figure 6.30: Displacement over time of a bare plate for a) a free air and b) a buried charge.

The graphs in Figure 6.31 show the midpoint displacement-time history of the target plates for all the free air and buried charge experiments. The first graph shows the raw data from the tests and displays the delay in the arrival time of approximately 1 ms for the buried tests. The buried tests have more variation in arrival time, corresponding to a greater variation in the time of peak displacement, and a slower uptake in the displacement. This is caused by the shock wave arriving before the soil, resulting in a two-stage loading. Meanwhile, in the free-air tests, all the loading is applied at once when the shock wave arrives. The magnitude of the peak displacements for the buried tests is more consistent than the free-air tests. The higher consistency may be caused by improvement in clamping the target plates flat before the test.

Shifting the data in time, as shown in Figure 6.31b, enables direct comparison of the displacement peaks. The peak displacements for the buried tests closely align with the middle of the free-air, however, the buried tests have a more significant rebound after the peak displacement. This finding was also reported by Clarke et al. (2020) from their blast experiments (Figure 6.32), where the level of soil confinement was compared. They found that the pressure data has a similar magnitude for a free-air and fully buried charge with the same stand-off distance, but the arrival time is delayed. The burial depth of the charge and the diameter-to-height ratio of the charge cylinder in this PhD and Clarke's investigation were the same. However, the mass of the explosive was considerably different, leading to the conclusion that this relationship between free-air and buried charges of similar stand-off is linked to the shallow burial depth.

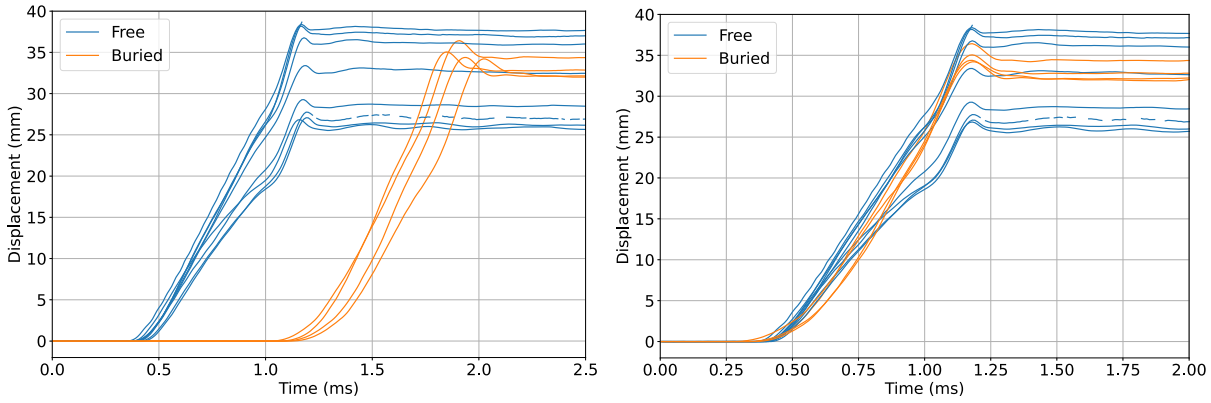

(a) (b)

Figure 6.31: Midpoint displacement for a bare plate for a free air and a buried charge; a) is raw data and b) is shifted so the peak displacement time line-up.

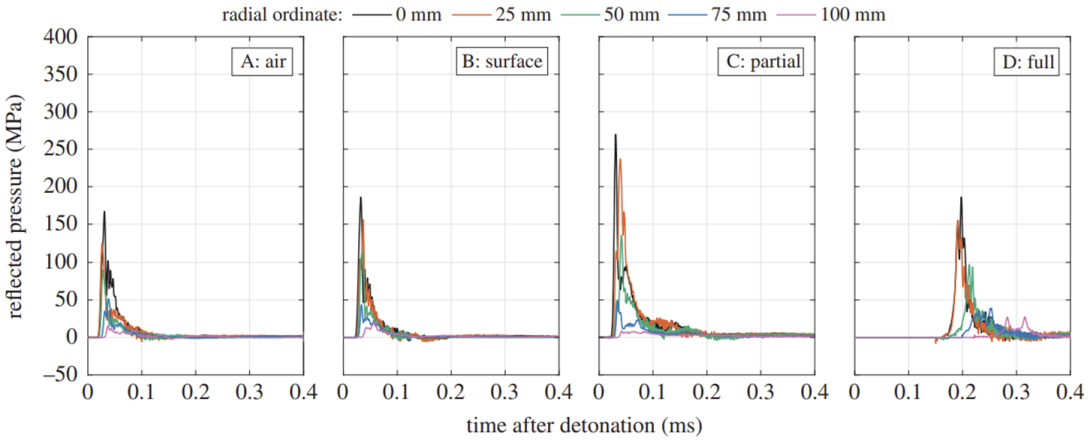

Figure 6.32: Influence of confinement from Clarke et al. (2020).

Figure 6.33 shows a comparison of the mid-line sliced velocity contour plots from free air and buried charge tests. The triangular shape of the velocity contours in Figure 6.33a are well defined, indicating a clear velocity wave travelling inwards to the centre from the edges until the peak velocity at the centre is reached, followed by a velocity inversion that lasted a short time. The buried charge contour plot has a similar form, but with "fuzzier" edges and a localisation of the peak velocities to one side of the midline. The inverted velocity following the peak is spread over a long time and wider central region than in the free air tests.

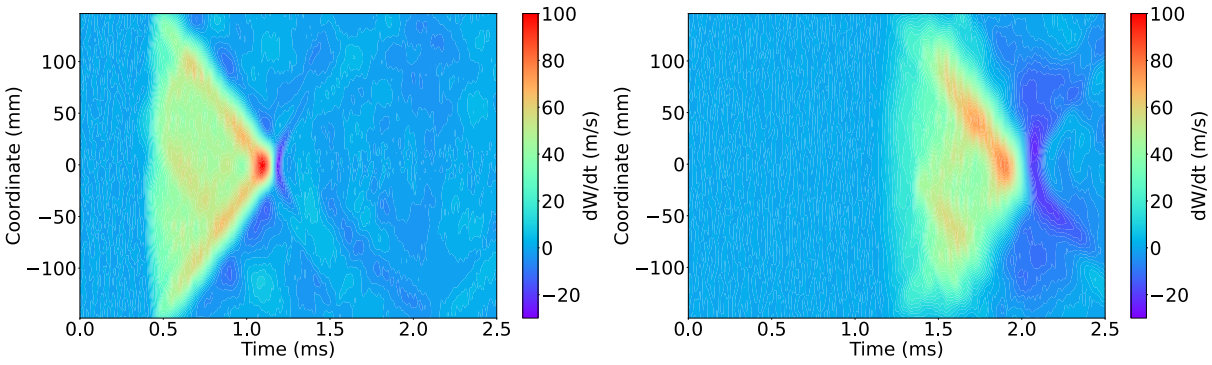

(a) (b)

Figure 6.33: Velocity over time of a bare plate for a) a free air and b) a buried charge.

The graphs in Figure 6.34 show the velocity of the target plate at the centre. The data from all the free air and buried charge experiments are plotted together here. Figure 6.34a shows the raw data from the tests and displays the delay in the arrival time of the buried tests. The data has been shifted on the second graph so all the peak velocities line up. The data from the buried tests clearly shows how the plates are initially loaded slower than the free-air tests. Later, the velocity gradient increases, increasing the velocity in the buried tests up to a similar initial peak velocity as the free-air tests, roughly 50 m/s. This two-stage loading seen in the buried tests is thought to be caused by the soil ejecta arriving after the shock wave. Whereas in the free-air tests, all the loading is applied when the shock wave arrives. The buried plates seem less affected by the velocity wave travelling towards the centre than the free-air plates. This is shown by the free-air tests having a greater difference in the peak velocity from the initial loading and the peak velocity caused by the velocity wave. The buried tests also have a longer elastic rebound time than the free-air test.

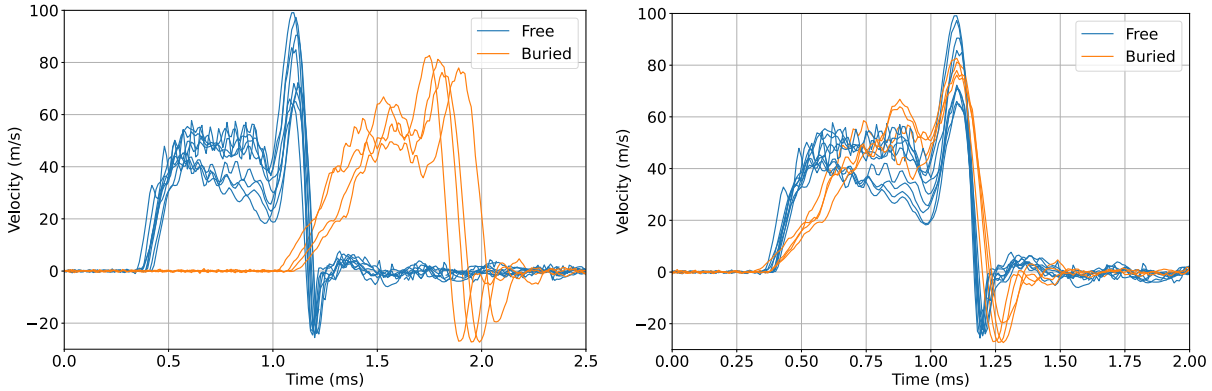

(a) (b)

Figure 6.34: Midpoint velocity for a bare plate for a free air and a buried charge; a) is raw data and b) is shifted so the peak velocity time line-up.

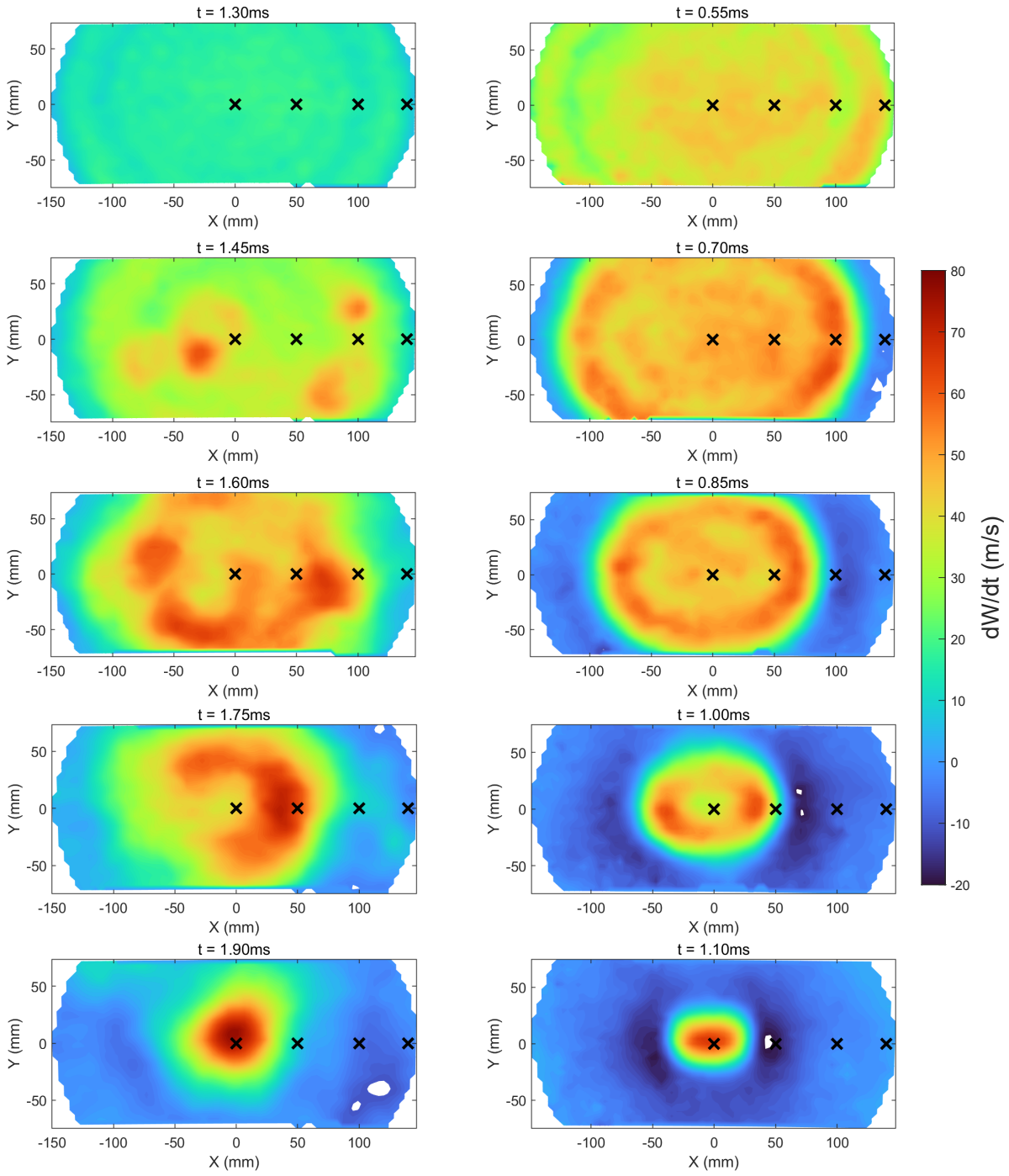

Figure 6.35: Plate velocity across five time steps for a buried (left) and free-air (right) experiment.

Figure 6.35 shows the velocity across the full view of the plate from a buried and free-air explosion at five different time steps. The five time steps are the same time intervals across each test, but the loading from the buried explosion starts later, as seen in previous graphs. These graphs help investigate how the two-stage loading seen in the buried tests affects the spatial behaviour of the plates. The first two graphs show how the blast wave's initial loading causes a uniform response across the full plates. However, the buried plate has half the average velocity across the plate compared to the free-air plate. The other four graphs for the free-air experiment display the plate responding to the clamped boundary condition, causing a velocity

wave to travel across the plate, with the peak at the centre. The rest of the response of the buried experiment is less clear. At 1.45 ms, the plate responds to the soil loading, increasing the velocity across the plate. The loading from the soil covers a 260 mm diameter of the plate, 82.5% of the surface area. Then, between 1.45 ms and 1.60 ms, the velocity wave starts to travel towards the centre of the plate. The peak response from the soil loading is unclear here, as the response is a combination of the soil loading and the velocity wave. The red ring from the velocity wave is wider than in the free-air experiment, possibly caused by the soil ejecta. This velocity wave continues propagating towards the centre, resulting in the peak velocity.

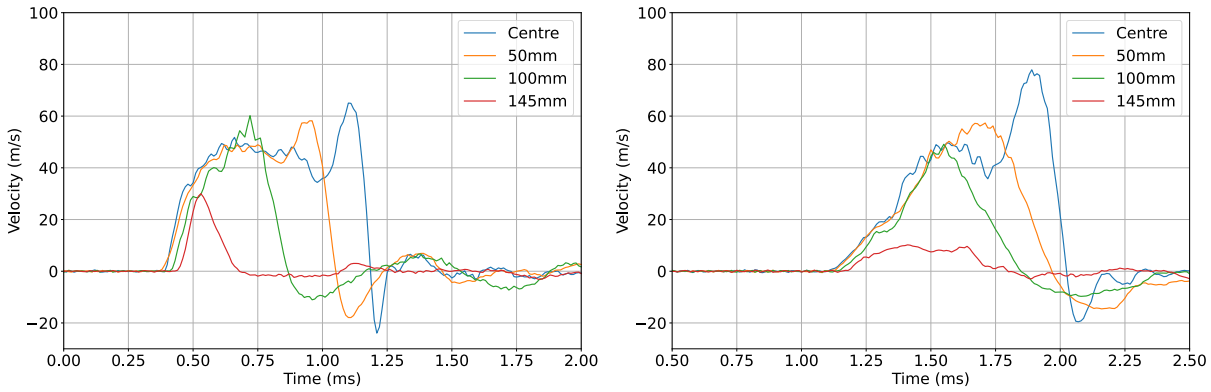

(a) (b)

Figure 6.36: Velocity across the width of a bare plate for a) a free air and b) a buried charge.

The graphs in Figure 6.36 show the velocity over the time of the experiment for a buried and free-air charge at the centre and 50 mm, 100 mm and 145 mm from the centre. As specific impulse is the plate mass multiplied by the velocity, these graphs can be used to compare the impulse transferred to the plate from the blast loading. In the free-air experiment, the initial response from the blast loading lasts 0.1 ms, resulting in a velocity across the plate of 35 – 30 m/s. The plate velocity within a 100 mm radius then continues to increase, at a slower rate, up to a maximum of 50 m/s at 0.6 ms. In the buried experiment, the inner 100 mm radius also reaches a maximum velocity of 50 m/s; however, because the loading arrives in two stages in the buried explosion, this initial loading stage lasts until 1.55 ms. This is double the duration of the free-air loading, affecting the total impulse transfer to the plate.

50 mm Gelatine plates

Results here are compared from the free-air and the buried experiments for target plates with 50 mm of gelatine glued in front. Figure 6.37 displays the out-of-plane displacement of the target plate for both a free-air charge and a buried charge. The target plates show a similar response for the initial displacement up to the maximum transient displacement. A small delay was seen in the arrival of the loading for the buried test, which is consistent with observations from the bare target plates. The free-air plate has a bigger elastic rebound than the buried plate. The buried plate's displacement stays positive throughout the response, whereas the free-air plate rebounds to -5 mm.

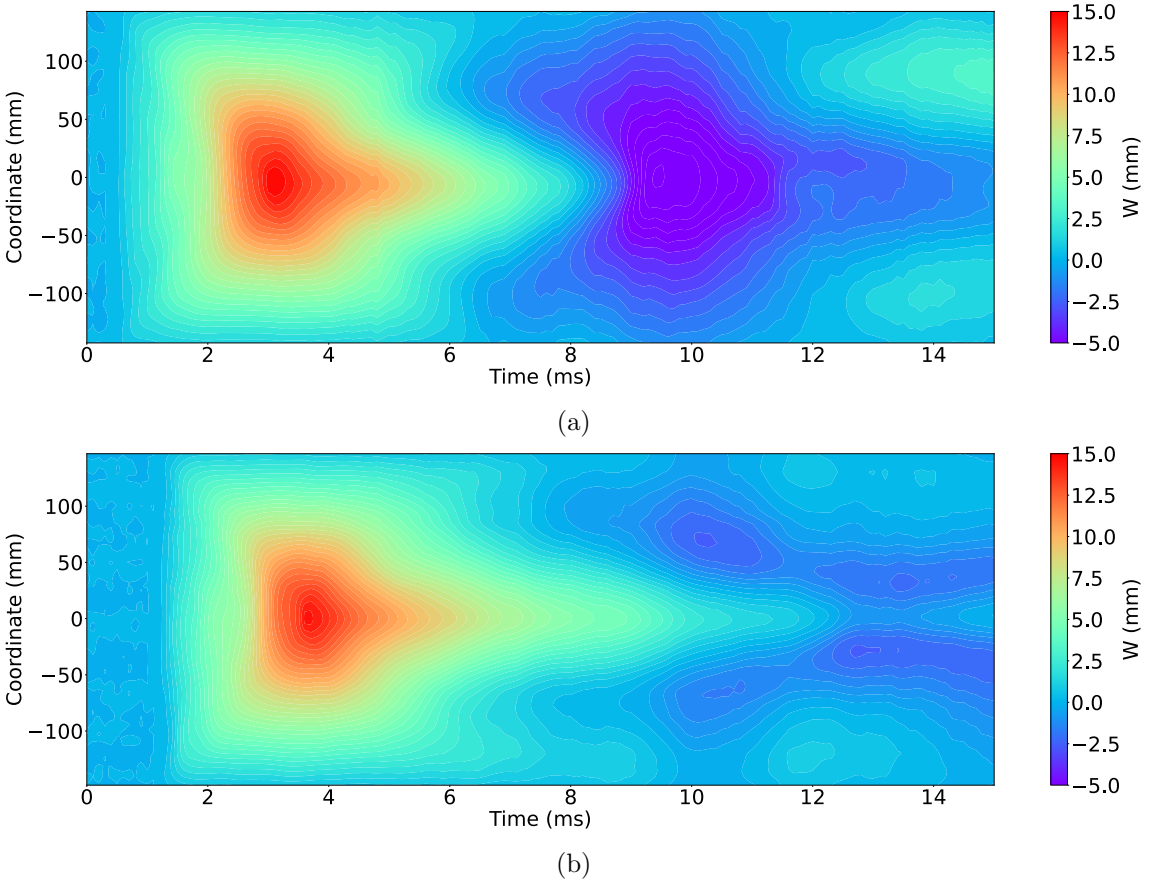

Figure 6.37: Displacement over time of a plate with 50 mm of gelatine for a) a free air and b) a buried charge.

Figure 6.38 depicts the out-of-plane displacement at the centre of the target plates, with the free-air and buried tests plotted together. The first two figures (6.38a and b) show the response of the plates for 15 ms, with Figure 6.38a showing the raw data and Figure 6.38b displaying the data when it is shifted so the maximum positive displacements line up. The figures show a similar response for both types of experiments, with the arrival of the buried signal being delayed by about 0.8 ms. This includes a parallel gradient for the initial positive displacement and a similar halfway relaxation in movement. The free-air and buried results reach a similar peak positive displacement between 13 and 16 mm. The delay is consistent with the delay seen in the bare plate tests. Figure 6.38c and d shows this initial movement up to 4.5 ms and supports the findings. After the maximum positive displacement, all the tests follow a similar decrease in displacement until 7 ms, where the buried results start to level off, and the free-air results continue to decrease to a negative displacement. This difference in behaviour correlates with the deviation in the contour plots discussed previously, Figure 6.37.

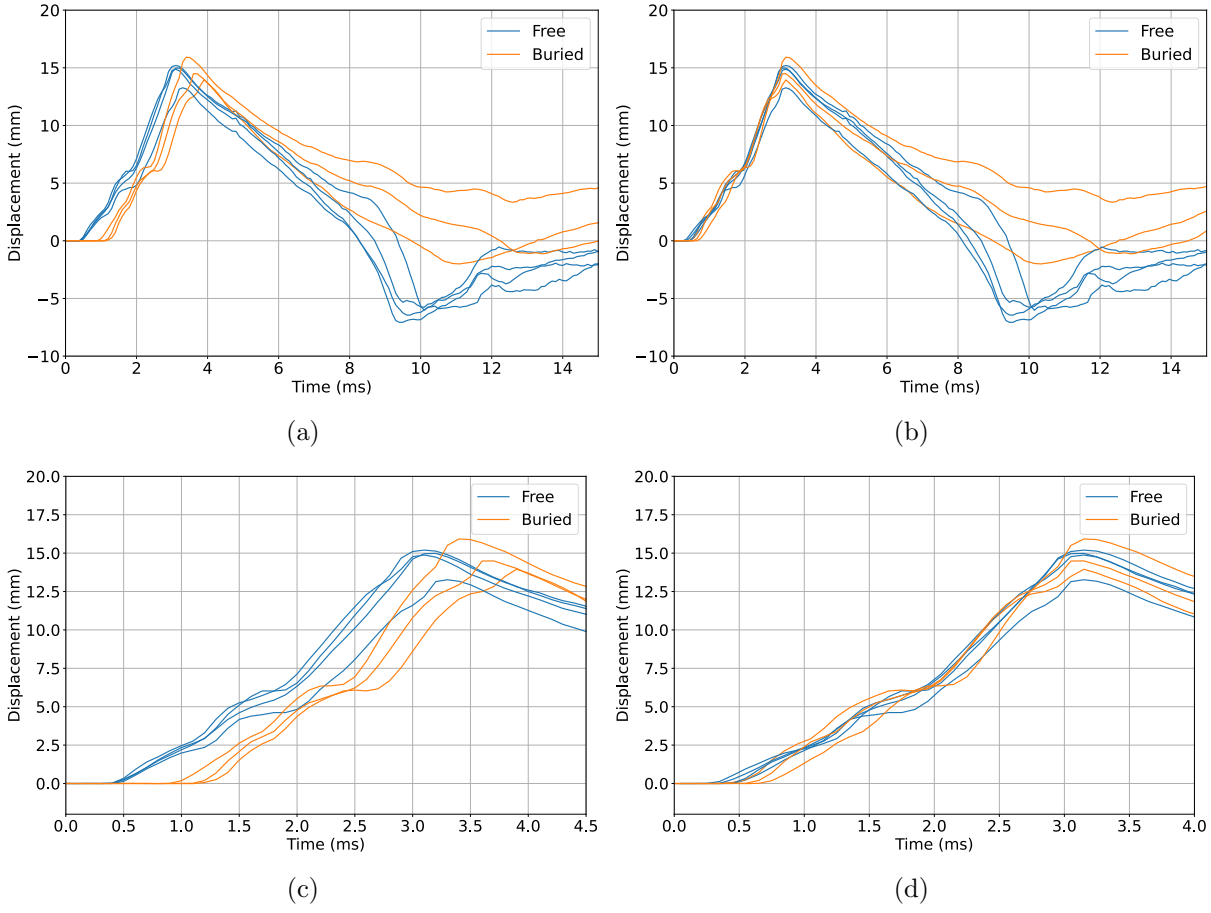

Figure 6.38: Midpoint displacement for plates with 50 mm of gelatine for a free air and a buried charge; a) & c) is raw data and b) & d) are shifted so the peak displacements line-up.

Figure 6.39 show the velocity of the target plate for both a free-air charge and a buried charge. The line slices taken of the target plate at each time step are plotted together on the contour graphs. These graphs also display how the arrival time of the loading is delayed when the charge is buried. Once the loading arrives, the plates see similar complex oscillations in the velocity across the width of the plate. A velocity wave propagates towards the centre, causing the peak velocity. This higher velocity is initially spread across 100 mm of the plate. In the free-air test, this velocity propagates to the midpoint of the plate, causing a final spike at 2.9 ms. Meanwhile, in the buried test, there is a period between 3.2 ms and 3.5 ms, during which the velocity decreases before the final spike is seen at 3.5 ms.

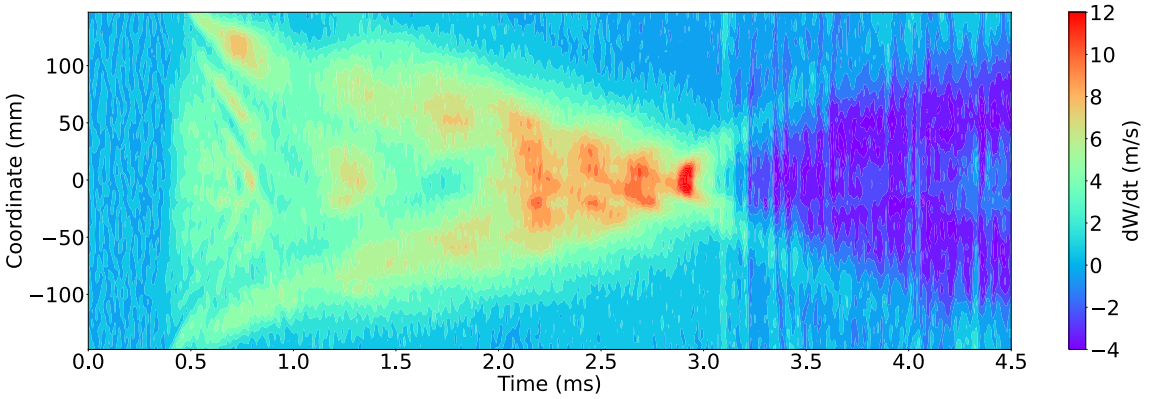

(a)

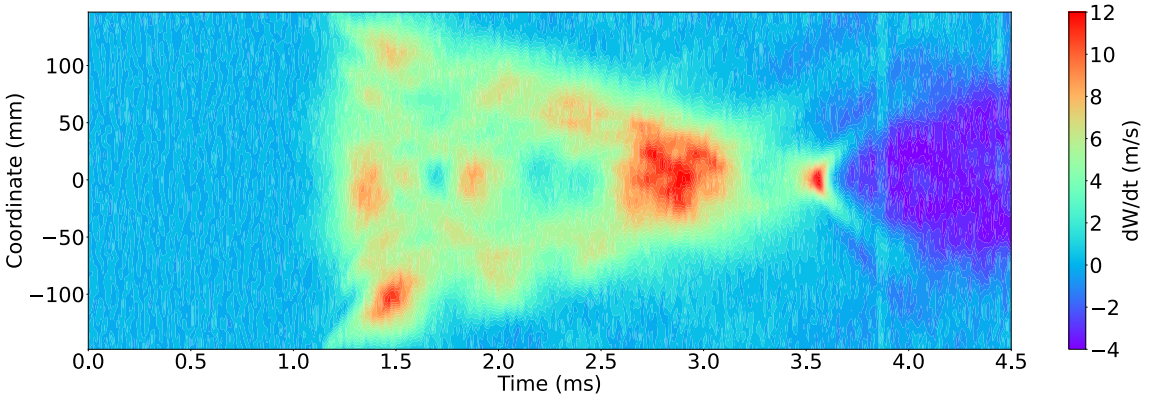

(b)

Figure 6.39: Velocity over time of a plate with 50 mm of gelatine for a) a free air and b) a buried charge.

The graphs in Figure 6.40 show the velocity of the target plate at the centre. The data from all the free air and buried charge experiments are plotted together here. The first graph shows the raw data from the tests and displays the delay in the arrival time of the buried tests. The data has been shifted on the second graph so all the arrival times of the velocities line up. Shifting the buried data helps to illustrate how the oscillations of the plates are very similar for the free-air and buried set-up. This supports the argument that this complex oscillating behaviour is linked to the movement of the gelatine specimen and not only the loading from the explosion. These signals deviate after 2 ms, with the buried tests having a higher initial peak velocity, then relaxing before receiving a sharp spike in velocity. Meanwhile, the free-air tests rise to a lower initial peak velocity and remain there before receiving a sharp spike in velocity. This was also seen in the contour plots in shown Figure 6.39.

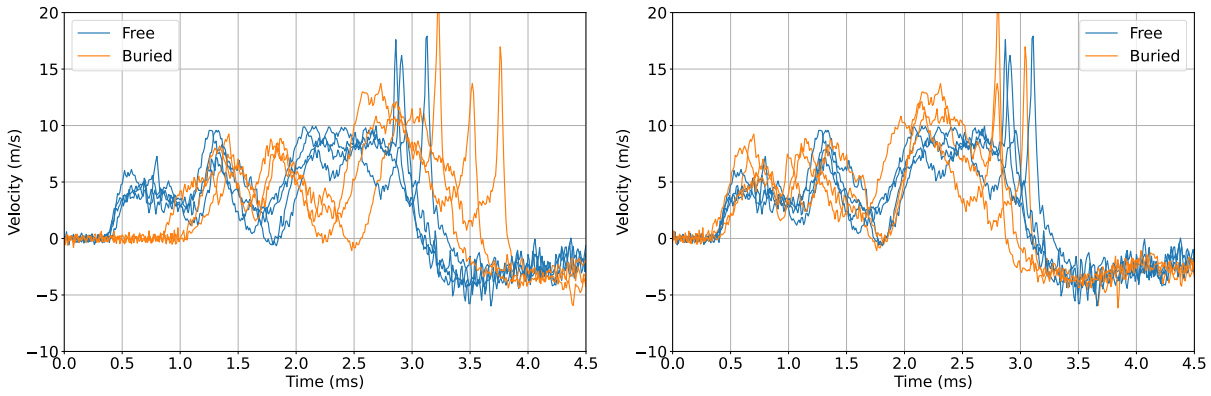

(a) (b)

Figure 6.40: Midpoint velocity for plates with 50 mm of gelatine for a free air and a buried charge; a) is raw data and b) is shifted so the arrival times line-up.

6.5 Summary of Findings

In this chapter, the Appliqué blast testing apparatus developed in Chapter 5 was adapted to investigate the behaviour of deformable plates from buried explosions. The response of fully clamped Aluminium plates with and without 50 mm of synthetic gelatine in front was compared to data from the free-air experiments. In both the bare and gelatine experiments, the plates responded later in the buried tests than in the free-air tests. The peak transient displacement and velocity in both the bare and gelatine experiments were found to be the same for a free-air and a buried charge. Showing that a shallow buried charge produces the same amount of loading to a target as the equivalent free-air charge. In the bare plate tests, the velocity data for the buried charge showed a plate response of two stages. This is linked to the loading from the soil arriving later than the shock wave. This was confirmed by using a third side-on high-speed camera to record the detonation of the buried charge. By tracking the arrival time of the shock wave and the soil, the gap in the loading of the plate was confirmed. The position of the soil as it arrived on the plate was also used to explain differences in the plate displacement profiles seen in the back surface data. The arrival time of the shock wave on the gelatine surface was also investigated to look at the time difference between that and the plate response. The arrival time of the soil and the interaction of the soil with the gelatine was not further investigated in this PhD. However, these video recordings and the final condition of the gelatine could be used in future work to explore how the soil particles interact with the gelatine surface.

Chapter 7

Conclusions and Future Work

7.1 Conclusions

This thesis has investigated the influence synthetic gelatine has on the structural response of aluminium panels from blast loading. A novel experimental setup was developed to measure the effect synthetic gelatine has on the response of a clamped aluminium plate to an explosion. The addition of gelatine reduced the peak displacement and velocity of the target plate. It was also found to increase the time to peak displacement and velocity. The gelatine was found to cause a lot of oscillations of the plate long after the loading had finished, lasting over 50 ms.

The novel experimental setup developed for free-air blast was adapted to investigate the behaviour of deformable plates and synthetic gelatine in buried explosions. The peak transient displacement and velocity in both the bare and gelatine experiments were found to be the same for a free-air and a buried charge. Showing that a shallow buried charge produces the same amount of loading to a target as the equivalent free-air charge in far-field explosions. In both the bare and gelatine experiments, the plates responded later in the buried tests than in the free-air tests. In the bare plate tests, the buried charge data showed a plate response of two stages. By tracking the arrival time of the shock wave and the soil, the plate loading gap was confirmed to be caused by the soil arriving later than the shock wave. The position of the soil as it arrived on the plate was also used to explain differences in the plate displacement profiles seen in the back surface data.

Quasi-static and high strain-rate experiments were conducted to determine the compressive properties of synthetic gelatine. Manufacturing gelatine specimens was refined to produce repeatable results during the experiments. The quasi-static and split-Hopkinson pressure bar (SHPB) experiments found that synthetic gelatine showed a clear strain rate sensitivity, with the final stress increasing as the strain rate of the experiment increased. Bulk modulus and Poisson's ratio were estimated for gelatine from the quasi-static experiments to refine a numerical model. These properties were used to develop a simplified numerical simulation of gelatine's response to compressive loading.

The simulation was developed further to model the response of blast-loaded aluminium/gelatine panels. The model for the bare plate set-up was found to correlate very well with the experimental data. The aluminium/gelatine simulation showed behaviour similar to that of the experiments. The numerical model was harnessed to investigate how the gelatine behaves during blast loading. Stresses were found to propagate across the width of the gelatine, possibly causing the complex oscillations seen in the plate velocity data from the blast experiments with 30 mm and 50 mm of gelatine. This numerical model is a step toward understanding how a blast wave from an explosion propagates through synthetic gelatine.

7.2 Future Work

This study produced a simplified numerical simulation of blast-loaded hybrid gelatine/aluminium panels. The development of this model could be further studied in future work. A more comprehensive characterisation of a range of strain rates and loading conditions is needed to develop this model into a full constitutive model for synthetic gelatine. This would include a more comprehensive SHPB experimental study to improve on experiments carried out in this PhD and include a bigger range of strain rates. Using forward and reverse Taylor impact tests could reduce some of the difficulties found with SHPB experiments. Experimental studies with loading conditions other than uniaxial would enhance the understanding of the spatial behaviour of synthetic gelatine.

The experimental method developed in this PhD to investigate the influence synthetic gelatine has on the loading from an explosion could be used for further investigations. For instance, the side-on camera could be used to explore how the shock wave from a free-air blast interacts with the structure. The test series could be expanded to include a range of sand-off distances and different concentrations of synthetic gelatine, such as 20%. This would further develop the understanding of how synthetic gelatine influences the loading from an explosion.

The analysis from the buried charge study focused on comparing free-air and buried loading and supporting findings from the DIC data in the bare plate experiments. For future buried experiments that utilise a side-on camera, a zebra board should be placed behind the setup to increase contrast between the edge of the soil eject and the background on the raw image. This could improve accuracy when tracking the shape of the soil ejecta. During the buried charge experiment where gelatine was in front of the target plate, sand particles penetrated into the surface of the gelatine. Future work could perform post-test analysis, e.g. CT scans, on the gelatine to investigate the spatial distribution of the sand particles and further our understanding of the loading transfer from a buried explosion. These gelatine specimens could also be analysed to determine the penetration depth of the soil and subsequently investigate the velocity of the soil on impact.

Bibliography

Aslam, M. A., Rayhan, S. B., Ke, Z. and Yu, W. J. (2020), 'Ballistic gelatin lagrange mooney-rivlin material model as a substitute of bird in finite element bird strike case studies', *Latin American journal of solids and structures* **17**, 1–15.

Bacon, C. (1998), 'An experimental method for considering dispersion and attenuation in a viscoelastic hopkinson bar', *Experimental Mechanics* **38**, 242–249.

Bergeron, D. M., Walker, R. and Coffey, C. (1998), *Detonation of 100-gram anti-personnel mine surrogate charges in sand, a test case for computer code validation*, National Defence, Defence Research Establishment Suffield.

Clarke, S., Fay, S., Warren, J., Tyas, A., Rigby, S. and Elgy, I. (2014), 'A large scale experimental approach to the measurement of spatially and temporally localised loading from the detonation of shallow-buried explosives', *Measurement Science and Technology* **26**.

Clarke, S., Fay, S., Warren, J., Tyas, A., Rigby, S., Reay, J., Livesey, R. and Elgy, I. (2015), 'Geotechnical causes for variations in output measured from shallow buried charges', *International Journal of Impact Engineering* **86**, 274–283.

Clarke, S., Rigby, S., Fay, S., Barr, A., Tyas, A. and Gant, M. (2020), 'Characterization of buried blast loading', *The Royal Society. Collection* .

Clear Ballistics (2023), '10% ballistic gelatin fbi block.'. (accessed: 19.12.2023).
URL: *https://www.clearballistics.com/shop/10-ballistic-gelatin-fbi-block/*

Clemedson, C. J. (1956), 'Blast injury', *Physiological Reviews* **36**(3), 336–354.

Clemedson, C. J. and Criborn, C. O. (1955), 'Mechanical response of different parts of a living body to a high explosive shock wave impact.', *The American journal of physiology* **181 3**, 471–6.

Clemedson, C. J., Frankenberg, L., Jönsson, A., Pettersson, H. and Sundqvist, A. B. (1969), 'Dynamic response of thorax and abdomen of rabbits in partial and whole-body blast exposure', *American Journal of Physiology-Legacy Content* **216**(3), 615–620.

Clemedson, C. J. and Jönsson, A. (1961), 'Transmission of elastic disturbances caused by air shock waves in a living body', *Journal of Applied Physiology* **16**(3), 426–430.

Clemedson, C. J. and Pettersson, H. (1955), 'Propagation of a high explosive air shock wave through different parts of an animal body', *The American journal of physiology* **184**(1), 119—126.

Cronin, D. S. and Falzon, C. (2011), 'Characterization of 10% ballistic gelatin to evaluate temperature, aging and strain rate effects', *Experimental Mechanics* **51**, 1197–1206.

Cronin, D. S., Williams, K. and Salisbury, C. (2011), 'Physical surrogate leg to evaluate blast mine injury', *Military Medicine* **176**(12), 1408–1416.

Curry, R. (2011), Implementation of viscoelastic hopkinson bars, Master's thesis, University of Cape Town.

Curry, R. (2017), Response of plates subjected to air-blast and buried explosions, PhD thesis, University of Cape Town.

Curry, R., Cloete, T. J. and Govender, R. A. (2012), Implementation of viscoelastic hopkinson bars, *in* '10th International Conference on the Mechanical and Physical Behaviour of Materials under Dynamic Loading'.

Curry, R. and Langdon, G. (2017), 'Transient response of steel plates subjected to close proximity explosive detonations in air', *International Journal of Impact Engineering* **102**, 102–116.

Cuvillo, R. D., Pernas-Sanchez, J., Artero-Guerrero, J. A. and Lopez-Puente, J. (2017), Impact of soft body material, an experimental and numerical approach using hopkinson tube: application to substitute bird, *in* '11th European LS-DYNA Conference 2017, Salzbury, Austria'.

Davids, S., Langdon, G. and Nurick, G. (2017), 'The influence of charge geometry on the response of partially confined right circular stainless steel cylinders subjected to blast loading', *International Journal of Impact Engineering* **108**, 252–262.

Dobratz, B. M. and Crawford, P. C. (1985), Llnl explosives handbook: properties of chemical explosives and explosives and explosive simulants, Technical report, Lawrence Livermore National Lab. (LLNL), Livermore, CA (United States).

Elgy, I. D., Williams, G. H., Gibson, C. S. and Pope, D. J. (2020), 'Response of hybrid iii and mil-lx atd legs to explosively driven vehicle floor loading', *Journal of Biomechanics* **101**, 109618.

Farrimond, D. G., Rigby, S. E., Clarke, S. D. and Tyas, A. (2022), 'Time of arrival as a diagnostic for far-field high explosive blast waves', *International Journal of Protective Structures* **13**(2), 379–402.

Fitzgerald, L. (2019), Final report, Master's thesis, University of Cape Town.

Fuller, B. J. (2018), Loading from Shallow Buried Blast Events and the Effect on Plate Deformations, PhD thesis, University of Sheffield.

Gilson, L., Rabet, L., Imad, A., Kakogiannis, D. and Coghe, F. (2016), 'Development of a numerical model for the ballistic penetration of fackler gelatine by small calibre projectiles', *The European Physical Journal Special Topics* **225**, 375–384.

Greer, A. (2006), Numerical modeling for the prediction of primary blast injury to the lung., Master's thesis, University of Waterloo.

Grujicic, M., Pandurangan, B. and Cheeseman, B. A. (2006), 'The effect of degree of saturation of sand on detonation phenomena associated with shallow-buried and ground-laid mines', *Shock and Vibration* **13**.

Hampton, C. E., Kleinberger, M., Schlick, M., Yoganandan, N. and Pintar, F. A. (2019), 'Analysis of force mitigation by boots in axial impacts using a lower leg finite element model', *Stapp Car Crash Journal* **63**, 267–289.

ICBL-CMC (2024), 'Landmine monitor 2024, geneva.'. (International Campaign to Ban Landmines).
URL: *https://www.the-monitor.org/reports/landmine-monitor2024*

iDICs (2018), 'A good practices guide for digital image correlation'. (International Digital Image Correlation Society).
URL: *https://doi.org/10.32720/idics/gpg.ed1.*

Jussila, J. (2004), 'Preparing ballistic gelatine—review and proposal for a standard method', *Forensic Science International* **141**(2), 91–98.

Karahan, M., Karahan, E. A., and Karahan, N. (2018), 'Blast performance of demining footwear: Numerical and experimental trials on frangible leg model and injury modeling', *Journal of Testing and Evaluation* **46**, 666–679.

Kolsky, H. (1949), 'An investigation of the mechanical properties of materials at very high rates of loading', *Proceedings of the Physical Society. Section B* **62**(11), 676.

Kwon, J. and Subhash, G. (2010), 'Compressive strain rate sensitivity of ballistic gelatin', *Journal of Biomechanics* **43**(3), 420–425.

Langdon, G., Ozinsky, A. and Chung Kim Yuen, S. (2014), 'The response of partially confined right circular stainless steel cylinders to internal air-blast loading', *International Journal of Impact Engineering* **73**, 1–14.

LST (2012), *LS-DYNA KEYWORD USER'S MANUAL*, volume ii - material models edn.

Menkes, S. B. and Opat, H. J. (1973), 'Broken beams', *Experimental Mechanics* **13**, 480–486.

Mooney, M. (1940), 'A theory of large elastic deformation', *J. Appl. Phys.* **11**, 582–592.

Nasri, M. T., Abbassi, F., Ahmad, F., Makhloufi, W., Ayadi, M., Mehboob, H. and Choi, H. S. (2023), 'Experimental and numerical investigation of sheet metal failure based on johnson-cook model and erichsen test over a wide range of temperatures', *Mechanics of Advanced Materials and Structures* **30**, 2087 – 2100.

Nemat-Nasser, S. (2000), Introduction to high strain rate testing, *in* 'Mechanical Testing and Evaluation', ASM International.

Neuberger, A., Peles, S. and Rittel, D. (2007), 'Scaling the response of circular plates subjected to large and close-range spherical explosions. part i: Air-blast loading', *International Journal of Impact Engineering* **34**(5), 859–873.

Park, J., Yoon, S., Kwon, T.-H. and Park, K. (2017), 'Assessment of speckle-pattern quality in digital image correlation based on gray intensity and speckle morphology', *Optics and Lasers in Engineering* **91**, 62–72.

Phillips, Y. Y., Mundie, T. G., Yelverton, J. T. and Richmond, D. R. (1988), 'Cloth ballistic vest alters response to blast.', *The Journal of trauma* **28**, 149–52.

Pickering, E., Chung Kim Yuen, S., Nurick, G. and Haw, P. (2012), 'The response of quadrangular plates to buried charges', *International Journal of Impact Engineering* **49**, 103–114.

Ramezani, M., Ripin, Z. M. and Ahmad, R. (2009), 'Plastic bulging of sheet metals at high strain rates', *International Journal of Advanced Manufacturing Technology* **48**, 847–858.

Ravikumar, N., Noble, C., Cramphorn, E. and Taylor, Z. A. (2015), 'A constitutive model for ballistic gelatin at surgical strain rates', *Journal of the Mechanical Behavior of Biomedical Materials* **47**, 87–94.

Read, J., Hazael, R. and Critchley, R. (2022), 'Soft tissue simulants for survivability assessment — a sustainability focussed review', *Applied Sciences* **12**(10).

Reay, J. J. (2014), An Investigation into the Dynamic Response of Cardboard Honeycombs, PhD thesis, University of Sheffield.

Reu, P. (2013), 'Stereo-rig design: Stereo-angle selection —part 4', *Society for Experimental Mechanics - Experimental Techniques* **37**.

Richler, D. and Rittel, D. (2014), 'On the testing of the dynamic mechanical properties of soft gelatins', *Experimental Mechanics* **54**, 805–815.

Rigby, S., Fay, S., Clarke, S., Tyas, A., Reay, J., Warren, J., Gant, M. and Elgy, I. (2016), 'Measuring spatial pressure distribution from explosives buried in dry leighton buzzard sand', *International Journal of Impact Engineering* **96**, 89–104.

Rigby, S., Fuller, B. and Tyas, A. (2018), Validation of near-field blast loading in ls-dyna, *in* '5th International Conference on Protective Structures. Poznan, Poland'.

Salisbury, C. and Cronin, D. (2009), 'Mechanical properties of ballistic gelatin at high deformation rates', *Experimental Mechanics* **49**, 829–840.

Saraf, H., Ramesh, K., Lennon, A., Merkle, A. and Roberts, J. (2007), 'Mechanical properties of soft human tissues under dynamic loading', *Journal of Biomechanics* **40**(9), 1960–1967.

Schutte, Z. (2017), Determining the load paths from seat to occupant during under body blasts, PhD thesis, University of Cape Town.

Singh, B. and Basri, M. A. (2022), 'Lower limb response to anti-personnel landmine blast explosions: Injury assessment and mitigation strategies', *Human Factors and Mechanical Engineering for Defense and Safety* **6**.

Spear, A. M., Davies, E. M., Taylor, C., Whiting, R., Macildowie, S., Kirkman, E., Midwinter, M. and Watts, S. A. (2015), 'Blast wave exposure to the extremities causes endothelial activation and damage', *Shock (Augusta, Ga.)* **44**(5), 470—478.

Spranghers, K., Vasilakos, I., Lecompte, D., Sol, H. and Vantomme, J. (2013*a*), 'Identification of the plastic behavior of aluminum plates under free air explosions using inverse methods and full-field measurements', *International Journal of Solids and Structures* **51**(1), 210–226.

Spranghers, K., Vasilakos, I., Lecompte, D., Sol, H. and Vantomme, J. (2013*b*), 'Numerical simulation and experimental validation of the dynamic response of aluminum plates under free air explosions', *International Journal of Impact Engineering* **54**, 83–95.

Thom, C. (2009), Soft materials under air blast loading and their effect on primary blast injury, Master's thesis, University of Waterloo.

Vedantam, K., Bajaj, D., Brar, N. S. and Hill, S. (2006), 'Johnson - cook strength models for mild and dp 590 steels', *AIP Conference Proceedings* **845**(1), 775–778.

Wen, Y., Xu, C., Wang, H., Chen, A. and Batra, R. (2013), 'Impact of steel spheres on ballistic gelatin at moderate velocities', *International Journal of Impact Engineering* **62**, 142–151.

Wolf, S. J., Bebarta, V. S., Bonnett, C. J., Pons, P. T. and Cantrill, S. V. (2009), 'Blast injuries', *The Lancet(London, England)* **374(9687)**, 405–415.